Transient multi-messenger astrophysics with imaging atmospheric Cherenkov telescopes

Halim Ashkar

université PARIS-SACLAY

Transient Multi-messenger Astrophysics with Imaging Atmospheric Cherenkov Telescopes

Astrophysique transitoire et multimessager avec les télescopes à imagerie Tcherenkov atmosphérique

Thèse de doctorat de l'université Paris-Saclay

École doctorale n° 576, Particules, Hadrons, Énergie, Noyau, Instrumentation, Imagerie, Cosmos et Simulation (PHENIICS)
Spécialité de doctorat : Astroparticules & Cosmologie
Unité de recherche : Université Paris-Saclay, CEA, Département de Physique des Particules, 91191, Gif-sur-Yvette, France
Référent : Faculté des sciences d'Orsay

Thèse présentée et soutenue à Paris-Saclay, le 29/09/2021, par

Halim ASHKAR

Composition du Jury

Tiina SUOMIJARVI Professeure, Université Paris-Saclay (IJCLab)	Présidente
Francesco LONGO Professeur associé, Université de Trieste (INFN)	Rapporteur & examinateur
Frédérique MARION Directrice de recherche, CNRS (LAPP)	Rapporteur & examinatrice
Jean-Pierre ERNENWEIN Professeur, Aix-Marseille Université (CPPM)	Examinateur
Andreas ZECH Maître de Conférences, Observatoire de Paris (LUTH)	Examinateur

Direction de la thèse

Fabian SCHUSSLER Ingénieur-Chercheur, Paris-Saclay (CEA/IRFU)	Directeur de thèse

Thèse de doctorat

NNT : 2021UPASP090

To my father Shawkat Ashkar

Acknowledgements

To Fabian Schüssler, my PhD supervisor who created this project and gave me this great opportunity. I am very grateful for having the chance to work with you on multi-messenger and transient astrophysics. Aside from science, I have learned a lot from you, especially when it comes to asking the right questions, and seeking for answers. I also learned on the micromanagement scale how to organize my work and communicate it clearly. I want to tank you for giving me the opportunity to be part of very interesting projects, for helping me in increasing my visibility in the astrophysical community and for pushing me further to become able to do research independently. Also a big thank you for your thorough review of this manuscript.

To the CEA/Irfu gamma-ray group and the H.E.S.S. members who made my journey more enjoyable and who always treated me as equal even if I was still a beginner scientist. I want to thank Jean-Francois and Emanuel for fruitful discussion during the lunch breaks, Francois, the head of A&R, for the help he provided me in the H.E.S.S. analysis and my first office-mate, Thomas, who I spent most coffee breaks with and learned a lot from. It has been a while since I visited the office but I hope that our ”garden” is still alive. I also want to thank H.E.S.S. members like Mathieu for exchange on the H.E.S.S. software and the people with whom I worked on projects with like Clemens, Sylvia, Alessandro, C, Gavin, Stefan, Dima, Heike and many more. I also want to thank the A&R reviewers, the internal referees and the collaboration members who provided feedback on my papers. I had the opportunity to learn from the best scientist in the H.E.S.S., LST and CTA collaborations and I had the chance to witness discoveries that will forever stay in my mind. I want to also thank the CEA/Irfu (DPhP) and the PHENIICS doctoral school heads for funding my thesis. Finally, a big thank you to Monica who was Fabian's first PhD student, my friend and colleague who I am still working with on gravitational waves follow-ups. I will always remember the exciting times when we were waiting patiently for a GW event to occur and I am looking forward for the revival of these moments in O4 (hopefully). Working with you has been a great experience and a lot of fun.

I want to also thank the H.E.S.S. on-site crew for their hospitality during my one month shift in Namibia. I want to mention Albert, who we lost this year to COVID-19. His barbecues were one of the highlights of my trip, hope he rests in peace. I am grateful that I had the chance to speak again with Albert few months before he died during one of my expert on call shifts. He was at the time taking extra shifts alongside the other on-site members to ensure the continuity of data acquisition during the pandemic.

I want to especially thank the the referees Francesco Longo and Frédérique Marion for their review of this manuscript and the members of the Jury Jean-Pierre Ernenwein, Tiina Suomijarvi, Andreas Zech and Fabian Schüssler.

On a personal note, I am grateful to the friends that I made at CEA. Monica, Luccia, Anke, Patrick and Alessandro, Frederica, Valentin, Atilla and Hector you made this journey more bearable. I will never forget the collaboration meeting that we attended together with Monica and Luccia in Annecy and the fun times we spent together inside and outside the office. I wish you all the best for your careers. I also want to thank the other PhD students and postdocs at CEA, especially the organizers of the Friday lunches.

The past two years have not been easy. The world got hit by the COVID-19 pandemic that not only affected our physical health, our economies and our lifestyle but also our mental health. In addition to that, my beautiful country of origin, Lebanon, is suffering from an economical, financial, political and security crisis that is affecting us all in addition to the aftermath of the Beirut port explosion. I hope that it will someday regain its prosperity. These past few years, I also suffered close personal losses that shaped my life, my beloved father Shawkat and uncles Asmat and Robert Gemayel. I want to thank my childhood friends from Lebanon, in addition to my older cousin Oliver in Vienna and the friends that I made in France during my studies for continuous and mutual support. I want to mention all the COVID-19 victims, hoping to shed the light on the importance of research and advancement in all fields to ensure a better quality of life and prosperity for the human race, and France, my home, the country I came in to follow my dreams, and fell in love with its charm.

Last but not least, to my (extended) family, I love you all and I am gratefully to have you by my side. I want to thank my mother Micheline who always roots for me. She and my father are the people responsible for what I am today and what I will ever be.

Contents

Synthèse

Pour étudier le ciel, quatre messagers astronomiques sont connus et utilisés de nos jours: les ondes électromagnétiques, les rayons cosmiques, les neutrinos et les ondes gravitationnelles. Le spectre des ondes électromagnétiques s'étend sur plus de 24 ordres de grandeur en énergie, des ondes radio, jusqu'aux rayons gamma à très hautes énergies de l'ordre du Téraélectronvolt (TeV). Ces rayons à très hautes énergies sont créés par des processus non-thermiques, notamment l'accélération de particules dans des milieux astrophysiques. Le rayonnement synchrotron et le rayonnement Compton inverse sont des processus d'émission résultant de ces accélérations. Les lieux astrophysiques candidats pour accueillir de tels événements sont nombreux: les noyaux actifs de galaxies, les supernovæ, les collisions d'objets compacts, les événements de rupture par effet de marée et beaucoup d'autre. Certains de ces lieux astrophysiques ont des émissions multi-messagers et transitoires. Par exemple, la collision d'étoiles à neutron peut aboutir à l'émission d'ondes gravitationnelles, d'ondes électromagnétiques, dont des sursauts gamma et des sursauts radio rapides ainsi que des neutrinos détectables sur Terre. Ces émissions sont transitoires et changent avec le temps. Dans ma thèse, je recherche des émissions de rayons gamma à très hautes énergies avec des télescopes à imagerie Tcherenkov atmosphériques venants d'évènements astrophysiques transitoires à aspect multi-messager. Je me focalise sur les évènements émetteurs d'ondes gravitationnelles et de sursauts gamma et sur les sursauts radio rapides.

Les rayons gamma à très hautes énergies sont détectés directement par des satellites tel que Fermi, ou indirectement sur le sol par des réservoirs d'eau Tcherenkov ou des télescopes à imagerie Tcherenkov atmosphériques. En fait, les rayons gamma de très hautes énergies interagissent avec les particules de l'atmosphère terrestre et créent des pairs électron-positron. Ces particules émergeantes interagissent encore avec les particules de l'atmosphère pour créer des cascades de particules appelés cascades électromagnétiques. Vu leurs vitesses superlumineuses, ces particules décélèrent et créent de

la lumière Tcherenkov. En même temps, des milliers de rayons cosmiques entrent dans l'atmosphère créant aussi de la lumière Tcherenkov atmosphérique à partir de leurs cascades hadroniques. Ces cascades hadroniques posent un problème de fond pour l'astronomie gamma au sol. Cependant les cascades électromagnétiques et hadroniques se distinguent par leurs formes, les dernières étant plus chaotiques et plus dispersées tandis que les cascades électromagnétiques ont un profil plus étroit. En fait, la lumière Tcherenkov résultante des cascades électromagnétiques se diffuse sous forme de cône et a une forme elliptique sur le sol. Ces caractéristiques permettent de filtrer les cascades hadroniques et de distinguer les rayons gamma. En fait, les télescopes à imagerie Tcherenkov atmosphériques enregistrent à l'aide de leurs cameras la lumière Tcherenkov et les données de ces images passent par plusieurs étapes d'analyse pour remonter aux propriétés du rayon gamma tel que sa direction et son énergie. Ces télescopes sont opérés quand la lumière de fond du ciel nocturne est minimale. C'est pour cela que l'altitude du Soleil, ainsi que la phase, l'altitude et la séparation de la Lune sont surveillés pour la prise de données. De plus, les sites de ces télescopes sont idéalement à une altitude de $\sim$2000 m pour pouvoir détecter la lumière Tcherenkov des cascades. L'analyse des données consiste en premier en une vérification de leur qualité pour s'assurer que les conditions d'observation tel que le passage des nuages n'affectent pas les données des caméras ainsi que pour s'assurer que ces dernières ne souffrent pas de mal fonctionnement. Après la sélection des données de bonne qualité pour l'analyse, un premier filtrage des cascades hadroniques est effectué. Ce filtrage permet de discriminer la majorité ($\sim$99%) des rayons cosmiques de fond. Cependant, ces derniers restent dominants et les rayons gamma sont immergés dans ce fond. Pour cela, une soustraction du fond est réalisée. Le résultat de cette soustraction permet après de remonter vers les propriétés de l'émission tel que la courbe de lumière et le spectre en cas de détection et de données suffisantes, et les limites supérieures en cas de non-détection.

Le premier type de sources transitoires, cible de ma recherche de rayons gamma à très hautes énergies sont les évènements émetteurs d'ondes gravitationnelles, notamment les coalescences des objets compacts tel que les trous noirs et les étoiles à neutron. Lorsque deux objets compacts sont en orbite spirale, ils perdent de l'énergie sous forme de rayonnement gravitationnelle et se rapprochent pour terminer en collision. Les ondes émises durant les dernières phases de spirale sont détectées sur Terre à l'aide d'instruments tel que LIGO et Virgo qui sont des interféromètres de Michelson géants. Le passage des ondes gravitationnelles modifie le trajet de lumière dans les bras des interféromètres. La coalescence d'objets compacts, surtout quand au moins une étoile à neutron est impliquée est à l'origine

de certain sursauts gamma (les sursauts courts). En fait, l'évènement GW170817, a établi la première preuve observationnelle du lien entre ce type de coalescences et les sursauts gamma. $\sim$2 secondes après la détection de l'onde gravitationnelle émanant de cette coalescence, un sursaut gamma a été enregistré par les satellites Fermi et INTEGRAL. En ce qui concerne les très hautes énergies, certains modèles théoriques prédisent l'émission de rayons gamma à très hautes énergies provenant des sursauts gamma notamment par le processus Compton inverse. De plus, trois sursauts gamma (longs) ont été détectés à très hautes énergies, GRB 180720B, 190114C et 190829A. Ces trois sursauts sont causés par un autre genre d'évènements, l'effondrement de noyaux stellaires, mais portent la preuve que ce type d'évènements cataclysmiques peut accélérer des particules et émettre des gammas à très hautes énergies.

Un des défis concernant la détection d'évènements d'ondes gravitationnelles est la localisation des évènements dans le ciel. En fait, la méthode de détection engendre des incertitudes sur la position de l'évènement de sorte que la région de localisation peut s'étaler sur des dizaines et des centaines de dégrées carrés sur le ciel. C'est pour cela que des méthodes spécifiques doivent être développées pour s'attaquer à ce problème de localisation et pour essayer de trouver la source et l'émission correspondante. Voici le premier défi de ma thèse: développer des méthodes pour maximiser la probabilité de détection de contreparties d'évènements d'ondes gravitationnelles. La région de localisation est fournie par les instruments détecteurs d'ondes gravitationnelles sous forme de cartes de probabilités. Chaque pixel de la carte contient une probabilité de trouver l'évènement dans cette région particulière du ciel en 2D. De plus, chaque pixel peut aussi contenir des informations sur la distance de l'évènement. Les informations contenues dans ces cartes sont utilisées pour développer des stratégies de recherche de contreparties. Cinq stratégies ont été développées en total dans notre groupe de recherche. Chacune de ces stratégies prend en considération deux contraintes: les contraintes de visibilité et de conditions d'observations. Les contraintes de visibilité sont définies par le fait que les télescopes à imagerie Tcherenkov atmosphérique doivent être opérés idéalement sous un angle zénithal petit. Cela est dû au fait que les cascades atmosphériques entrant dans notre atmosphère sous un angle zénithal élevé, sont plus difficiles à détecter et le seuil de l'énergie de détection est plus haut avec des angles plus grands. De plus, les télescopes que nous utilisons ont un angle zénithal limite au-delà duquel ils ne peuvent plus être opérés. Pour l'instrument principal que j'utilise (the High Energy Stereoscopic System, H.E.S.S.) cet angle est de 60 degrés. Pour les conditions d'observations, il faut prendre en compte les mouvements du Soleil et de la Lune dans le

ciel. Par exemple, H.E.S.S. ne peut être opéré que si le Soleil est à une altitude de -18 degrés sur le site et la Lune est à une altitude de moins de 65 degrés, une phase de moins de 40% et à une séparation de moins de 45 degrés de la cible observée. De plus, le temps minimum d'observation pour accumuler suffisamment de statistiques est aussi pris en compte. La première stratégie développée est une approche simple qui permet de suivre le pixel le plus chaud de la carte pendant un temps d'observation donné ou une fenêtre d'observation. La région observée est masquée et le pixel le plus chaud dans la carte restante est observé durant la fenêtre d'observation suivante. Cette méthode est appelée `Best-Pixel`. `Best-Pixel` pose un problème de chevauchement des observations, pour cela une seconde stratégie a été créée, `PGWinFov` où la probabilité 2D est intégrée dans le cercle représentant le champs de vision des télescopes. Pour créer des positions de test où la probabilité intégrée est calculée, j'introduis une méthode qui consiste à créer une grille de coordonnées. Pour faire cela, j'utilise la carte de probabilité de l'évènement ondes gravitationnelles et réduis sa résolution. Les centres des pixels dans la carte à basse résolution sont utilisés comme centre du cercle représentant le champ de vision du télescope. La probabilité est intégrée dans chaque champ de vision et la position contenant la plus grande probabilité intégrée est choisi pour être observée durant une fenêtre d'observations. La région observée est masquée et la même procédure est répétée pour la fenêtre suivante. Les trois stratégies suivantes prennent en considération les informations sur la distance de l'évènement ondes gravitationnelles et la distribution de la matière, les galaxies, dans l'Univers proche. Ainsi, les régions de recherche de contreparties sont réduites de plusieurs dizaines de degrés dans le ciel à quelques galaxies. Pour faire cela, des catalogues de galaxies tel que GLADE sont utilisés. Une probabilité 3D d'accueillir l'évènement est assimilée à chaque galaxie dans la région de la localisation de l'onde gravitationnelle. Cette probabilité est en fait la densité de probabilité par unité de volume normalisée à l'unité. Des propriétés tel que la masse de la galaxie peuvent être aussi prises en considération pour favoriser les galaxies massives qui contiennent plus d'étoiles. La troisième stratégie, `Best-Galaxy` de suivi d'ondes gravitationnelles consiste à cibler la galaxie avec la probabilité la plus grande et à observer la région tombant dans le champs de vu du télescope. Les galaxies dans la région observée sont masquées et le processus est répété pour la fenêtre d'observation suivante. Pour la quatrième stratégie, `PGalinFoV`, la probabilité des galaxies est intégrée dans le champs de vu du télescope. Similairement à `PGWinFov`, la région avec la probabilité 3D est choisie pour être observée pour un temps donné. Les galaxies dans le champ de visibilité du télescope représentent les centres des champs de vu où la probabilité est calculée. Cependant, le nombre de galaxies croit drastiquement avec l'incertitude sur la région de localisation dans le volume de

localisation de l'onde gravitationnelle et le temps de calcul augmente aussi. Pour tacler ce problème, j'introduis une cinquième stratégie, `PGalinFoV-PixRegion` qui utilise la grille de coordonnées introduite pour `PGWinFov` et l'intégration de la probabilité 3D de `PGalinFoV`. Cette méthode permet de réduire le nombre de fois le calcul est achevé vu que le nombre de pixel dans le ciel en 2D est plus petit que le nombre de galaxies dans le volume 3D. Elle permet aussi de préciser dans quel contour de probabilité la recherche de la contrepartie doit être faite. Les cinq stratégies sont implémentées dans un planificateur global d'observation de suivi d'ondes gravitationnelles. Pour tester ces méthodes, j'utilise 250 cartes de localisation d'évènements ondes gravitationnelles simulées de going-the-distance. Je construis aussi un pipeline de test qui saisit la carte de localisation et des temps de réception d'alerte aléatoires, 10 pour chaque carte, et qui simule une planification d'observation pour les 2500 cas pour chaque stratégie. La couverture de la probabilité de localisation pour chaque cas est prise en compte. Les résultats de ces tests Monte Carlo montrent que pour les méthodes 2D, `PGWinFov` est plus performante que `Best-Pixel`. Cela est due au fait que `PGWinFov` pose moins de chevauchement que `Best-Pixel` et permet ainsi de couvrir des région plus étendues. Pour les stratégies 3D, je trouve que `PGalinFoV` et `PGalinFoV-PixRegion` ont des performance similaires. Cependant, le temps de calcul de `PGalinFoV` augmente avec l'incertitude de localisation tandis qu'elle reste plus ou moins constante pour `PGalinFoV-PixRegion`. En fait, le temps de calcul de `PGalinFoV-PixRegion` est plus petit que celui de `PGalinFoV` pour les évènements dont la régions de localisation à 90% est plus petite que $\sim 400\,deg^2$. `PGalinFoV` sera utilisé par H.E.S.S. vu que majoritairement les évènements qui ont de petites régions de localisation seront suivis par cet instrument.

La collaboration H.E.S.S. est l'une des expériences de pointe à la chasse aux rayons gamma à très hautes énergies de sources transitoires. Le système de suivi des sources transitoires de H.E.S.S. contient le système d'alerte ToO (Target of Opportunity) responsable de la réception et du traitement des alertes transitoires. En fait, les alertes sont envoyées par des instruments détecteur d'émissions transitoires vers des courtier tel que GCN (Gamma-ray Coordinates Network) sous format VoEventT 2.0 et les courtiers distribuent les alertes aux télescopes abonnés tel que H.E.S.S. Le système d'alerte ToO est en charge de prendre la décision d'observer, ou non, une alerte, d'alerter les observateurs et les experts et de déclencher les télescopes en cas de décisions favorables. Durant les observations, les données sont analysées en temps réel mais d'une manière non optimale. En même temps, le télescope optique ATOM (Automatic Telescope for Optical Monitoring) sur le site de H.E.S.S. observe aussi les mêmes cibles. Les programmes de suivi de sources transitoires sont divers dans la collaboration H.E.S.S. La collaboration

suit surtout les sursauts gamma. Plus de 56 sursauts ont été suivis entre 2012 et 2018 sans aucune détection. Cependant en 2018 et 2019, des rayons gamma à très hautes énergies ont été détectés par H.E.S.S. des sursauts GRB 180720B et GRB 190829A. Ces deux sursauts ont prouvé que, en fait, l'émission à très hautes énergies peut durer plusieurs heure et jours, que les rayons gamma émis peuvent avoir une énergie au-delà du TeV, que les émissions des rayons X et rayons gamma à très hautes énergies évoluent de manières similaires, suggérant une origine commune, et finalement que les sursauts gamma ont des comportements plus divers que ce qui est déjà connu dans le domaine des émissions à hautes énergies. En complément de mon travail dans le programme de suivi des sursaut gamma, j'étais aussi responsable du programme de suivi des ondes gravitationnelles avec H.E.S.S. J'ai créé le module de suivi des ondes gravitationnelles dans le système d'alerte ToO pour automatiser le suivi de ces alertes. Grâce à ce module, H.E.S.S. peut discriminer les alertes d'ondes gravitationnelles provenant probablement de bruit Terrestre. Celle provenant de sources astrophysiques sont assimilées à des cas scientifique selon si elles proviennent de sources inconnues, où de coalescence d'objets compactes. Dans ce dernier cas, si l'un des objets est une étoile à neutron, les conditions pour observer sont desserrées. Si la distance de la source est estimée à moins de 150 Mpc et que la source est localisée en dehors du plan galactique, une stratégie 3D est choisie pour planifier le suivi. Dans les cas contraires, une stratégie 2D est choisie. Cela est dû au fait que les catalogues de galaxies sont incomplets dans les régions du plan galactique et à grande distance. Dans le cas où l'alerte arrive durant la journée, quand les observations sont impossibles, un plan d'observation pour la nuit est préparé par le module et distribué au observateurs et experts. Dans le cas où l'alerte arrive durant la nuit, le module calcule la meilleure position à observer au moment de la réception de l'alerte et les télescopes tourneront automatiquement vers cette position dès que la position est déterminée sans attendre le plan d'observation complet. Ce sont des observations rapides. En ce temps, le module calcule le plan d'observation pour le suivi pour le reste de la nuit. En cas de coalescence impliquant une étoile à neutron, il suffit d'avoir une couverture de 10% de la probabilité de localisation pour déclencher des observations. Dans le cas de trous noirs binaires, où il n'y a pas de prédictions claires d'émission à très hautes énergies, il faut couvrir au moins 50% de la carte de localisation pour déclencher des observations. Cela assurera une bonne couverture de la région de localisation pour l'obtention de limites supérieures contraignantes en cas de non détection. Le seuil de couverture est de 20% pour les sources d'origines inconnues. Pour déclencher des observations rapides, au moins 5% de la carte de probabilité doit être couvert durant la première observation. Les observateurs sont fournis des fenêtres d'observations durant lesquelles la cible reste observable au cas où le temps

indiqué dans le plan n'est pas respecté à cause de mal fonctions, de nuages ou de pluies. Le temps de réaction de H.E.S.S. aux alertes ondes gravitationnelle les plus prometteuses est calculé et estimé à moins que 1 minute en général et moins que 2 minutes dans tous les cas (inclue le temps de mouvement des télescopes). Avec les méthodes développées, H.E.S.S. a pu observer 6 évènements d'ondes gravitationnelles avec des délais de suivi variants de plusieurs heures à plusieurs jours. Parmi ceux, H.E.S.S. a été le premier instrument au sol a observé la coalescence des étoiles à neutron GW170817 avec $\sim$5 heures de délai avant que la contrepartie optique soit détectée. Ces observations ont abouti aux premières limites supérieures contraignants l'émission à très hautes énergies des coalescences d'étoiles à neutron. Cette source a été observée plus tard pendant plusieurs semaines durant un suivi à long terme. H.E.S.S a aussi observé une coalescence d'un trou noir et d'une étoile à neutron, mais à cause de nuages une partie non significative de la région de localisation a été observée et les données ne sont pas contraignantes. Enfin, H.E.S.S a observé 4 évènements de coalescence de trous noirs, GW170814, S190512at, S190728q et S200224ca. Les analyses de ces 4 observations sont présentées dans le paragraphe suivant. Je note que j'ai aussi construit un système de réponse aux alertes ondes gravitationnelles pour le premier télescope du future Cherenkov Telescope Array (ou CTA), le Large Size Telescope (ou LST), en se basant sur les outils décrits dans le paragraphe précédent.

Les délais des observations des 4 évènements de coalescence de trous noirs varient de $\sim$3 heures à $\sim$2 jours. J'ai effectué les étapes d'analyses présentées dans le second paragraphe et j'ai calculé des cartes d'excès et de signifiances qui ne montrent pas de détections significatives de signaux de rayons gamma à très hautes énergies. L'étape suivante est de contraindre l'émission en calculant des limites intégrales supérieures. Les premières cartes de limites supérieures sont calculées pour des énergies de 1 à 10 TeV en supposant une source intrinsèque avec un spectre de puissance E^{-2}. Cependant, ces cartes contraignent l'émission intrinsèque. Pour contraindre l'émission observée sur Terre, l'effets d'absorption des rayons gamma par la lumière de fond extragalactique doit être pris en compte. De plus, pour ce type de contraintes, nous avons décidé d'utiliser le domaine en énergie le plus grand possible. Pour cela, pour chaque évènement ondes gravitationnelles spécifique, l'énergie dans laquelle les limites supérieures intégrales vont être calculées sont les énergies où la surface effective du télescope est à 10% de son maximum et où le biais en estimation de l'énergie de rayons gamma est plus petit que 10%. Le spectre absorbé est assumé être un spectre de puissance équivalent calculé à l'énergie de seuil. Les variations des limites supérieures dépendant de l'énergie à laquelle le spectre est déterminé

et du modèle de l'absorption par la lumière de fond extragalactique est aussi calculé. Ainsi, des cartes de limites supérieures de l'émission intrinsèque et observée sont calculées. Ces cartes sont converties en limites supérieures sur le flux en énergie et sur la luminosité en prenant en considération la variation, par pixel, de l'estimation de la distance de l'évènement ondes gravitationnelles dans la carte de localisation. Ces cartes sont moyennées et les limites calculées sont comparées à l'émission de sources transitoires à hautes énergies, notamment les deux sursauts gamma détectés par H.E.S.S. Pour agrandir l'échantillon de sursauts gamma nous ajoutons aussi l'émission extrapolées de sursaut gamma détectés à hautes énergies par Fermi-LAT et les limites supérieures calculées lors des observations à court terme de GW170817 par H.E.S.S. En comparant les limites sur la luminosité intrinsèque on trouve que les limites obtenues sont contraignantes. Cependant, pour obtenir des limites plus contraignantes, il faut que les observations aient lieu plus tôt dans le temps et de manière plus profonde. Une études sur les perspectives des futures observations d'ondes gravitationnelles me montre que cela se produira naturellement vu que le nombre de détections d'évènements ondes gravitationnelles augmentera, permettant d'avoir plus de chance de recevoir une alerte durant les heures d'observation (la nuit) et donc d'observer avec un délai plus court. De plus, la localisation des évènements ondes gravitationnelles s'améliorera, ce qui permettra de focaliser les observations vers une seule région et donc d'obtenir des observations plus profondes.

H.E.S.S. a observé la contrepartie de GW170817 pendant $\sim$54 heures de 124 jours après la coalescence jusqu'à 272 jours après. Ces observations coïncident avec la montée des émissions radio et rayons X provenant de la source et le plafonnement de ces émissions 160 jours après la coalescence. Cette montée est censée être due au fait que nous observons l'évènement GW170817 sous un angle de vu hors axe de $\sim$21 degrés et que l'ouverture du cône du jet causant le sursaut gamma s'agrandit quand la matière éjectée atteint le milieu interstellaire. Le rayonnement synchrotron est à l'origine des émissions radio et X. Dans l'environnement de la coalescence des deux étoiles à neutrons noyé de rayonnements et d'accélérations de particules non-thermiques, une diffusion Compton inverse des photons par les électrons est prévue, ce qui donne lieu à l'émission Compton inverse. Dans le cas de domination du rayonnement synchrotron, ce qui est probablement le cas durant les périodes d'observations de H.E.S.S., le processus synchrotron self-Compton est prévu. Les mêmes électrons responsables de l'émission synchrotron percutent les rayons émis qui atteignent les très hautes énergies. Cela est en fait la motivation derrière les observations du suivi à long terme avec H.E.S.S. L'analyse des données de H.E.S.S. ne montrent pas de détections significatives de rayons gamma à très hautes énergies. Des lim-

ites supérieures sont calculées et ces limites sont utilisées pour contraindre le champ magnétique dans les restes de la coalescence GW170817. L'émission synchrotron sonde le produit de la densité d'énergie des électrons et du champs magnétique dans les restes de GW170817 mais ne peut pas démêler ces deux composantes. La mesure additionnelle de l'émission inverse Compton qui permet de sonder le produit de la densité d'énergie des électrons au carré et du champs magnétique permet de démêler les deux composantes. Moins les limites (ou l'émission) sur le rayonnement à très hautes énergies sont élevés, pour maintenir le niveau du rayonnement synchrotron, plus le champ magnétique est puissant. Les limites inférieures placés par les observations de H.E.S.S. sur le champ magnétique sont $> 24\,\mu\mathrm{G}$ pour le cas d'un jet relativiste et $> 210\,\mu\mathrm{G}$ pour le cas d'une expansion isotrope.

Le troisième type de sources transitoires auquel je m'intéresse dans ma thèse sont les sursauts radio rapides. Comme leur nom l'indique, ce sont des sursauts qui surgissent dans le ciel avec des durées de l'ordre de la milliseconde. Les processus physiques à leurs origines ne sont pas encore très connus à ce jour. Cependant, plusieurs théories et modèles associent ces phénomènes à des phénomènes violents et explosifs. Les candidats les plus prometteurs aujourd'hui sont les magnétars. Les observations ont montré que les sursauts radio rapides sont divisés en deux catégories: les sursaut radio rapide répéteurs et les non répéteurs. Parmi les centaines de sursauts détectés, 22 sont des répéteurs. Certains sursaut radio rapides sont aussi localisés à des galaxies hôtes, cependant ces galaxies hôtes ont des particularités diverses et plus d'observations sont requis pour découvrir des propriétés d'environnement communes. En total, 12 sursauts ont été associés à des galaxies dont 3 sont répéteurs. Les modèles théoriques sont diverses et variés. Certains parmi eux prédisent des contreparties en autres longueurs d'onde et dans le domaine des hautes énergies aussi. Pour vérifier ces modèles, les suivis de sursauts radio rapides est indispensable. C'est pour cela que H.E.S.S. s'intéresse à ce type de sources.

Deux méthodes sont utilisées au sein de la collaboration H.E.S.S. pour chercher des rayons gamma provenant de sursauts radio rapides: le suivi des alertes de détections de sursauts, et l'observation d'une partie du ciel en même temps qu'un télescope radio en attendant la détection de sursauts radio. Vu la rapidité des sursauts, la première méthode vise surtout à observer la phase de rémanence des sursauts. H.E.S.S. est le premier télescope à établir un suivi automatique de sursauts radio rapides détectés par le télescope radio UTMOST. J'étais responsable du travail technique de la part de H.E.S.S. et notamment en ce qui concerne le système d'alerte ToO. J'ai implémenté la réponse automatique: H.E.S.S.

aujourd'hui suit automatiquement les alertes de UTMOST distribuées à condition que l'alerte soit vérifiée, que le ration signal bruit soit supérieur à 10 et que le décalage vers le rouge (redshift) du sursaut soit éstimé à moins que 1, pour éviter l'absorption importante des rayons gamma par la lumière de fond extragalactique. Le redshift des sursauts est estimé à partir de la mesure de dispersion du signal radio. Le premier sursaut à être observé automatiquement par H.E.S.S. est FRB 20190806 détecté par UTMOST. Le délai d'observation est de $\sim$4.5 heures. Les analyses des données de H.E.S.S. ne montrent pas de signal significatif. Pour les sursauts radio, je cherche aussi des signaux transitoires en utilisant des tests de variabilité. Pour faire cela, le temps d'arriver des rayons gamma candidats sont utilisés après une correction prenant en compte l'acceptance de la camera des instruments. Après cette correction, des tests tel que la somme cumulative qui cherche des variations dans l'arrivé du signal et le test ON-OFF qui cherche une augmentation/diminution du signal dans une certaine fenêtre de temps sont utilisés. Aucun test n'a abouti à une détection de variabilité. H.E.S.S. a aussi participé à des campagnes d'observations avec d'autres télescopes comme indiqué au début du paragraphe. J'ai participé à une campagne de suivi avec le télescope MeerKAT de trois sursauts, FRB 20171019A, 20190714A et 20190711A. Les deux derniers sont localisés à des galaxies hôtes. H.E.S.S. n'a rejoint la campagne que pour les observations de FRB 20171019A. Des observations Swift ont été aussi déclenchées pour cette source. L'analyse des données H.E.S.S. ne me montre pas de détection de contreparties à très hautes énergies durant ces observations. J'effectue aussi l'analyse Swift des télescope XRT pour les rayons X et UVOT pour les rayons ultraviolets. Pour les données XRT, je trouve une source de rayons X dans le champ de Swift qui est associées à l'étoile Wolf 1561. Pour UVOT, je détecte une trentaine de sources UV dans le champ. Une contre-vérification avec des catalogues de sources connues me montre que 28 de ces sources sont associées à des étoiles dans le champ, seulement une seule est associée à une galaxie dans le champ et une autre n'a pas d'association. Mais vu l'incertitude importante sur la position du sursaut ces sources ne peuvent pas être associées de manière définitive au sursaut et plus d'observations sont nécessaires. Je conclu que les observations H.E.S.S. et Swift n'ont pas abouti à des détections de contreparties. De la part des observations radio, les données ont montré une émission persistante associée au FRB 20190714A. En utilisant cette émission, les analyseurs estiment que l'âge de la nébuleuse, possiblement hôte du magnétar responsable du sursaut radio, est entre 20 et 500 ans. Cela est fait en comparant l'émission radio persistante à celles associées à des sursaut répéteurs connu tels que FRB 20121102A, et FRB 20180916A. Enfin, je note que j'ai aussi participé du 24 au 29 Juin 2019 avec H.E.S.S. dans une autre campagne d'observations, Deeper Wider Faster (ou DWF), où 9 télescopes,

dont H.E.S.S., ont regardé simultanément trois régions dans le ciel sans détections claires de sursaut ou de contreparties. Ces observations sont en fait les premières observations de H.E.S.S. au clair de Lune.

Les sursauteurs gamma mous sont associés au magnétars. Ce sont des sources à émissions gamma transitoires causées par de brusques changement du champ magnétique qui causent des éruptions dans une partie de la croute de l'étoile. Le terme mou vient du fait que les énergies des rayons gamma atteintes sont dans le domaine des basses énergies, mais en fait ces sources de rayons gamma sont des plus brillantes dans l'Univers. En fait, des éruptions géantes dans le passé, tel que celle du 27 Aout 1997 et celle du 27 Décembre 2004, étaient si violentes qu'elles ont influencé l'ionosphère et le champ magnétique de la Terre. Je m'intéresse à un sursauteur gamma qui est l'un des plus actifs de nos jours, SGR 1935+2154. Le 27 Avril 2020, H.E.S.S. a déclenché des observations de SGR 1935+2154 après la réception de deux alertes du Satellite Swift. Durant cette période j'étais l'expert sur appel. Le jour suivant, un sursaut radio rapide a été détecté provenant de la même source. Ce sursaut est en fait le premier sursaut radio rapide provenant s'une source galactique, vu que toutes les autres détections sont extragalactiques. Plus intéressant encore, INTEGRAL et d'autres satellites ont détecter une éruption de rayons X, qui pour la première fois, présente une contrepartie d'un sursaut radio rapide, celui provenant de SGR 1935+2154. La période d'activité de SGR 1935+2154 s'étend d'Avril jusqu'à Mai, et la source manifestait encore de l'activité en 2021. J'ai recueilli des données multi-longueur d'ondes de sursauts provenant de cette source jusqu'à la fin de l'années 2020. Bien que les observations de H.E.S.S. ne coïncident pas avec des sursaut radio rapide provenant de SGR 1935+2154, 4 éruptions de rayons X ont été détectées simultanément à ces observations. L'analyse des données H.E.S.S. ne montre pas de détections significatives d'émission à très hautes énergies. Les outils de détection de variabilité aboutissent au même résultat aussi. J'utilise les temps d'arrivée des rayons gamma candidats corrigés par l'acceptance, et je créé un outil qui me permet de chercher une variation de l'émission durant un intervalle de temps précis. Aucune variabilité n'a été détectée autour des temps des 4 éruptions de rayons X. Je calcule des limites supérieures de l'émission persistante et transitoire de la source pour contraindre ces deux types d'émission. Je note que ces limites supérieures contraignent pour la première fois l'émission à très hautes énergies d'un sursauteur gamma mou en plein activité. La non détection suggère que l'émission à très hautes énergies, si existante, est faible dans l'environnement du magnétar, rendant l'émission des très hautes énergies trop faible pour être détectée. Cela peut être causé par le fait que cette émission se produit trop près de la surface du magnétar et la production de paires et la séparation des photons pourraient entraîner des

pertes d'énergie. Les observations de H.E.S.S. ne permettent pas de tirer des conclusions sur les contreparties des sursauts radio rapides vu que ces sursauts ne sont pas coïncidents avec les observations de H.E.S.S. et que les contreparties X de ces sursauts radio semblent différer en nature des éruptions X contemporaines au observations de H.E.S.S.

En résumé, durant ma thèse, j'ai travaillé sur trois types de sources transitoires sous aspect multi-messager en cherchant des émissions de rayons gamma de très hautes énergies en contreparties. Ces trois sources sont les sursauts gamma, les évènements ondes gravitationnelles et les sursauts radio rapides. Pour faire cela, je me suis attaqué à trois types de défis. Le premier est un défi pré-observationnelle qui concerne la préparation des observations, comme le planning, la création d'outils pour le suivi de différents types de sources transitoires, et l'automatisation des processus. Le second défi est les observations elles-mêmes auxquelles j'ai participer en tant qu'observateur sur le site de H.E.S.S. durant un mois en Mars-Avril 2019 et en tant qu'expert sur appel pour les programmes des sources transitoires des différentes collaborations desquelles je fais partie. Le troisième défi consiste à analyser les données et de chercher un signal ou une détection et d'interpréter les résultats obtenus. Les outils développés pour la phase pré-observationnelle ont permis d'optimiser les observations. Le résultat de l'analyse des données a permis de placer des contraintes physiques sur des sources ondes gravitationnelles, des sources de sursauts radio rapides et de sursauts gamma, trois sources intrigantes de l'astrophysique moderne candidates d'être hôtes d'émissions non-thermiques à très hautes énergies. Les suivis de sources transitoires continuent pour acquérir de nouvelles données qui permettrons de répondre aux questions sans réponses. En ce temps, le travail continu pour améliorer les outils développés et pour créer de nouveaux outils pour les instruments courants et pour les préparations pour de futures instruments plus avancés.

Preamble

Multi-messenger astrophysics is a field of science that combines information from different messengers in order to study an astrophysical phenomena or object. Astrophysical messengers are particles, waves, or any other entity that carries information from space to Earth. Nowadays we know four different kinds of messengers: electromagnetic waves, gravitational waves, neutrinos and cosmic rays. Transient astrophysics is the branch of astrophysics that deals with transient phenomenom. A transient phenomenon is a changing event that is characterized by its spatial and temporal occurrence. These phenomena vary from events occurring inside our solar system, like the passing of a comet, to cosmological violent events like the outburst of an active galaxy core or the merger of two supermassive black holes. Extragalactic transient events are mostly unpredictable in nature these days. Multi-messenger astrophysics provides a complete set of tools to understand and study transient events. For example, the coalescence of two neutron stars can be detected by its gravitational wave signature that also provides early information on the masses and inclination axis of the merging system. Electromagnetic emission provides accurate localisation and information on short and long term physical changes that are ongoing in the aftermath of the merger. Possibly, mysterious unknown emissions caused by the merger, like the rapid flashing of radio waves could also be observed from such events. Very-high energy (VHE) γ rays from the coalescence can be an indicator of non-thermal physical phenomena that involve cosmic rays and particle acceleration. Finally, the detection of emanating neutrinos can break the ambiguities on the γ-ray creating process whether it is hadronic or leptonic. To top it all, the event described here is transient. It starts with a violent explosion followed by an expansion of outflows that is followed by the interactions of ejected material, the ambient space and the magnetic field in the remnant. Observations of the different phases of such events will show the ongoing processes taking place, hence the importance of the temporal aspects of transient multi-messenger events.

The mentioning of the neutron star coalescence is not by coincidence since the main focus in this

thesis will be on cataclysmic cosmic events. The aim of this thesis is to search for non-thermal VHE γ rays from transient multi-messenger cosmic events with Imaging Atmospheric Cherenkov Telescopes (IACT). I will be focusing on three types of events: Gamma-ray Bursts (GRB), Gravitational Waves (GW) events and Fast Radio Bursts (FRB).

In chapter 1, I discuss non-thermal emission processes leading to γ-ray production, then discuss VHE γ rays, their interaction with the atmosphere and the methods of detection and analysis. In chapter 2, I present the three classes of transient events that will be mentioned in the thesis: GRBs, GWs and FRBs. This is the introductory part. In the following 3 parts (6 chapters) I present my work. Part 2 of the thesis deals with GW events and GRBs. I tackle the pre-observation challenges, focusing on the selection of the most promising events for observation and on the optimization of follow-up observation scheduling. In chapter 3, I tackle the follow-up of gravitational waves events that have large localisation uncertainties. I discuss the development of new techniques, the improvement of old ones, testing simulations and performance estimation and the creation of a GW observation scheduler. In chapter 4, I present my technical contribution to the High Energy Stereoscopic System (H.E.S.S.) and the Cherenkov Telecope Array's (CTA) Large Size Telescope (LST) GW and GRB programs. I start with an overview of transient alert systems, then present the H.E.S.S. GRB program and highlight my technical work that tackles the pre-observation challenges of GRB follow-up. I also present my contribution to the GRB 190829A discovery. Then I move on to the description of the development and commissioning of the H.E.S.S. GW program using the tools described in the previous chapter. I also discuss the observations that were obtained using the developed tools. I conclude with my work in the LST collaboration and prospects for the GW and GRB programs. In part 3, I present the VHE analysis of the most promising GW events that were followed by H.E.S.S., the results of these analysis and their implications. In chapter 5, I present the analysis of the BBH merger events and in chapter 6, I present the long-term follow-up campaign on GW170817 that I was part of. In part 4, I switch the conversation to FRBs. I discuss in chapter 7 the FRB follow-up program in H.E.S.S. I present past observations of FRBs with IACTs then present two methods for FRB observations: ToO follow-up from links to radio telescopes and MWL observation campaign with other radio facilities. I present the results of observations obtained with both methods. Finally, in chapter 8 I focus on a particular source, SGR 1935+2154, that establishes the first observational link between galactic magnetars, FRBs and X-ray bursts. I start with the discussion of SGR 1935+2154 and present a MWL overview of the source. I then present the VHE analysis and the implications of the H.E.S.S. observations on our understanding of the source.

Part I

Introduction to very-high-energy (VHE) messengers

Chapter 1

VHE gamma-rays

1.1 The multi-wavelength non-thermal Universe

The electromagnetic (or EM) emission spectrum ranges from radio waves with wavelength ranging from thousands of meters (few 10^{-10} eV) to very-high energy (VHE) γ rays with energies above 100 GeVs. The Universe is very different when observed in different wavelengths. As an example the Crab nebula is one of the most studied galactic objects. It is illustrated in Fig. 1.1 as seen in different wavelengths. Each wavelength range brings different information. The infrared, optical and X-ray emission describes the thermal emission that informs the observer on the dust mass and properties in the nebula([250] and references within) while the radio, X and γ rays can be used to study the non-thermal emission from the Crab [161]. In this section, I present the different non-thermal mechanism that could lead to the production of γ rays.

1.1.1 Introduction to non-thermal emission mechanisms

Photon emission in astrophysical sources is caused either by thermal or non-thermal processes. VHE photons have energies from 100 GeV and can reach several hundreds of TeV. They are emitted by very high energy particles reaching above the TeV-PeV level. This kind of energies is reached through particle acceleration. In this section, I present charged particle acceleration processes. In the second part, I present the different emission signatures of non-thermal phenomena that can lead to γ-ray emission, in particular VHE γ rays.

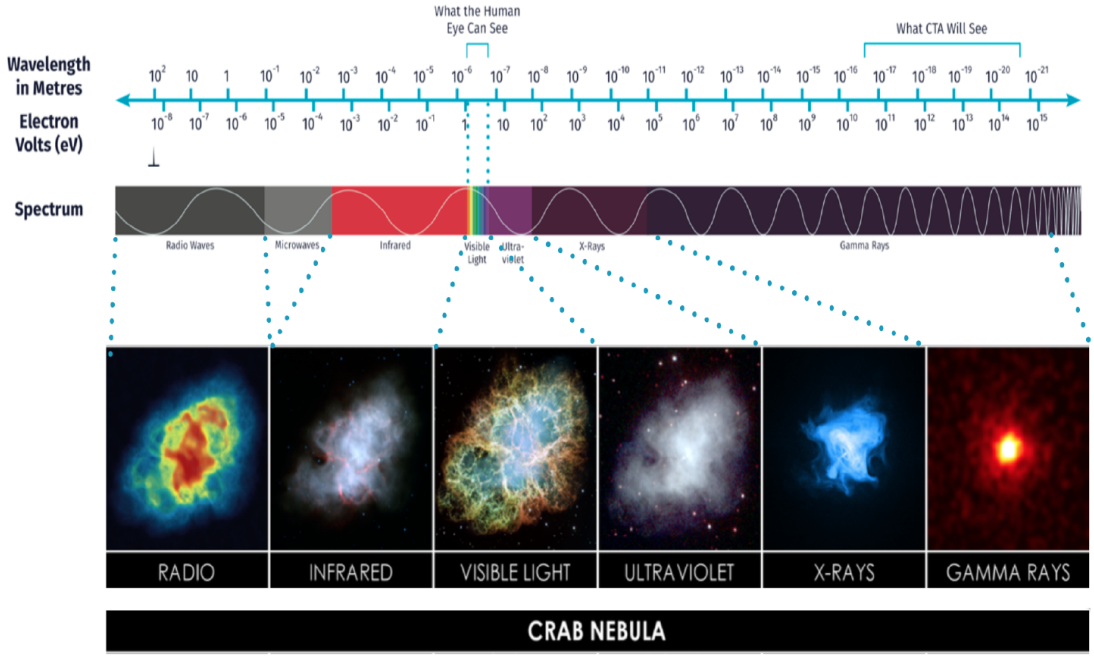

Figure 1.1: Multi-wavelength observations of the Crab Nebula with the corresponding wavelengths for each observational image. From `https://commons.wikimedia.org/wiki/File:Crab_Nebula_in_Multiple_Wavelengths.png`

Charged particle acceleration

Charged particles should be accelerated to energies in the order of hundreds of TeV or PeVs in order to radiate non-thermal VHE γ rays. Such acceleration sites are in principle impossible to find nowadays on Earth and are constrained to astrophysical high energy sources. Most astrophysical accelerators are stochastic accelerators. Several stochastic acceleration mechanisms are proposed but the most popular ones are the first and second order Fermi acceleration.

The second order Fermi acceleration was suggested first. It concerns scattered particles in a moving magnetized cloud [118] with velocity V. Let's consider a particle in a moving cloud with initial particle energy $E' = \gamma E + \beta\gamma p\mu$ and a momentum along the x-axis $p'_x = \beta\gamma E + \gamma p\mu$ in the cloud frame, where γ is the Lorentz factor, p is the particle momentum, β is the velocity of the cloud divided by the speed of light c, μ is $cos\theta$ with θ the angle of collision. The particle undergoes head-on and tail-on collision with the moving cloud. Head-on collisions are more probable to occur than tail-on collisions. The cloud is unaffected by the scattering since it is assumed to be massive in comparison to the particle. Therefore, for a head-on collision the energy of the particle is conserved and its momentum in the X-direction is

reversed $p'_x -> -p'_x$. The final energy of the particle in the lab frame after scattering is:

$$E'' = \gamma E' + \beta\gamma p'_x = \gamma^2 E(1 + \beta^2 + 2\beta\mu\nu) \tag{1.1}$$

leading to

$$\frac{E'' - E}{E} \sim 2\beta^2 + 2\beta\mu\nu \tag{1.2}$$

where ν is now the dimensionless particle velocity.

The probability to scatter a cloud at the given angle is

$$P(\mu) = A\frac{\beta\mu + \nu}{1 + \nu\beta\mu} \sim A(1 + \beta\mu) \tag{1.3}$$

The condition of normalization to unity gives $A = 1/2$. Depending whether the particle-cloud scattering is head-on or tail-on, the fractional energy change can be positive or negative. Taking the probability of a scattering occurring head-on or tail-on, Eq.1.2 leads to a positive energy gain for the particle:

$$< \frac{\Delta E}{E} >= \int_{-1}^{1} P(\mu)d\mu = \frac{8}{3}\beta^2 \tag{1.4}$$

due to the fact that head-on collisions are more probable than tail-on collisions.

The first order Fermi acceleration takes place when particles are accelerated in a shock wave [200] [60] [69] [51]. The conditions to create a shock is to have a fluid moving at higher velocities than the local sound speed, a magnetized medium or particle reflection by electromagnetic barriers on microscopic level. In a scenario where particles are bouncing between approaching magnetic mirrors, first order Fermi acceleration takes place. When a particle crosses a shock front with upstream velocity ν_1 and downstream velocity ν_2, the energy increae of the particle is:

$$\Delta E = E\frac{\nu_1 - \nu_2}{\nu}\mu \tag{1.5}$$

by considering the crossing probability which is proportional to μ and averaging over the incident

angles the average energy increase becomes:

$$< \frac{\Delta E}{E} >= \beta \int_0^1 2\mu^2 d\mu = \frac{2}{3}\beta \tag{1.6}$$

The average energy increase over a full shock-wave cycle is

$$< \frac{\Delta E}{E} >= \frac{4}{3}\beta \tag{1.7}$$

After n cycles the energy of the particles is:

$$E_n = E_0(1+ < \Delta E/E >)^n \tag{1.8}$$

The spectrum of of the high energy particle emerges as a power law E^{-2}.

Non-thermal emission processes

Accelerated particles can produce electromagnetic emission through leptonic and hadronic processes.

Leptonic processes:

Bremsstrahlung: Bremsstrahlung is known as deceleration radiation. When a charged particle like an electron gets close to another charged particle like a nuclei, it is decelerated and deflected by the electric field. This deceleration produces electromagnetic radiation.

Synchrotron: Synchrotron radiation is emitted when a relativistic charged particle is accelerated radially (the acceleration is perpendicular to the velocity) in a magnetic field. If the particle is non-relativistic, this emission is called cyclotron radiation. The energy of a synchrotron photon is:

$$E_\gamma = 0.67eV(\frac{E_e}{1TeV})^2(\frac{B}{\ln T})sin\theta \tag{1.9}$$

where E_e is the energy of the electron, B is the magnetic field and θ is the angle formed by the velocity vector and the magnetic field [233].

Energy loss by synchrotron radiation is given by :

$$\frac{-dE}{dt} = 2\sigma_T c U_B \beta^2 \gamma^2 sin^2(\theta) \tag{1.10}$$

where $U_B = B^2/2\mu_0$, σ_T is the Thompson cross section (σ_T is proportional to the classical radius squared and is typically equal to 66.53 fm^2 for an electron), c is the speed of light, β is the velocity divided by c and μ_0 is the permeability of free space. For an isotropic electron population averaging over the angles yields:

$$\frac{-dE}{dt} = \frac{4}{3}\sigma_T c U_B \beta^2 \gamma^2 \tag{1.11}$$

The emission is proportional to γ^2 and B^2 and it is beamed in a cone of opening angle $1/\gamma$ in the direction of the motion, due to relativistic motion. It is bipolar in the particle frame.

The electron cooling time is the time that the electron needs to lose energy through synchrotron emission. It is defined in the electron frame as $\gamma_e m_e c^2/P$ where P is the synchrotron radiation power emitted by a single electron and is defined as $P = \frac{4}{3}\sigma_T c U_B \beta^2 \gamma_e^2$. It can also be defined as:

$$\tau = (\frac{1}{E} \times \frac{dE}{dt})^{-1} = \frac{1}{bU_B E} \tag{1.12}$$

where $b = \frac{4\sigma_T c}{3m_e^2 c^4}$, and E is the energy of the electron.

Synchrotron emission is characterized by a broad spectrum ranging from the radio to the X rays and potentially can reach much higher energies. The maximum energy reached by synchrotron photons is limited by the electron cooling time and it reaches higher energies with higher Lorentz factors. Eq. 1.12 shows that increasing the magnetic field decreases the synchrotron cooling time, which will limit electrons reaching higher energies. Synchrotron emission created by a population of electrons following a power-law distribution

$$N(E_e)dE_e \propto E_e^{-\alpha_e} dE_e \tag{1.13}$$

takes the form

$$dN(E_\gamma)/dE_\gamma \propto E_\gamma^{-(1+\alpha_e)/2}. \tag{1.14}$$

This means that measurements of the synchrotron spectrum allows the observer to probe the electron spectrum at the source or other properties of the source like the Lorentz factor of the relativistic material and the magnetic field.

Annihilation: This process is the inverse of pair production. When a particle and an anti-particle, like an electron and a positron collide, they create two energetic photons that share their initial total energy.

Inverse Compton: Inverse Compton (IC) takes place when an ultra-relativistic particle like an electron scatters on a photon and transfers a part of its energy to the photon. If in the particle rest frame the energy of the photon $E < 2m_e c^2$, the probability of scattering can be described by Thomson scattering cross section $\sigma_{\rm T} = 0.66\,{\rm barn}$. Otherwise the scattering occurs in the high energy Klein-Nishina regime [194] and the calculation of the scattering cross-section includes quantum and relativistic effects. In the lab frame, the scattered photon energy is on the order of $\gamma m_e c^2$ where γ is the Lorentz factor of the electron in the lab frame. The energy loss by Compton scattering for a single electron is:

$$\frac{-dE}{dt} = \frac{4}{3}\sigma_T c U_R \beta^2 \gamma^2 \tag{1.15}$$

where U_R is the target photon energy density. IC emission produces photons with the highest energies in the electromagnetic spectrum reaching the TeV level. For example, a 1 TeV γ ray is produced by an electron with 20 TeV energy scattering on photons from the Cosmic Microwave Background (CMB $\sim 10^{-3}{\rm eV}$). These photons usually constitute the VHE γ rays that we hunt with Imaging Atmospheric Cherenkov Telescopes (IACT). IC emission created by the scattering from a population of electrons following a power-law distribution $N(E_e)dE_e \propto E_e^{-\alpha_e} dE_e$ has the same form as the synchrotron spectrum and takes the form $N(E_\gamma)/dE_\gamma \propto E_\gamma^{-(1+\alpha_e)/2}$. This means that measuring the IC spectrum allows the observer to probe the electron spectrum at the source. The radiated IC and synchrotron power scale as the ration of the radiated and magnetic fields:

$$\frac{P_{IC}}{P_{sync}} = \frac{U_r}{U_b} \tag{1.16}$$

In the IC process, and in the Klein-Nishina regime, electrons are less efficiently cooled than in the synchrotron process. The cooling time becomes:

$$\tau_{KN} = (\frac{1}{E} \times \frac{dE}{dt})^{-1} = \frac{1}{bU_B E} \ln(\frac{2E}{m_e c^2} + \frac{1}{2}) \tag{1.17}$$

where $b = \frac{1}{2}\frac{\sigma_T c}{m_e^2 c^4}$.

In some astrophysical environments with efficient particle acceleration, the synchrotron self-Compton (SSC) mechanism can take place. During this process, the electrons emitting synchrotron photons will scatter on these same photons and create IC emission. Finally one can express the ratio of IC energy

losses over synchrotron as:

$$-\frac{dE}{dt})_{IC} = -\frac{dE}{dt})_{syn} \times \frac{U_R}{U_B} \propto -\frac{dE}{dt})_{syn}^{\ 2} \times \frac{1}{U_B} \tag{1.18}$$

Hadronic processes:

Pion decay: When proton-proton or proton-photon interact, charged pions (π^- or π^+) or neutral pions (π^0) are produced as result. While charged pions decay into charged leptons and neutrinos, neutral pions create γ rays. π^0 decay into two γ rays with energy $E_\gamma = m_{\pi_0}c^2/2 \sim 67.5\,\mathrm{MeV}$ (in the center of mass reference system). The simultaneous detection of neutrinos (from charged pions) and γ rays (from neutral pions) from an astrophysical source provides direct evidence of hadronic processes taking place in the observed source.

Synchrotron: Just like electrons, protons can radiate through synchrotron in the presence of a magnetic field. The contribution of the hadronic synchrotron emission is less important than the leptonic synchroton emission since it shows a dependency on the mass of the accelerated particle as m^{-4}.

The non-thermal emission presented in this section can produce γ rays at high energies. In particular, synchrotron and IC can produce VHE γ rays under certain conditions. In the following sections, I explain how the arrival of VHE photons on Earth and their interaction in the atmosphere creates Cherenkov light that can be used to indirectly detect VHE γ rays by ground based observatories.

1.1.2 Non-thermal emission candidate sites

Particle acceleration sites should follow conditions established by Hillas [159]. The relation of the maximum energy that can be acheived is

$$E_{max} \sim n\beta Z_e BL \tag{1.19}$$

where n is the efficiency ($n = 1$ if no losses), Z_e is the charge of the particle and L is the size of the acceleration region. Fig. 1.2 is a modified version of the Hillas diagram that shows the potential sites that follow the condition for particle acceleration.

Non-relativistic astrophysical accelerators can be found in supernovae remnants, stellar winds and

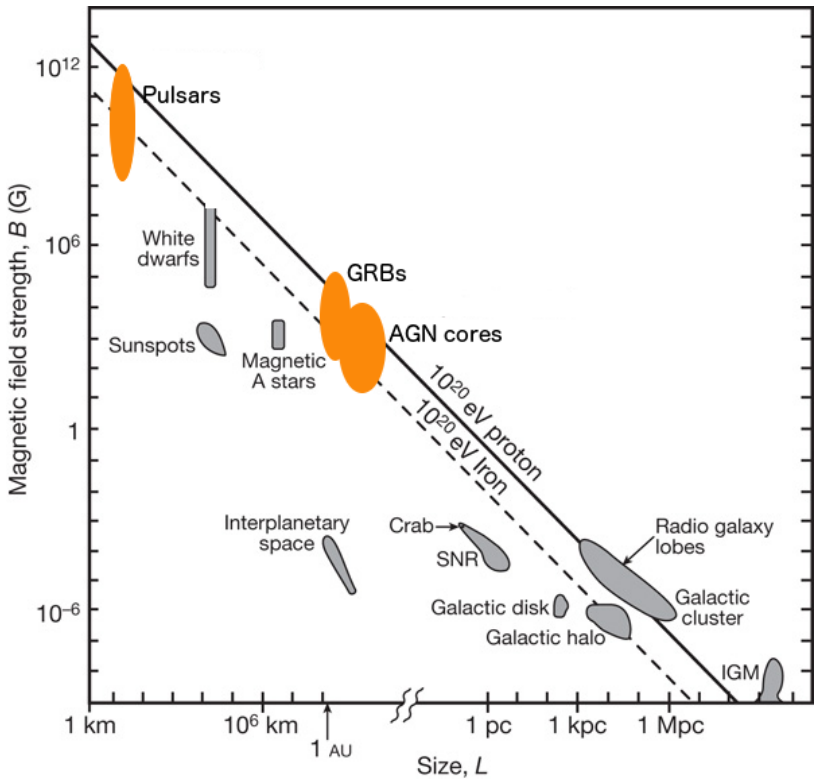

Figure 1.2: Modified version of the Hillas diagram. The diagonal line (dashed) shows the approximate maximal achievable energy given by $E_{max} \sim L \times B$ for a proton (for Iron). From [330].

magnetospheres, interstellar medium, galactic winds and galaxy cluster shocks. Relativistic shock can be found in Active Galactic Nuclei (AGNs) jets, cataclysmic fireball scenarios like GRBs and pulsar winds. Non-thermal emission that could ”potentially” lead to VHE γ-ray emission can be found everywhere in the galactic and extra-galactic Universe. To cite a few: AGNs, Compact Binary Coalescence (CBC) like Binary Black Holes (BBH), binary neutron star (BNS) or neutron star black hole mergers (NSBH), Supernovae (or SN) and novae, Fast Radio Bursts (FRB) events, Magnetars and soft gamma-ray repeaters (SGR) and Micro-quasars.

The observation of these events in different wavelengths sheds light on different aspects of the mechanisms driving them. Non-thermal emission like synchrotron can range from radio to VHE γ rays and observations in different wavelength can be connected to the same process. Some of the non-thermal emission candidates also have a multi-messenger aspect. Aside from electromagnetic emission, they could also emit neutrinos (like AGNs and SNs) and GWs (like BNS mergers).

TeV sources

VHE γ rays are produced by non-thermal emission mechanism. VHE source, also called TeV sources, can be divided into galactic and extragalctic sources. From the galactic sources I cite Pulsar Wind Nebulae (PWN), SN remnants, globular clusters, micro-quasars and from the extragalactic VHE sources AGNs, GRBs (from stellar core collapse or CBCs) or starburst galaxies. An extensive list of sources and their characteristics can be found in the TeVcat catalogue [367].

The distribution of these sources in the sky can be found in Fig. 1.3.

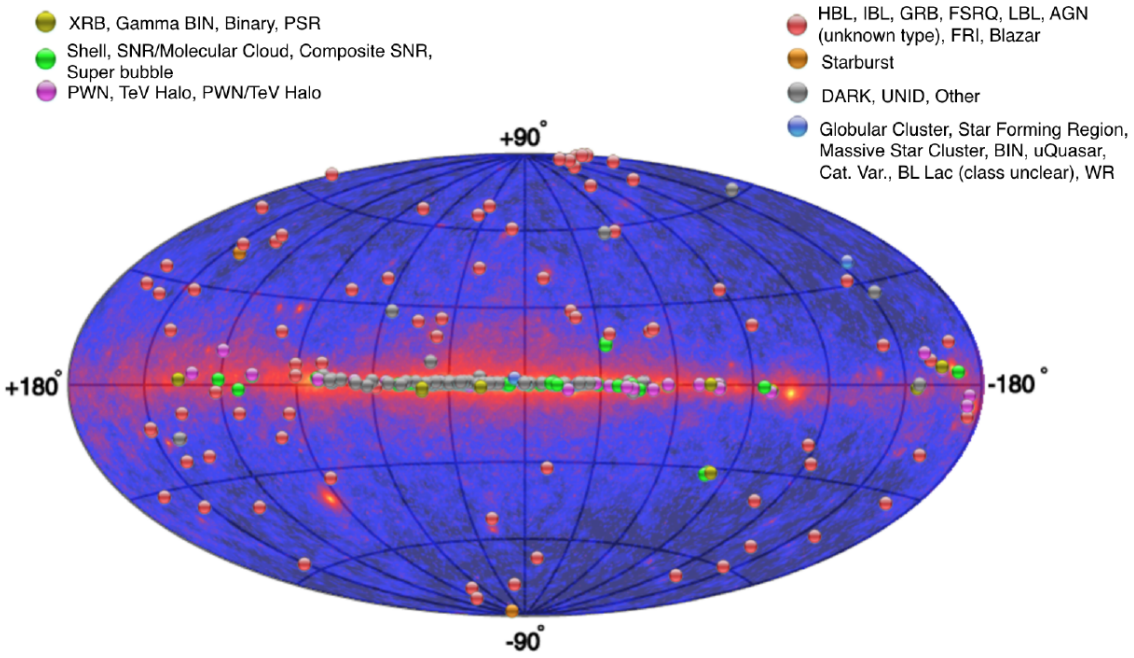

Figure 1.3: Catalog of TeV sources. From http://tevcat.uchicago.edu/

The VHE Universe horizon: EBL absorption effects

Among the several diffuse photon fields which are present in the interstellar and intergalactic medium, the Extragalactic Background Light (EBL) is the diffuse emission produced by all galaxies in the Universe with photons in the ultraviolet, optical, and infrared bands that is the main candidates for interaction with TeV photons. Emitted γ rays interact with EBL photons via electron-positron pair production and are partially absorbed. Therefore, EBL is a source of opacity for VHE γ rays and limits the distance to which they are detected especially at the higher end of the spectrum. The attenuation effects from EBL depends on the

energy of the emitted TeV photons and on the redshift of the emitting source:

$$F_{det} = F_{ini} \times e^{-\tau(E,z)} \tag{1.20}$$

where F_{det} is the detected flux, F_{ini} is the emitted flux from the source and τ is the optical depth that is dependent on the TeV photon energy and redshift. Several models are developed to describe EBL absorption effects like [126] [108], [121] and [134]. An example of the evolution of τ is shown in Fig. 1.4 for different EBL absorption models.

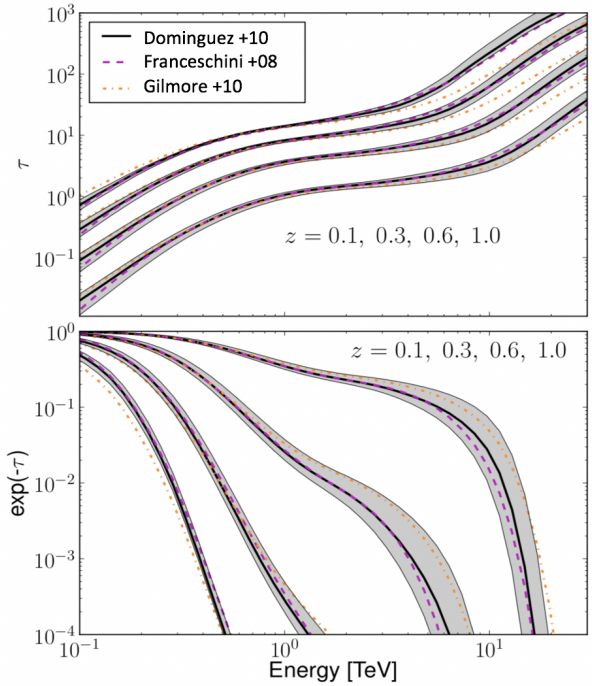

Figure 1.4: Optical depth (upper) and flux attenuation (lower) versus observed energy of γ-ray photons for sources at different redshifts. Adapted from [108].

1.2 VHE gamma-rays and atmospheric showers

1.2.1 Atmospheric showers

In this section, I explain the interaction of VHE γ rays with Earth's atmosphere that leads to their indirect detection by ground based instruments. When a VHE γ ray enters the atmosphere, the incident photon interacts with the Coulomb field of the nuclei in the upper atmosphere and produces an electron positron

pair following:

$$\gamma + \gamma \longrightarrow e^+ + e^- \tag{1.21}$$

Electromagnetic and hadronic showers: The emerging particles interact also with the field of other charged particles in the atmosphere. The electrons and positron will undergo Bremsstrahlung that will create new photons. These new photons will continue to interact with charged atmospheric particles. This will result in the creation of particle and photon cascades: electromagnetic showers.

A similar process occurs when a cosmic ray enters the atmosphere with some differences. The charged incoming nucleus interacts with the charged atmospheric particles resulting in a shower of secondary particles like charged and neutral pions, mesons and kaons. These secondary particles will continue to interact with other particles from the atmosphere and create three types of components: electromagnetic, hadronic and muonic. This type of cascades induced by the primary cosmic ray is called hadronic shower.

The development of air showers in the atmosphere initiated by a γ ray and by a cosmic ray is presented in Fig. 1.5. For the hadronic showers, different interaction and components are taking place in the evolution of the air shower. Due to deep inelastic interactions with large transverse momentum transfer, the shape of the hadronic showers is chaotic and results in wider and broader showers than electromagnetic showers.

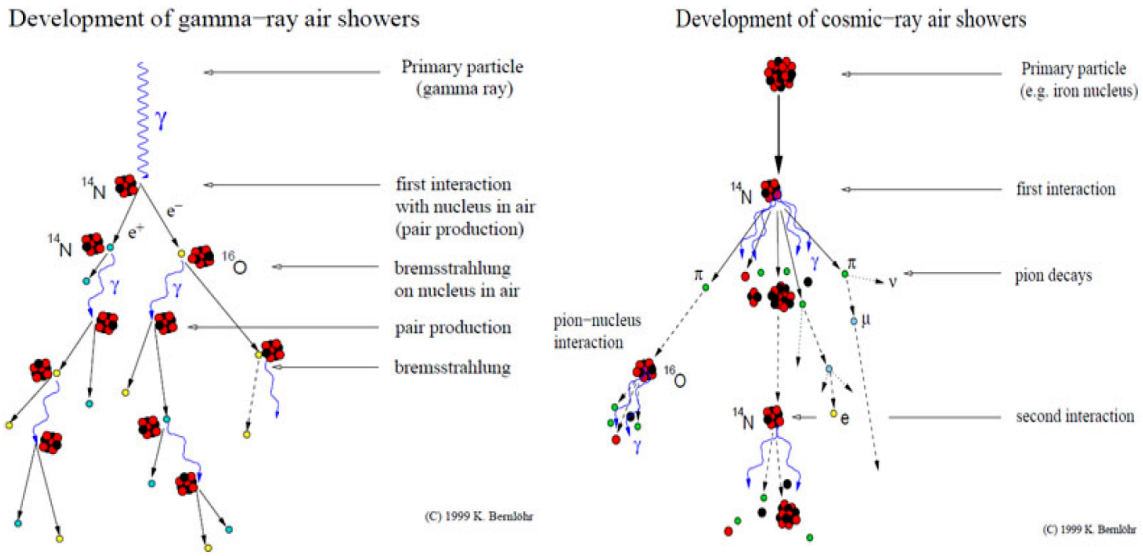

Figure 1.5: Development of electromagnetic (left) and hadronic (right) showers in the atmosphere. From: `https://ned.ipac.caltech.edu/level5/Sept09/Cui/Cui1.html`.

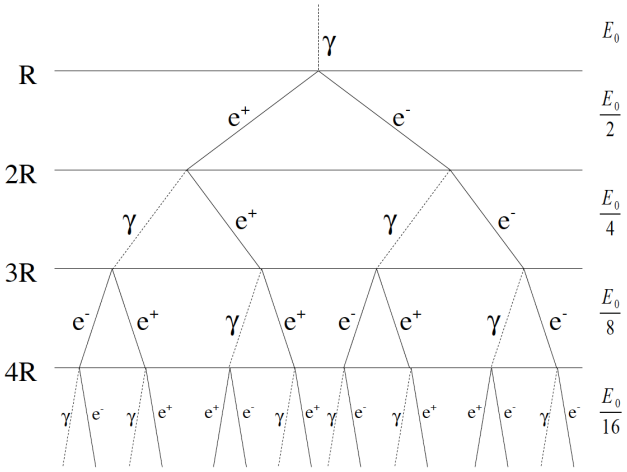

Figure 1.6: Heitler model of shower development. From [101].

The topology of the development of hadronic and electromagnetic showers is illustrated in Fig 1.8. It is different for both types of showers and depends heavily on the energy of the primary particle entering the atmosphere. Hadronic showers have a broader lateral distribution due to their chaotic behaviour mentioned above. Hadronic showers become even wider and more chaotic when the energy of the primary particle is greater.

Shower development: In the Heitler model [150], the shower is dominated by Bremsstrahlung and pair creation. Electromagnetic showers start to develop at an altitude around 25 km. They are characterized by the electromagnetic radiation length defined as $1/X_0$ (in g cm^{-2}). The radiation length corresponds to 36.7 g cm^{-2} in the atmosphere considering dry air from [230]. The loss of energy by Bremsstrahlung in function of traverse depth defined as $X = \int_z^\infty \rho(z)dz$ follows:

$$E(X) = E(0)exp(-X/X_0)(1+b) \tag{1.22}$$

where $b = 0.0122$ in air. Each electron loses half of its energy (initially E_0) to γ-ray production after a depth $R = X_0 ln2$ where $1/X_0$ is the electron radiation length as mentioned above. Each photon undergoes also pair-creation after the same depth. The model by Heitler for electromagnetic showers is illustrated in Fig. 1.6.

The number of shower particles is 2^t after a normalized depth $t = X/R$. The shower develops for several kilometers in the atmosphere until ionization losses become dominant. The depth of maximum of

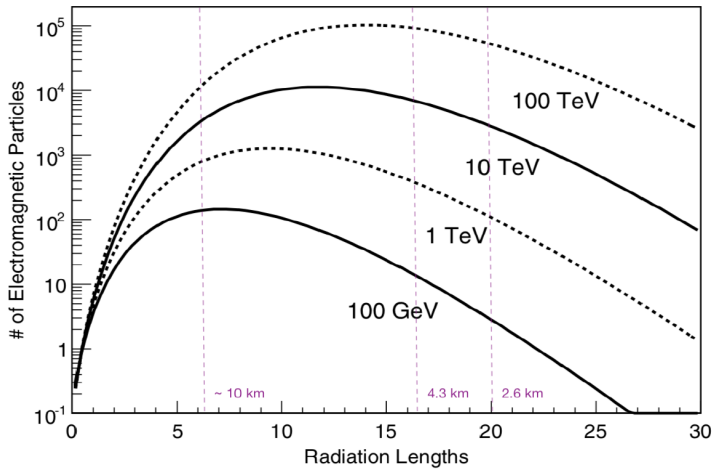

Figure 1.7: Evolution of the number of particles in an electromagnetic air shower with the number of radiation lengths, for different primary γ-ray energies 100 GeV, 1 TeV, 10 TeV and 100 TeV. Purple dashed lines correspond to the altitude. From [29].

shower development is $X_{max} = X_0 ln(E_0/E_c)$ corresponding to maximum depth $t_{max} = ln(E_0/E_c)/ln(2)$, where E_c is the critical energy at which ionization losses become important. Considering a hydrostatic atmosphere, at 1 TeV, $t_{max} = 13.5$ leading to an altitude of maximum of shower developement $\sim$9 km [101]. The evolution of the number of particles in function of the radiation length and primary energies 100 GeV, 1 TeV, 10 TeV and 100 TeV is given in Fig. 1.8.

In Fig. 1.8, I show the difference in shower development for a 300 GeV photon, a 1 TeV proton and a 5 TeV iron nucleus.

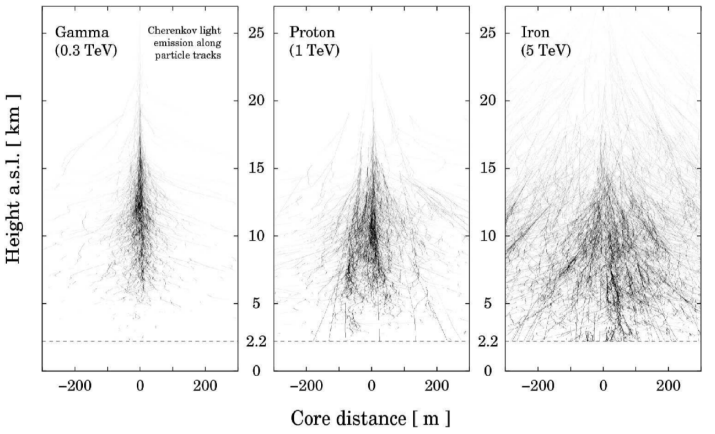

Figure 1.8: Simulation of shower propagation for a 300 GeV γ ray (left), a 1 TeV proton (middle) and a 5 TeV comic ray (right). From [65].

Cherenkov radiation emission: The particles created in any type of shower enter the atmosphere at superluminous velocities. They lose energy by emitting Cherenkov light photons [175] in order to stay under the speed of light limit in the atmosphere characterized by c/n where n is the refraction index of the medium. The speed of the superluminous particles in the atmosphere is greater than the speed of light in the atmosphere medium and smaller than the speed of light in vacuum: $c/n < v_{part} < c$. In fact, when the particle enters the atmosphere it is subjected to a velocity threshold that is defined by c/n and an energy threshold E_{th}:

$$v_{th} = c/n \longrightarrow E_{th} = \frac{m_0 c^2}{\sqrt{1 - \frac{1}{n^2}}} \tag{1.23}$$

Where m_0 is the mass of the particle. The radiated light from these particles is named after the Nobel-award winner Pavel Cherenkov. The number of Cherenkov photons emitted is defined by:

$$\frac{d^2N}{dxd\lambda} = \frac{2\pi\alpha Z_e^2}{\lambda^2}(1 - \frac{1}{\beta^2 n^2}) \tag{1.24}$$

Where α is the fine-structure constant, λ is the wavelength of the emitted photon, x is the length of particle path and Z_e is the electric charge of the particle. Cherenkov light extends from the ultraviolet to the visible part of the spectrum peaking at 420 nm (violet). The radiated electromagnetic wave front takes the shape of a cone when the particle moves through the atmosphere. The emission angle is given by:

$$cos(\theta) = \frac{1}{\beta n} \tag{1.25}$$

The Cherenkov light emitted by a particle in the atmosphere and its projection on the ground is illustrated in Fig. 1.9.

The particles of the air shower spread laterally away from the axis defined by the primary particle. The projection of the shower front on Earth takes the form of an ellipse. The incidence angle plays a role in the ability to see a shower: The shower, created by several particles and photons, has a cone shape with a spherically curved disk at the bottom. The projection of this disk front is seen differently with different incident angles. The shower front presents a curvature with respect to the position of the primary particle interaction. With increasing zenith angle, the distance crossed by the air shower in the atmosphere increases, and therefore the absorption of shower light during its passage through the atmosphere increases and it becomes more difficult to detect the relatively dim Cherenkov light from low

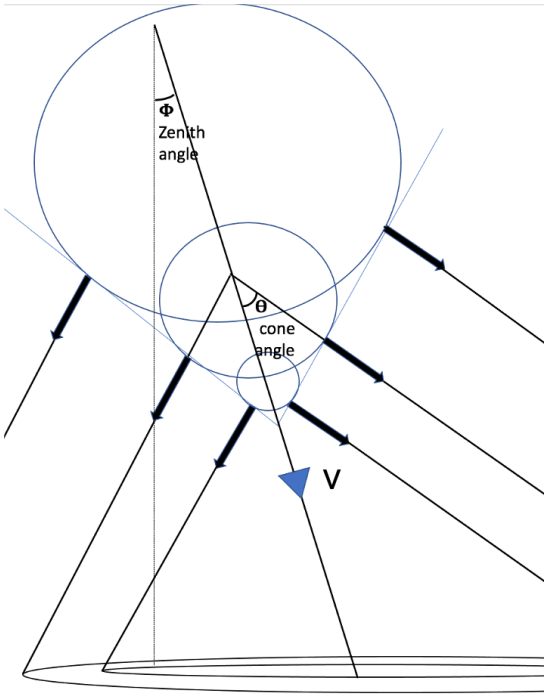

Figure 1.9: Cherenkov radiation cone created when a charged particle is moving at superluminous velocities.

energy particles.

1.2.2 Detection techniques of VHE gamma-rays

Two methods are widely used in order to detect VHE γ rays on the ground: Extensive Air Shower (EAS) arrays, like water Cherenkov tanks, and IACTs. Both techniques are indirect, meaning that they rely on the detection of Cherenkov light in order to detect the incoming γ-ray photon. The difference is that water Cherenkov tanks record the Cherenkov light of the shower particles when they pass through the water in the tanks while IACTs record an imprint of the atmospheric Cherenkov light emitted by the shower in the instrument's camera. This is why the ideal altitude for IACTs is $\sim$2 km, to be able to see the light from below and it is $\sim$5 km for air shower arrays aiming at detection of sub-TeV gamma rays, in order for the shower particles to pass through their detectors.

VHE γ rays can also be detected by space-based instruments like Fermi-LAT by the pair-creation process induced by the passage of γ rays in their detectors (see 2.1.2). These space-based instruments have a greater duty cycle and Field of View (FoV) than IACTs but have a much lower sensitivity especially at high energies.

	Space-based (Fermi-LAT)	Ground-particle arrays	IACTs
Field of view	$\sim 137^\circ$	90°	3°-10°
Duty cycle	$>95\%$	$>95\%$	10-30%
Energy range	20 MeV - $>$ 300 GeV	~ 500 GeV - >100 TeV	30 GeV - >100 TeV
Angular resolution	$0.15^\circ (>$ 10GeV)	0.4°-0.1°	0.05-0.02°
Energy resolution	15% $>$ (100 MeV)	60% - 20%	$\sim 7\%$
Background rejection	$< 10\%$	90% – 99.8%	$>95\%$
Effective area	0.8 m^2	several 10^4 m^2	several 10^4 m^2

Table 1.1: Properties of three type of VHE detectors.

An illustration of the three types of detection techniques is presented in Fig. 1.10. In Tab. 1.1 I present the different properties of the three types of γ-ray detectors with information gathered from [32] and the Fermi-LAT website [1]. All three techniques complement each other in order to cover the whole γ-ray energy range.

I will focus on IACTs and their detection techniques in the upcoming sections.

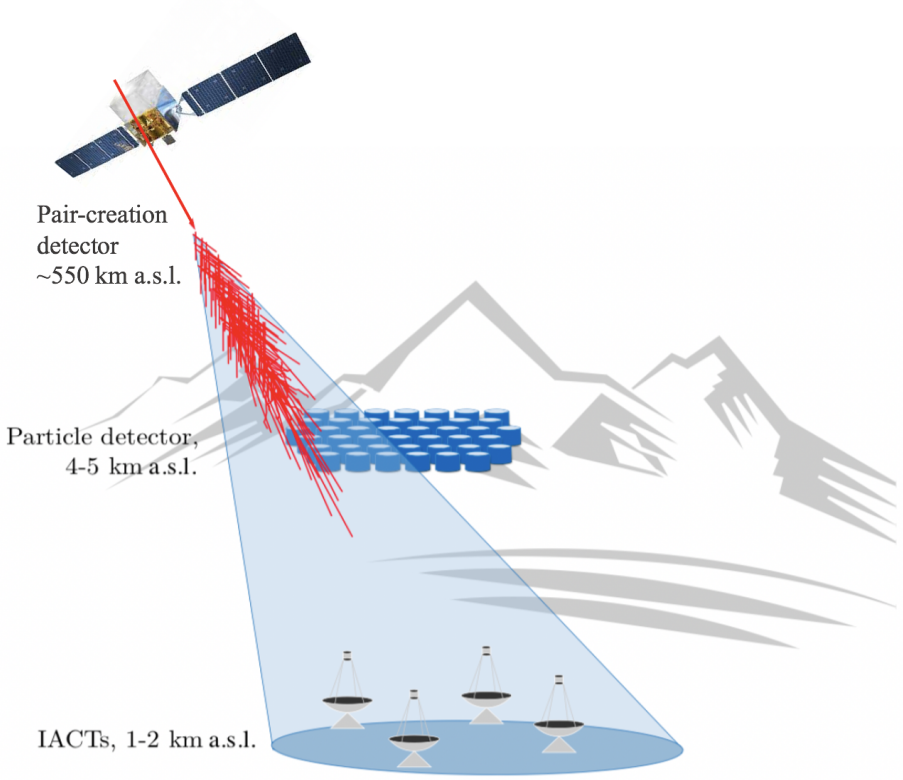

Figure 1.10: Illustration of an electromagnetic shower with space-based and ground based (water Cherenkov tanks and IACTs) VHE detectors at their preferred site altitudes. Adapted from [32].

[1] https://fermi.gsfc.nasa.gov/ssc/data/analysis/documentation/Cicerone/Cicerone_Introduction/LAT_overview.html

History of detection of VHE gamma-rays with IACTs

Three generations of IACTs have passed since the beginning of ground based VHE astronomy. The Whipple telescope was the first experiment to discover TeV emission from the Crab Nebula in 1989 [369]. The Whipple telescope is a 10-meter diameter γ-ray telescope constructed in 1968 in Mount Hopkins (Arizona, USA). Whipple also discovered the first VHE extra-galactic source, the Markarian 421 AGN [205]. The first stereoscopic system was the High-Energy-Gamma-Ray Astronomy (HEGRA) telescope array composed of six telescopes in La Palma (Canary Islands). The Major Atmospheric Gamma Imaging Cherenkov Telescopes (MAGIC), one of the leading VHE ground based experiments nowadays, is built on HEGRA's site. It is a second generation IACT composed of two 17-m diameter telescopes. The First G-APD Cherenkov Telescope (FACT) is a monitoring Cherenkov telescope also mounted in La Palma [38] (using a refurbished HEGRA telescope). Instead of photo-multiplier (PMT) tubes, FACT uses Geiger-mode avalanche photodiodes that require lower operation voltage and can be operated with strong background light. H.E.S.S., or the High Energy Stereoscopic System, is an array of 12-m diameter telescopes located in the Khomas Highland (Namibia). In 2004 it was the first IACT to record a two-dimensional image of an extended VHE source RX J1713.7-3946. In 2012, a 28-m telescope was installed in the middle of the array. It remains to this day the largest optical system ever built. Operational IACTs are MAGIC, H.E.S.S., the Very Energetic Radiation Imaging Telescope Array System (or VERITAS, successor of Whipple) and FACT. A third generation VHE observatory is being built, the future Cherenkov Telescope Array (CTA). It will be located in two sites: a northern site in La Palma and a southern site in Chile. It will also contain three types of telescopes, Large Size Telescopes (LST), Medium Size Telescopes (MST), and Small Size Telescopes (SST). The first LST (LST1) is built in La Palma and is now operational. The expected sensitivity of CTA will be at least an order of magnitude higher than current IACTs. I am a member of the H.E.S.S., LST and CTA collaborations.

1.3 Imaging Atmospheric Cherenkov Telescopes (IACTs)

VHE γ rays interact with the atmosphere and therefore can only be detected indirectly on the ground. The ground based telescopes dedicated for the detection of VHE γ rays are either IACTs like H.E.S.S. MAGIC and VERITAS or Water Cherenkov detectors like the High Altitude Water Cherenkov (HAWC [105]) and the The Large High Altitude Air Shower Observatory (LHAASO [52]). In the following I will focus on IACTs,

H.E.S.S. and CTA in particular.

1.3.1 The High Energy Stereoscopic system experiment (H.E.S.S.)

Figure 1.11: H.E.S.S. array with the telescopes parked-in during the day. Taken during my shift on the H.E.S.S. site in March-April 2019.

H.E.S.S. is a ground based experiment dedicated to the detection of VHE γ rays ranging from tens of GeVs up to 100 TeV. It is located in Farm Göllschau site in the Khomas highlands of Namibia at an altitude of 1835 m [28]. The experiment started in 2006 with four telescopes (CT1, CT2, CT3 and CT4) with 12-m mirror diameter each, constituting what is known as the H.E.S.S. I experiment. The telescopes are 100 m apart from each other in a square. In 2012 a fifth 28-m telescope (CT5) [73] was added in the center of the other four and the array is now designated as the H.E.S.S. II experiment. The addition of the fifth large telescope permitted to lower the energy threshold to $\sim$30 GeV. H.E.S.S. II is today one of the largest ground based γ-ray instruments on Earth with an effective area in the order of $10^5\,\mathrm{m}^2$. The HESS array is capable of detecting a point source with a flux of 1% of the Crab nebula in 25 hours [28].

H.E.S.S. telescopes

For cost reasons, the H.E.S.S. mirrors are segmented; the 12-m telescopes consist of 382 round mirrors with a diameter of 60 cm each summing to a total area of $108\,\mathrm{m}^2$. They are arranged in a Davis-Cotton

layout with a 15-m focal length [64]. The Davis-Cotton layout minimizes geometrical aberrations at the expense of gradual asynchronism between the edges and the center of the spherical surface at the level of the photon reception. The 28-m telescope consists of 875 hexagonal shaped mirrors with a 90 cm facet summing to a 614 m^2 collecting area. To this day, this telescope is the largest optical instrument on Earth. The large size of this telescope induces important asynchronism associated to the David-Cotton design, therefore a parabolic design to minimize dispersion is adapted. For all the H.E.S.S. telescopes, the mirrors are dedicated to the detection of Cherenkov light in the 300-600 nm range. They are focused towards a point in the sky at an altitude of 10 km corresponding to the typical distance of an air shower from the telescopes and they focus the light towards a highly sensitive camera described in the following. Each mirror mount is controlled by a motor used to remotely align the mirrors. A CCD is mounted in the camera's lid and another one in the center of the telescope dish. The alignment is performed by comparing the image of stars as seen by both CCDs.

H.E.S.S. cameras

Unlike the majority of optical telescopes, the H.E.S.S cameras are designed to detect ns faint flashes of light due to the fast and faint aspects of atmospheric Cherenkov light. Therefore the detectors are highly sensitive PMTs that are capable of detecting a single photon. The CT1-4 cameras contain 960 PMTs with their dedicated readout electronics while the CT5 camera contains 2048 PMTs. The PMTs and the electronics are encased and protected by a lid in the front. The CT1-4 cameras have a FoV of ~ 5 deg in diameter in the sky in contrast to the ~ 3.2 deg for CT5. Given the rapid nature of Cherenkov flashes of the order of ~ 10 ns, the camera's electronics have a fast readout capability of 273 μs, an event transfer capability of 144 μs, and a camera dead-time of 446 μs. Fig. 1.12 shows a simulation of images recorded by the camera for different integration times. If the integration time is too large, the signal will be embedded in background light. This shows that cameras need to have a fast and efficient electronics which enables to detect the γ photons.

Except for PMTs, the CT1-4 camera recently underwent an upgrade of all their hardware (trigger, readout electronics, cooling and mechanical components) and their control and data acquisition software in order to increase their performance [49]. The upgraded array is designated HESS-IU. Lowering the camera dead time and the readout time decreases the fraction of events lost. After the upgrade the camera dead time is reduced by a factor of 60.

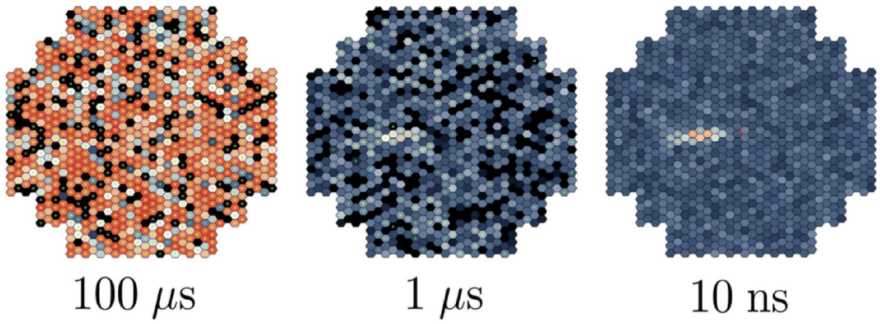

Figure 1.12: Simulated image of a shower in a H.E.S.S.-1 like camera with 100 μs, 1 μs and 10 ns integration time. The color scale indicates the intensity per pixel. Fom [65].

H.E.S.S. trigger system

The H.E.S.S. trigger system presents dual trigger levels, a *local* trigger on the telescope's camera level and a *central* trigger [129] between the telescopes. The *local* trigger performs a spatial and temporal correlation between adjacent pixels in order to detect Cherenkov light. This prevents the cameras from triggering due to high Night Sky Background (NSB). Each PMT is here treated as a pixel. The CT1-4 cameras are divided into 38 overlapping regions of 64 pixels and the camera is triggered only if a minimum required number of pixels (3 in standard operations) inside the same region reaches a threshold of photoelectrons (p.e.) (4 p.e. in standard operations) in the PMT. The *central* trigger ensures trigger correlation between the telescopes. This functionality has a dual benefit: it ensures that telescopes are not being triggered by isolated muons and it also ensures the stereoscopic reconstruction of atmospheric showers described in Sec. 1.3.2.

Other instruments on the H.E.S.S. site

It is also worth mentioning that the H.E.S.S. site is also host to a 75-cm optical telescope named ATOM [148] which is short for Automatic Telescope for Optical Monitoring. ATOM provides optical observations and monitoring of H.E.S.S. sources in the B, V, R and I bands. It can be used as a trigger for ToO observations, AGNs in particular if optical flares are detected.

Other instruments can also be found on the H.E.S.S. site: a LIght Detection And Ranging (LIDAR) that measures the aerosol composition of the atmosphere and an atmospheric monitoring system. The system contains a weather station that constantly measures humidity, temperature and pressure and a

scanning radiometer that monitors cloud movements around the site. Each telescope also has a scanning radiometer in order to enable the monitoring of clouds and temperature in the telescope's FoV. These weather monitoring systems are crucial for the observers in order to firstly avoid damage to the telescopes and secondly to efficiently operate the telescopes and take good quality data when the weather permits.

H.E.S.S. data acquisition

H.E.S.S. data acquisition constraints can be divided into four categories: visibility conditions, observation conditions, weather conditions and data acquisition mode.

Visibility conditions: For IACTs the energy threshold of observations range from a few tens to hundreds of GeV, depending on the zenith angle under which the source is observed. This is due to the absorption of shower light during its passage through the atmosphere, which is higher for larger zenith angles. The effect can be as strong as one order of magnitude of difference in energy threshold when passing to observations at zenith ($\theta z = 0\,\mathrm{deg}$) to observations at large zenith angles ($\theta z > 60\,\mathrm{deg}$), following an exponential increase. Therefore H.E.S.S. observations at low zenith angles, are preferred. The maximum allowed zenith angle is $\theta z < 60\,\mathrm{deg}$. This angle determines the H.E.S.S. visibility for a given time.

Observation conditions: In IACTs the sensitive PMT based cameras require strong limits on the maximal allowed light levels during observations therefore, they are operated observatories with low levels of light pollution. H.E.S.S. observations were typically restricted to times when the moon is below the horizon. These times are called *dark* time. The requirement for *dark* time are that the sun altitude is $<$ 18 deg and the moon's altitude is $<$ -0.5 deg. In 2019, H.E.S.S. started observing under low levels of moonlight in order to increase the data acquisition time. Observation falling under this category are called *moonlight* observations. The low levels of moonlight require that the moon's altitude is $<$ 65 deg - this constraint was loosened later on to 50 deg and then removed later on - the moon phase is $<$ 60% - which was reduced to 40% - and the separation of the moon to the observed source is $>$ 45 deg. *Twilight* observations are performed when the sun's altitude is between -18 deg and -12 deg. These values can change with further studies. The *moonlight* and *twilight* observations have higher trigger threshold per pixel than standard dark time operations (5.5 p.e. to 6.6 p.e.).

Weather conditions: H.E.S.S. data acquisition requires good weather and low levels of humidity. Other than the fact that the telescopes can not be operated on rainy and cloudy nights, H.E.S.S. is also sensitive to lightning, that causes high levels of light to fall in the PMTs and could potentially damage the cameras. Moreover, low levels of clouds can disturb operations especially when clouds move in or out which can affect the triggering of the camera since more or less showers will be detected (see Sec. 1.3.2).

Data acquisition mode: H.E.S.S. takes data in observation periods that have a standard duration of 28 minutes. These periods are called observation runs. The minimum allowed run duration is 5 minutes in order to gather enough statistics for the data analysis presented in the next section.

Fig. 1.13 shows an example of a night under which a source can be observed during dark time and moontime. Overall H.E.S.S has a duty cycle of $\sim$12% which sums to $\sim$1000 hours per year. The moonlight and twilight observations increase this number by 10%-15%.

1.3.2 H.E.S.S. data analysis

H.E.S.S. calibration

The calibration process allows to convert the signal recorded by the PMTs to a physical interpretation in terms of density of Cherenkov photons.

The collected charge inside the camera is first transformed into collected p.e. measures. Each pixel representing a PMT has an offset voltage. The variation of this offset voltage due to noise in the electronics is represented by the pixel pedestal. The pixels pedestal depend on the NSB and the temperature inside the camera. This relation is established by the dark pedestal 2 minutes runs that are performed every 2 to 3 nights. The pixel pedestals in real data is estimated by using the running average of 2 minutes.

The camera is operated in high and low gain mode simultaneously. The relative electronic gains of high versus low gain channel is determined offline from real data. In order to determine the PMT gain, a dedicated calibration run is performed by flashing a LED with know parameters in front of the camera in order to trigger it. This will allow to transform the charge into collected p.e.

Possible electronic failures can lead to broken pixels that are flagged and excluded from the analysis.

Flat fielding runs are used to make the camera response uniform, using UV laser or a pulsed LED at the centre of the mirror. Finally the Cherenkov emission of muons can be calculated and the amount of

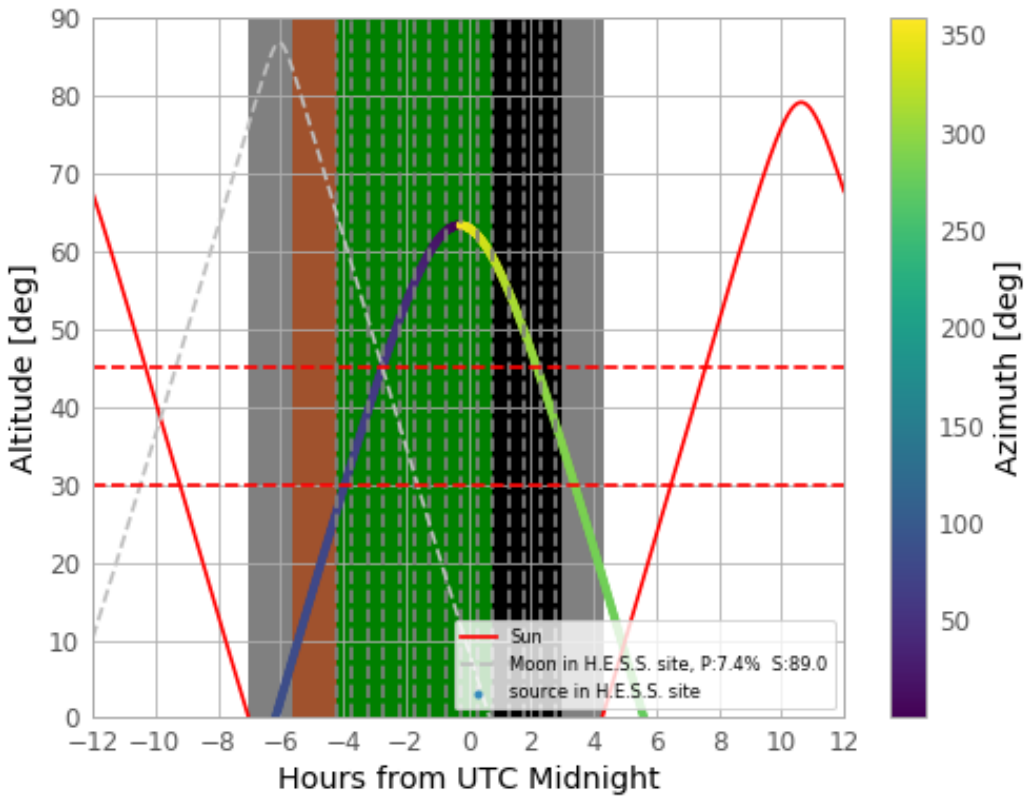

Figure 1.13: Altitude of a source as seen from the H.E.S.S site at a given time. The region shaded in black represents H.E.S.S. dark time observation conditions. The green region represent the time when H.E.S.S. can observe under moderate moonlight. The brown region represents times when H.E.S.S. can not observe due to high moon light levels. In the legend P is the moon phase and S the separation from the source at a given time. The moon Observation conditions here are : moon-phase $<$ 30%, moon altitude $<$ 65 deg, moon-source separation $>$ 45 deg. The dotted grey lines divide the available observation time into 30 minutes observation windows.The source can be observed when its altitude is $>$ 30 deg.

light depends on atmosphere refractive index and detector optical efficiency. Optical Efficiency calibration using muons from hadronic showers provides a direct way of measuring light yield.

H.E.S.S. data quality check

After selecting the observation runs to be analysed a data quality check is recommended. This step is crucial for the selection of good quality data for the analysis. This means that at the end of this process, all observation runs presenting hardware or weather and sky induced malfunctions will be filtered out. This step limits the number of times the analysis is performed, thus limiting the trial factor number. For ToO observations, checking the selection of good quality data is crucial since a potential signal cannot be

verified by re-observations. After a thorough data quality check the analysis will only have to be performed once. I perform this data quality check every time I want to analyse H.E.S.S. data. More information on the quality check can be found in [28]. The following key plots, called low level plots, can help assess the quality of the data.

Trigger rate plots: Trigger rate plots represent the number of cascade's Cherenkov light detections (hadronic or electromagnetic) as function of time. The number of incoming events from the same direction in the clear sky is more or less constant within a 28 minutes period. Trigger rates could slightly increase or decrease steadily during the run due to the zenith angle variation that causes more or less events to be seen by the telescope. With higher zenith angle, low level events will be less detectable by the telescope, therefore slightly lowering the trigger rate and vice versa. The trigger rate plot allows to asses the sky quality during observations. For example, strong variation in the trigger rates of a telescope, as shown in the right panel of Fig. 1.14, can be caused by clouds moving in or out blocking Cherenkov light. Such observation runs are excluded from the analysis. Elevated trigger rates (exceeding ~ 1500 for CT5) could indicate excessive NSB light caused by moonlight for example. This excessive light might falsely trigger the PMTs. The analyser should use data for the analysis where the trigger rates are steady like the example in the left panel of Fig. 1.14 for all telescopes.

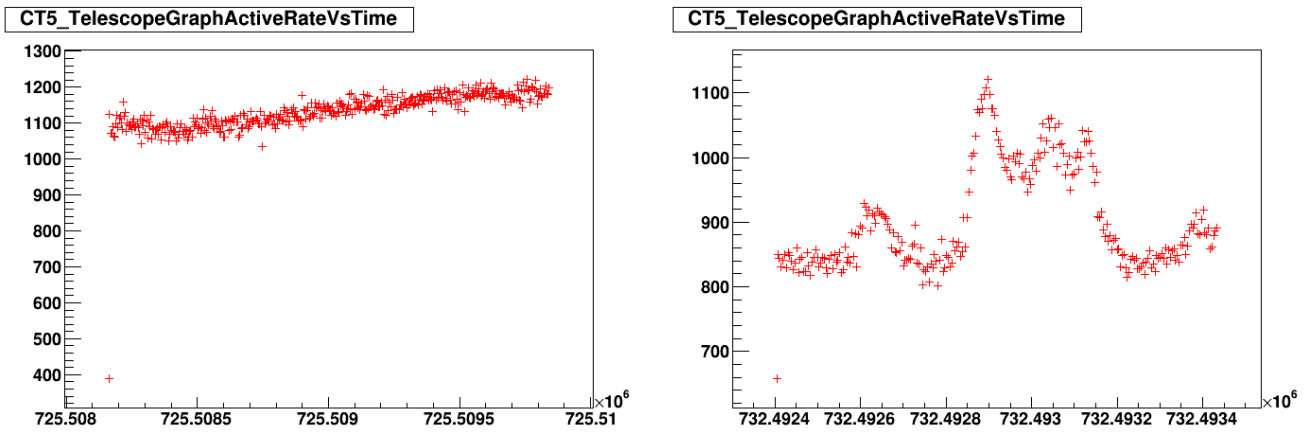

Figure 1.14: Trigger rates vs time (s) of the CT5 telescope taken on EM170817 for the VHE long-term follow-up campaign during different nights

Pedestals and bad pixels plots: In order to check the status of pedestals and broken pixels, we compute status plots like the one shown in Fig. 1.15. Accounting for different night sky conditions, the camera

is always operated in both low gain (LG) and high gain (HG) mode as mentioned above. In Fig. 1.15, the plots on the left side show the pixel pedestals status for high (upper plot) and low (lower plot) gain modes and the plots on the right side show the broken pixel status for the same gains. The colors represent the time fractions within the run during which the pixels are flagged as bad due to a deviation in the pedestal level. The status plot shown in the left panel of Fig. 1.15 shows a large number of bad pixels and pixels with significant deviations in pedestal levels during the entire observation run (pixels in red). The right panel of Fig. 1.15 shows the bad pixel and pedestal timeline. It shows the fraction of pedestal deviation (left) and bad pixel (right) fraction in function of time for both high (up) and low (down) gain. For the run shown in the figure, the defected pixels correspond to more than 5% of the entire pixels for the whole observation time. Runs showing similar features are excluded from the analysis due to the large number of abnormal pixels.

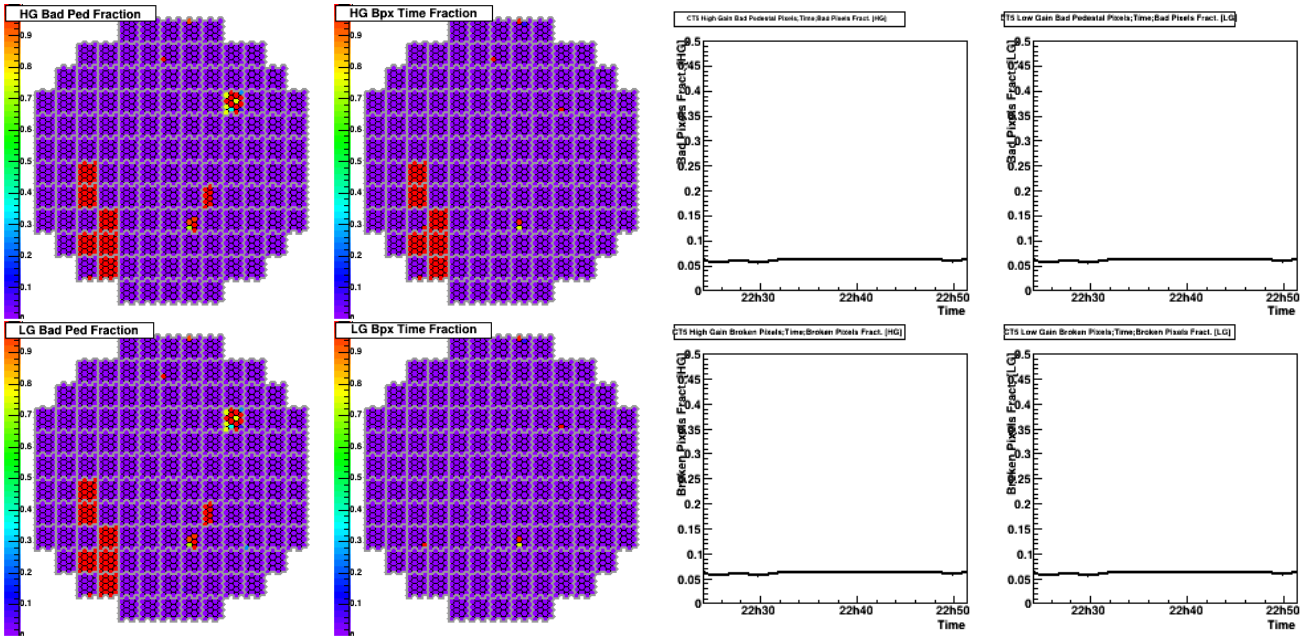

Figure 1.15: Pedestal and bad pixel status (left) and timeline (right) of the CT5 telescope during run 138426 taken on EM170817 for the VHE long-term follow-up campaign. These plots we selected explicitly to illustrate a problematic run with such rare behavior.

Center of gravity maps: The position of the detected events (hadronic and electromagnetic) on the camera is represented spatially to create an event map. The map is then smoothed in order to create the center of gravity (CoG) maps that will ease the detection of malfunctions. These maps are used to check the radial homogeneity of the camera, and to detect any hot or cold spots in the camera's FoV. Hot spots are usually caused by a pixel or cluster of pixels that have an unusual higher trigger rate, therefore shifting

the reconstructed event position towards the malfunctioning pixels and biasing the analysis. In a similar way, a cold spot is caused by a broken pixel or a cluster of broken pixels that are not participating in the data taking therefore creating an ”empty” event spot in the camera. In the example shown in Fig. 1.16 the spatial distribution of all detected events is shown in the upper plots while only the gamma-like (gamma-candidate) events are shown in the bottom part. In this particular example, we can clearly detect a cold spot of events that might be caused by malfunctioning pixels in that part of the camera. This particular run is removed from the analysis. For better understanding of the issues presented in the CoG maps, the analyser can cross-check the detected malfunctions in the CoG maps with more low level plots.

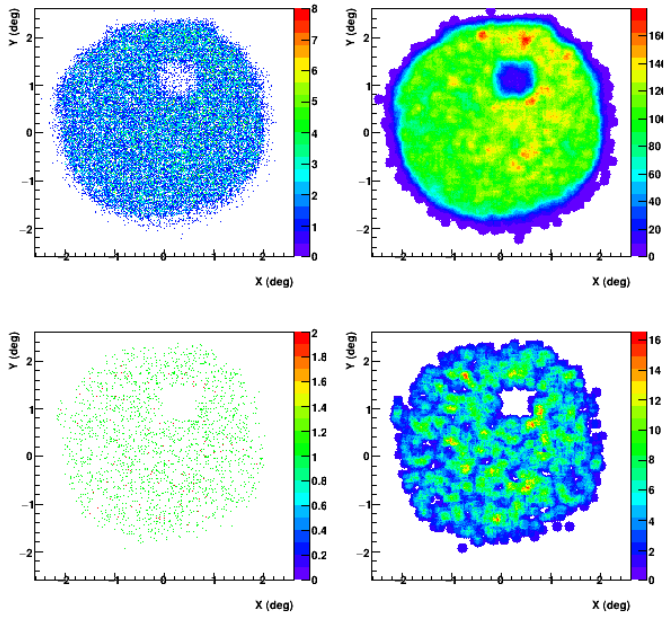

Figure 1.16: Center of gravity maps of the CT4 telescope during a follow-up observation run taken on SGR1830-0645.

NSB, CoG in the camera frame and pixel participation plots: NSB maps are a projection of the recorded pedestals during observations on the visible night sky in the camera’s FoV. PMTs will have higher pedestal levels if they detect star or moon light. These maps are useful to check if high pedestals are caused by a bright star instead of a pixel malfunction. I show an example of the NSB plot in Fig. 1.17. The same run to produce the CoG map in Fig. 1.16 is used. We notice that the pedestal levels for one of the pixel drawers is missing.

For a better understanding of the root of the problems detected, further checks can be performed. For example, the CoG maps in the frame of the camera can directly relate any hot or cold spots to the

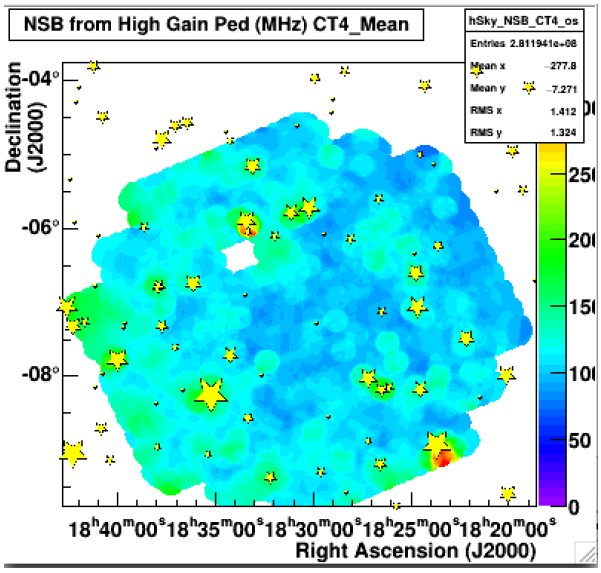

Figure 1.17: Night Sky background map of CT4 during an observation run taken on SGR1830-0645. Thew same run to produce the CoG map in Fig. 1.16 is used.

relevant pixel cluster and the pixel participation plot identifies the pixels that are not participating in the observation. I show on the left panel of Fig. 1.18 an example of the CoG maps in the frame of the camera that shows a cold spot that relates to the one shown in Fig. 1.16. The pixel participation plot on the right panel of Fig. 1.18 shows that the pixels in the region of the cold spot identified have a low participation fraction in the data taking. It turns out that the cold spot identified in Fig. 1.16 is due to a electronic failure in the corresponding pixel drawer. Note that the axis in Fig. 1.16, 1.17 and 1.18 are not the same.

H.E.S.S. shower reconstruction

After the calibration process is done and the recorded Cherenkov photons are obtained, shower reconstruction is the first step of the analysis. The recorded data include showers from γ rays (causing electromagnetic showers), muons and other charged particles like electrons, protons or heavy nuclei entering the atmosphere. Unfortunately, hadronic showers are largely dominant (by a factor of ~ 1000), and constitute an overwhelming background signal that needs to be filtered out in order to detect the γ-ray photons. Fortunately, electromagnetic and hadronic showers leave different kinds of imprints on the camera that allows to differentiate and filter out the biggest part of hadronic showers. This is done through shower parametrization.

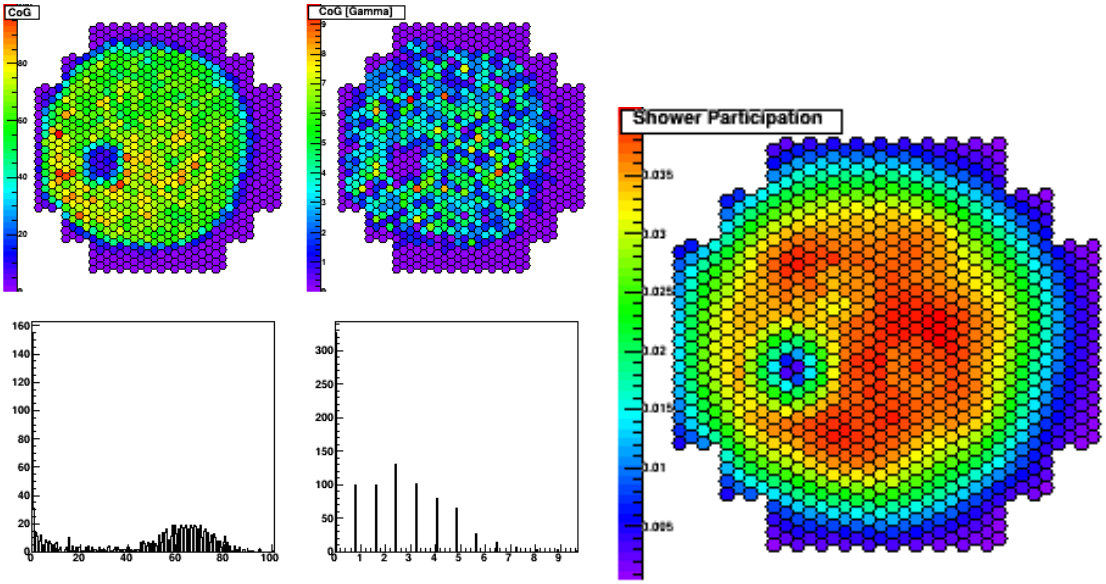

Figure 1.18: Center of Gravity map as shown in the camera frame (left) and pixel participation fraction of the CT4 telescope during follow-up observation run on SGR1830-0645. Thew same run to produce the CoG map in Fig. 1.16 is used.

Hillas reconstruction:

The oldest and most standard method for shower parametrization is the Hillas method described in [160]. Hillas noticed that the image of electromagnetic showers on the camera have an elliptical shape with a 2-dimensional Gaussian distribution along the longitudinal and transverse axis. He created a set of parameters represented in Fig. 1.19 that characterize the image:

- L (or sometimes l) the length of the shower is a measure of the longitudinal development of the cascade.
- W (or sometimes w) the width of the shower is a measure of the lateral development of the cascade.
- T_{ch} is the total charge inside the ellipse that leads to the amplitude of the shower.
- ϕ the azimutal angle between the center of the camera and the barycenter of the ellipse.
- α the orientation angle is the angle between the major axis of the ellipse and the axis defined by the center of the camera and the barycenter of the ellipse.
- d (or sometimes d) the nominal distance is the distance between the camera center and the barycenter of the ellipse.

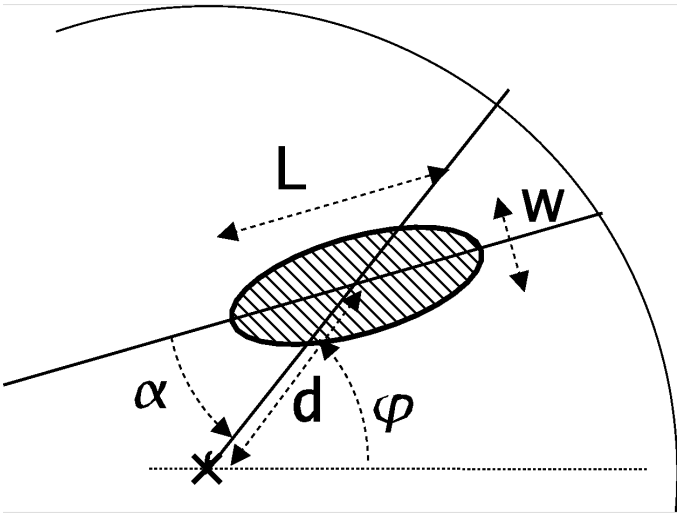

Figure 1.19: Geometrical parametrization of an elliptical image coming from an electromagnetic air shower using Hillas parameters. From [102]

Single telescope reconstruction: In single telescope analysis, or *mono* analysis that can be used for the CT5 telescope, the shower direction is estimated from the length, width and total charge of the recorded images with lookup tables computed from Monte Carlo (MC) simulations or with ad-hoc analytical functions. The shower energy is estimated the same way using the total charge and nominal distance

Stereoscopic reconstruction: In stereoscopic mode a shower will be recorded if it is detected by at least two telescopes. The direction of the incoming photon is given by the intersection of the main axis of each ellipse image in the camera. The impact on the ground is given by the intersection of the telescope lines (angle Φ_i on the ground) as shown in Fig. 1.20. The energy of the photon is reconstructed using lookup tables computed with MC simulations.

Gamma-hadron separation: The separation between γ candidates and hadrons can be achieved through comparison of the image width w and length l to expectation value and variance obtained from simulation as a function of image impact distance and size. Two parameters can be used, the Scaled Width (S_w) and Scaled Length(S_l).

$$S_W = \frac{w(q,\rho) - < w(q,\rho) >}{\sigma_{w(q,\rho)}} \tag{1.26}$$

$$S_l = \frac{l(q,\rho) - < l(q,\rho) >}{\sigma_{l(q,\rho)}} \tag{1.27}$$

Where q and ρ are the image charge and reconstructed impact distance. In stereoscopic observations these paramteres are averaged over all telescopes giving the mean scaled width (MSW) and mean scaled length (MSL) as selection parameters:

$$MSW = \frac{\sum S_W}{N_{tel}};\ MSL = \frac{\sum S_L}{N_{tel}} \tag{1.28}$$

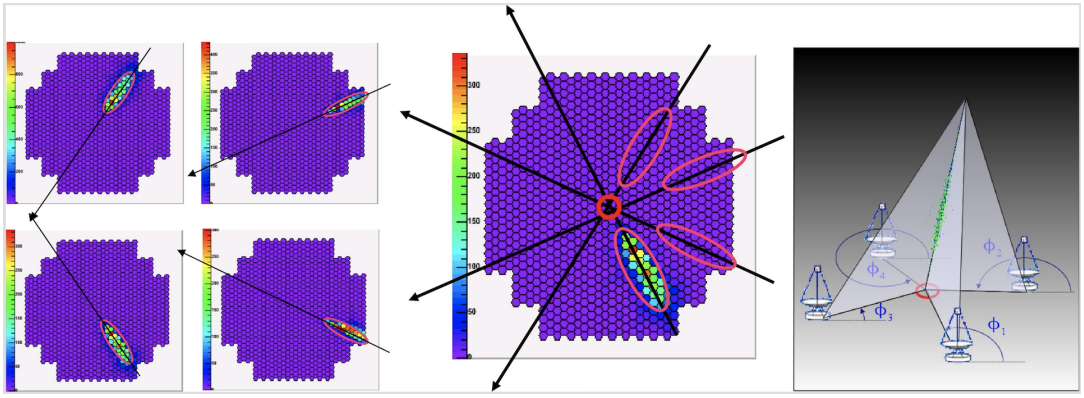

Figure 1.20: Incoming direction reconstruction of the Cherenkov air shower. From [102]

Model reconstruction: Semi-analytical image parametrization:

A semi-analytical model for the parametrization of shower images was created in the 1990s and was further developed by [103]. This model is used today in most of the analysis that will be presented in this thesis. The level of sensitivity achieved with this method is $\sim$2 times better than the one achieved with the Hillas parameters. It relies on the comparison of the camera image to MC simulations of hadronic and electromagnetic showers.

The MC shower simulations take into consideration collection efficiency, atmospheric absorption conditions, depth of first interaction and NSB and can produce a predicted image of the shower in the camera for a given set of primary particle parameters: energy, direction, impact distance and development depth. The light density due to a shower in the camera is calculated by an eight-fold integral over the longitudinal development, energy, direction with respect to the telescope, position with respect to the shower main axis, shower Cherenkov photon wavelengths and Cherenkov photon azimuthal angle around the electron (see Sec. 2.1 in [103]). Models are generated for a wide range of parameter space. An output bank of

images is produced and the actual image obtained on the camera is compared to the predicted images.

Under the hypothesis that the primary particle is a VHE γ-ray photon, a minimisation procedure is done to compare the intensity in each pixel of the camera with the prediction from the model using a log-likelihood approach (the number of detected photons in each pixel follow a Poisson distribution). The telescope log-likelihood is the sum over all the pixels assumed independent.

In order to assess the compatibility of the recorded events with a pure γ-ray hypothesis a goodness-of-fit G approach is chosen to compare the model prediction and the actual shower images:

$$G = \frac{< \ln L > - \ln L}{\sqrt{2 \times N_{dof}}} \tag{1.29}$$

Where $\ln L$ is the actual log-likelihood, $< \ln L >$ is the analytical calculation of likelihood value expectation and N_{dof} is the number of degrees of freedom. The goodness-of-fit is used to discriminate hadronic showers.

Several distinct features can be used for the discrimination between γ-ray and hadronic showers:

- Hadronic showers contain several electromagnetic sub-showers.
- Hadronic showers emit additionally low intensity Cherenkov light spread over a large fraction of the camera around the main Cherenkov light on the camera.
- Some nucleus particles entering the atmosphere emit Cherenkov light before the beginning of the cascade. This light is detected on the camera and produces a faint light spot near the main Cherenkov light from the shower.

Fig. 1.21 is a representation of the features described above of the light detected by the camera of emitted by hadronic showers.

The goodness distribution shown in Fig. 1.22 shows that the real data distributions are well reproduced by the simulations while the background distributions have a different shape. This indicates that the goodness-of-fit can be used in order to discriminate between hadrons and gammas. For example requirement for a goodness-of-fit < 0.6 will result in retaining 70% of γ rays and rejects more than 95% of background events [103].

Finally a maximum nominal distance cut can be applied in order to remove the events close to the edge of the camera for which the characteristics are hard to reconstruct due to image cut-off. Usually a

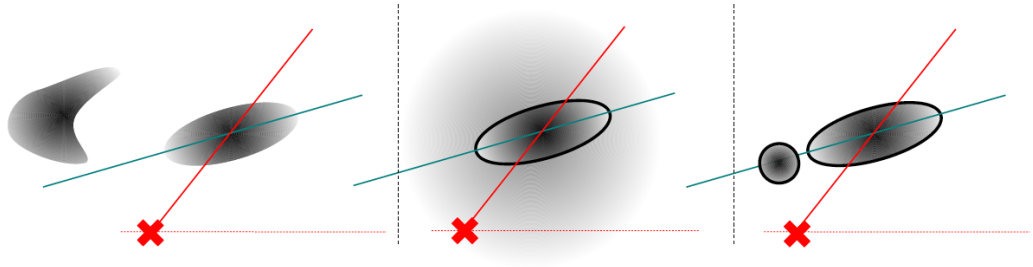

Figure 1.21: Examples of image topology that can discriminate between γ-ray and hadronic induced showers. **Left:** image subdivided in several clusters corresponding to electromagnetic sub-showers. **Middle:** hadronic rain emitted by the hadronic component of the shower. **Right:** Cherenkov emission from the primary particle (nucleus) entering the atmosphere before the actual shower development. The red cross denotes the centre of the camera. From [103]

nominal cut of 2 deg is applied for a camera radius of 2.5 deg (CT1-4 cameras). This improves the angular resolution at the expense of smaller effective area (see [100]).

H.E.S.S. Acceptance effects in the FoV

The acceptance shows a zenith angle dependency. It decreases with increasing zenith angles. This motivates observations at low zenith angle

Moreover, the acceptance of showers varies in the camera FoV. For example, at the edge of the camera, truncation effects are important and less showers will be recorded than at the center. In order to account for this effect, acceptance models are derived [63]. The acceptance shows a radial dependency; it decreases when we move towards the edges of the camera. An example of the variation of the acceptance with angular distance and zenith angle is shown in Fig. 1.23. The acceptance drop motivates the choice of pre-defined FoV radius R_{FoV}. When we trigger follow-up observations we use the following values to define the FoV: $R_{FoV} = 2.5\,\mathrm{deg}$ deg for CT1-4 and $R_{FoV} = 1.5\,\mathrm{deg}$ for CT5. If CT5 is included in the observations we choose the more conservative $\mathrm{R_{FoV}} = 1.5\mathrm{deg}$.

H.E.S.S. background subtraction

After filtering the biggest part of hadronic showers as mentioned in the previous section, the resulting photon counts are still highly dominated by background events (around 99% of the events are still due to cosmic rays). All registered events that pass the filtering are stored; each event is assigned a position in the sky and an energy. Plotting the events on a skymap will give the event count map. In general, background subtraction requires the definition of two regions: an OFF region that contains the gamma-like events from the background and an ON region which contains the gamma-like events from the source and

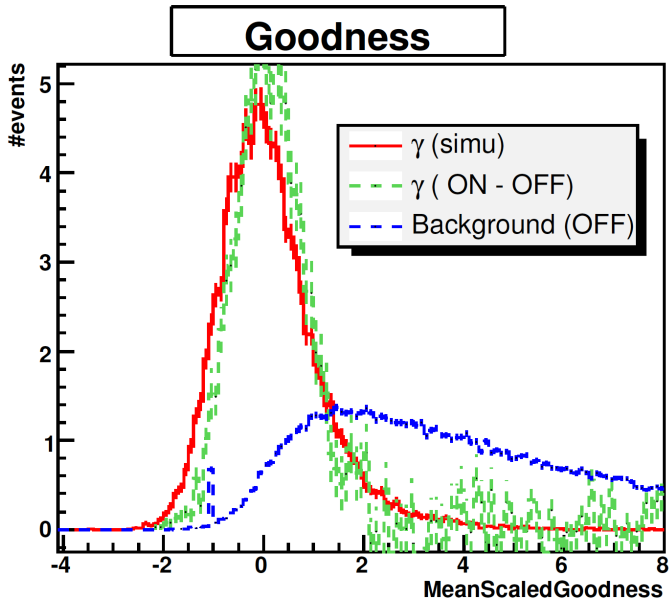

Figure 1.22: Distribution of goodness-of-fit parameter obtained for each analysis for simulated gammas (simu), real background data (OFF) and gammas obtained from real data (ON - OFF). From [100].

background. Moreover, the FoV of the instrument presents significant in-homogeneity in the response function that depends on the off-axis angle (the angle between the center of the camera and the source observed) of observation. Therefore, one would want to arrange control OFF regions (background regions) and ON regions at the same distance from the center of the camera. To do so, the method would be to observe two different regions in the sky (with slightly different right ascension), a region containing the source and a region containing no gamma sources. However using this techniques will involve having different observation conditions, and twice the number of observations needed per source. Therefore, we instead observe a source with an offset with respect to the pointing direction of the system (*wobble* offset). The *wobble* offset will allow to have the OFF regions at the same camera acceptance as the ON region. That will be useful for the background subtraction techniques. The main methods used in this thesis for the definition of source and background regions is described in the following.

Multiple off method: The "Multiple off" method illustrated in Fig. 1.24 allows to have the source and background region at the same distance from the center of camera. Several adjacent OFF regions are laid in a circle around the ON (target) region in order to estimate the background. The response to background-events is similar in all the regions (with $\sim$1% differences due to different zenith angles). The number of gamma events inside the target region is designated N_{ON} and the number of events averaged

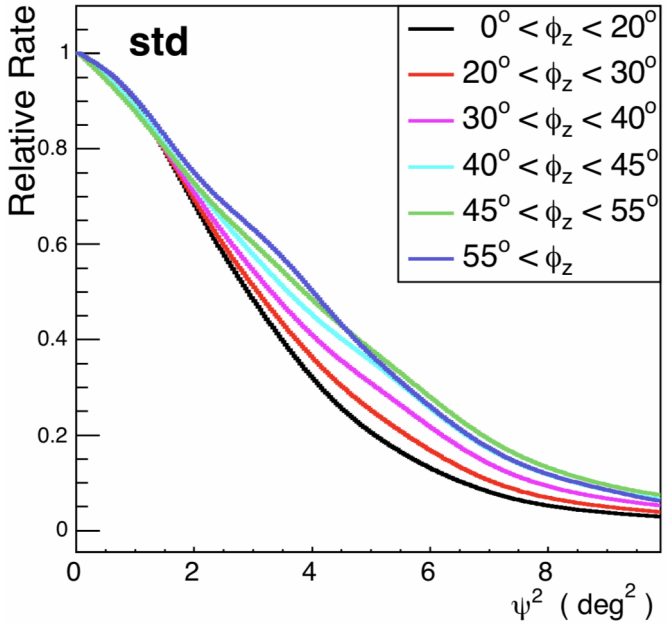

Figure 1.23: The variation of the radial system acceptance function (for H.E.S.S. I) with the squared angular distance Ψ^2 from the center of the camera for different zenith angle ϕ_z bands. From [63].

over the background regions is designated N_{OFF}. Due to the *wobble* offset the radial system acceptance can be extracted from the data set under study.

Ring background method method: The "Ring background" method as described in Fig. 1.24 is used for efficient background subtraction and map construction. This method consists in building a circle around the position to be analysed (position of the source for example); the number of counts inside this circle is designated N_{ON}. An exclusion region is then built around this circle in order to prevent counting gamma-like events from the source region. A ring is then built around the excluded region, the events in this region are considered background events and this number is labeled N_{OFF}. This is not done on a run-by-run basis but when all events from all runs are accumulated. Since the OFF region is not symmetrical with respect to the center of the camera, a precise estimation of background events in the ON and OFF regions needs to be determined by introducing an α factor. This determination is explained in Eq 1.30. The "Ring background" technique is still not used for spectral determination due to the complexity of determining the acceptance precisely from the different regions. However it is used in several H.E.S.S. analysis in order to create 2D maps.

Other background subtraction techniques exist like the template background technique where the es-

timation of the background comes from the source region itself instead of other regions in the FoV. These background events are selected due to their ”hadron-like” characteristics estimated during the reconstruction.

No matter what background subtraction technique is used, the regions in the FoV known to emit significant VHE γ ray should be excluded (masked) when estimating the background.

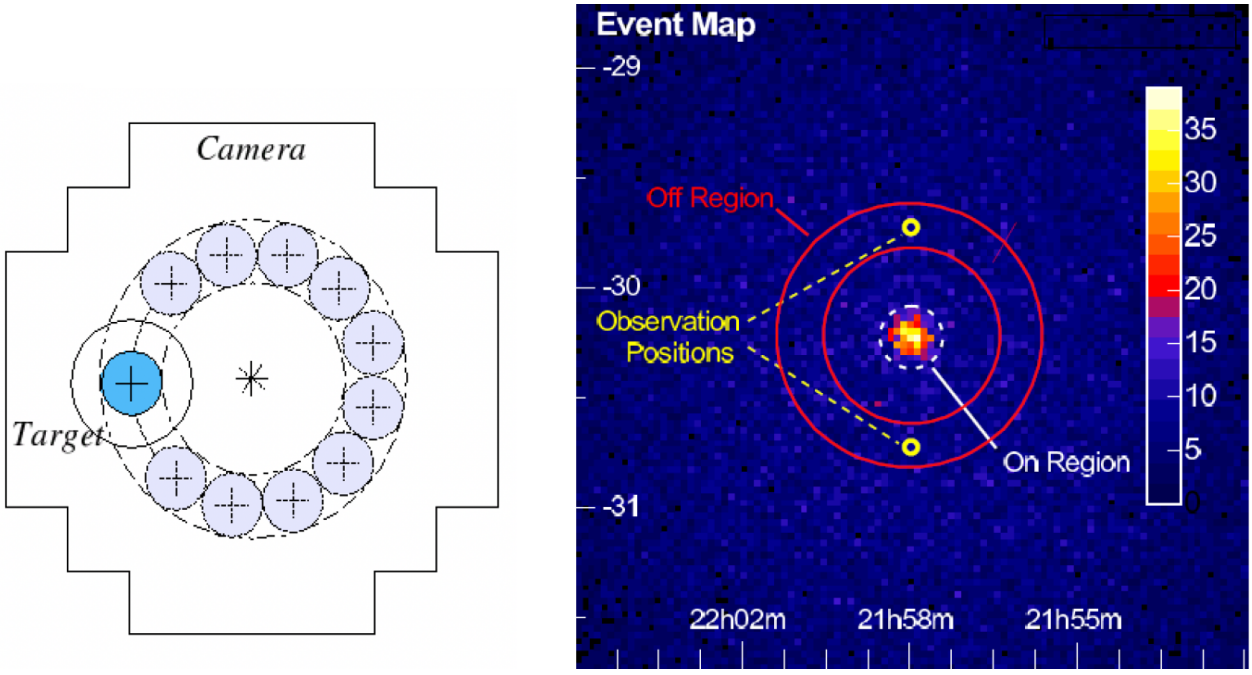

Figure 1.24: An example of the ”Multiple off” (left) and ”Ring background” (right) techniques for background subtraction on an event map. The color bar indicates the number of gamma ray like events. From [63].

2D Maps: *Artificial* maps are created with pixel size typically equal to 0.02 deg. On each pixel of the map the background subtraction method is performed and the values of N_{ON} and N_{OFF} are filled creating N_{ON} and N_{OFF} maps. One can specify a minimum number of background events per bin in order to define the edges of the analysed region. The effective FoV is therefore determined after the analysis by the number of background events.

H.E.S.S. signal extraction

A coefficient α is computed on each position of the map. α is a ratio that takes into consideration, the area, the acceptance and the exposure time of the N_{on} and N_{off} regions following Eq. 1.30 where $A^{\gamma}_{ON,OFF}$ is the system acceptance of gamma-like events and background like events and depends on the positions θ_x and θ_y of the source in the field of view, the zenith angle ϕ_z and the exposure time t. The acceptance

is assumed to be radial for most cases.

$$\alpha = \frac{\int_{ON} A^{\gamma}_{on}(\theta_x, \theta_y, \phi_z, t) d\theta_x d\theta_y d\phi_z dt}{\int_{OFF} A^{\gamma}_{OFF}(\theta_x, \theta_y, \phi_z, t) d\theta_x d\theta_y d\phi_z dt} \tag{1.30}$$

Excess maps are built following Eq. 1.31 on each position of the map.

$$N_{Excess} = N_{ON} - \alpha N_{OFF} \tag{1.31}$$

As the name indicates these maps show the expected excess number of photons that exceeds the background limit in this particular position and show any excess signal detected by the analysis.

However not all excess values have a significant meaning since most of them are due to statistical fluctuations. The significance S of an excess value is the number of excess events divided by its standard deviation (Eq. 1.32):

$$S = \frac{N_{Excess}}{\sigma[N_{Excess}]} = \frac{N_{ON} - \alpha N_{OFF}}{\sqrt{N_{ON} + \alpha^2 N_{OFF}}} \tag{1.32}$$

However, [210] developed a formalism in Eq.17 of their article based on the likelihood ratio method better suited for γ-ray astronomy. By the use of the statistical "null hypothesis" that expects the number of source photons to be only due to background, the significance of any given signal follows Eq. 1.33.

$$S = \sqrt{2}(N_{on} ln[\frac{1+\alpha}{\alpha}(\frac{N_{on}}{N_{on}+N_{off}})] + N_{off} ln[(1+\alpha)(\frac{N_{off}}{N_{on}+N_{off}})])^{\frac{1}{2}} \tag{1.33}$$

Significance maps are built from Excess maps using Eq. 1.33. In H.E.S.S., a signal on the map is considered significant if $S > 5$ at the position of the signal on the significance map. In case no significant signal was detected, the distribution of the significance values follows a Gaussian distribution.

H.E.S.S. analysis configurations and performances

In this section, I present the different configurations of analysis that I use in this thesis called `M++` analysis based on the *model* reconstruction analysis. H.E.S.S `M++ analysis` can be performed using different configurations. I present three configurations: `H.E.S.S.I Stereo` which include the four 12-m telescopes (CT1-4), `H.E.S.S.II Mono` which include only the 28-m telescope (CT5) and `H.E.S.S.II Stereo` which include all five telescopes. The *stereo* analysis requires that an event be recorded by at least 2 telescopes (for `H.E.S.S.II Stereo`, CT5 should be one of these telescopes). Finally the *combined* analysis

combines events from CT5 (*mono*) and from stereoscopic analysis from all five telescopes.

Moreover, different cuts can be used: `Standard` and `Loose`. `Standard` cuts have stricter shower selection criteria. They are used when the studied region is embedded in noise emission like the galactic plane. `Loose` cuts are used when the low energy expected signal is strong but is in regions with high signal to noise ratio. It maximises the γ-ray efficiency for strong sources at the expense of a poorer background rejection. Tab 1.2 presents the different reconstruction configurations used for `Standard` and `Loose` cuts.

	Min image charge	Min tel. (*stereo*)	Max shower goodness
Standard	60 p.e.	2	0.6
Loose	40 p.e.	2	0.9

Table 1.2: Reconstruction configurations for `Standard` and `Loose` cuts [103]

.

Effective area: Fig. 1.25 shows an example of effective areas comparison between H.E.S.S. *model* analysis configurations. `H.E.S.S.II Mono` has a larger effective area at low energies as expected while stereoscopic analysis with 4 or 5 telescopes has a larger effective area above $\sim$200 GeV to $\sim$300 GeV. The combination of CT5 *mono* analysis and CT1-4 *stereo* analysis provides the highest effective area in all the H.E.S.S. VHE range knowing that at TeV energies, stereoscopic analysis and combined analysis are similar.

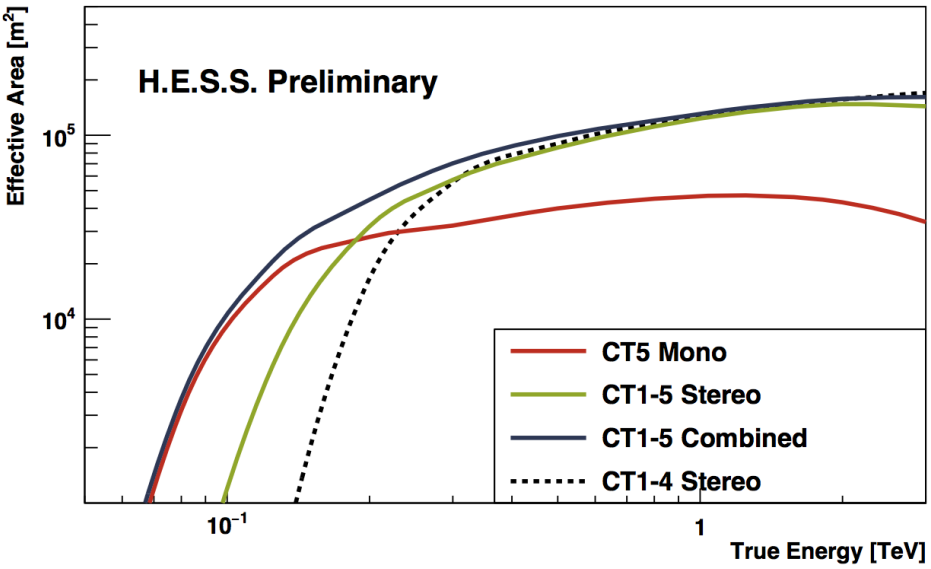

Figure 1.25: Effective area of different H.E.S.S. Model configurations. From [170].

Energy threshold: The energy threshold is the minimum energy of the primary γ ray in order to produce Cherenkov shower light that can be detected by the instruments. The energy threshold depends primarily on the zenith angle. It is defined as the energy where the acceptance is at 10% and 15% of its maximum value for the *stereo* and *mono* configurations respectively. After application of cuts on the parameters of the reconstructed showers with CT1-4 the energy threshold is roughly 160 GeV for observations at zenith, 220 GeV at zenith angle 30 deg, 400 GeV at zenith angle 45 deg and 1.2 TeV at zenith angle 60 deg. For H.E.S.S. II the evolution of the energy threshold with increasing zenith angles is illustrated in Fig. 1.26 for different sets of cuts.

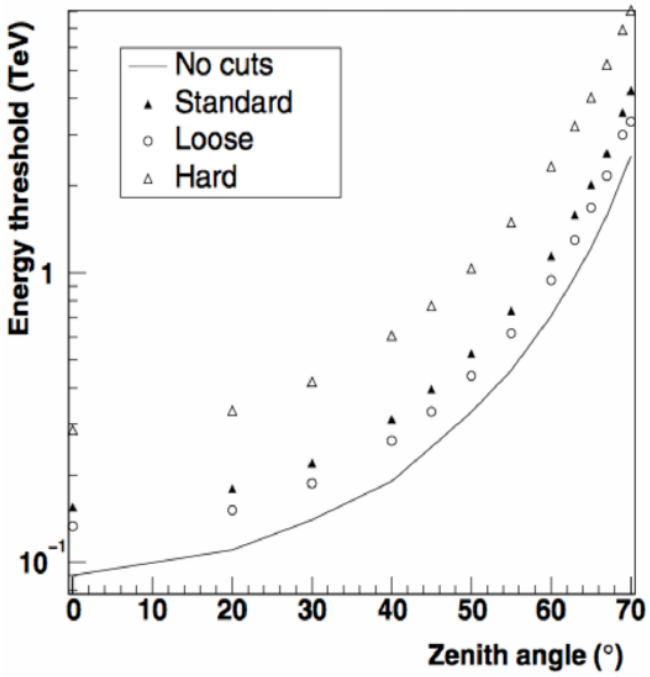

Figure 1.26: Zenith angle dependency of the energy threshold of H.E.S.S. II observations applying different data selection cuts. From [331].

Energy resolution: The energy resolution is defined as the rms of:

$$\frac{\Delta E}{E} = \frac{|E_{reconstructed} - E_{true}|}{E_{true}} \tag{1.34}$$

Fig. 1.27 shows the energy resolution and bias for the `M++ H.E.S.S. I Stereo` and two types of Hilas analysis. `Hillas` 60 with *standard* cuts and `Hillas 200` with *hard* cuts which require a minimum charge of 60 and 200 p.e. respectively. The energy resolution of the `M++` analysis varies around 10%, and is less

than 12% for all the energy range. The bias of the reconstruction is less than 5% for the whole energy range and can reach up to 20% at low energies (around the threshold energies).

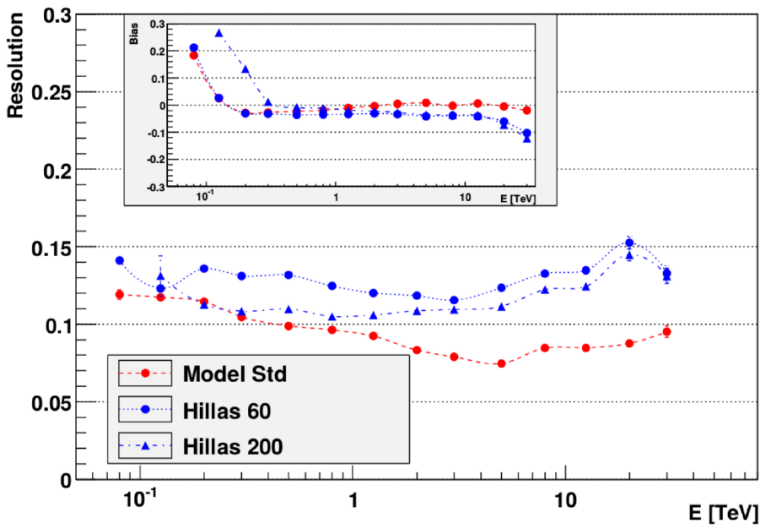

Figure 1.27: Energy resolution (main plot) and bias (inset) in function of energy for the `M++ H.E.S.S.I stereo standard`, `Hillas 60` and `Hillas 200` analysis. From [103].

Angular resolution: The angular resolution is defined as the 68% containment radius of the point spread function. It is dependent on the zenith angle and the energy of the γ ray. Fig. 1.28 shows the evolution of the angular resolution with zenith angle and the energy. For `M++` the angular resolution is less than 0.1 deg and is around 0.06 deg in H.E.S.S. core energy domain (1 TeV - 10 TeV).

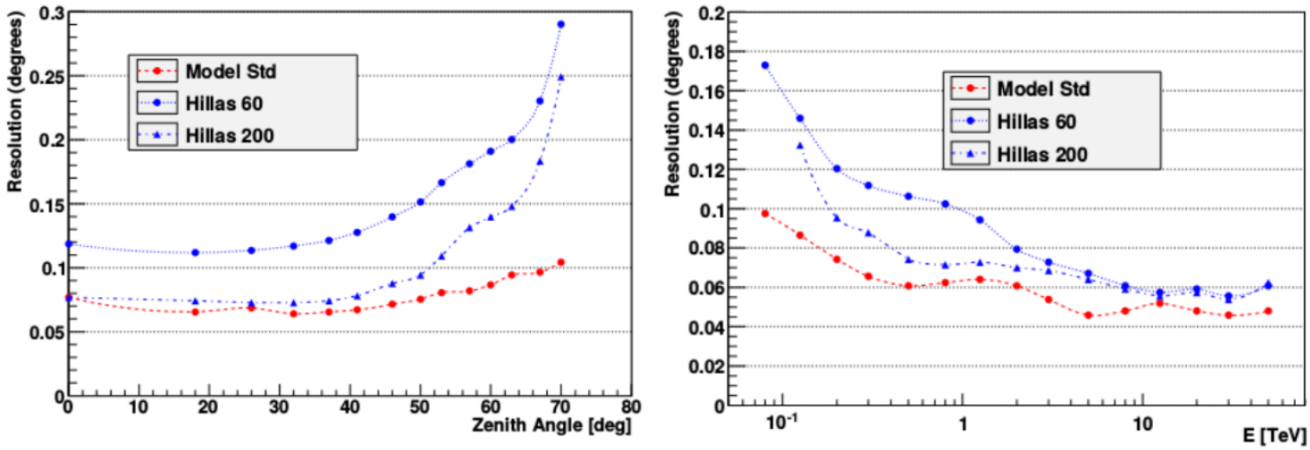

Figure 1.28: Angular resolution in function of the zenith angle (left) and energy (right) for the `M++ H.E.S.S.I stereo standard`, `Hillas 60` and `Hillas 200` analysis. From [103].

1.3.3 The Cherenkov Telescope Array observatory

CTA will be located on two sites, a northern site in La Palma in the Canary islands, and a southern site in Chile. It will be host of three types of telescopes LSTs, MSTs and SSTs.

LSTs have a segmented mirror with a 23-m diameter summing to a collection area of 400 m^2. The camera on board has a FoV of 4.3 deg. The large surface area of LSTs makes them sensible to low Cherenkov light and hence it makes them able to detect VHE γ rays down to 20 GeVs. LSTs are efficient ToO response machines since they are designed with a low weight and a drive system that allows them to re-position within 20 seconds. The construction of the CTA observatory has begun on the northern site. The first telescope to be completed is the first LST [94] in the northern site, LST1 [253]. The LST collaboration is starting to use this telescope for data acquisition and transient follow-ups.

MSTs have a mirror (segmented) with a $\sim$12-m diameter. The cameras on board will have large FoV of about 8 deg. They are mostly sensitive in the core energy range of CTA, from about 150 GeV to 5 TeV.

SSTs have a small collecting area of few meters in diameter ($\sim$4.3 m) and a large FoV of 10.5 deg. They outnumber all the other telescopes and will be spread over several kilometers on the southern site and will be able to detect γ rays from 1 TeV up to 300 TeV.

The final layout of the observatory is still under discussion. The final design should comprise in the northern site two types of telescopes, 4 LSTs and 15 MSTs. The southern hemisphere is expected to observe cosmic accelerators that can emit the highest photon energies (like the galactic center), therefore it will host 40 MSTs and 70 SSTs. Overall, CTA is expected to have a sensitivity to VHE γ rays at least an order of magnitude higher than current IACTs and it will be able to detect 1/1000 of the Crab Nebula flux within 50 hours of observing time. It will be first and by far the largest VHE observatory in the world [85, 252].

Chapter 2

Gamma-ray bursts (GRB), gravitational waves (GW) and fast radio bursts (FRB): transient messengers

The first astrophysical messenger is light or electromagnetic radiation. Astronomy started as observations of optical light coming from the stars and planets allowing to track their movements. It changed in the last two centuries due to the discovery of a wide spectrum of electromagnetic radiation ranging from radio, to γ rays with microwaves, infrared, optical, ultraviolet and the X-ray bands in between. γ rays in particular span more than 7 order of magnitudes in energy ranging from 100 keV to hundreds of TeVs. In the 1940s the second type of astrophysical messengers, cosmic rays, were detected from solar flares [125]. In the 1960s the first gamma-ray Bursts (GRB) were observed by the Vela experiment which were military satellites dedicated to the detection of γ rays from nuclear weapons. The information was declassified and published in 1973 [193] [89] [372]. In 1987, a major event for both multi-messenger and transient Astrophysics occurred: the nearby SN 1987 supernova in the large Magellanic cloud. Astrophysical neutrinos (third type of astrophysical messengers) were detected in the Kamiokande-II [163], IMB [67] and Baksan neutrino observatories [35] followed by the supernova light that lasted several weeks. In 2007, a mysterious Fast Radio Burst (FRB) [234] was detected in the archival data of the Parkes Observatory. FRBs are still to this day not fully understood. In 2015, LIGO directly detected for the first time gravitational waves (GW, fourth messenger) emanating from the coalescence of stellar mass binary black holes [5]. In 2017, LIGO and Virgo detected for the first time also GWs emanating from the merger of binary neutron stars

followed by a short GRB detected by Fermi and several electromagnetic counterparts later on [8] [264]. This event started a new era of multi-messenger and transient astrophysics, the current era. In September 2017, IceCube detected for the first time neutrino emission associated with γ-ray flare from the blazard TXS 0506+056 [2]. TXS 0506+056 is the first known source of high energy astrophysical neutrinos. In 2018 and 2019, IACTs detected for the first time VHE emission from GRB 180720B, GRB 190114C and GRB 190829A. In April 2020, the first galactic FRB was observed from the SGR 1935+2154 and for the first time an X-ray counterpart to FRBs was detected simultaneously.

The astrophysical events mentioned in the previous paragraph are transients. They are ”changing” events characterized by their temporal occurrences. Observations of the different phases of such events will show the ongoing processes taking place. Today we know four types of astrophysical messengers emanating from astrophysical (transient) events: electromagnetic radiation, gravitational waves, neutrinos and cosmic rays. The transients that will be studied in the scope of this thesis often have multi-messenger particularities like neutron star mergers that are emitters of GWs and electromagnetic radiation.

Having said that, multi-messenger and multi-wavelength studies remain crucial for the understanding of these transient events. That is why, the term Target of Opportunity (ToO) is widely used in our field. The discovery of a new GW event by ground based GW interferometers is a ToO that will trigger follow-up observations across the globe with all kind of instruments in order to detect counterparts to this event permitting a deeper understanding of the transient. Every new ToO brings us closer to understanding these phenomena.

Observing facilities are costly and limited by observational constraints like weather, daylight and moonlight in some cases. Therefore, telescope time is extremely valuable and efficient discrimination between ToOs is needed in order to be able to observe the most interesting events in a limited time. Therefore, scientists need to optimize three aspects of ToO follow-up and observation campaigns:

- Pre-observation: An observer must optimize follow-up strategies in order to observe the best locations in the sky of a poorly localised (potentially interesting) ToO. Also limited telescope time imposes on the observer ToO selection criteria and the rapid fading emission from transient requires a fast response. This requires a rapid, automated telescope response that is capable of making decisions without human intervention.

- Observations: Efficient data acquisition is key in providing good quality data to be analysed for the

search of transient signals.

- Post-observations: The analyser should be able to efficiently select and process the data and identify significant signals in order to discover and characterize the emission.

In this thesis, I work with IACTs like H.E.S.S. and the future CTA. As a member of the transient and multi-messenger working group in the H.E.S.S., LST and CTA collaborations, I focus on the VHE observation of GW events, GRBs and FRBs. These three classes of transients are connected by their potential VHE non-thermal emission in burst form. In order to hunt for VHE emission from GWs, GRBs and FRBs, I tackle the pre-observation, observation and post-observation challenges to attempt to establish connections between their multi-messenger and non-thermal multi-wavelength (transient) aspects. In the following I give an overview of these three transients.

2.1 GRBs

GRBs are short and energetic emissions of X rays and γ rays lasting from a few seconds to several minutes. GRBs are the most energetic EM events known to occur in the Universe and are a million trillion times more luminous than the Sun. Typical know source of GRBs are the core collapse of massive stars leading to the formation of new compact objects, the merger of two compact objects (typically neutron stars) or magnetars.

2.1.1 Emission model

To our day, the emission process of GRBs is not fully understood. However, some models are accepted within the astrophysical community. For GRBs in general, the *fireball* [288] model is one the most promising ones. When a new compact object is formed (by the collapse of a massive star for example), matter falls into the core of the star (a newly formed black hole in most cases) driving a cone shaped relativistic jet of charged particles and γ-ray photons as illustrated in Fig.2.1. Photons inside the jet can undergo electron positron pair creation making the medium optically thick. Relativistic particles inside the jet will interact within internal shocks that can be caused by magnetic re-connections inside the jet and will radiate through non-thermal processes like synchrotron and Inverse Compton. This is the prompt phase of the emission. γ-ray production processes are explained in Sec. 1.1.1. When relativistic outflows from the jet reach the interstellar medium the accelerated particles of the jet will interact with the surrounding

material and radiate in the afterglow phase. Two emission mechanisms can explain the non-thermal high energy components of the emission observed from GRBs. The non-thermal emission in the radio to X-ray (and soft γ-ray) bands can be explained by synchrotron emission and is fitted by a power-law spectrum. The IC process is predicted to be at the origin of the high energy component observed at energies above 100 MeV and could also lead to GeV to TeV emission. However, since few GRBs have been detected at energies above few tens of GeVs the signature of the IC emission is not clear. In Sec. 2.1.3 I discuss VHE GRBs where IC emission have been potentially observed.

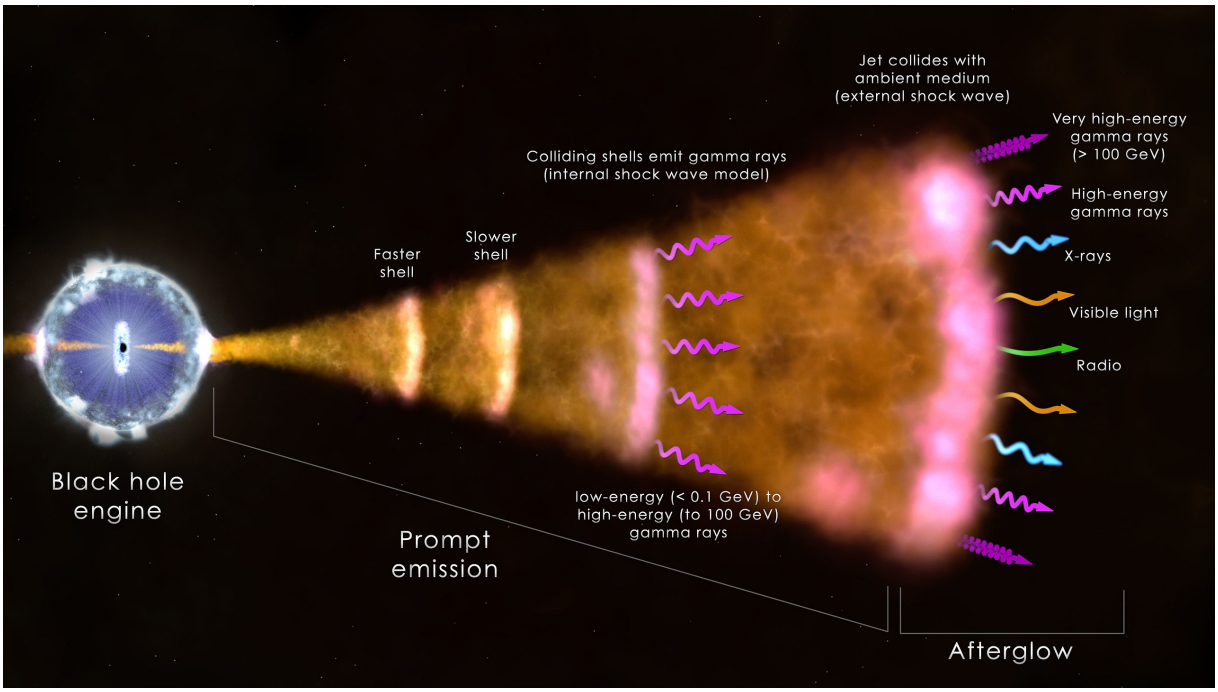

Figure 2.1: Gamma-ray Burst *fireball* emission model. From `https://imagine.gsfc.nasa.gov/news/21nov13.html`.

The collimated jet loses energy when expanding and the opening angle increases. The angle of observation of the jet plays a role in the observed emission from Earth. When a jet front is facing Earth, the observed jet is said to be on-axis and the brightest emission from the jet can be observed. When the jet is observed from an off-axis angle, only a fraction of the maximum brightness is accessible to the observer and the observed emission is smaller than if the GRB was on-axis. Moreover, when the jet reaches the interstellar medium, the jet slows down and the cone opening angle increases. An observer that does not have the jet in his line of sight in the beginning might observe delayed emission at later stages when the jet opening angle starts to increase. An illustration of a GRB jet observed at different angles is shown in Fig. 2.2.

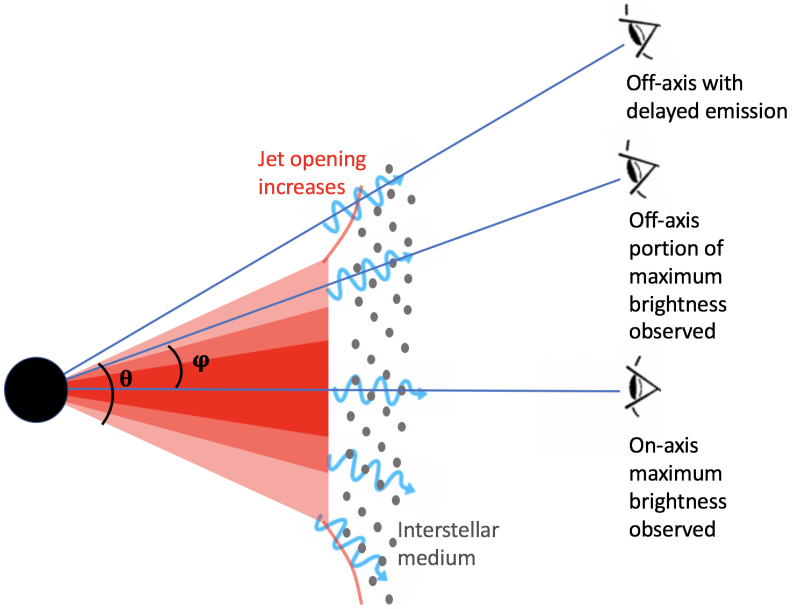

Figure 2.2: Illustration of GRB cone-shaped jet viewd at different angles. The black disk is the core collapse remnant. The red cone is the GRB jet. The shades of the red cone depicts the isotropic energy observed (energy decreases with opacity: illustrative only). θ is the cone opening angle and ϕ is the observation angle of the observer.

2.1.2 Detection overview

X rays and γ rays constitute the high energy electromagnetic spectrum. High energy photons cannot penetrate Earth's atmosphere, therefore the majority of instrument dedicated to the direct detection of X rays and γ rays, in particular GRBs, are sent to space.

Space-based observatories

The detection of X rays and γ rays in space can be achieved through different methods. For the low energy γ rays (below few MeVs) detectors are based on the Compton scattering or the photo-electrical effect in materials like Cadmium Zinc Telluride (CZT). For high energy γ rays (above tens of MeV) detectors are based on the pair production process. Over the past decades several space missions where dedicated to the detection of X rays and γ rays. From the Proton satellites (in the 1960s) to the Astrosat satellite launch in 2015, a total of 36 X-ray and 16 γ-ray satellite missions have been launched into space. A large number of these mission are dedicated to the detection of GRBs. From the currently available space observatories capable of detecting GRBs like Fermi [81], Swift [132], INTEGRAL [373], HXMT [386], Konus-Wind [42], AGILE [348], and the future GRB observatory SVOM [370], I present in the following the most relevant GRB observatories to this thesis which are Swift and Fermi.

Swift: The Neil Gehrels Swift Observatory is an observatory with three instruments on board for the detection and follow-up of GRBs.

The Burst Alert Telescope (BAT) is a large FoV instrument designed to detect and localise GRBs with an arcmin precision (3-4 arcmins). It consists of a two-dimensional coded aperture mask in front of a CZT detector. The incoming energetic photons create electron hole pairs proportionally to the energy of the incoming radiation. The detecting area of this instrument is 5200 cm^2. It has a 1.4 sr FoV that allows the instrument to monitor large parts of the sky ($\sim$ 8%) at once and detect GRBs in the hard X-ray energy range from 15 to 150 KeV. The localisation uncertainty is in the order of few (typically $\sim$ 3) arcmin.

The X-ray Telescope (XRT) is a follow-up instrument on board the Swift observatory. It is a grazing incidence Wolter 1 telescope that focuses X rays on a 600 $\times$ 602 pixels highly sensitive CCD. When a GRB is detected Swift automatically slews to the position of the GRB. XRT's provides X-ray observations in the soft X-ray domain ranging from 0.2 to 10 KeV. The XRT FoV (23.6 $\times$ 23.6 arcmin) is larger than the BAT localisation uncertainty which makes it efficient to detect X-ray counterpart emission from a GRB detected by BAT. XRT can pinpoint a GRB to 5 arcsec accuracy and it has an estimated sensitivity of $8 \times 10^{-14}\,\mathrm{erg\,cm^{-2}\,s^{-1}}$ in 10 ks of observation.

The UltraViolet and Optical Telescope (UVOT) is Swift's telescope dedicated for the follow-up of GRBs like XRT. It has a FoV of 17 $\times$ 17 arcmin and a PSF of 2.5 arcsec at 350 nm. UVOT has an eleven position filter wheel in front of a CCD detector and two grisms that can be used to obtain low resolution spectra of bright sources. It operates in the ultra-violet to optical domain ($\sim$ 200 to $\sim$ 800 nm) .

Fermi: The Fermi Gamma-ray Space Telescope originally called the Gamma-Ray Large Area Space Telescope (GLAST), is a primary observatory for monitoring the high energy sky, with its two instruments on board: The Large Area Telescope (LAT) and the Gamma-ray Burst Monitor (GBM).

LAT is a γ-ray telescope with a large FoV covering $\sim$ 20% of the sky and good localisation capabilities. It is capable of detecting γ rays in the range of 20 MeV to several hundreds of GeVs. With this ability to detect photons at such high energies it complements ground based telescopes that operate at TeV energies and are not capable of detecting photons at energies $<$ 20 GeV. Both Fermi-LAT and ground based VHE telescopes ensure a complete coverage of the VHE γ-ray energy range. The LAT detector is formed of layers of tungsten. When a γ ray hits the tungsten material it creates an electron and positron through the pair creation process which are tracked by silicon strips detectors. The direction of the incoming particle

is deduced by tracking the direction of these cascading pair particles in the layers of Tungsten. The total energy of the particles created inside the instrument is measured by a calorimeter at the bottom and they sum up to the total energy of the primary γ-ray photon.

GBM is sensitive in the 8 keV to 40 MeV range, therefore sensitive to GRBs in the X-ray and γ-ray domain. GBM consists of several detectors on board Fermi with different pointing angles allowing to cover more than half the sky at a time. The detectors are scintillators that will luminescence when they absorb a photon. The amount of light produced is proportional to the energy of the detected radiation. The position of the GRB is reconstructed by due to the count rate difference in several detectors the signal detected by several detectors. In fact, GBM provides rough GRB localisation (typically 3 deg) and can be used to re-point LAT towards interesting bursts.

Space instruments like Fermi are at a disadvantage when it comes to effective area due to the technical difficulty of having large photon collecting areas in space. But what these instruments lack in terms of effective area is accounted for with their large duty cycle, given that they are less constrained by daylight compared to ground-based instruments. The duty cycle of space-based telescopes is not 100% due to losses by occultation by the Earth and passages through the South Atlantic Anomaly when detector high-voltages are turned off.

Alerts overview

With telescopes like Fermi and Swift, the amount of GRBs detected over the past 2 decades has increased significantly. In less than 14 years of operation, Swift has detected more than 1300 GRBS at an average rate of about 100 per year. Swift-BAT GRBs are well localised, which makes it easier for other instruments to search for GRB counterparts in multi-wavelength bands. Fermi-GBM has a higher trigger rate of roughly 240 GRBs per year but a poor GRB localisation and energy estimation. On the other hand, Fermi-LAT, has a significantly smaller detection rate of a few GRBs per year but LAT GRBs have a potential extension of their spectrum to very high energies. The distribution of GRB alerts is ensured to the interested parties by the GCN network[1]. Relevant information related to detected GRBs, like MWL observations, are distributed via GCN circulars or ATels[2].

[1] `https://gcn.gsfc.nasa.gov/`
[2] `http://www.astronomerstelegram.org/`

Alerts contents

Each GRB observatory has a specific sequence of distributed alerts that contain specific information providing the basis for potential follow-up observations with other observatories like H.E.S.S. The sequence and content of the alert is considered when building a telescope response system dedicated to the follow-up of ToOs. The most relevant notices from Fermi-GBM are the initial notice `Fermi-GBM-FLT-POSITION` sent when the telescope detects a GRB with an on-board derived position. The notice contains also other crucial information like alert time, the uncertainty on the position and the significance of the detected signal. This information is then sent to the ground base and a refined set of parameters are computed and sent in a new notice `Fermi-GBM-GND-POSITION`. Finally the position of the GRB is recomputed and a `Fermi-GBM-FINAL-POSITION` is sent with a link to HEALPix localisation map computed with RoboBA [135] (more info in Chap. 4) . The final notice does not contain information on the significance of the signal. For Swift-BAT GRBs the alert notice is sent in one GCN notice `SWIFT-BAT-POSITION` containing the alert time, the position of the GRB with a few arcmin error and BAT photon count. A series of GCN circulars is expected afterwards containing preliminary and refined analysis results of the three instruments on board (BAT, XRT and UVOT). I note that several space based observatories also send re-pointing notices every time they are re-positioned. These notices are usually filtered out by the follow-up telescope's response system.

Classification of GRBs

Nowadays, GRBs are characterised by their emission phases, prompt and afterglow. This emission temporal characteristic divides GRBs in two main categories. Long GRBs (or lGRBs) and short (or sGRBs). Long GRBs are associated with core collapse of stellar objects [130]. Short GRBs are associated with CBCs [110] [124] and recently magnetars [77]. Long GRBs have a prompt emission phase that lasts several tens of seconds while short GRBs have a shorter prompt emission phase of a few seconds. Afterglows of GRBs can last several hours to years. Some GRBs are also characterized as Ultra-long GRBs that last more than 10000 seconds. They are proposed to become their own class of GRBs caused by the collapse of a blue supergiant stars [282], tidal disruption events [279] or new-born magnetars [393] [178].

History of GRBs

GRBs were discovered by accident during the cold war. The USA's Vela project, dedicated to monitor compliance with the 1963 Partial Test Ban Treaty by the Soviet Union by detecting nuclear detonations, detected for the first time on July 2 1967 a mysterious signal that was misinterpreted at first for a nuclear test. This event was later recognized as a burst of γ-ray emission from an astrophysical source and the discovery was published in [193]. The next decade witnessed several space missions dedicated to the study of these new bursts that brought some insight on the duration, and spectrum of these emissions. They were found to be bright emission of γ rays that lasted few seconds in most cases. The origin of these bursts remained a mystery. In 1995, a debate between their galactic and extra-galactic origin emerged. With the development of technology, GRB satellites became able to roughly localise these events in the sky. The BATSE satellite GRB catalogue [123] showed an isotropic distribution in the sky. Comparing this catalogue with galactic object catalogues like planetary nebulae and stellar clusters, scientist were obliged to recognized the extragalactic/cosmic origin of GRBs. The first GRB host galaxy and optical counterpart were identified in 1997 for GRB 970228 [70]. The localisation of GRBs to host galaxies provided definitive proof of the extragalactic origin of GRBs.

2.1.3 GRBs in the VHE domain

. From the thousands of GRBs detected over the years with space-based telescopes, I mention here two exceptional GRBs. GRB 130427A [22] is a lGRB that was exceptionally bright and was detected by Fermi and Swift. The Fermi-LAT recorded photon energies reaching $\sim$ 94 GeV from this event. It was the brightest GRB detected by Swift at the time, and was one of the closest with a redshif of $\mathrm{z} = 0.340$ [208]. The discovery of a hard spectral component in the high energy bands is reported by [347]. The authors argue that the high energy component in the afterglow emission from GRB 130427A might arise from IC emission in the afterglow phase. Another GRB that marked GRB sciences is the sGRB 090510 observed by Swift and Fermi [276] [24] at a redshift of $\mathrm{z} = 0.903$ [300]. Photons from GRB 090510 were detected at 30 GeV. It is the most energetic GeV emission from sGRGs at the time providing proof that sGRBs can also produce emission at the GeV band.

The synchrotron emission is thought to be at the origin of the non-thermal emission observed from GRBs afterglows from the radio bands to the X ray and soft γ rays [326]. It is the result of the external

shock at the interface of the jet and the interstellar medium. For years, scientist have predicted that SSC mechanisms in GRBs could lead to emission at higher energies in the VHE domain. However, the scarcity of GRB observations in these bands has not allowed a clear conclusion to be drawn [258] [375] [325] [266]. The observations of GRB at VHE with IACTs might help detect SSC emission.

GRBs detected by IACTs: In 2018 and 2019 two long GRBs were detected at VHE for the fisrt time by IACTs, GRB 180720B [17] by H.E.S.S. and GRB 190114C [21] by MAGIC. The discoveries were published at the same time.

GRB 180720B was detected by Fermi-GBM [315] on July 20 2018 at 14:21:39.65 UTC and Swift-BAT [336] 5 seconds later. It was observed by several MWL instruments, and it was detected by LAT in the high energy band with a maximum photon energy of 5 GeV. This GRB has a very bright prompt emission and is amongst the brightest five GRBs ever detected by GBM. H.E.S.S. triggered observations of this GRB with a 10.1 hour delay and a duration of 2 hours. The offline analysis showed for the first time a significant VHE signal spatially consistent with the GRB position. The host galaxy was localized at $\mathrm{z} = 0.653$ by VLT/X-shooter [99]. The evolution of the MWL high energy components of the flux from GRB 180720B are well described in the H.E.S.S. discovery paper [17]. The GRB was detected around the 5 σ level with photon energies ranging from 100 to 440 GeV. The VHE energy flux 11 hours after the initial detection is $\sim 5 \times 10^{-11} \mathrm{erg\,cm^{-2}\,s^{-1}}$ and is at the same level as the X-ray flux as shown in Fig 2.3. The X-ray light curve shows a steady flux decrease $\propto t^{-1.2}$. This GRB is particularly featured by its strikingly bright X-ray afterglow flux that ranks second after the exceptional GRB 130427A [22] and was detectable 30 days after the initial trigger. GRB 180720B establishes a potential observational link between bright X-ray emission and the possibility of significant VHE emission from GRBs. It also shows that VHE emission can be observed from GRBs several hours after the burst.

GRB 190114C was detected by Fermi-GBM [145] and Swift-BAT [141]). MAGIC was able to observe the GRB in the early afterglow phase under extreme conditions (high zenith angle $>$ 60 deg during Moon time) in less than 1 minute after the burst. The emission from the GRB was detected at energy range of 0.2–1 TeV. The afterglow emission from this GRB was detected by six satellites and 15 ground based instruments in several wavebands spanning 17 orders of magnitude from radio to TeV γ rays [244]. The detection of the GRB at several wavelengths allowed to model the source in the VHE bands. Fig. 2.4 shows the spectrum of GRB 190114C derived from data taken during two epochs in the X-ray, γ-ray and VHE γ-ray bands, 68 s - 110 s and 110 s - 180 s after the burst. The blue thick line represents the model used to fit the data taking into consideration EBL attenuation and internal absorption mechanisms such

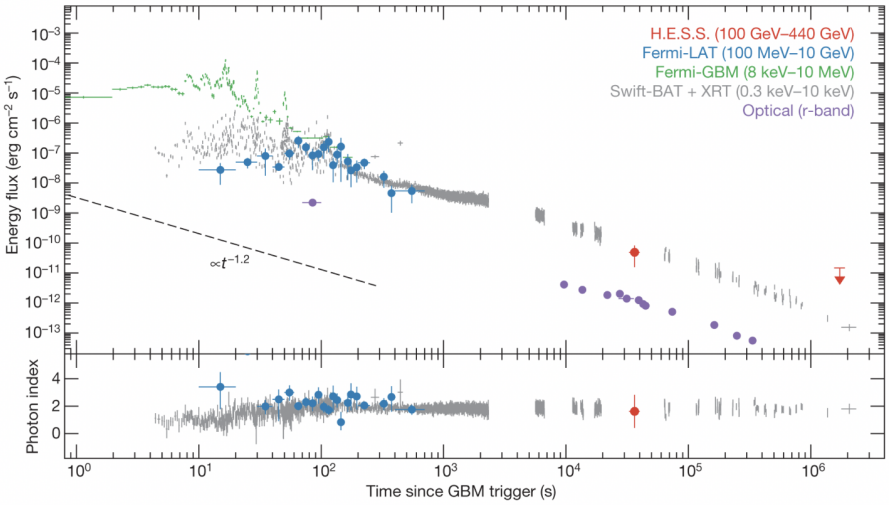

Figure 2.3: **Top:** Energy flux light curve of the X rays and VHE γ rays detected from GRB 1807209B. **Bottom:** Photon index of the Fermi-LAT, Swift and H.E.S.S. spectra. Error bars correspond to 1 σ. From [17].

as pair production. The first bump represents the synchrotron emission that explains the non-thermal emission up to the γ rays in the GeV level and the second bump represents emission by SSC. The overall flux decreases from the first to the second epoch. The total energy by the two components (synchrotron and SSC) is comparable during the two phases and is equivalent to the total energy emitted during the prompt phase. In other words, half of the total energy from the GRB was radiated during the prompt phase and the other half is shared by the synchrotron and SSC components in the afterglow phase. This means that the observations of GRBs in the VHE band shed the light on an important fraction of the total energy emitted.

A third long GRB, GRB 190829A was observed by H.E.S.S. at very high energies. GRB 190829A was detected by Swift-BAT on August 29, 2019 at 19:56:44.60 UT [274] and it was one of the closest GRBs ever detected with a redshift of $z = 0.0785 \pm 0.0005$ measured by the 10.4-m GTC telescope [172]. H.E.S.S detected significant VHE energy emission from the source during the following three nights of the trigger. The discovery and modelisation paper from H.E.S.S. [158] describes the striking similarities in the evolution of the X-ray and VHE flux further strengthening the link between the X-ray and VHE γ-ray afterglow flux from GRBs. Unlike the other GRBs detected at VHE i.e. GRB 180720B [17], GRB 190114C [21] and GRB 130427A [346], this GRB is not particularly bright. In fact in terms of luminosity and isotropic energy it ranks as one of the lowest amongst Fermi and Swift detected GRBs as shown in Fig. 2.5. However, its proximity is the reason why high flux levels were detected by the X-ray and H.E.S.S. instruments.

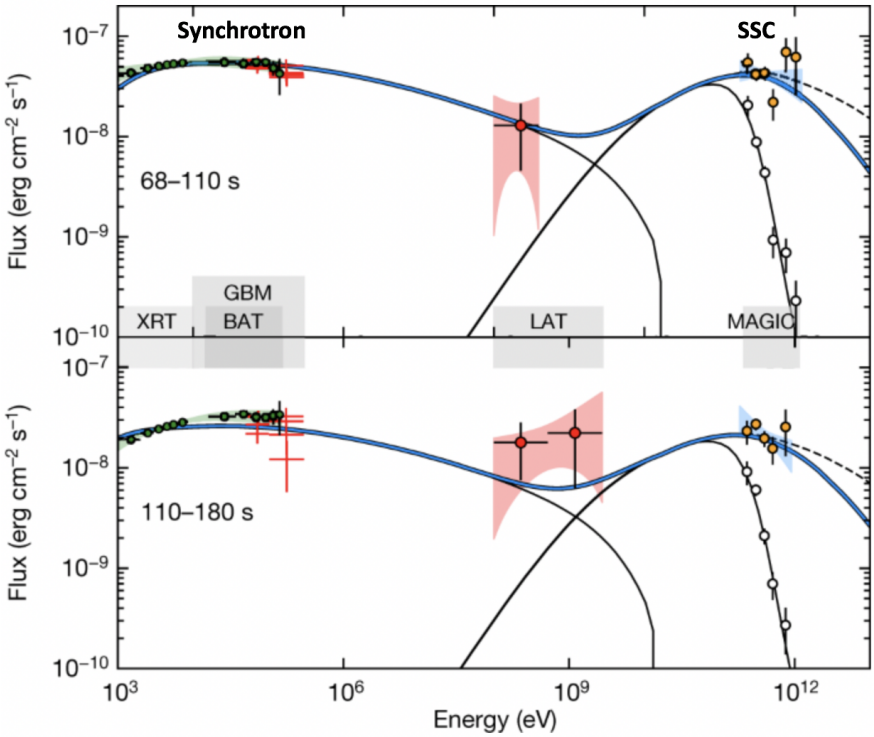

Figure 2.4: Modeling of the emission in the X-ray to the VHE band from GRB 190114C observations at 68 - 110 s (top) and 110 - 180 s (bottom). The black thick line represents the model, synchrotron for the first bump and SSC for the second bump, wihtout taking into consideration EBL absorption. The sum of the synchrotron and the SSC emission gives the dotted balck line which represents the model without taking into consideration internal absorption effects. Taking into consideration these effects results in the thick blue line that represents the model of the emission from the GRB during the afterglow phase. Modified from [244].

GRB 190829A X-ray flux level is in fact comparable to the three *giants* mentioned above. Other than the similarities in the X-ray and VHE γ-ray afterglow, GRB 190829A was detectable for three consecutive nights by H.E.S.S., which is an unprecedented for GRB VHE afterglows. In fact, the observations showed significant detection (with statistical significance of 21.7 σ, 5.5 σ and 2.4 σ for the three nights respectively) between 4.3 and 55.9 hours after the burst and energies ranging from 0.18 to 3.3 TeV. This is the first GRB to be observed at VHE energies over three nights, showing that VHE emission can last up to several days in the afterglow phase and can reach several TeVs. Due to the proximity of the GRB, EBL absorption effects are small, which results in smaller uncertainties on the VHE spectrum.

The implication of these VHE GRBs on the H.E.S..S program and GRB physics in discussed briefly in Sec. 4.2.1.

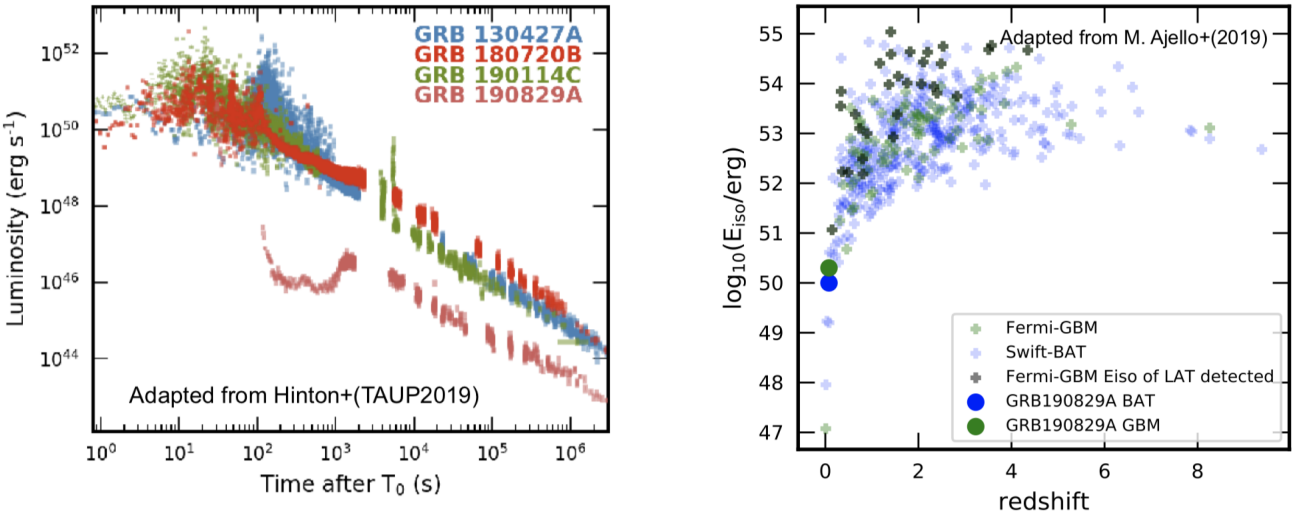

Figure 2.5: Left: Luminosity of GRB 190829A compared to the three bright VHE GRBs, GRB 130427A, GRB 180720B, GRB 190114C. From [30] Right: Isotropic energy as seen in Fermi-GBM and Swift-BAT in function of redshsift of GRB 190829A compared to other of Swift, Fermi-GBM and Fermi-LAT GRBs. From [162]

.

2.2 GWs

Gravitational Waves are disturbances in the space-time fabric that travel in wave form at the speed of light. When GWs pass in space, whether the space contains an object or not, the space-time itself will increase and decrease its size rhythmically. GWs are predicted by Einstein's general theory of relativity [111] [112]. This chapter does not aim to discuss the theory of GWs, therefore I refer the reader to [207] for a theoretical description. By adding a "small" perturbation to the Minkowski metric, GWs are introduced as solutions of the linearized Einstein equation around flat space-time. GW radiation is generated by any time-varying quadrupole moment, while monopolar or dipolar gravitational radiation are forbidden. The quadrupole formula (Eq. 89 of [207]) can be used to estimate an order of magnitude of the amplitude h of gravitational waves. For a source with mass M and size R Eq. 90 of [207] gives:

$$h \sim \frac{R}{r}\frac{R_s}{R}(\frac{v}{c})^2 s \tag{2.1}$$

where R_s is the Schwarzschild radius of the GW emitting source ($R_s = 2GM/c^2$), v is the internal velocity ($v \sim Rw$ for a rotating source), r is the distance of the source and s is an asymmetry fudge factor. For a spherically symmetric source $s = 0$. This means that in order to have a GW that in order to increase the

size of the GW amplitude, the source should be asymetrical, compact ($R < R_s$) moving at relativistic high speed and at a small distance r. Potential astrophysical sources filling these requirements are typically:

- Two heavy rotating compact objects like black holes, neutron stars, and white dwarfs.
- A spinning asymmetrical object like rapid rotating heavy object with a bump or dimple on the equator.
- An asymmetrical supernovae.

with CBCs being the most favourable sources (hence the detection of several CBC coalescence nowadays by their GW emission). Even in the most favourable cases, the GW amplitude is still small with $h < R/r$. In the case of a 3 $M_\odot$ source located at 200 Mpc, for instance the coalescence of two neutron stars in a distant galaxy, this gives the estimate $h < 10^{-22}$.

2.2.1 Compact Binary Coalescence

In the case of CBCs the two rotating objects will loose energy through GW radiation and will get closer to each other until they merge. Their rate of orbital decay can be approximated by:

$$\frac{dr}{dt} = \frac{-64G^3(m_1 m_2)(m_1 + m_2)}{5c^5 r^4} \tag{2.2}$$

where r is the distance between the two objects, G is the gravitational constant, and m_1 and m_2 are the masses of the two objects. This gives an expected time of merger:

$$t = \frac{5c^5 r^4}{256G^3(m_1 m_2)(m_1 + m_2)} \tag{2.3}$$

The merger product or *remnant* of a CBC depends on the nature/masses of the objects involved in the merger. An example of the evolution of a Binary neutron star (BNS) and a Binary Black Hole (BBH) is illustrated in Fig. 2.6.

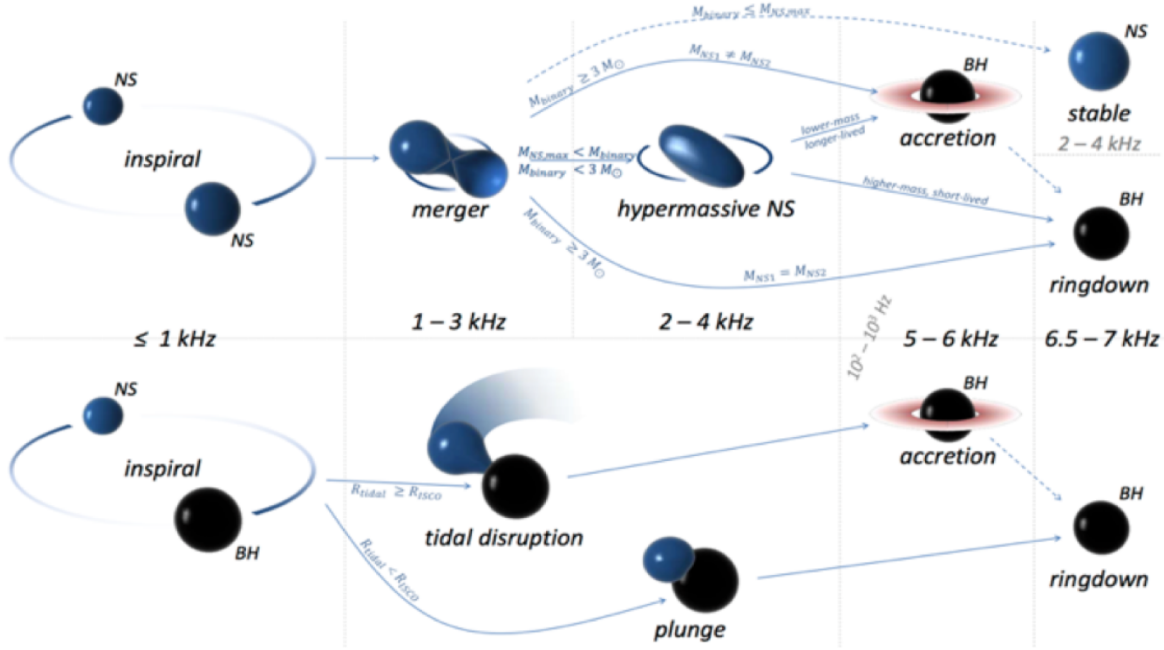

Figure 2.6: Schematic diagram of the possible evolution of BNS and BH-NS compact binary coalescences depending on the initial conditions. The frequency of the emitted GW is indicated for the different stages. From [58].

2.2.2 Instruments: operation and performance

Four instruments are dedicated to the detection of GWs, of which three are currently active with a sensitivity good enough to detect GWs from astrophysical origin. These instruments are the two Laser Interferometer Gravitational-Wave Observatory (LIGO) in Hanford and Livingston in the USA and the Virgo experiment in Italy. They are second generation GW detectors that underwent a series of upgrades. The names of the instruments after the upgrade is *Advanced* LIGO and *Advanced* Virgo. GW detectors are Michelson laser interferometers designed to detect minuscule distortions in space-time caused by the passage of GWs. They consist of two L-shaped arms of lenght L with a laser and two extremely sensitive mirrors at the end of the arm extension as shown in Fig. 2.7. GWs passing will cause different modifications in the length of the orthogonal arms; a quantity known as strain defined by $h(t) = \frac{L_x - L_y}{L}$. This strain will cause a phase difference in the laser beam that is detected by a photo-detector. This measured quantity can lead back to physical properties of the GW like the intensity and the polarization [267].

These instruments are operated in limited time observing runs with upgrade breaks in between. The timeline of past and future observation runs are shown in Fig. 2.8. The first observation run, O1, started in 12 September 2015 untill 19 January 2016, the second observation run, O2, lasted from 30 November

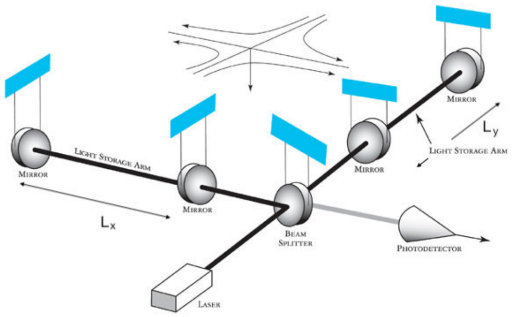

Figure 2.7: Interferometer design used to detect gravitational waves. From ligo.org

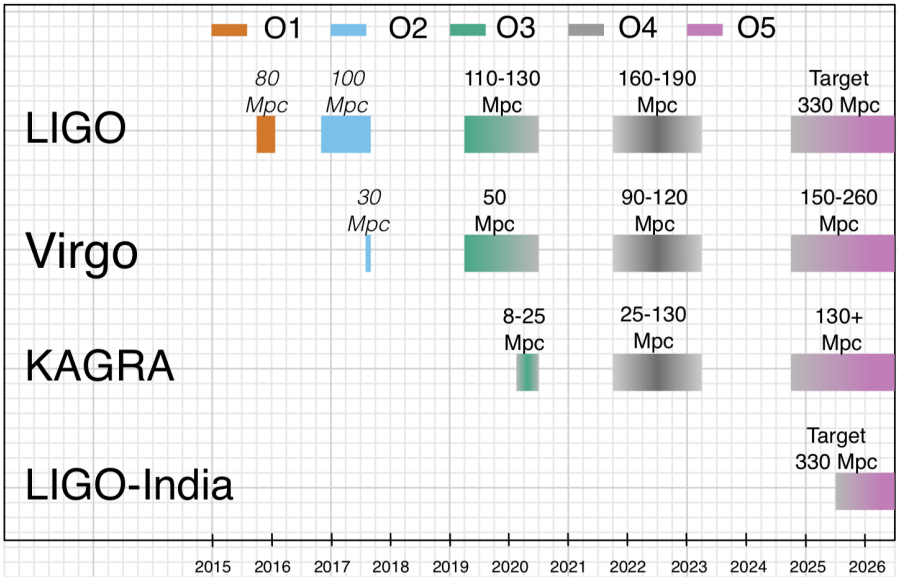

Figure 2.8: Long-term observing schedule of the Ligo Virgo and KAGRA interferometers. From [7] (Version 58).

2016 untill 25 August 2017 and the first part of the third observation run, O3a, started in 1 April 2019 followed by a month of commissioning break in October 2019. The second part, O3b, resumed in 1 November 2019 and was interrupted on 27 March 2020 due to the COVID-19 outbreak.

The sensitivity of the interferometers and their ranges are shown in Fig. 2.9 for BNS in O3b. The configuration of current GW instruments allows the detection of GW emanating from CBCs in the local Universe (like BBH, BNS or NSBH megers) or a nearby asymmetrical violent event like a galactic supernova. Some properties of current and future GW instruments are presented in the following.

LIGO: The LIGO [10] instruments consist of two interferometers in Hanford and Livingston with 4 km long arms. They are responsible for the first direct detection of GWs in 2015, GW150914 [5]. The LIGO

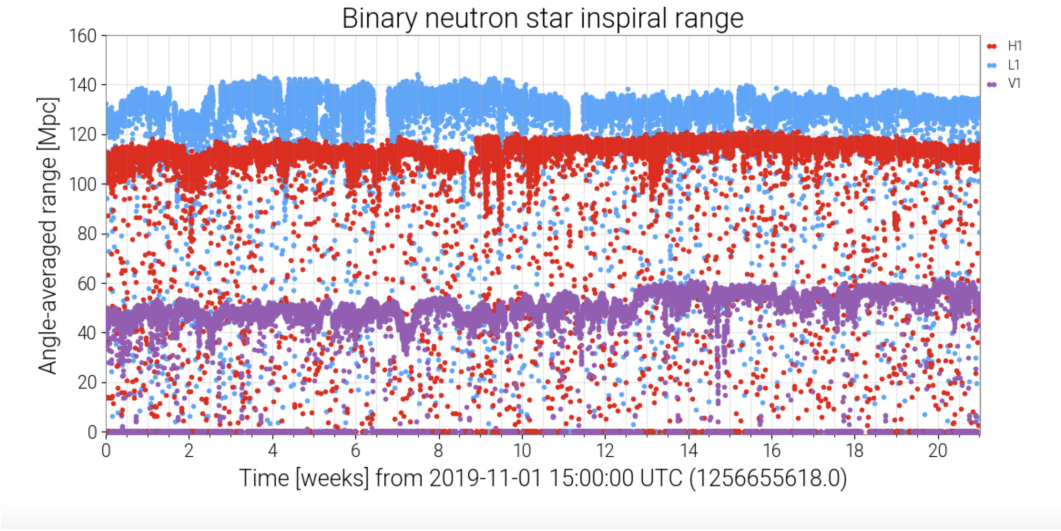

Figure 2.9: BNS range of the LIGO and Virgo interferometers during O3b. From gw-openscience.org

Hanford and Livingston sensitivities kept on increasing during the three observing runs and reached respectively a BNS range of ~ 120 and ~ 140 Mpc during O3b. A third LIGO detector is being built in India with 4 Km arms. It is expected to be operated in 2025 [357].

Virgo: The Virgo interferometer [20] in Italy is a 3 km arm long interferometer. The addition of the independent baseline from Virgo allowed a much better localisation with three interferometer detection (see Sec. 2.2.3) during O2 and O3 which allowed efficient multi-wavelength counterpart searches. The first event to be detected by Virgo and localised with three interferometers emanated is the BBH merger GW170814 [9]. During O3b Virgo sensitivity kept on increasing after the maintenance break in October 2019 and exceeded 60 Mpc for BNS mergers in the end of the run.

KAGRA: The Kamioka Gravitational Wave Detector [50] is a Japanese underground interferometer with arms length of 3 km that joined LIGO and Virgo in the end of O3b. However, it was still under commissioning with a very limited sensitivity and did not detect any GWs during that period.

GEO: GEO [328] is a German detector dedicated for calibration and mirror testing. It is an interferometer with 600 m arms where key technologies used in the other three interferometers are developed.

ET: The Einstein Telescope (ET) [242] is a future proposed third generation GW underground detector

with a triangular shape and 10 km arms. It is expected to detect GW signals from BBH and BNS mergers up to redshifts $z \sim 20$ and $z \sim 2-3$ respectively. It will also be able to detect GWs from BBH with masses ranging from hundreds to thousands $M_{\odot}$.

CE: The Cosmic Explorer (CE) [302] is a proposed third generation GW instrument with 40 km L-shaped observatory in the United States. The project will be realized in two stages, 1 first stage where LIGO and Virgo technologies will be used for 40 km long arms and a seconds stage wher the core optics will be upgraded using cryogenic technologies to achieve sensitivities one order of magnitude higher than LIGO.

LISA: The Laser Interferometer Space Antenna (LISA) [55] is a proposed interferometer in space dedicated to the detection of GWs. It will be composed of three spacecrafts arranged in an equilateral triangle with sides 2.5 million km long. LISA will be able to probe very low frequency GWs like the ones emanating from the merger of super massive BHs (SMBH). It is planned to be launched around 2034. The LISA Pathfinder (2016) is a successful mission designed to test the technology that will be used in LISA [254].

Other methods of detecting GWs exist like pulsar timing array with radio telescopes [362]. The deviations in the timing signature of pulses from pulsars is monitored to detect changes that are induced by low-frequency changes GWs passing by in the galaxy. This is similar to interferomters with arms extending between Earth and each pulsar in the array.

2.2.3 GW detection overview

Detection methods

The detection of GW by LIGO and Virgo is done through two methods: template searches and burst searches [6].

Template searches anticipate GW waveforms (from models) and find the best template that fits the data. The templates libraries are created from the Einstein's equations and predict the gravitational wave emission associated with the event. These template searches are characterized by their accuracy and their ability to infer distance information of the location of the event. Several online pipelines are developed for template searches like GstLAL [257], PyCBC [268] and MBTAOnline [25]. Differently from offline pipelines, the online tools consider a limited amount of parameter space to scan in order to match the

waveform with the templates. The parameters used for the rapid online search are the total mass, the mass ratio, the spin magnitude and the SNR threshold for triggering. Low latency offline search takes into account larger parameter space.

Burst searches look for excess power time–frequency patterns consistent in multiple detectors. These burst searches are dedicated to the hunt of un-modeled sources like nearby supernova. The pipelines dedicated for burst searches are cWB and oLIB [196] [237].

The GW events are then transferred to the Gravitational-wave Candidate Event Database (GraceDB[3]) which is a web interface for aggregation of information concerning the event. Further vetting of the GW events are posted on GraceDB and it is the main interface that is used for follow-up information.

GW localisation

Gravitational Waves localisation methods

The localisation of a GW source depends heavily on the timing accuracy of the detectors [116]. Considering a two-detector network separated by a distance **D**, if a source of GWs is located at a position **R** in the sky, then the recorded arrival time difference of the GW to detectors 1 and 2 is $t_1 - t_2 = \mathbf{D}.\mathbf{R}$. The localisation of the source is done by triangulation using the time delay registered in different detectors. As shown in Fig. 2.10, in a two-site network, the source localisation yields an annulus on the sky concentric about the baseline between the two sites taking in consideration timing and timing uncertainties. When the phase and amplitude of the GW signal are also taken into consideration (in addition to the all sky sensitivity depicted by the antenna pattern), the localisation is restricted to some regions of the annulus. These region can spam several hundreds of deg^2 in the sky. In a three-site scenario, the localisation region is restricted to two mirror regions in the sky with respect to the plane passing through the three sites. The localisation region spams few tens of deg^2. Moreover, with a four-site network, the localisation region can be restricted to only one region less than 10 deg^2 in the sky by using only timing information. Hence the importance of having multiple detectors.

GW localisation is performed by two pipelines. A low latency pipeline called BAYESTAR [340] which is short for BAYESian TriAngulation and Rapid localization and a pipeline called LALInference [361]. The BAYESTAR algorithm takes into consideration only the arrival timing, phase, and amplitude of the signal in order to obtain a marginal posterior as a function of the sky location. It is a fast approach capable of

[3] https://gracedb.ligo.org/superevents/public/O3/

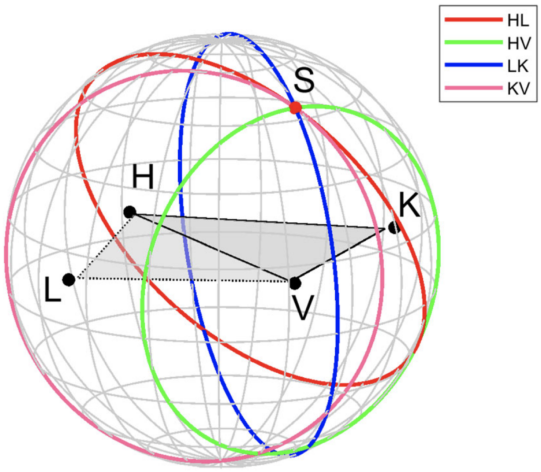

Figure 2.10: Source localization by timing triangulation for the *AdvancedL* LIGO-Virgo–KAGRA network with different combinations of interferometers involved. The location of the Hanford (LIGO) Livingston (LIGO), Virgo and KAGRA interferometers is indicated by the black dots near their initials. S represents the unique intersection region when 4 interferometers are used. From [7]

.

producing localisation maps in less than a minute. LALInference uses Markov chain Monte Carlo methods and scans the entire parameter space of a CBC GW signal. It is a robust approach to create localisation skymaps with expenses on the latency which is in the order of hours to days.

Gravitational Waves localisation maps

The GW localisation map is provided in a HEALPix format[4] [392] [138] and contains four layers of information for each pixel. HEALPix is the acronym for Hierarchical Equal Area isoLatitude Pixelization of a sphere, the pixelization scheme subdivides the spherical surface in equal area pixels. The resolution of the map is defined by the N_{side} parameter and the total number of pixels of the map is $N_{pix} = 12 \times N_{side}^2$. The first layer contains the probability ρ_i of the GW emission coming from a certain sky direction, and the remaining three layers contain event distance information [339] [338]. The posterior Gaussian probability along the line of sight is defined by

$$\rho(r|\mathbf{n}) = \frac{\hat{N}(\mathbf{n})}{\sqrt{2\pi}\hat{\theta}(\mathbf{n})} exp[-\frac{(r-\hat{\mu}(\mathbf{n}))^2}{2\hat{\theta}(\mathbf{n})^2}]r^2 \tag{2.4}$$

The three distance layers of the HEALPix map contain the location parameter $\hat{\mu}_i = \hat{\mu}(n_i)$, the scale $\hat{\theta}_i = \hat{\theta}(n_i)$ and the normalization $\hat{N}_i = \hat{N}(n_i)$, where i represents a pixel. Therefore the probability that

[4] `https://healpy.readthedocs.io/en/latest/`

GW event source is contained inside a pixel *i* and at a distance between r and r + dr is

$$P(r|\mathbf{n}_i)dr = \rho_i \frac{\hat{N}(\mathbf{n}_i)}{\sqrt{2\pi}\theta(\hat{\mathbf{n}}_i)} exp[-\frac{(r-\hat{\mu}(\mathbf{n}_i))^2}{2\hat{\theta}(\mathbf{n}_i)^2}]r^2 dr \tag{2.5}$$

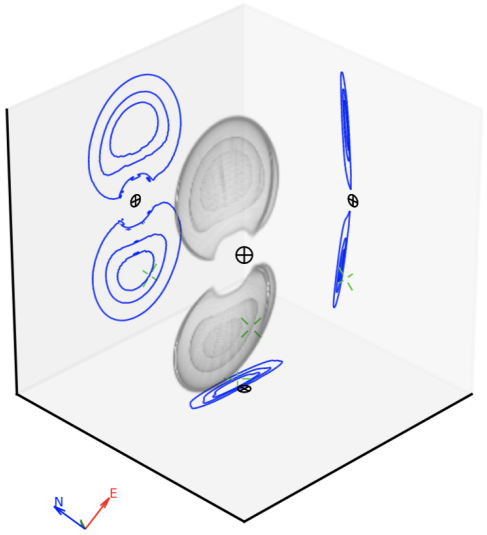

Figure 2.11: Volume rendering of the 20%, 50%, and 90% credible levels of a 2-detector (Advanced LIGO) simulated GW event. The three planes are perpendicular to the principal components of the probability distribution. The Earth representing the observer's position is at the origin. The green reticle represents the true position of the simulated source. The compass in the bottom left corner shows the basis vectors of the equatorial coordinate system. From [339].

An example of the volume rendering of the localisation of a GW event and its projection on the 3 space planes is given in Fig. 2.11. The localisation map is normalized in a way that the sum of the probability inside all the pixels is equal to 1 giving:

$$\sum_{i=0}^{N-1} \rho_i = 1 \tag{2.6}$$

and

$$\sum_{i=0}^{N-1} \int_0^{\infty} P(r|\mathbf{n}_i) = 1 \tag{2.7}$$

An example of a GW localisation map is given in Fig. 2.12

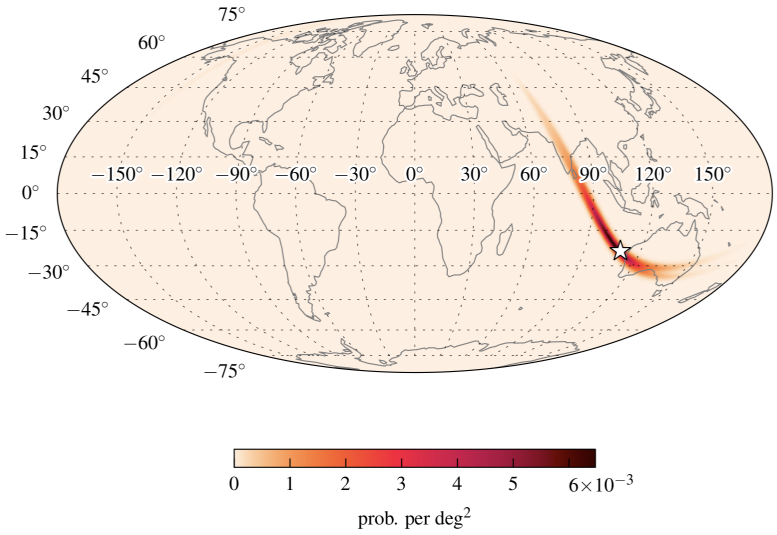

Figure 2.12: Typical localisation map of a GW event detected with a two-interferometer network. From [341].

Alerts overview

An alert is issued and sent by the Ligo and Virgo Collaboration (LVC) to the astrophysics community whenever a significant GW signal is detected, allowing rapid searches for counterparts, i.e. associated electromagnetic emission or neutrinos. During O1 and O2, and O3, alerts were issued by LVC through GCN. For each detected signal, several types of GCN notices were emitted at different timescales. The first *preliminary* notices, emitted automatically by the LVC real-time data analysis system during O3, have been made available within 1 to 10 minutes after the arrival of the GW signal. Within the next few hours, either an *initial* or a *retraction* notice and a GCN circular were issued. These and all subsequent messages (*updates*), containing refinements on the analysis and localization reconstruction, are human-vetted. The expected timeline of this alert sequence is presented in 2.13. Moreover in future runs, it will be possible for GW detectors to detect the event already during the inspiral phase before the merger itself and issue a pre-merger *Early Warning* alert. Details can be found in [213].

The most important content of the distributed alert messages include the GW localisation map url, a first classification into CBC or Burst alert depending on the detection pipeline, the detection time, and a classification of the initial system depending on the mass of the colliding objects: binary black hole (BBH), binary neutron star (BNS), binaries comprising a neutron star and a black hole (NSBH) or a signal due to terrestrial noise (Terrestrial). GW localisation maps in the *preliminary* and *initial* notices are computed with BAYESTAR while the *update* map is computed with LALInference. The classification of the colliding

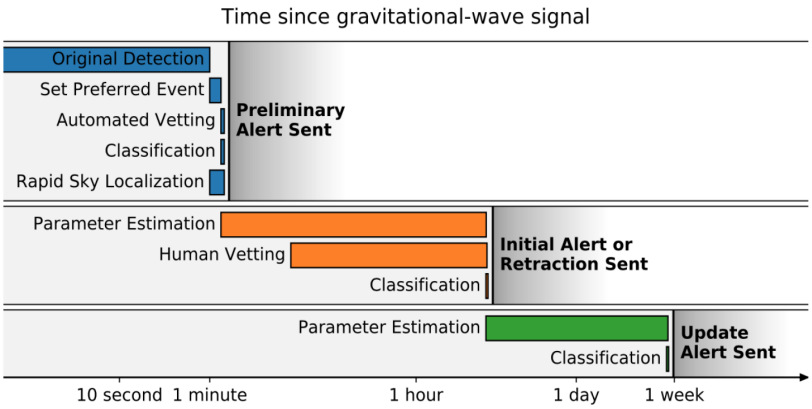

Figure 2.13: Sequence of LIGO/Virgo alerts for a GW event that are distributed through GCN during O3. From `emfollow.docs.ligo.org`.

objects relies on the their masses following Fig. 2.14. This information is used to classify and filter these events for potential follow-up observations. In some cases, the objects involved in the merger falls in the MassGAP between the minimum black hole mass and the maximum neutron star mass.

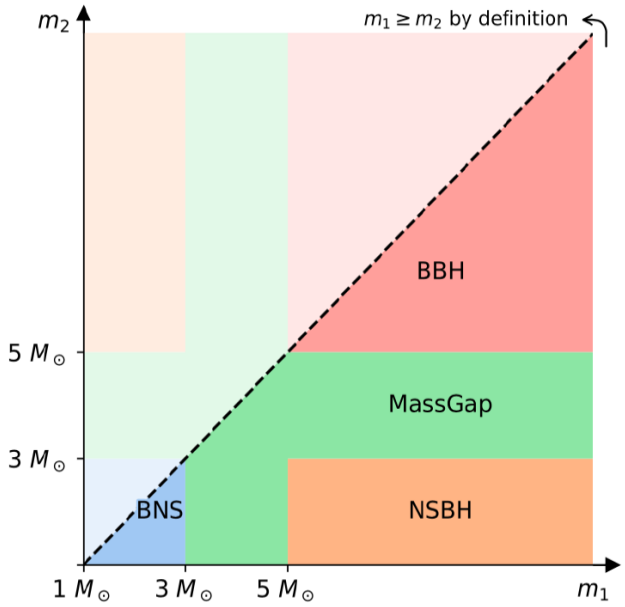

Figure 2.14: Classification of GW events depending on the compact binary mass for CBC searches. From `emfollow.docs.ligo.org`.

Discoveries in GW science until the end of O2

GWs were first proposed by Henri Poincaré in 1905 [292] and were predicted by Einstein as a consequence of the general relativity theory [113]. Joseph Weber envisaged the first method of detection of such faint signals [368]. In the 1980s, Russell Alan Hulse and Joseph Hooton Taylor, Jr. made the first indirect observation of GWs by observing a binary system composed of a neutron star and a pulsar, the Hulse–Taylor binary. Using the Arecibo telescope, they noticed that the arrival time of the pulsar pulses was shifting systematically [371]. They deduced that the system was loosing energy by GW radiation and the two orbiting objects were getting closer and closer. This discovery landed them the Nobel Price in 1993. Almost 100 years after the Einstein's prediction, direct observation of GWs was made with LIGO's interferometers; LIGO's construction was completed in 1999, and it took 16 years of upgrades in order to reach the level of sensitivity required to detect GWs from astrophysical origin and first direct detection of GW happened in 2015 with the GW150914 BBH merger [5]. This discovery brought a direct observational proof of the existence of black holes. In 2017, the first three interferometer detection occured with GW170814 [9] that had for the first time a localisation uncertainty small enough for telescopes like H.E.S.S. to follow. In 2017, the *golden* event GW170817 [8] is a BNS merger detected by LIGO and Virgo that has major implications on Astrophysics, Cosmology, Stellar Physics, Relativity, Emission Physics and many more.

GW170817: 2 seconds after the detection of GW170817, a sGRB emanating from the BNS merger was detected by Fermi-GBM and INTEGRAL [8]. This is the first observational proof linking sGRBs to CBCs. Few hours later, an optical counterpart was detected linking the BNS merger to the host galaxy NGC 4993 [164] at $\mathrm{z} = 0.00987$. This is the first and only GW event (until now) with an electromagnetic counterpart and an identified host galaxy. An X-ray then a radio signal started rising respectively $\sim$9 and $\sim$16 days after the merger [354]. The implications of the MWL observations of GW170817 and the H.E.S.S. short-term and long-term follow-up observations campaigns will be discussed in Chap. 6.

2.2.4 Electromagnetic counterparts of GWs

After the detection of the GW170817 BNS merger and its associated GRB GRB 170817 [8], a worldwide observation campaign was triggered across the globe. While no neutrino counterparts were detected, several EM counterparts were [12]. These EM observations shed the light on the physical phenomena surrounding the BNS merger. The aftermath of this merger illustrated in Fig. 2.15 is characterized by a

short GRB with a weak prompt γ-ray emission, followed by the optical brightening of the *kilonova* followed by the late GRB afterglow.

The *kilonova* [261] is a thermal transient event, mostly visible in the optical range. It is powered by the r-process which is the rapid neutron capture nucleosynthesis of the material ejected from the merger. Aside from being partly responsible of enriching our Universe with heavy elements such as gold, the unstable resulting nuclei undergo rapid radioactive decay powering the *kilonovae*, that is responsible for thermal transient emission in the optical domain. These emissions are the most promising for the localisation and redshift estimation of GW counterparts to BNS mergers [259] like the case of SSS17a which was the first BNS optical counterpart associated to GW170817 [191].

The non-thermal emission is the most relevant one for the topic treated in this thesis. It is powered by the merger's resulting GRB (short in the BNS case). The processes behind these non-thermal emissions are synchrotron and possibly Inverse Compton scattering. Right after the merger, the internal shocks within the GRB jet are behind the prompt emission caught promptly by space telescopes like Fermi and INTEGRAL. When the swiped material reaches the interstellar medium, the afterglow emission kicks in. It is caused by the interaction of the explosion's material with the interstellar medium. This afterglow emission is sometimes delayed by several days due to the opening angle of the jet being outside the line of sight of the observer [122]. As time passes, the opening angle increases and the jet becomes more visible to the observer who will be able to detect a rising afterglow emission that will eventually plateau and drop again.

Multi-messenger astrophysics with GW and GRBs: One of the goals of multi-messenger astrophysics is to obtain and combine information provided by multiple messengers coming from a source, in order to derive the source and environment properties. In the case of CBCs, GW and EM emission (notably GRBs) are complementary; the detection of GWs can provide information on the mass, spin, eccentricity and orientation of the binary while the detection of electromagnetic emission can provide information on the location, the redshift, the interaction of the merger products with the system environment and on acceleration mechanism giving rise to non-thermal emission. While the gravitational wave detection describes the dynamics of the system, the electromagnetic detections describes the energetics and the environment of the coalescence.

GWs and VHE γ-rays: sGRBs are expected to emanate from CBC involving one neutron star. [363] argue that short GRBs can reach synchrotron self-Compton powered GeV to TeV afterglow flux that can be detected by current and future TeV instruments in certain scenarios. In this paper, the authors consider

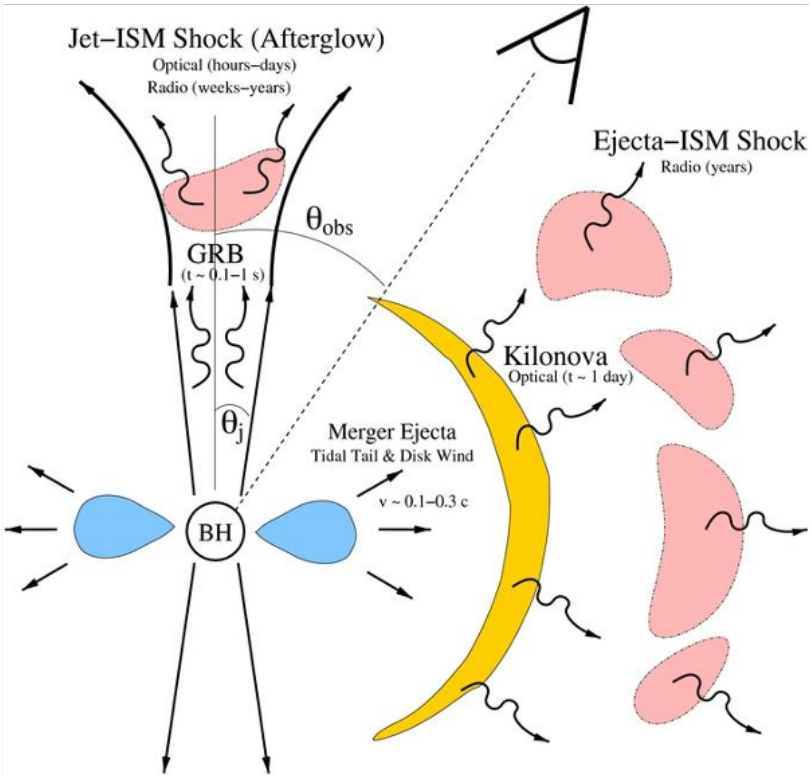

Figure 2.15: Summary of electromagnetic counterparts of NS–NS/NS–BH mergers. From [259]

.

a model where materia are promptly expelled by a jet creating a forward shock onto the environment of the source and a reverse shock into the ejecta. Both shocks are re-energized by the slower and later arriving material. They also consider another model where the central engine (which could be a magnetar or a black hole) continuously ejects material over long-lasting period. The ejected material continuously re-energizing the shocks formed by the preceding shells of ejecta. They calculate the SSC radiation components taking into consideration TeV emission suppression effects such as pair absorption in the source and pair suppression on the EBL and find that VHE emission can be detected by current IACTs for both models if the total isotropic energy is of the order of 10^{53} erg given that observations start after $\sim$ 1000 seconds form the merger.

Moreover, [264] (and references within) predict the possibility of long-lasting powerful VHE emission from neutron star mergers involving a short GRB. The authors argue that for such long-lasting emission cases, sGRBs can generate VHE emission by IC process. In particular, in the afterglow of a long-lasting jet, not only SSC but also external IC processes can occur where external photons from the long-lasting jet can be scattered by forward external shock electrons. They consider several viewing angles of the sGRB jet. The lightcurve of the expected VHE emission at 100 GeV is shown in Fig. 2.16.

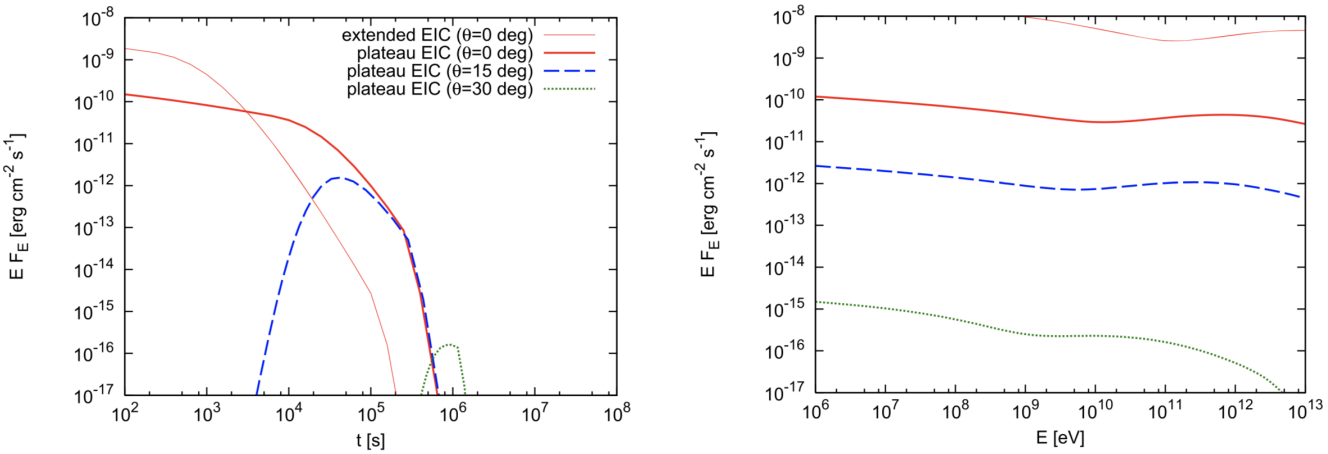

Figure 2.16: **Left:** Light curves of high-energy γ rays generated by external inverse Compton radiation, for $\mathrm{E} = 100\,\mathrm{GeV}$. Three different viewing angles (measured from the jet axis) are considered, and extended emission and plateau emission are assumed as seed photons. The distance is set to 40 Mpc. **Right:** γ-ray spectra corresponding to the light curves in the left plot. For the extended emission the spectrum at $\mathrm{t} = 10^2\,\mathrm{s}$. For the plateau emission with, the spectra at $\mathrm{t} = 10^4\,\mathrm{s}$, $\mathrm{t} = 2.5 \times 10^4\,\mathrm{s}$ and $\mathrm{t} = 8.2 \times 10^5\,\mathrm{s}$, (from the second top to bottom). From [264].

Other than GRB 090510, short GRBs have been observed in high energies [23] like the case of GRB 160821B for which MAGIC found evidence of γ-ray emission above 0.5 TeV [243]. Another milestone in our understanding of GRBs was reached with the detection of VHE emission from GRB 180702B [17] and GRB 190829A [153] as well as the detection of GRB 190114C [21] by MAGIC. These observations show that the cataclysmic events causing GRBs can trigger efficient particle acceleration, possibly via relativistic jets. The accelerated particles are able to emit γ rays in the VHE domain over an extended period of time from the very early (e.g. GRB 190114C) to the late afterglow phase (e.g. GRB 180720B and GRB 190829A). As mentioned above the VHE GRBs shed the light on the striking similarities between the fading X-ray and VHE γ-ray flux levels. According to [270], the X-ray behaviour of short GRBs is similar to long GRBs except for typically fainter flux level, thus spawning hopes for possible VHE emission of short GRBs. Assuming the tentative link between the X-ray and VHE fluxes holds for short GRBs, the fainter fluxes make the afterglow detection of short GRBs in the VHE band even more challenging than for long GRBs.

2.3 FRBs

Fast Radio Bursts are the newest mystery of the high energy transient sky. As their name indicates, they are bright flashes of coherent radio waves that last from a fraction of a millisecond to a few milliseconds.

Since the discovery of the first FRB, FRB 20010724 known as the Lorimer Burst [234], in 2007 by the Parkes radio telescope, astronomers started finding these strange burst in real-time observations and in archival data also and the rate of detection has increased.

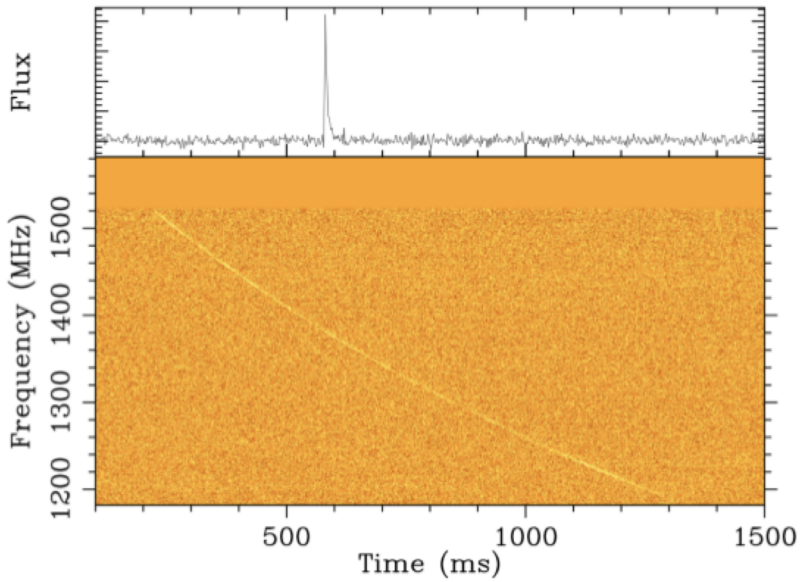

Figure 2.17: **Top:** Frequency integrated flux of FRB 20110220 detected by Parkes as function of time after removal of the dispersion. **Bottom:** Frequency-time plot of the spectral brightness of FRB 20110220. The general speckle is thermal noise in the detector. The dispersion of the radio waves causes a "waterfall" like delay in the brightness in the different frequency bands. From [188].

.

An example of what the radio observations of a FRB look like is shown in Fig. 2.17. The top panel shows the frequency integrated flux coming from the direction of FRB 20110220. The sudden increase in the emission (pulse of emission) marks the detection of the FRB. The distance of FRBs can be estimated by their dispersion measure (DM) and they are detected over a wide range of frequencies. The free electrons in the interstellar and intergalactic medium delay low frequencies more than high frequency components. This will result in a dispersion of the signal. In the bottom panel of Fig. 2.17 the dispersion delay is illustrated by the "waterfall" shape created by the brightness measurement at different frequencies. This DM is a convolution of the cosmic distance and the electron density, therefore FRBs can be used as new cosmological distance measures [202]. The distance of the FRB can be deduced from the following equation [390]:

$$DM \sim n_0 f_e D_L [1 + 0.932z + (0.16\Omega_m - 0.078)z^2]^{-0.5} \tag{2.8}$$

Where DM is the dispersion measure, z is the redshift of the FRB, n_0 is the mean number density of nucleons at $z = 0$, f_e is the electron mass fraction and Ω_m is the matter density parameter which accounts

for the baryonic and dark matter in the Universe. This relation is updated by [179] in order to account for the contributions from the cosmological distribution of ionised gas, the FRB host and from the Milky Way's interstellar medium and halo:

$$DM = DM_{cosmic} + DM_{host} + DM_{ISM} + DM_{halo} \tag{2.9}$$

The DM from observed FRB, the association of some FRB to host galaxies (discussed below) and the random distribution of FRBs all over the sky (see Fig. 7.13 in Chap. 7) supports their extra-galactic origin.

2.3.1 FRB detection overview

FRB detection methods

Several radio telescopes are used for the detection of FRBs. FRBs are usually intentionally discovered in large radio surveys or by coincidence in the field of large FoV radio telescopes while data taking.

The telescope that holds the record for the detection of FRBs today is the Canadian Hydrogen Intensity Mapping Experiment (CHIME) [37] with more than 1000 detections until mid-2020 according to its website[5]. It is a telescope that has no moving parts with a very large FoV $\sim$200 deg^2 that makes CHIME a unique telescope for discovering new FRBs in the 400 GHz - 800 GHz. Before CHIME, Parkes [318] a 64-m radio dish instrument in Parkes town in Australia was leading the hunt for FRBs. It was the first telescope to discover a FRB by coincidence in 2007, the Lorimer Burst [234]. After that, several FRBs were detected in archival data from 2001. The UTMOST telescope [54] is the refurbished MOLONGLO telescope located in New South Wales (Australia) and is dedicated to probe the radio transient sky in real time with an 8 deg^2 FoV on the meridian. It is composed of an 800 m east-west radio arm. Due to the shape of the telescope UTMOST has a very elongated localisation with typically 10 arcsec by 3 to 6 deg. A second north-south arm is currently being comissioned and is expected to be in operation in 2021 allowing UTMOST to localise FRBs within 10 arcsec in both orthogonal directions. UTMOST operates at 843 MHz and it has detected a number of FRBs as part of commissioning science during a major ongoing upgrade [80].

Other facilities are dedicated to the detection, and the follow-up of FRBs also. From these facilities, I mention first the gigantic Chinese Five-hundred-meter Aperture Spherical Radio Telescope (FAST) [265] which constitutes the largest radio dish in the world (500-m) nearly twice the size of the next-largest

[5] `https://chime-experiment.ca/en`

single-dish telescope, the decommissioned Arecibo Observatory in Puerto Rico [36]. MeerKAT [182, 251] and ASKAP [181] are two precursors of the Square Kilometre Array (SKA) located in Australia and South Africa with a FoV of 2.7 deg^2 and 30 deg^2 per dish respectively. Due to their high angular resolution, these instruments are often used to follow-up and localise FRBs. ASKAP was responsible for the localisation of the first non-repeating FRB, FRB 20180924. The Very Large Array (VLA) [280, 281] consists of 28 25-m dishes operable in the 1 GHz - 50 GHz band and is located in New Mexico.

Dozens of radio telescopes exist today around the globe and can be used for FRB observations like STAR2, the Westerbork and Onsala dishes, ATCA, the Nançay Radio Observatory and many more. The purpose of this section is to give an overview of the instruments that will be mentioned in the thesis, especially in Part IV and does not aim to provide an exhaustive review of current radio telescopes.

FRB database and VoEvents: Before 2020, FRB detections were stored in the FRB online catalog[6], until the database moved to the Transient Name Server (TNS)[7]. The most important information that can be found are the location with the uncertainties, information on the host, the discovery date, the redshift of the host galaxy if it exists, the DM measurements, the nature of the FRB (repeating, non-repeating) and other counterparts if found.

Some facilities are now sending VoEvents [287] upon the discovery of a FRB. These VoEvents are in the form of XML machine readable files. UTMOST is one of these radio facilities that is using VoEvents and H.E.S.S was one of the first observatories to build an automatic response scheme to handle UTMOST FRBs (more details in Chap. 7).

Properties, classification and hosts

Observations show no evidence for a minimum FRB emitted energy. FRB emitted energies can be as low as 10^{34} erg observed from FRB 20200428 and can reach 10^{43} erg [385]. According to [385], the isotropic energy distribution of FRBs follows a power law with exponential cutoff at Energy $E_c = 10^{41}\,\mathrm{erg}$.

$$\frac{dN}{dE} \propto (\frac{E}{E_c})^{\alpha} e^{-\frac{E}{E_c}} \tag{2.10}$$

With $\alpha \sim 0.18$.

FRB are divided in two categories: non-repeating and repeating FRBs. From the hundreds of FRBs re-

[6] http://frbcat.org
[7] https://www.wis-tns.org

ported until now, 22 FRB have been seen to repeat. The first FRB discovered to repeat is FRB 20121102A [342]. FRB 20121102A and the second discovered repeating FRB, FRB 20180814 [87], appear to repeat in a periodical way. FRB 20171019A is a repeating FRB with an initial bright burst detected by ASKAP [334] and two additional dimmer bursts detected later on with no periodical feature [203]. This FRB might belong to a class of FRBs associated to BNS mergers [180]. A study on this particular FRB will be presented in Chap. 7.

12 FRBs have been localised to host galaxies[8]. 3 out of the the 22 FRB repeaters are localised to host galaxies: FRB 20121102A, FRB 20180916A and FRB 20190711A.

FRB 20121102A is localised to a dwarf galaxie with redshift $z = 0.19273$ [350, 59]. The repeating nature of the burst shows that the emitting engine survived the event that caused the initial burst. It showed that it is physically associated with a compact ($\leq$ 0.7 pc), persistent radio source of luminosity $\nu L_\nu \sim 10^{39}\,\mathrm{erg\,s^{-1}}$ at a few GHz [82]. This source is detectable from 300 – 26 GHz [303, 82] and is seen to exhibit $\sim$10% variability on day timescales. Astronomers started speculating on the nature of FRB hosts and thought that FRBs originate in dwarf galaxies with important star formation rate [350] like FRB 20121102A.

However, the second repeating FRB to be localised, FRB 20180916A, is localised to a nearby spiral galaxy [246] at $z = 0.0337$ [241]. This contradictory finding sheds again a mystery on the nature of FRB hosts. In contrast to FRB 20121102A it showed no associated persistent radio emission.

It is possible that younger, more active FRBs like FRB 20121102A are associated with persistent radio emission while the emission might have faded over time for the older ones.

2.3.2 FRB emission models and potential sites

In their review, [286] explains that the high temperature brightness and short intrinsic duration of FRBs implies coherent emission processes. The short duration also implies that the emitting region is small (in the order of few kilometers) which makes us naturally think of compact objects. Some of the coherent mechanism relative to astrophysics are presented and reviewed in [291] and [239]. Bunched particles accelerating along electromagnetic field lines (through magnetic reconnection or braking in the plasma of a pulsar's magnetosphere for example) and simultaneous electron phase transitions or masers are some of the favoured models. Masers occur when an incoming photon is absorbed by an excited electron

[8] `https://frbhosts.org/`

and emit two photons with same wavelength. The two photons excite two additional electrons and more photons will be emitted and so on. If the number of exited electrons is superior to the number of electrons in the ground state (that absorb the radiation), emission exceeds absorption. If the electrons are phase bunched (in the case where the frequency of the electromagnetic wave is close to the electron synchrotron frequency), they will simultaneously jump to the ground state and emit photons of the same wavelength to start the chain of stimulated emission. Another possible emission mechanisms is Dicke's superradiance that happens when several particles are entangled and emit coherently at the same time.

As for the potential sites, magnetars are the primary candidates as FRB generators. Therefore, in the following I give a brief overview of the link between FRBs and magnetars.

FRBs and magnetars

Some of the FRB models link FRBs to magnetars, with the first one suggested more than a decade ago [295]. For example, some magnetars could produce FRBs through strongly magnetized pulses that interact with the material in the surrounding nebula and produce synchrotron maser emission (e.g. [238, 260, 62]) as explained above. Some models suggest that repeating FRBs are generated not far from the surface of the magnetar through ultra-relativistic internal shocks and blast waves in the magnetar wind associated with flares (e.g [61]). Coherent radio emission can be produced in re-connecting current sheets in a magnetically dominated plasma with wavelength comparable to the Larmor radius of the emitting particles.

These are just few mechanisms among others that could explain FRB emission. The existence of relativistic flow of particles and strong magnetic fields in the recipe of FRB emission makes magnetars, in particular SGRs, strong potential site candidates for such events. Magnetar can be SGRs or anomalous X-ray pulsars (AXPs). SGRs are stellar objects that emit irregularly X-ray and γ-ray outbursts. AXPs are isolated, highly magnetized neutron stars characterized by a slow rotation period (in the order of seconds) and large magnetic fields. Both SGRs and AXPs are associated with highly magnetized neutron stars or magnetars. Since SGRs are discussed in Chap. 8, I give a brief overview of SGR flares in the following.

SGRs: SGRs generate bursts of emission at irregular time intervals. The crust of the neutron star is thought to break due to the intense shifts of the ultra-strong magnetic field and releases bright emission of hard X rays and soft γ rays. During these short bursts, the brightness of these objects can increase by a factor of 1000 or more. A total of 30 magnetars (24 confirmed sources and 6 candidates) are detected

today[9] [271]. Magnetars can also emit giant flares. The rare giant flares within this category are the most extreme γ-ray outburst ever detected, so intense that, in the case of the 27 December (2004) event from SGR 1806−20, they can influence the Earth's ionosphere and magnetic field (e.g. [176]). The 27 December event is the most powerful magnetar flare detected to date. Another noticeable event is the giant flare detected from SGR 1900+14 on August 27 1998 [120].

[84] argue that the radio afterglow from the August 27 giant flare could be consistent with mildly or sub-relativistic outflow from the SGR expanding into the interstellar medium. Reconnection of the magnetic field during the period of the giant flare could be responsible in that case for the ejection of matter from the magnetar's crust. For many years it was unclear whether high energy non-thermal emission mechanisms were involved in these burst activities, until just recently the Fermi-LAT telescope detected GeV γ-ray emission from an extragalactic magnetar in the Sculptor galaxy group [119]. The burst location is consistent with several galaxies including the starburst galaxy NGC 253 (the Sculptor Galaxy) at 3.5 Mpc distance. The unusually long delay (19 s) to the GeV emission and quasi-periodic oscillation seen in the MeV signal suggest a giant magnetar flare. At present the GeV emission is attributed to optically thin synchrotron emission suggesting the presence of relativistic electrons.

The potential for TeV γ-ray emission is still open to question since the existence of a strong magnetic field and high velocity expelled electrons and positrons from the magnetar makes SGRs a good candidate for such mechanisms. However, the strong magnetic field of the photon production region could trap the electrons and positrons around the surface and induce electron-position pair cascades that can quench any VHE γ-ray emission. The emitted X rays and γ rays bounce against this trapped material and create new electron positron pairs and regenerate by annihilation which further impedes their motion. In this trapped fireball scenario [351], only at the surface of the trapped fireball can the photons stream freely away. If non-thermal mechanisms like inverse Compton are creating VHE γ rays, they should most likely occur far away from the surface of the magnetar in order to be detectable.

The connection between FRBs and magnetars became considerably more notable with the detection of short, intense radio bursts from the direction of the magnetar SGR J1935+2154 by CHIME [88, 329] (c.f. Sec.2.3.1) and STAR2 [72] coincident with X-ray bursts detected by the AGILE [349], Konus-Wind [314], HXMT [209] and INTEGRAL [256] observatories. This overlap is the first convincing evidence that magnetars are linked to fast radio bursts (FRBs), or at least, to repeating FRBs. A study on SGR 1935+2154 and the connection between SGR bursts and FRBs is presented in Chap. 8.

[9] http://www.physics.mcgill.ca/~pulsar/magnetar/main.html

Other potential sites for FRB emission are compact object interactions, neutron stars in particular. Neutron stars have the components to be a potential site for FRB emission like strong magnetic fields and a turbulent environment in most cases. According to [240] and [353] respectively, FRBs can be generated at the time of collision of a neutron star with another (compact) object or from the magnetic braking associated with the same event. Not only interacting or colliding neutron stars are potential candidate sites for FRB emission but also isolated neutron stars like in the case of magnetars. An exotic model of isolated neutron stars FRB emission is the *blitzar* model (for non-repeating FRBs), where a massive neutron star collapses into a black hole and emits FRBs as a last sign of its supermassive existence [117]. Black holes are also considered as potentially responsible for FRB emission especially the ones interacting with their surrounding environment.

Some progenitor theories for FRBs, like binary neutron star mergers and collisions [353, 376], giant pulses from extragalactic pulsars [93, 297], hyperflares and giant flares from magnetars [296, 294], binary white dwarf mergers [184], neutron star ”combing” [383], interactions of neutron stars with active galactic nuclei [364] and merger of a Kerr-Newman black hole binary [231] (refer to [291] for a complete list) predict radio afterglows accompanying an FRB with timescales of days to years.

[97] suggest that the persistent emission is due to ultra-relativistic pulsar wind nebula sweeping up its ambient medium with FRBs repeatedly produced through some mechanism. In the magnetar model by [247], FRBs produced by binary neutron star mergers and accretion induced collapse are expected to be accompanied by persistent synchrotron radio emission on timescales of months to years. The persistent emission is powered by the nebula of relativistic electrons and magnetic fields inflated by the magnetar flares [247]. The existence of persistent emission associated with FRBs could provide vital clues to their origin.

I notice that most of these potential sites are high-energy astrophysical sites that could potentially have VHE emissions. A small section in the introduction of a thesis is certainly not enough to present all the potential FRB emission models. Up to a certain point in the beginning of 2018, the number of models and theories potentially explaining FRB progenitors exceeded the number of actual FRB detections. Therefore, I refer the interested reader to the frbtheorycat[10] wiki page containing most of the FRB theories.

[10] `https://frbtheorycat.org/index.php/Main_Page`

The models contained in this page present potential progenitors ranging from confirmed astrophysical sources like magnetars, to unconfirmed sources like alien spaceships, passing by exotic models like cosmic strings. The aim of most observational studies, including the one that will be presented in part IV of this thesis, is to provide confirmation or discrimination of the proposed FRB emission models and theories by attempting to detect the expected (counterpart) emissions from these models.

Part II

GWs and follow-ups

Chapter 3

GW follow-up algorithms

One of the main issues with transient astrophysics is the localisation of the cosmic transient events that are detected such as GRBs, neutrinos and GWs. From these classes of events, GWs suffer the most from poor localisation due to their detection method (more info in Sec.2.2.3). Depending on the method of detection of GRBs, they can also suffer from poor localisation. The coded mask techniques that Swift-BAT uses can limit the localisation uncertainty to few arcmin, however other techniques, like the scintillators on board Fermi-GBM can have poor angular resolution that can reach several tens of degrees in the sky especially if the detected signal is weak. In this chapter, I present the different techniques and methods developed during my thesis in order to tackle the poor localisation issue in ToO follow-up. Although these techniques are developed for GW events, they can be used for all kinds of ToO events given that their localisation is provided through uncertainty maps similar to the ones described in Sec. 2.2.3.

Several techniques have been developed which aim to use the information contained in a GW map to guide the search for counterparts to GW events in an efficient way, in particular in the case of telescopes whose FoV is smaller than the typical GW localisation uncertainty. In order to tackle the poor localisation problem, dedicated algorithms (here designated as GW algorithms) are developed in order to efficiently observe GWs. Much of the work presented in this chapter and in Chap. 4 is published in [45]. The algorithms take into consideration specific telescope constraints defined in the following.

The main telescope constraints are the specific observation conditions for each telescope defined in Sec. 3.1 for H.E.S.S. Another thing that has to be taken into consideration is the data taking method of each instruments. For example, some IACTs like H.E.S.S. have a standard 28 minutes optimized

observation window, this means that H.E.S.S. observation windows are divided into 28 minutes periods. In general, GW algorithms will assess the available observation time during a given astronomical night, divide this time into optimized observation windows and find the best position to observe during each observation window

This is done by following these steps:

1. Select the most probable sky location fulfilling the IACT observation conditions (e.g. zenith angle range, dark time, etc.)
2. Schedule observation for this direction at a time T_0 with a duration Δt.
3. Mask a circular sky region representing the effective IACT field-of-view around that region.
4. Using the modified visibility window $T_i = T_0 + i \cdot \Delta$t, where i is the observation number, and the iteratively masked skymap is used starting with the new position of the skymap in the sky at T_i, steps 1-3 are repeated until γ-ray emission is detected by the real-time analysis, the covered probability for the next observations is insignificant or the allocated observation time is used (end of ToO).

To find the best position several methods are considered. These methods either rely solely on the posterior probability contained inside the first layer of each pixel (2D follow-up) of the GW localisation map, or take into consideration the distribution of the galaxies in the local Universe and correlates it with the probability and distance information from the GW map contained inside the four layers of the pixels (3D follow-up) in order to reduce the search to few galaxies instead of entire region in the sky.

3.1 Observation conditions for IACTs

For IACTs, observation conditions can be divided in two categories: visibility and observation constraints.

- The visibility is defined by the parts of the sky that are accessible by the telescope depending on its location on Earth and the maximum allowed zenith angle for observations. For optical telescopes, the zenith angle determines the air mass. The air mass is the column density that one is looking through. The higher the air mass the higher the atmospheric absorption of light. In a similar way, for IACTs the energy threshold of observations range from few tens of GeVs to hundreds of GeVs, depending on the zenith angle under which the source is observed. Visibility conditions for IACTs are discussed in Sec. 1.3.1. Based on the soft spectrum of GRBs observed [23], observations

reaching a low energy threshold, i.e. at low zenith angles, are preferred. Moreover, for telescopes like H.E.S.S there is a maximum zenith angle allowed: 60 deg for H.E.S.S.

- As explained in Sec. 1.3.1, we can schedule observations for IACTs under *dark* or *moonlight* operations. In order to schedule observations under these conditions, moon and sun altitude, moon phase and moon-to-source distance need to be monitored and considered as additional parameters in the scheduling algorithms. These parameters are defined in Sec. 1.3.1 for H.E.S.S. In general observations under moonlight increase the total duty cycle of an IACTs by 10%. The available observation time is divided into 30 minutes observation windows that represents 28 minutes of data acquisition and 2 spare minutes for technical issues like telescope slewing and starting the camera. The algorithms should consider the observation windows that fulfill either *dark* or *moonlight* observation constraints. The algorithms should also consider if the remaining available time after the last full window meet observation constraints. I note that for other IACTs (notably the future CTA) the observation window duration is not fixed. One way to determine the duration of a window is to derive expectations on the observation time needed to detect a certain signal (for GWs a simulated short GRB for example) under the given observation conditions. Such studies are currently conducted for CTA [333] and are not discussed in this chapter.

A particular example that illustrates how visibility and observation conditions are taken into consideration while observing a GW event is given in Fig. 3.1. The visibility constrained to a zenith angle $<$60 deg is shown inside the enclosed blue region. It determines which parts of the sky can be observed by the telescope during an observation window. The presence of the moon in the sky implies more constraints. Considering the sun and moon altitude and the moon phase is smaller than the maximum allowed values defined in Sec. 1.3.1, the telescope located in Namibia can only observe the parts that fall between the orange line that represent the minimum required moon-source separation and the blue line.

Probability threshold per pointing: In order to not waste observations on low probability regions, a threshold is set for the required probability coverage for a given region to be observed. The threshold varies depending on the nature of the GW merger events. It is set to a minimum of 5% probability coverage for BBH mergers and 2% for mergers including a neutron star for H.E.S.S. More information are given later on in Sec.4.3. In other words, in order to observe a region, we need to make sure that we have good coverage in order to minimize wasting time on *empty* fields.

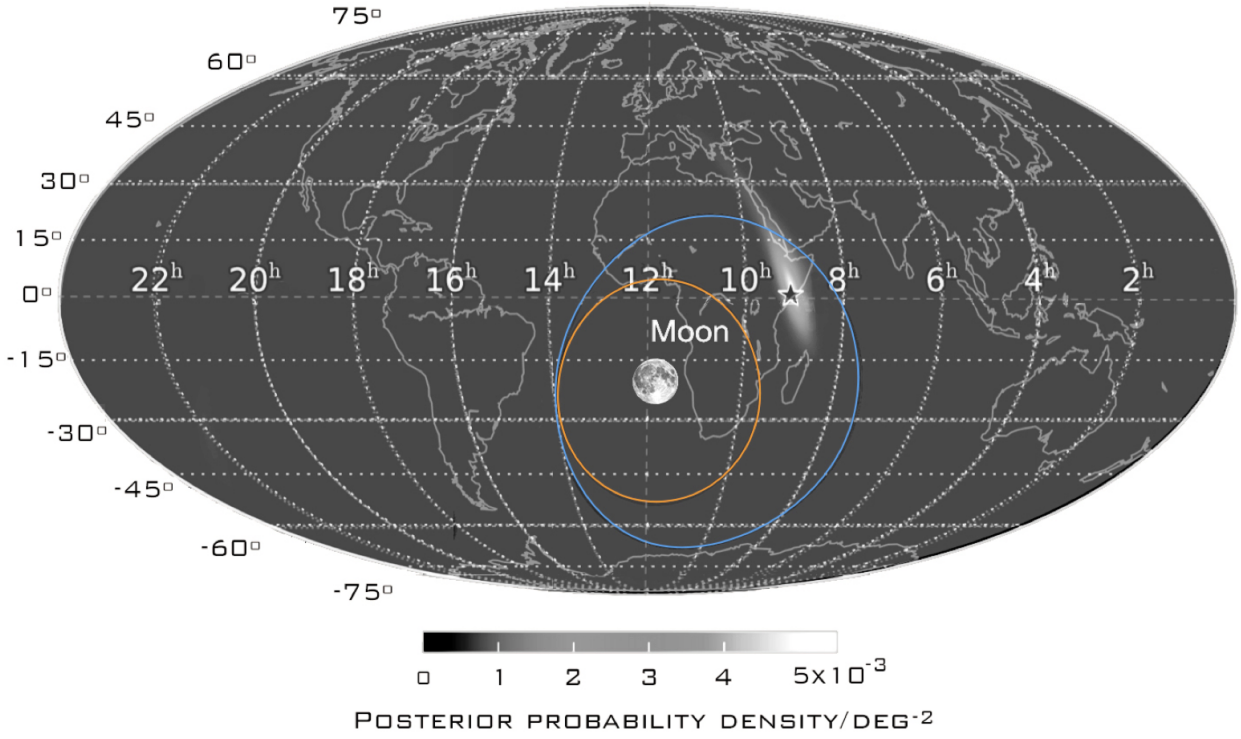

Figure 3.1: Illustration of the moon, the H.E.S.S. visibility at $\theta = 60\,\mathrm{deg}$ in blue and a gravitational wave simulation from the GWCOSMoS database [278], where the orange line illustrates the minimum angular distance that fulfills the angular separation condition. A projection of the Earth is shown in the background.The GW event localization is indicated by the light gray area and the true position of the simulated merger by the star. From [332].

Prioritizing sensitivity with IACTs: Independent of the option chosen, the scheduling should prioritize sensitivity to low γ-ray energies. This is based on the soft spectrum observed from short LAT GRBs [30] and the maximum VHE photon energy observed from these GRBs which corresponds to energies which an IACT could only observe under the lowest zenith angles. Therefore, a module is included in the scheduling algorithms allowing to favor low zenith angle observations. This prioritisation is performed via a scan of different maximum zenith angles allowed for each pointing and using a weight that relates the expected gain in energy threshold to the less optimal coverage of the GW uncertainty region. The scanning is done with 5 deg steps and the covered probability inside the region is compared to the weighted previous one. The region will be selected for observations if it meets the condition following [331]:

$$Prob^{i}_{\theta_{zenith}} < weight \times Prob^{i+1}_{\theta zenith+5^{\circ}} \tag{3.1}$$

Depending on the observatory used this weight can be changed. For now it set to 0.75 following [331].

It can change with further observations of sGRBs at very high energies. In Fig. 3.2, an illustration of the visibility decreased by steps of $\theta + 5\,\mathrm{deg}$ for a fixed observation time and a given GW wave localisation map is shown.

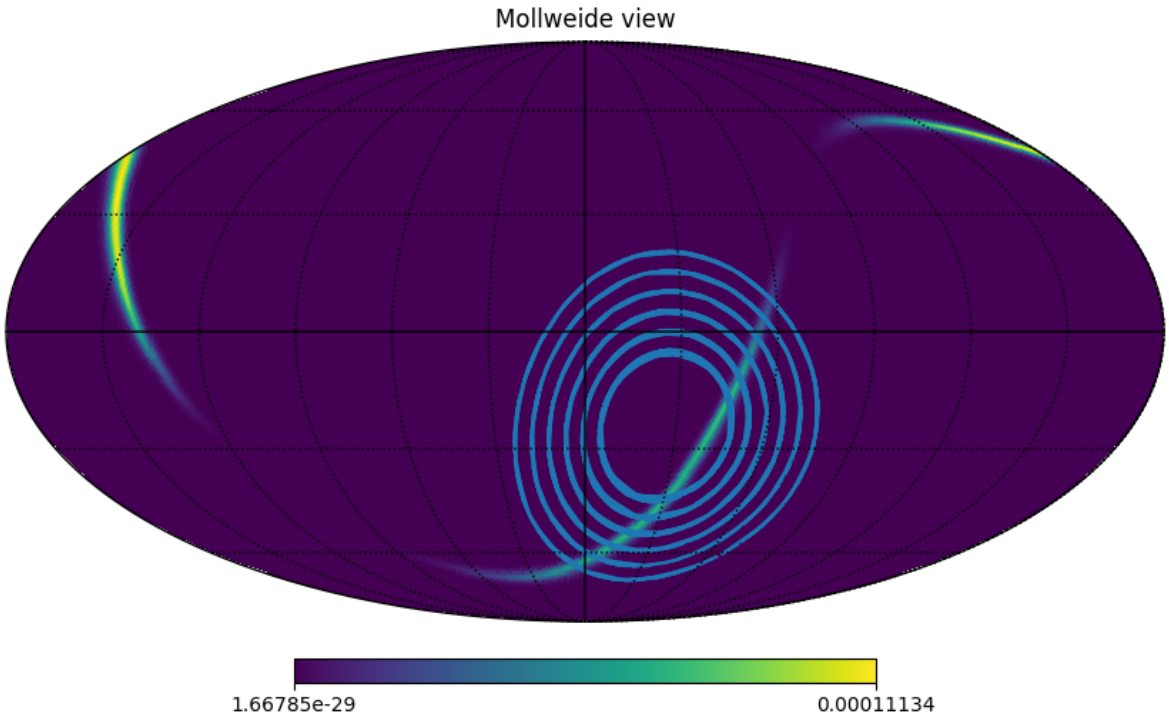

Figure 3.2: Gravitational wave sky localization where decreasing 5 deg-steps in zenith angle between an altitude of 45 and 70 deg on the H.E.S.S. site and for a given time. From private communication with Monica Seglar-Arroyo.

Second round option: The GW follow-up scheme that will be developed in the following inherits also an option from previous research in [331], which is the option to have a second round of observations. This can be applied to situations where a region is covered by a pointing, but turns out that it could be covered by another pointing later on in the night with a much lower zenith angle, hence benefiting from low energy threshold. An additional module is introduced to the GW follow-up algorithms (introduced in the next sections) allowing them to compare two possible observations: the observations of non-covered regions of the sky, and the re-observations of the most probable localization region (re-observe the GW map without taking into consideration the masked regions). From [331], the criteria to re-observe a region a second time are that the already observed regions (masked regions) constitute more than 40% of the total probability and that the initial observation of the most probable regions after masking provides less than twice the threshold probability per pointing. I note that none of the GW presented in the following

sections were observed with a second round option.

3.2 2D GW follow-up algorithms

In order to determine the best position to observe the most straight forward approach is to use the 2-dimensional localization probability provided with the GW alerts, ρ_i. ρ_i represents the posterior probability that the source is contained inside pixel i. The strategy aims to maximize the ρ_i covered inside the FoV of the telescopes. In the following a FoV of 1.5 deg radius corresponding the FoV of H.E.S.S. (CT5) is used.

3.2.1 `Best-pixel` algorithm

The `Best-pixel` algorithm was used in 2017 by the H.E.S.S. collaboration. The algorithm was written by the former PhD student in our group Monica Seglar-Arroyo. This strategy is based on observations according to the selection of individual high probability pixels ρ_i in the HEALPix skymap provided by the GW instruments, which correspond to coordinates (RA$_i$, Dec$_i$). Each pointing is centered on the pixel with the highest probability value; i.e. the pixel designated by the blue dot in the panel 1 of Fig. 3.3. The region around the pixel falling into the region defined by a circle of radius r = r_{FoV} is assumed as covered and is designated by P^i_{GW}. This region is masked for the next observation window (panel 2 of Fig. 3.3). The algorithm selects regions based on a single-pixel probability whose coordinates the observation is centered on, this means that the coordinates for the observations for N_{obs} >1 will be selected to be next to the edge of the already covered region in previous observations. Due to this effect, the resulting pointing pattern is typically characterized by a significant degree of overlap between the individual pointings as shown in panel 3 of Fig. 3.3.

This is in general an undesired scenario when searching for a transient source in a large sky region because we want to cover the most of the GW localisation during the available observation time. One way to avoid this problem is to change the binning of the skymap (by choosing a smaller N_{side})) in order to obtain large pixels with size comparable to the telescope FoV. However, this will result in a decrease of accuracy in the computation of the probability. Taking the example of S190728q shown in the first panel of Fig. 3.3, if we choose $N_{side} = 64$, the integrated probability inside the FoV gives $P_{GW} = 9.8\%$. I we choose $N_{side} = 32$, the pixel size is comparable to the H.E.S.S. FoV (see 3.4) and we get P_{GW} = 4.6% since less pixels will be counted inside the FoV. If we choose $N_{side} = 16$, the hostpot of the map shifts to a totally different location in the upper part of the map with a $P_{GW} = 13\%$. Integrating the probability in the

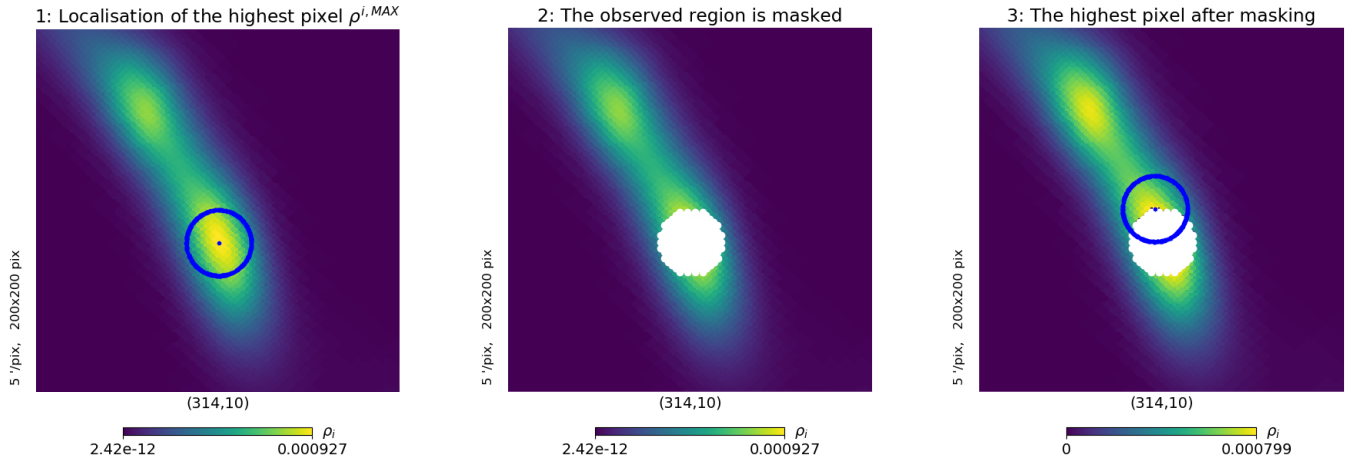

Figure 3.3: Graphical representation of the `Best-pixel` algorithm steps to compute the best observable position for two consecutive window. These steps are repeated to determine the best position to observe for each observation window. The *initial* map for the GW event S190728q is used as an example. For representation purposes N_{side} has been reduced to $N_{side} = 256$ in order to be able to see the pixels. The blue dot represents the location of the pixel with highest probability ρ_i. The blue circles are the considered FoVs . The white region is masked.

more accurate high resolution map ($N_{side} > 512$) gives $P_{GW} = 8.7\%$ with a discrepancy of $\sim$12% in the best case scenario. Therefore, an optimised algorithm which matches the capabilities of an intermediate FoV telescope like H.E.S.S. is described in the following.

3.2.2 `PGW-in-FoV` algorithm

This algorithm was developed by Monica and myself. Instead of selecting the pixel with the highest probability, one can investigate the most probable region and harness the integrated probability inside the FoV. Like the *greedy* strategy used by the Zwicky Transient Facility (ZTF) [133], it considers the integrated probability inside the FoV. In practise, this integrated probability is the sum of the probability of all the pixels inside the FoV. The pointing is chosen for the coordinates where $P_{GW}^{FoV,i}$ is maximized. It is defined as

$$P_{GW}^{FoV,i} = \int_0^{2\pi} \int_0^{r_{FoV}} \rho(r,\phi)\, \mathrm{d}r\mathrm{d}\phi, \tag{3.2}$$

where r is the radius and ϕ the angle of the FoV represented by a circle. Typically all the positions (pixels) in the sky would be tested in order to determine which one has the maximum integrated probability $P_{GW}^{FoV,MAX}$ in respect to other P_{GW}^{FoV}. The issue is the large number of possibilities to be tested that increases computation time significantly because Eq. 3.2 will have to be performed as many times as

there are positions in the sky. In order to reduce the computation time, an additional feature has been added to the algorithm which profits from the fast re-pixelizations of the HEALPix maps. The method is based on the use of an auxiliary probability skymap which is rebinned in a way that the bin areas are close to the $\mathrm{FoV}_{\mathrm{IACT}}$. The centers of the new bins define a grid of coordinates as shown in panel 1 of Fig. 3.4 and represent the center of the H.E.S.S. FoVs inside which P_{GW}^{FoV} is calculated, or in other words they represent the centers of the positions that will be tested in order to find $P_{GW}^{FoV,MAX}$ using the high resolution map as shown in panel 2 of Fig. 3.4. For each one of these test positions P_{GW}^{FoV} is calculated inside the telescope's FoV overlaid in panel 3 of Fig. 3.4. The region with the highest integrated probability $P_{GW}^{FoV,MAX}$ is chosen for observations (red circle in panel 3). Thus, the algorithm considers in parallel two skymaps: a low resolution one, which is used as a grid of coordinates to scan the GW localisation region and a high resolution one, in order to obtain a good computation of P_{GW}^{FoV} by summing the probability of all the high resolution pixels inside the FoV which is centered on the low resolution pixel. Then the highest probability sky region that fullfils $P_{GW}^{FoV} = P_{GW}^{FoV,MAX}$ is chosen to be observed and is masked from the high resolution map for the next observation window as shown in panel 4 of Fig. 3.4.

Using the low-resolution skymap, one should determine the extension of the coordinate grid. Therefore, one should select localisation contour inside which the coordinate grid should be contained. The pixels of the coordinate grid will therefore be the ones contained inside this probability contour. To choose the regions of the sky to be tested, I define the x% of the localisation region inside which I want to obtain the best position to observe. This means that if I choose the 90% contour, the coordinate grid will be limited to the 90% localisation region borders. Of course if the FoVs are large, they might cover the outer regions. I use this option in all the algorithms that use the parallelisation of two different resolution skymaps in the case of a 2D or a 3D strategy. After the region with $P_{GW}^{FoV,MAX}$ is selected to be observed during a certain window, it is masked for the next computation corresponding to the following visibility window. Steps 1,2,3 and 4 are repeated for the following window taking into consideration changes in observation conditions, the movement of the localisation region in the sky and previously masked regions of the skymap.

`PGW-in-FoV` relies on a time and space dynamic tiling that tracks and adapts to the motion of the GW localisation region in the sky during the night. The scheduling algorithm performance is optimised using the following feature; the computation time which increases linearly with the number of tested pixels, as well as the accuracy of the calculation which scales with the difference between the resolution of the map and the size of the $\mathrm{FoV}_{\mathrm{IACT}}$. The mean spacing between pixels for $N_{side} = 64$ is 0.9161 deg in

the sky. For H.E.S.S., I usually choose $N_{side} = 64$, due to the fact that above this value ($N_{side} = 128$ and above) the computation time becomes very large and below this value ($N_{side} = 32$ and below) the mean spacing between the pixels will be equal or larger than the H.E.S.S. FoV radius which will leave

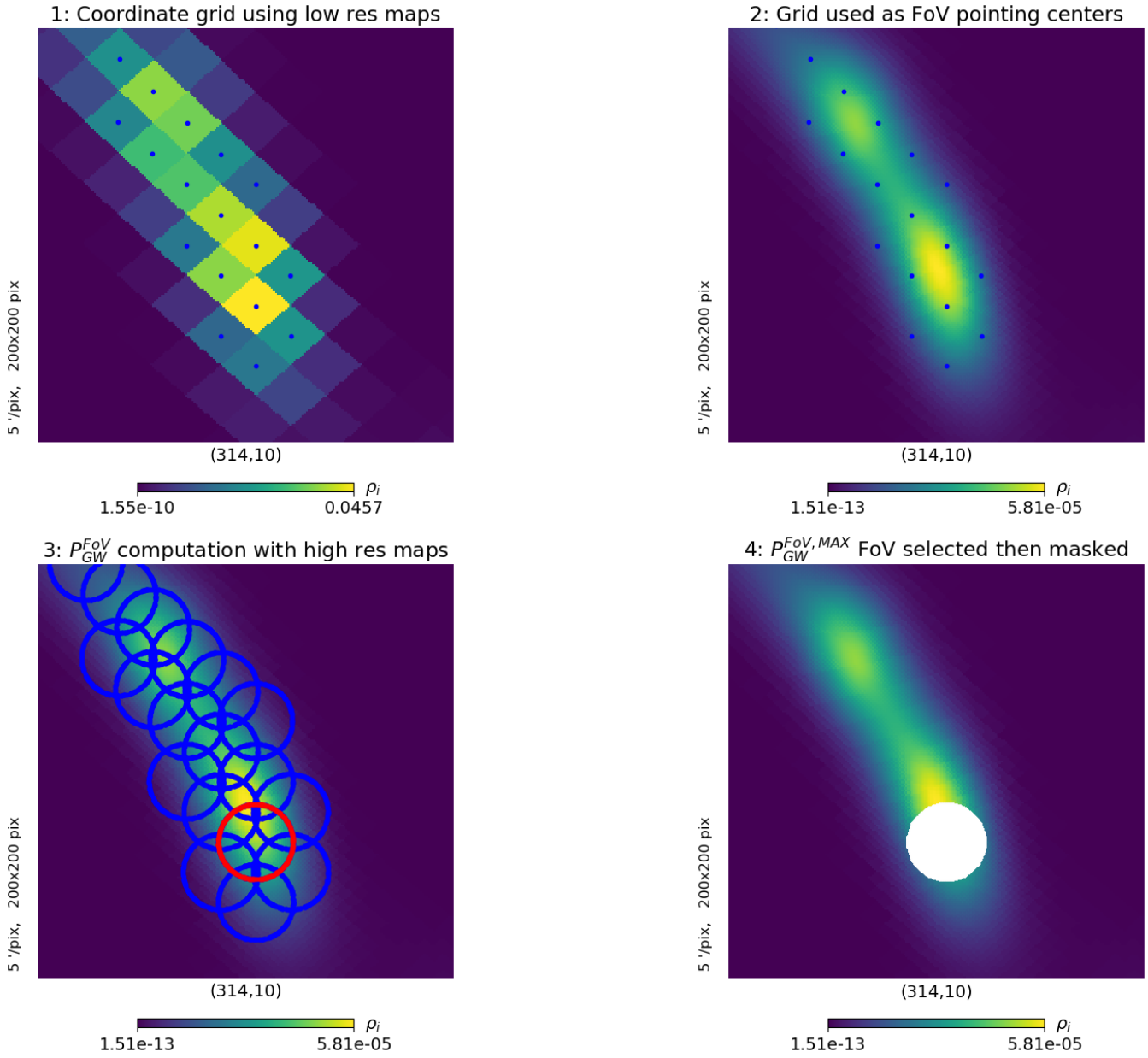

Figure 3.4: Graphical representation of the `PGW-in-FoV` algorithm steps to compute the best observable position for one time window. These steps are repeated to determine the best position to observe for each observation window. The *initial* map for the GW event S190728q is used as an example. For representation purposes the region enclosed in the 50% localisation uncertainty and $N_{side} = 32$ are chosen for the construction of the low resolution coordinate grid. The blue dots represent the grid of coordinates of the IACT FoVs inside which P_{GW}^{FoV} will be calculated. The blue circles are the considered FoVs. The red circle represents the region with $P_{GW}^{FoV,MAX}$. The white region is masked.

unexplored regions of the skymap between the different FoVs. The value of N_{side} can be changed for other observatories according to their FoVs. Note that in Fig. 3.4 a value of $N_{side} = 32$ is chosen for graphical representation reasons.

3.3 3D GW follow-up algorithms

The matter distribution in the local universe is inhomogeneous and can be traced by the distribution of galaxies. Galaxies are often grouped in small and large cluster linked by galaxy filaments. Given that stellar event such as CBC systems form predominantly within galaxies, we can exploit the inhomogeneities to improve the search for the remnants of such events as well as limit the number of false positives [3]. Following this reasoning, the search region can be reduced, and the chances of detecting the EM counterpart can be increased by correlating the GW localization region with the galaxies that could plausibly host such events.

Following [339], a posterior probability *volume* can be defined, which represents the probability that the source is located within a pixel *i*, corresponding to the coordinates (RA$_i$, Dec$_i$) at a distance [z,z+dz], from which the probability density per unit volume normalised to unity in cartesian coordinates is given as:

$$\frac{\mathrm{d}P}{\mathrm{d}V} = \rho_i \frac{N_{\mathrm{pix}}}{4\pi} \frac{\hat{N}_i}{\sqrt{2\pi}\hat{\sigma}_i} \exp\left[- \frac{(z-\hat{\mu}_i)^2}{2\hat{\sigma}_i^2} \right] \tag{3.3}$$

where $\hat{\mu}_i = \hat{\mu}(n_i)$, $\hat{\sigma}_i = \hat{\sigma}(n_i)$, $\hat{N}_i = \hat{N}(n_i)$ refer to the mean, the scale, and the normalization. $\frac{\mathrm{d}P}{\mathrm{d}V}$ is evaluated for the location of each galaxy with a distance z inside the GW localisation region and a value $\frac{\mathrm{d}P}{\mathrm{d}V}$ is assigned for each galaxy. The correlation of the 3D posterior probability distribution of the localization of a GW and a three dimensional distribution of potential hosts in the Universe, define a new normalized probability which in the following is referred as $P_{GW\times GAL}$. It is defined as:

$$P^i_{GW\times GAL} = \frac{\mathrm{d}P^i/\mathrm{d}V}{\sum_j \mathrm{d}P^j/\mathrm{d}V} \tag{3.4}$$

where $\sum_i P^i_{GW\times GAL} = 1$.

Galaxy catalog: In order to use the correlation introduced in the previous section, the Galaxy List for the Advanced Detector Era (GLADE) catalog is considered [98]. The latter is currently being used in the H.E.S.S. GW program due to its easy availability and continuous updating.

The GLADE catalog has been built by cross-matching five, non-independent astronomical catalogs

(GWGC, 2MPZ, 2MASS XSC, HyperLEDA and SDSS-DR12Q), including galaxies and quasars. The catalog completeness has been assessed by the authors in terms of cumulative blue luminosity outside the Galactic plane (that we also call *avoidance zone* due to low galaxy statistics). It is found to be fully complete up to $d_L = 37^{+3}_{-4}\,\mathrm{Mpc}$, and it has a completeness of $\sim$61%, $\sim$54% and $\sim$48% within the maximal value of single-detector BNS ranges during O2 $\sim$100 Mpc, the minimal planned BNS range during O3 $\sim$120 Mpc and the design sensitivity $\sim$173 Mpc respectively [98].

Additional galaxy properties: Additional galaxy proprieties can be taken into consideration like the stellar mass, star formation rate or galaxy type. For example, [245] found that due to metallicity effects, BNS system most likely form and merge in massive galaxies while BBH and NSBH are more likely to form in small galaxies and can merge in larger galaxies with a long time delay between formation and merger that permits for galaxy merger to occur meanwhile. [44] propose that early-type galaxies (elliptical galaxies) host most of the CBC events in the Universe with $\geqslant 60\%$, $\geqslant 64\%$ and $\geqslant 73\%$ for BNS, BHNS, and BBH respectively and the CBC rate for a galaxy strongly correlates with the stellar mass. Therefore, I decided to add an option to our algorithms in order to use the stellar mass of galaxies in the search for GW counterparts. To do that, I use the stellar masses provided in the MANGROVE [109] catalog. The usage of stellar mass, M_{galaxy}, allows to prioritize massive galaxies in the search for GW event counterparts. The correlation of the galaxies in the Universe with the GW maps will follow Eq. 3.5 as defined by the authors:

$$P^{i}_{GW\times GAL,new} = G_{tot} = \frac{\mathrm{d}P}{\mathrm{d}V}(1 + \alpha\beta G_{mass}) \tag{3.5}$$

where β is a parameter that is used to weight the importance of G_{mass} and is determined statistically by a sample of GW host. However, since only one GW host galaxy is known (NGC4993), the authors of [109] choose $\beta = 1$ (which might change when more BNS host galaxies are found),

$$G_{mass} = \frac{M_{galaxy}}{\sum M_{galaxy}} \tag{3.6}$$

and

$$\alpha = \frac{\sum \frac{\mathrm{d}P}{\mathrm{d}V}}{\frac{\mathrm{d}P}{\mathrm{d}V} G_{mass}} \tag{3.7}$$

After assigning each galaxy in the region of interest a probability, we have three optimized strategies

for GW events occurring at distances for which complete galaxy catalogs are available.

3.3.1 `Best-galaxy` algorithm

This strategy was implemented in the H.E.S.S framework before 2017. Only galaxies above a certain minimum probability threshold $P^{i}_{GW\times GAL}$ are considered. In each iteration, the galaxy with the highest probability, $P^{i}_{GW\times GAL}$ is chosen to be observed and it guides the observations. The galaxies included in the region defined by the FoV of the telescope are indirectly observed. The motivation of such algorithm is the trade-off between the speed of computation, which is a key point for transient searches, and the astrophysical motivation. However, the observation schedule resulting from this technique can present important overlapping of covered regions, as it was the case for the `Best-pixel` algorithm. Furthermore, although such galaxy-targeted searches can be very performant for small FoV instruments, like optical and X-ray telescopes (such as Swift-XRT [131] the GRANDMA collaboration telescopes with $FoV < 1deg^2$ [41] and Magellan [137]), the relatively large FoVs of IACTs motivate a further step in the selection of the observation coordinates.

3.3.2 `Galaxies-in-FoV` algorithm

This strategy was also developed and implemented in the H.E.S.S framework before 2017. Medium-FoV experiments like IACTs do benefit from the integration of probability regions in the sky following Eq. 3.8, where the goal is to probe the distribution of the galaxies and target galaxy clusters and groups instead of individual galaxies in order to cover the maximum probability region. FoV-targeted search methods are used by the GRANDMA telescopes with $\mathrm{FoV} > 1\mathrm{deg}^2$ [41] and ASCAP [107] for GW counterpart searches. In this approach, we define $P^{FoV,i}_{GW\times GAL}$ as:

$$P^{FoV,i}_{GW\times GAL} = \int_0^{2\pi}\int_0^{r_{FoV}} P^{i}_{GW\times GAL}(r,\phi)\,\mathrm{d}r\mathrm{d}\phi. \tag{3.8}$$

where r is the radius and ϕ the angle of the FoV represented by a circle. The galaxies that are above minimum probability threshold (in H.E.S.S we use 0.01 for small maps with 90% localisation < 400 deg^2) are here taken as positional seeds at the center of the $\mathrm{FoV}_{\mathrm{IACT}}$ and the total probability of all individual galaxies contained in the FoV is computed. The highest probability sky field, which fulfilled $P^{FoV,i}_{GW\times GAL} =$

$P_{GW\times GAL}^{FoV,MAX}$ is chosen[1] to be observed during the given window, and is masked for the following iterations. This methods is one of the most effective ones to efficiently cover GW localisation areas. The seeds of the FoV are the centers of the galaxies. An example of the steps of `PGalinFoV` are illustrated in Fig. 3.5.

However, for large localisation maps with large uncertainties on the distance of the event, the number of galaxies in the 3D volume increases drastically. If we choose the galaxies as positional seeds to test their positions, the algorithms will have to test a very large number of positions and integrate the probability inside all of these regions. This will drastically increase the computation time. During the testing of the algorithms (see Sec. 3.5.2), I find that maps with a 90% localisation contour $> \sim 400$ deg^2 start to have a computation time that can be reduced if we rely on the pixelization of the maps like for `PGWinFov`. In order to find a solution for this problem with large maps, I developed a new algorithm based on `Galaxies-in-FoV` in the following.

3.3.3 `PGalinFoV-PixRegion` algorithm

The `Galaxies-in-FoV` algorithm is updated with one of the main features of the `PGW-in-FoV` algorithm: the parallel use of two different resolution skymaps. The `PGalinFoV-PixRegion` algorithm uses a low resolution re-binned skymap (typically with $N_{side} = 64$ for H.E.S.S.) as a coordinate grid for the pointing seeds like the `PGW-in-FoV` algorithm instead of individual galaxies. The algorithm chooses $P_{GW\times GAL}^{FoV,MAX}$ which is computed from a higher resolution map correlated with the galaxy catalog as illustrated in Fig. 3.6. This modification to the `Galaxies-in-FoV` algorithm also requires us to choose the percentage of the localization uncertainty to be covered by selecting the pixels from the coordinate grid enclosed in the x% probability uncertainty region. A value of 90% can be choosen like for `PGWinFoV`. A 90% values means that there is approximately a 10% chance for the GW events to be located outside the chosen contour (at the edge of their GW skymaps hotspots) without taking into considering the Fov going overboard on the edges.

[1] `Galaxies-in-FoV` is referred to as `PGalinFoV`, $P_{GW\times GAL}^{FoV,MAX}$ as P_{GAL} and $P_{GW}^{FoV,MAX}$ as P_{GW} in the following.

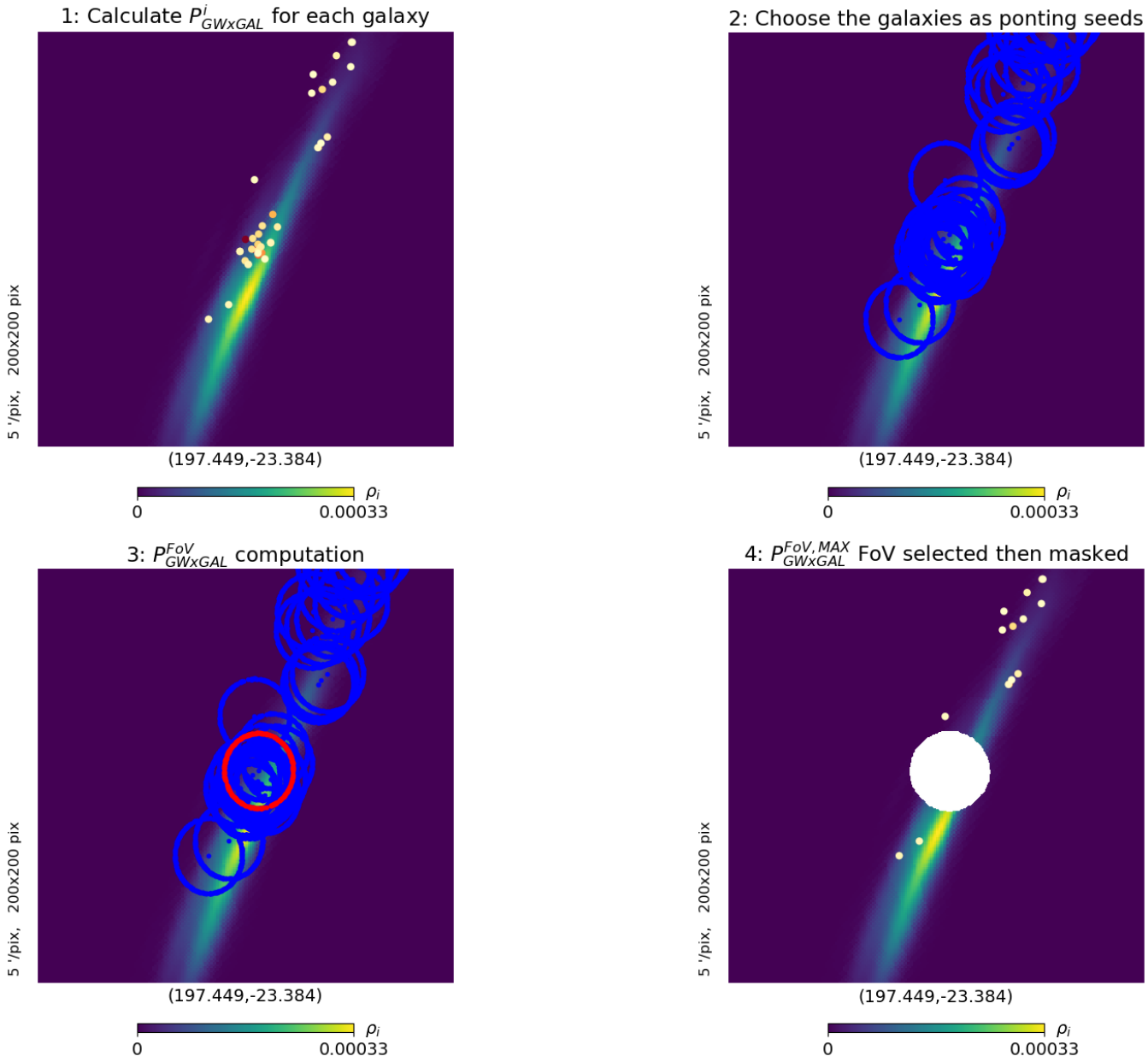

Figure 3.5: Graphical representation of the `PGalinFoV` algorithm steps to compute the best observable position for one window. These steps are repeated to determine the best position to observe for each observation window. The *updated* map for GW170817 is used. The blue dots represent the centers of the IACT FoVs inside which $P^{FoV,i}_{GW\times GAL}$ will be calculated. The blue circles are the considered FoVs. The red circle represents the region with $P^{FoV,MAX}_{GW\times GAL}$. The white region is masked. The colored dots represent the galaxies with the highest $P^{i}_{GW\times GAL}$ in the region on the YlOrRd color scale in: `https://matplotlib.org/stable/gallery/color/colormap_reference.html` (yellow for lowest values and red for highest values).

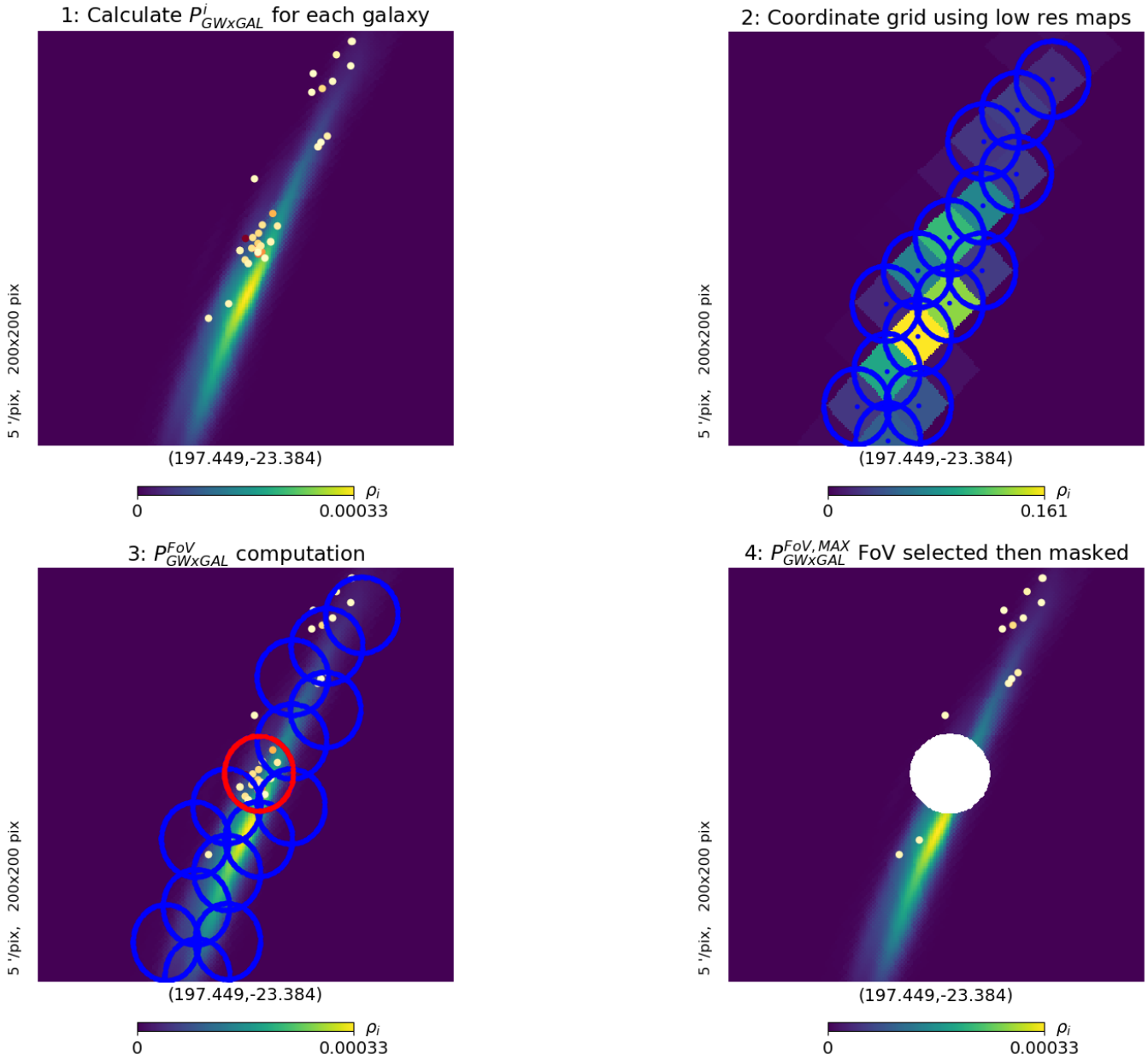

Figure 3.6: Graphical representation of the `PGalinFoV-PixRegion` algorithm steps to compute the best observable position for one window. These steps are repeated to determine the best position to observe for each observation window. The *updated* map for GW170817 is used. For representation purposes the region enclosed in the 90% localisation uncertainty and $N_{side} = 32$ are chosen for the construction of the low resolution coordinate grid. The blue dots represent the grid of coordinates of the IACT FoVs inside which $P^{FoV,i}_{GW\times GAL}$ will be calculated. The blue circles are the considered FoVs. The red circle represents the region with $P^{FoV,MAX}_{GW\times GAL}$. The white region is masked. The colored dots represent the galaxies with the highest $P^i_{GW\times GAL}$ in the region on the YlOrRd color scale in: `https://matplotlib.org/stable/gallery/color/colormap_reference.html` (yellow for lowest values and red for highest values).

3.4 GW follow-up scheduler

We use the algorithms described above in order to build a scheduler for GW event follow-ups. The main feature of this offline scheduler is its flexibility. For instance it can be adapted for every desired observatory just by adding a configuration file with high level telescope parameters such as the FoV, the location and other observation requirement such as the minimum duration of observations allowed. It can also take into consideration positions in the sky to be avoided, like in the case of previously observed fields during the night (before the arrival of an update). For instance, if follow-up observations of a GW event have already started and an *update* of the GW maps is received after the start of the observations, the scheduler can take as input the positions that were already observed during the night before the arrival of the *update*, mask these positions from the GW map, and compute a new schedule to cover the *updated* map without re-observing these regions..

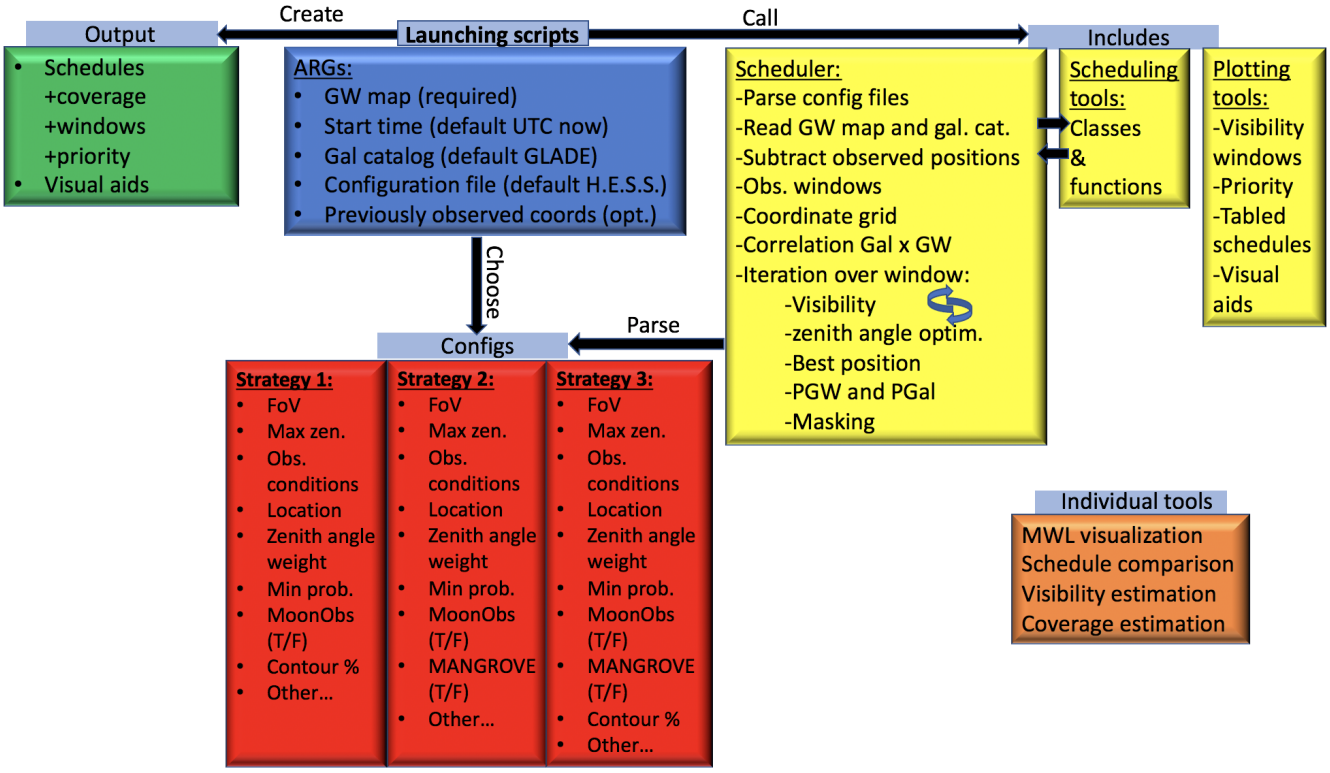

Figure 3.7: Schematics of the gravitational waves scheduler

The scheduler and algorithms described here have been derived using Python [360] primarly with the HEALPix/healpy [392] [138], Astropy [299], Numpy [272] [146], Matplotlib [173], PyEphem [304], and MOCPy [71] packages.

The schematics of the scheduler is illustrated in Fig. 3.7. It is launched by one of the **launching** scripts. For each GW algorithms we have a different script. The inputs of these scripts are shown in the blue box in Fig. 3.7.

The launching file will read the high level telescope parameters from a configuration file stored in the configurations directory. Each algorithm has its own configuration file. The parameters in the configuration files are shown in the red boxes in Fig. 3.7.

In the scheduling scripts, the follow-up steps for each algorithm are defined following this sequence:

- The scheduler loads the parameters that should be considered.
- The scheduler loads the galaxy catalog if a 3D algorithm is used.
- The scheduler loads the GW map.
- The scheduler correlates the GW map and the galaxy catalog if a 3D algorithm is used.
- The schedule subtracts the regions in the sky that should not be observed if needed.
- The schedule computes the available observation windows after the given start time following the observation conditions defined above.
- The scheduler creates the coordinate grid if `PGWinFoV` or `PGalinFoV-PixRegion` are used.
- The scheduler starts looping over the observation windows
  - It computes the visible positions at the observation window time to be tested for the maximum probability. In the case of `Best-galaxy` or `PGalinFoV` these positions are substituted by galaxies.
  - Each of these positions is assessed either using a 2D or a 3D integral probability with the zenith angle weighting.
  - The total probability in the FoV is calculated for the chosen position and the region inside the FoV is masked.
  - The new positions are appended in a table.

After the schedule has been computed, the launching scripts also call ranking and plotting scripts contained in the includes that will rank the observations depending on the different individual probabilities (the

probability is assessed individually for each pointing without masked regions), will compute observation windows for each positions in case the optimal start time could not be respected (due to weather and technical issues) and will compute visual aid plots.

The output of these scripts will be stored in the output directory. It contains several tabled schedules with information adapted for experts and non-experts and several visual aid plots like the variation of the zenith angle of each position during the night and an overlay of the positions on the GW map in the sky. An example of the output plots is given in Fig. 4.10 and in Tab. 4.1 of Chap. 4.

Finally, the offline scheduler also contains a tools directory that contains several individual script for experts on call. These tools allow for example to compare two observation schedules, or to plot MWL information on the GW map.

3.5 Performance and comparison

In order to asses and compare their performance, I test the algorithms on 250 simulated BAYESTAR GW maps from [339]. These maps are derived from simulated BNS merger events provided by the LIGO-Virgo collaboration before O2. The BAYESTAR maps are used because we want to simulate a prompt response, and BAYESTAR maps are the ones that are sent first in the alerts. These maps are distributed in the entire sky and not only the southern hemisphere where H.E.S.S is located.

From these 250 maps, 28 maps have $N_{side} = 256$, 163 map have $N_{side} = 512$, 26 maps have $N_{side} = 1024$ and 33 maps have $N_{side} = 2048$.

In Fig. 3.8, I compute their distance and distance uncertainty distribution. The events are located at distances between $\sim$7 and $\sim$183 Mpc with uncertainties between $\sim$1 and $\sim$54 Mpc. In comparison, GW170817 is located at 40 Mpc with an uncertainty of 8 Mpc and S190425, the first confirmed BNS merger event in O3 has a distance of 160 Mpc with an uncertainty of 70 Mpc. The completion of the GLADE catalog (see Sec. 3.3) is at 48% at a distance of 173 Mpc.

I also calculate the areas of these simulated maps in the sky. The areas of 90% localisation contour range from few deg^2 to $\sim$4500 deg^2. The area of the O3 events can also range from a few deg^2 but can reach several 10000 of deg^2 in the sky. However GW maps with very large localisation uncertainties will not be followed by H.E.S.S. The simulated GW maps present a variety of GW map area ranges to test our 2D and 3D algorithms. The area enclosed in the 90% localisation contour are shown in Fig. 3.9. I also overlay the areas of the 90% localisation contour from the O3 BAYESTAR maps with areas $<$ 5000 deg^2.

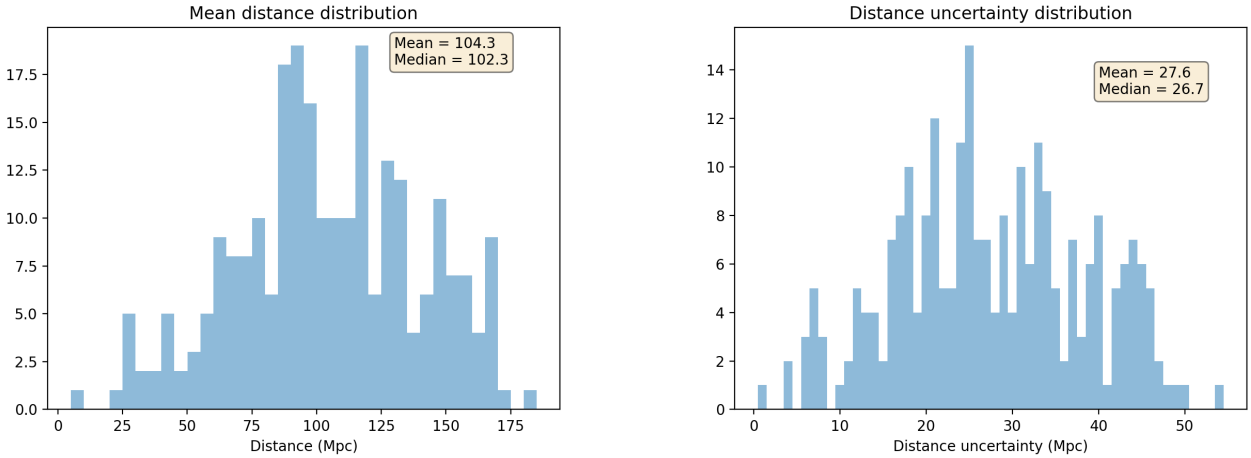

Figure 3.8: Distance and distance uncertainty of the 250 simulated BAYESTAR GW events from [339].

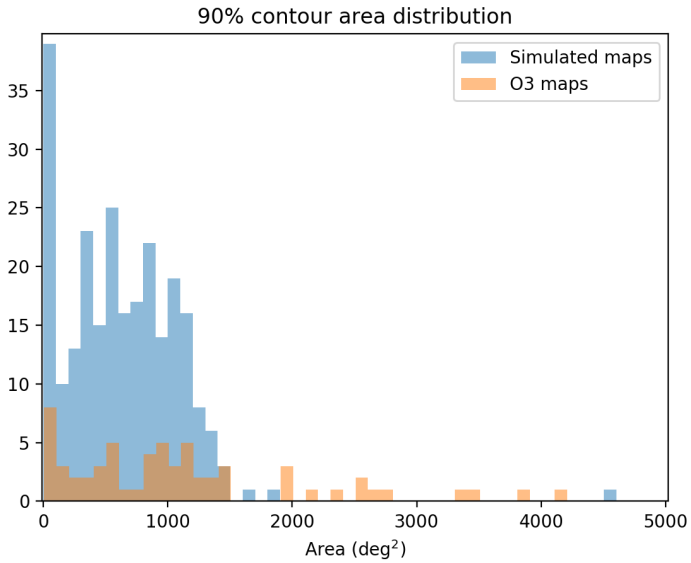

Figure 3.9: Area of the region enclosed inside the 90% localisation contour for BAYESTAR maps from simulated GW events from [339] and O3.

I inject the events at random times throughout a whole year. For each map an optimized observation schedule following both algorithms is derived for 10 different times which gives a total of 2500 MC scheduling simulations for each algorithm. I set up the testing pipeline on a server in Lyon. The GW maps and random times are injected to the scheduler and the output is saved in a output directory containing schedules for each simulation and summary files.

On the server in Lyon, it takes on average $\sim$30 seconds to load a high resolution map with $N_{side} =$

2048, while it takes only $\sim$8 seconds to load a map with resolution $N_{side} = 1024$. Maps with $N_{side} = 512$ require in average less than 2 seconds and maps with $N_{side} = 256$ require less than 1 second to be loaded. These information will be useful for the discussion in Sec. 3.5.2. I note that, unfortunately, high resolution maps with $N_{side} = 2048$ correspond generally to relatively well localized GW events. As the localisation uncertainty is related to the signal strength as well as the number of participating GW interferometers, these events are rare (only 5 of the 80 events detected during O3 have been distributed with $N_{side} = 2048$), but are at the same time the promising ones for rapid detection of counterparts which poses as a limitation to our time saving measures.

The testing pipeline can be used for all types of localisation maps and it is used later on to test GBM tiling strategies (more info in Chap. 4). In the following sub-sections I show the results of theses tests and discuss them.

3.5.1 2D algorithms performance

Considering the necessary observation conditions for H.E.S.S. defined in Sec. 3.1 and imposing a minimum requirement coverage of $P_{GW} = 2\%$ per observation, I compare in Fig. 3.10 the total P_{GW} coverage that can be achieved in the first night of observation and the cumulative P_{GW} in Fig. 3.11 for the `PGW-in-FoV` and `Best-pixel` algorithms. For `PGW-in-FoV` I use a 90% localisation contour to determine the coordinate grid. Looking at Fig. 3.11, we notice that for `Best-pixel`, $\sim$63.3% of the GW maps had a coverage less than 4%, while this number is smaller ($\sim$58.5%) for `PGW-in-FoV`. This "lag" in coverage is dragged up to values of $\sim$86% coverage. This means that a bigger part of the simulated maps have a smaller coverage when `Best-pixel` is used instead of `PGW-in-FoV`.

I note that a large fraction of GW maps could not be covered ($\sim$55%) or had a very low coverage. This number is large due to the fact that the simulated maps are not localised only in the southern hemisphere but in the entire sky and that some parts of the sky are simply not reachable for a single ground-based experiment. Therefore in the following, I only take into consideration maps where observations have been scheduled.

The cumulative P_{GW} per pointing (for one night) for the two algorithms is computed up to 10 pointings for each simulation. In Fig. 3.12, the violin plot shows only simulations where the `PGW-in-FoV` algorithm was able to schedule observations. I find that `Best-Pixel` is not able to achieve the minimum required coverage of 2% in some of these cases. This is why the red lines for `Best-Pixel` start at 0% coverage while the blue lines for `PGW-in-FoV` don't. The violin plot also shows that the probability distributions are

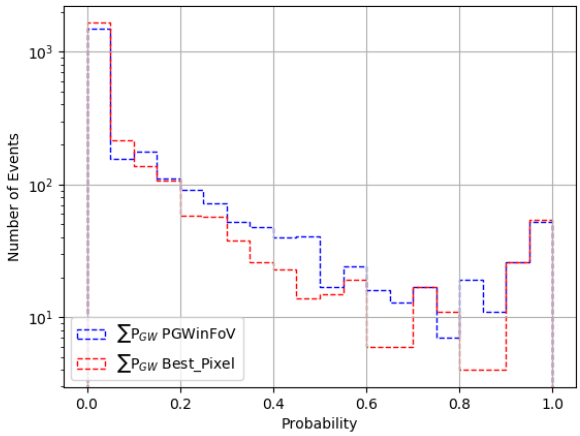

Figure 3.10: Total P_{GW} simulated coverage distribution for the `PGW-in-FoV` and `Best-pixel` algorithms.

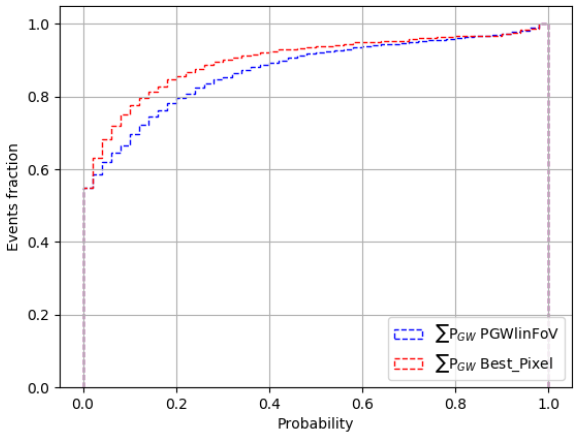

Figure 3.11: Total cumulative P_{GW} coverage distribution for the `PGW-in-FoV` and `Best-pixel` algorithms.

.

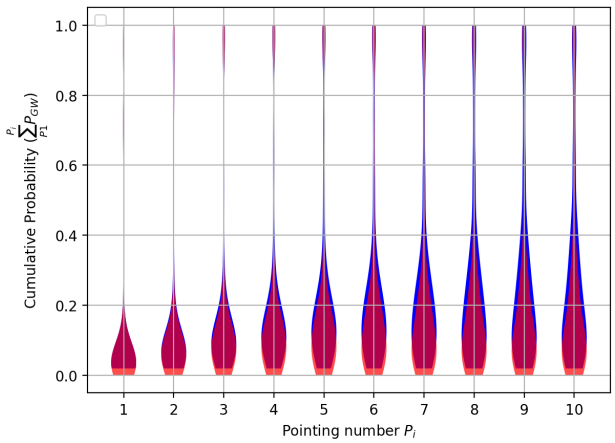

Figure 3.12: Total P_{GW} simulated coverage distribution for the `PGW-in-FoV` and `Best-pixel` algorithms.

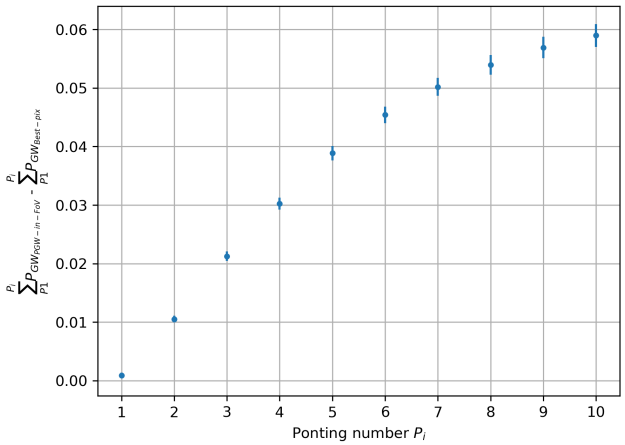

Figure 3.13: Difference of the cumulative P_{GW} per pointing between `PGW-in-FoV` and `Best-pixel`

.

slightly larger for `PGW-in-FoV` for both poorly (bottom part of the plot) and well covered (upper part of the plot) maps. The mean (and error on the mean) of the difference between the two cumulative P_{GW} per pointing computed with each algorithm for the 2500 simulations are shown in Fig. 3.13 up to 10 pointings. The coverage per pointing is lower for `Best-pixel` as the pointing number increases during a follow-up. `PGW-in-FoV` starts to improve coverage immediately after the first observation and this improvement reaches up to 6% on average within 10 observation runs.

The lower efficiency of `Best-pix` can be explained by the FoVs overlap described in Sec. 3.2.1. This

overlap causes the `Best-pixel` strategy to struggle with achieving the minimum coverage requirement per pointing in the case of extended GW maps (large localisation regions) since fewer effective pointings will pass the minimum coverage requirement. I remind the reader that the observed position is masked for the next iterations meaning that if the next pointing covers part of the masked region, the probability inside this masked part will not be counted in to check if P_{GW} is more than the minimum 2% coverage per pointing requirement. As mentioned previously, overlap could be reduced by significantly lowering the GW resolutions for the `Best-pixel` algorithm but this comes at the cost of accuracy in probability computation. Therefore I conclude that `PGW-in-FoV` performance is superior to `Best-pixel`.

3.5.2 3D algorithms performance

To asses the efficiency of `PGalinFov` and `PGalinFov-PixRegion`,I repeat the test for these two algorithms. I show the distribution of the total P_{GAL} and P_{GW} coverage that can be achieved in the first night of observation while taking into account the necessary observation conditions for H.E.S.S. in Fig. 3.14 and their cumulative distribution in Fig. 3.15. The plots are computed for events where at least one observation could be scheduled. Even though the 3D algorithms rely on the computation of P_{GAL} to determine the best position to observe, I also compute the covered P_{GW} by these "best" pointings. P_{GAL} and P_{GW} are two different entities that cannot be compared to each other due to the inhomogenity in the galaxy distribution in the Universe. Each entity for a given strategy should be compared with the same entity from the other strategy. Both figures show that the coverage efficiency of P_{GAL} and P_{GW} for both algorithms is similar.

Since the performance of both algorithms is comparable, I now compare their computation time. To do that, I compare the times it takes for the main steps described in Sec. 3.7 to be executed. While the loading of the the telescope parameters and the galaxy catalogs can be performed at the beginning of the observation period, to save time, the download and analysis of the GW map happens on an event-by-event basis and can only be performed after the alert has been issued by LVC. Any potential map re-binning takes place of course after it is loaded so the loading time poses as a limitation to fast computing time. Fig. 3.16 shows the time required by each of these steps for the `PGalinFoV` algorithm as a function of the size of the GW localisation area of the simulated events (defined as the 90% localisation contour). The time required to load and analyze the GW map varies depending on the N_{side} resolution as explained in

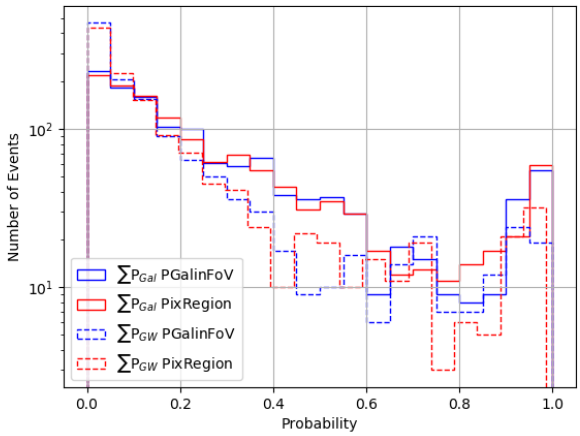

Figure 3.14: Total P_{GAL} and P_{GW} simulated coverage distributions for `PGalinFoV` and `PGalinFoV-PixRegion`.

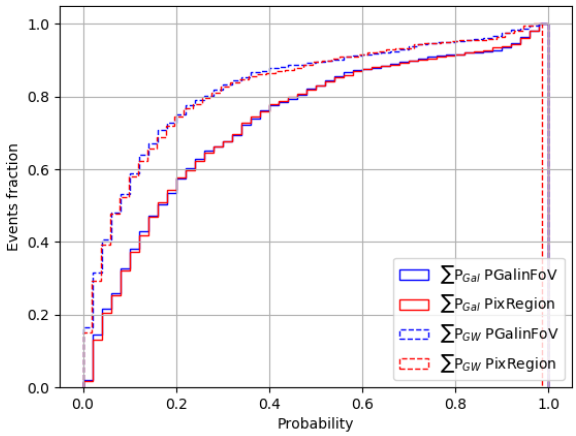

Figure 3.15: Total P_{GAL} and P_{GW} coverage cumulative distributions for `PGalinFoV` and `PGalinFoV-PixRegion`.

the beginning of Sec. 3.5. Due to limited number of available simulations, I here concentrate on the most common maps, those with $N_{side} = 512$.

Fig. 3.16 shows that, while the time required for each step in the computation of the schedule is constant as a function of the size of the GW map the time to define the best pointing direction, i.e. the "probability computation" necessary to define each P_{GAL}, increases with the GW localisation uncertainty for `PGalinFoV`. This is an effect of the increasing number of galaxies used as seeds with increasing uncertainty *volume*, thus requiring more calculations to be preformed.

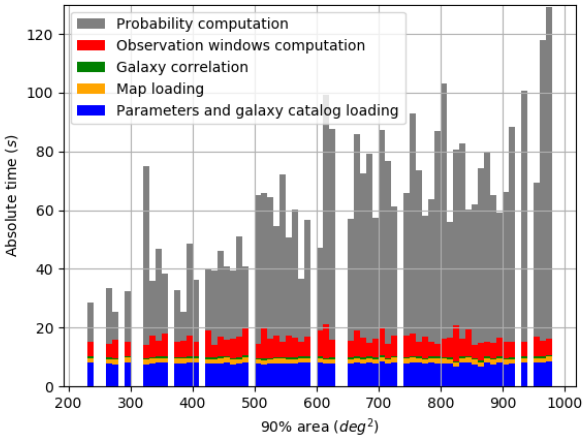

Figure 3.16: Absolute time for the computation of each step of the PGalinFov algorithm for $N_{side} = 512$.

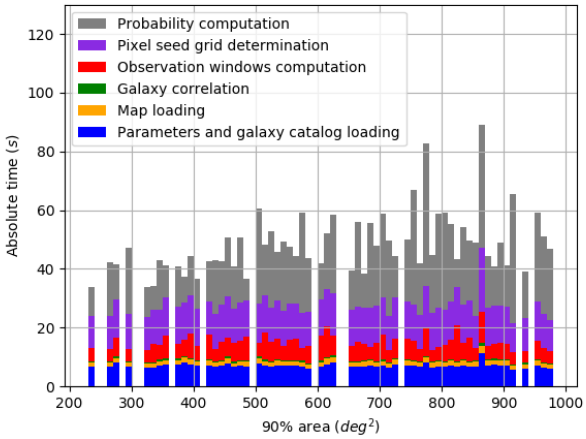

Figure 3.17: Absolute time for the computation of each step of the PGalinFov-PixRegion algorithm for $N_{side} = 512$.

To determine the time required by each step of `PGalinFoV-PixRegion`, I repeat the previous study for this algorithm. As illustrated in Fig. 3.17, the time required for the ”probability computation” defining P_{GAL} remains stable when the localisation uncertainty increases. This is due to the fact that the number of pixels used in the 2D observational seeds grid is based on a low resolution map and therefore does not increase as drastically as the number of target galaxies within the uncertainty volume. However, the additional step necessary to define the 2D seeds grid adds a considerable amount of time to the overall budget.

I note that the absolute values of the computation time shown here are dependent on the parameters and performance of the machine(s) performing the operation and only the general behavior of the data should be taken into consideration. However these tests have been performed on several machines/servers and gave similar results.

In conclusion, the `PGalinFoV-PixRegion` algorithm allows to cover large maps (where the 90% localisation contour is $>$ 400 deg^2) faster than `PGalinFoV` which makes it more suitable for the coverage of poorly localised events. On the other hand, `PGalinFoV` is slightly faster for smaller maps (well localized events) and does not require a coordinate grid computation step, therefore it is the preferred option for the most interesting, high signal-to-noise GW events detected by the full LVC network.

3.6 Prospects for GW follow-up scheduling

Continuous optimisation of counterpart search strategies beyond the speed improvements and extension of the time coverage of the observations is crucial for effective hunting for electromagnetic emission from *golden* events like GW170817.

Within the GW group in H.E.S.S., we are currently working on GW follow-up strategies with several telescopes located in different sites. The aim is to efficiently cover a GW map by taking into consideration rapidity and simultaneous telescope observations of different parts of the sky (with or without overlap) by prioritizing coverage and higher sensitivity observations. This can be useful for collaborations with observatories on different sites like CTA or GRANDMA. For observatories like CTA with multiple telescopes on the same site, this can also be used in case the telescope arrays are divided into sub-arrays for observations. Moreover, parameters beyond the mass of galaxies can be taken into consideration for the 3D algorithms. Such parameters can include the morphology and type of the galaxy.

For the testing part, to compare 2D and 3D algorithms, GW simulations based on real galaxy catalogs

where the position of the CBC event is known are needed. Such simulations are being developed now. Knowing the location of the GW event will allow to compare the rate of detection of the algorithms developed for GW follow-up. However, the GW simulations should be based on real galaxy catalogs. Moreover, realistic GW event simulations that take into consideration galaxy parameters such as the stellar mass, will allow to test strategies using galaxy properties such as the one developed by [109]. However, we do not have access to such simulations yet.

Chapter 4

The H.E.S.S. GW and GRB program

4.1 The H.E.S.S. Transients follow-up system

Covering the reception and processing of transients alerts, changing the observation schedule and providing preliminary analysis results in real-time, the H.E.S.S. transients follow-up system [168] [45] plays a central role in the execution of any observation program related to transients such as GRBs and GWs. In order to deal with the ever increasing number and variety of information on transient phenomena, the H.E.S.S. transient follow-up system is fully automated and does not require human intervention at any stage. An overview of the system is given in Fig. 4.1 and more details will be provided in an upcoming publication [168].

The system accepts transients alerts in the VoEvent2.0 format [344], which is commonly supplied by current transients brokers. A broker receives alerts from observatories (authors) that detected a transient like a GRB or a GW. To do that, the author opens a connection to the broker and transmits the VoEvent. The broker redistributes the VoEvent to other facilities (subscribers). In fact, the subscriber (like H.E.S.S.) has an open connection to the broker, which remains open indefinitely, and receives the VoEvent over this connection.

The ToO alert system is the part of the H.E.S.S. transient system that handles the transient alerts. It subscribes to the NASA Gamma-ray Burst Coordinates Network (GCN [1]) alert broker which publishes (among others) alerts from the Fermi-GBM and -LAT, Swift-BAT, neutrino detections by IceCube and ANTARES, as well as the alerts from the GW observatories. Further alerts are received via the 4PiSky system [343], providing alerts from ASAS-SN. IceCube and ANTARES alerts are directly submitted to

[1] `https://gcn.gsfc.nasa.gov/`

H.E.S.S.

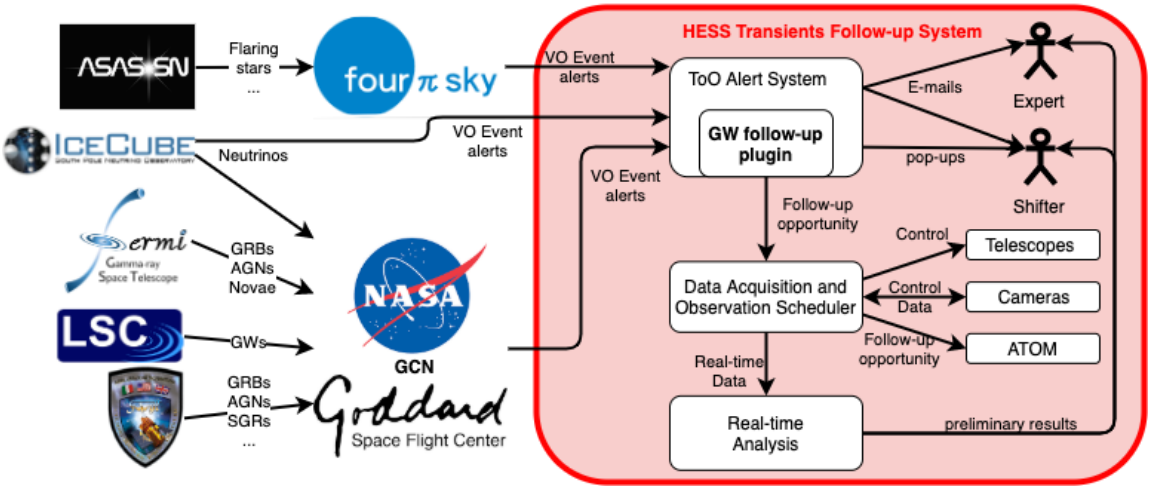

Figure 4.1: Schematic view of the H.E.S.S. Transient Follow-up System alert system providing automatic and real-time reactions to multi-wavelength and multi-messenger alerts. From [45].

The ToO alert system: The ToO alert system computes the visibility conditions for incoming alerts and applies configurable selection criteria in order to decide if follow-up observations should take place. The schematics of the ToO alert system are illustrated in Fig. 4.2. The alert is processed from top to bottom. The system starts by loading the general configurations like the strictness of selection cuts that will be used. The strictness can be set to *standard* or to *loose*. For example *standard* cuts will not allow observations under 45 deg zenith angle while *loose* cuts will allow it. The `VoEvent` module parses the information from the alert and stores them. The alert is then forwarded to the `Alert Identification` module that will define the alert type, the science case, and specify the filtering cuts for each alert. The last step is done by parsing the cuts from the configuration files. Each type of alert has a specific configuration file where the observation criteria parameters (maximum zenith angle, maximum delay, minimum observation duration, moonlight observation parameters), and selection criteria are defined. For example, for a `Fermi-Gnd-alert` one of the selection criteria is the minimum requirement in significance value. For GW alerts, the specific cuts contained in the configuration files of the GW scheduler (see Chap. 3), the selection parameter on the nature of the GW event, and the observation criteria are contained in these configuration files. After, the alert identification, the `Special Notice` module will send an email to experts on call to notify them of the reception of the alert. The alert is then forwarded to the `Decision` module. This module will make the decision on whether an alert is worth following or not. To do that, it calls the `Filtering` module where each parameter will be assessed. For example, the `Filtering` module will as-

sess if the significance of a `Fermi-Gnd-alert` is higher than the minimum required, and will forward this information to the `Decision` module that will either instruct the system to move on or to stop pursuing the alert. For special cases, the filtering of the alert requires the assessment of complex parameters that can't be found in the alert, like in the case of GWs where the total achieved coverage should be assessed. In that case, the `Filtering` module calls the `Special Cuts` module where these "more complex" assessments happen. The `Special Cuts` module contains a GW follow-up scheduler and is connected to the `GW tools` module that contains all the functions and classes needed to schedule GW follow-up observations. After that, the position of the alert is forwarded to the `Visibility` module that will assess when an event is observable to H.E.S.S. and if the event is observable now. The alert is then forwarded to the `Forwarding` module that will compute the message and send it to the contact persons and the shift-crew (also called shifters or observers) on the telescope site. The `VoMail` module will choose a list of recipients from the `Contacts` module based on the `Alert identification` science case. The `Forwarding` module also triggers the telescopes automatically if an alert can be observed now (*prompt*[2] alert) and will also generate pop ups to alert the shifters on the telescope site.

In case of a positive selection, the shifters and experts are informed via pop-ups on the main screens in the H.E.S.S. control room and via e-mails. If a prompt reaction is possible, the data acquisition system of H.E.S.S. will initiate automatic re-positioning of the telescopes by altering the planned schedule. In addition to the H.E.S.S. telescopes, ATOM [148] is notified in order to provide contemporaneous data in several optical bands. With the onset of the H.E.S.S. observations a real-time analysis of the incoming datastream is started. To provide best sensitivity at low energies where VHE signals of transients are generally expected to be stronger, the real-time analysis is running in monoscopic-mode, i.e. using only data from the large 28-m telescope. At predefined signal thresholds, alerts are generated to alert the shift-crew of a possible detection. The results are archived for inspection over the course of the following days. Alerts are ranked in priority - according to the likelihood of a VHE signal to be detected and the interests of the H.E.S.S. collaboration - in case several alerts arrive during the same night. GRB *prompt* alerts from Fermi-LAT and Swift-BAT take the priority over all alerts, followed by CBC alerts including at least one neutron star, then the other types of GW alerts like burst and BBH merger alerts. The rest of the alerts are ranked as follows: Fermi-GBM GRBs, then SGR alerts, then IceCUBE neutrinos then FRBs.

[2]Although the *prompt* and *afterglow* observation modes take the names of physical emission phases they are not directly related to them.

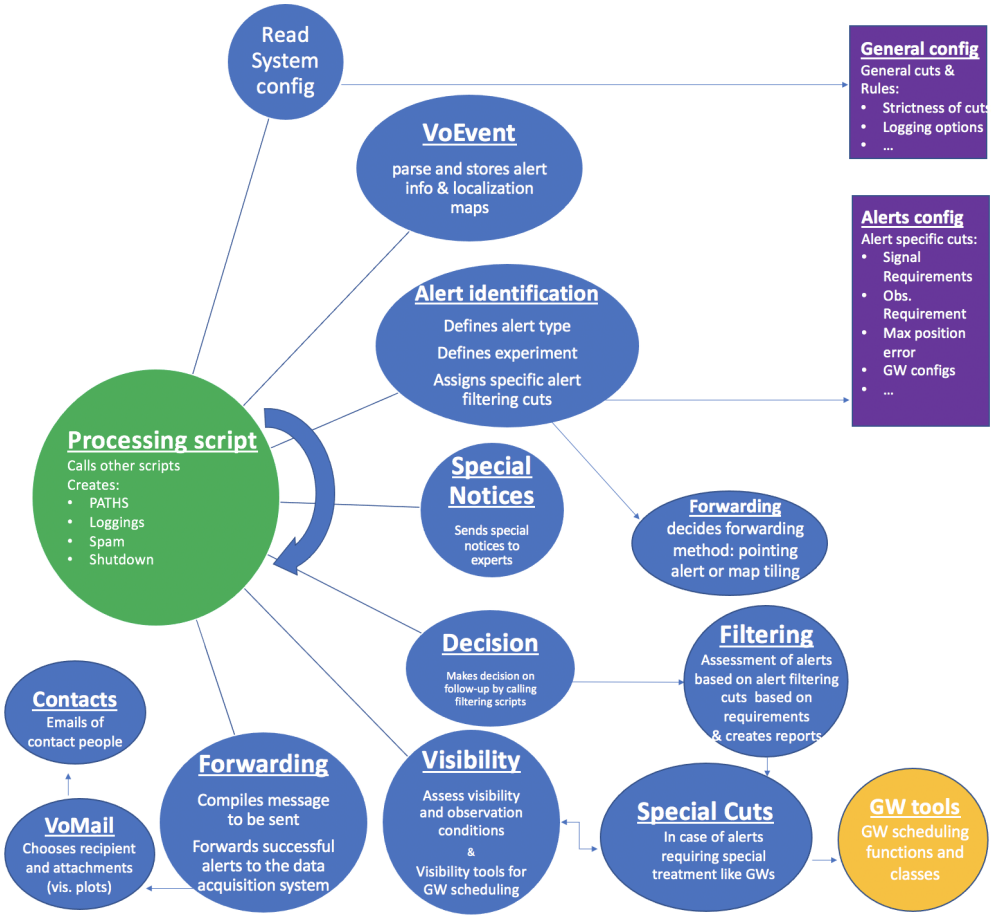

Figure 4.2: Schematic view of the H.E.S.S. ToO alert system.

4.2 H.E.S.S. follow-up of GRBs

Until early 2019, the H.E.S.S. collaboration GRB program was focused on the follow-up of well localised GRBs from SWIFT-BAT, Fermi-GBM and Fermi-LAT, with a special interest for the Fermi-LAT GRBs for their potential VHE component. Initial follow-up conditions consist mainly on favoring shorter follow-up delays, favouring closer GRBs by using redshift information of host galaxies, and on monitoring MWL information especially on the high energy part of the spectrum. The EBL attenuation of VHE γ rays imposes that the follow-up be concentrated on GRBs with small redshift ($z <\sim 1$). However, the scarcity of redshift information does not allow to rely solely on this information for a potential follow-up. H.E.S.S. performed from 2012 (installation of CT5) to 2018 (before the detection of GRB 180720B) 56 GRB observation attempts, without any detection of VHE emission. These observations are described in [154].

If the difference between the observation time and the GRB event time is less than 6 minutes, the follow-up observations are scheduled in *prompt* mode. In that case, ongoing observations are interrupted

and the telescopes will slew automatically to the position of the GRB and start taking data. The follow-up criteria for the *prompt* alerts are:

- Fermi-GBM GRBs are followed if the localisation uncertainty provided in the `Fermi-GBM-GND-POSITION` alert (see Sec. 2.1.2) is less than 2 deg and if the significance is larger than 10. The maximum zenith angle is 60 deg.
- All Fermi-LAT GRBs are followed provided the zenith angle is below 60 deg.
- All Swift-BAT GRBs are followed provided the zenith angle is below 60 deg.

If the difference between the observation time and the GRB event time is greater than 6 minutes, observations are scheduled in *afterglow*[3] mode. The following describes the general *afterglow* follow-up conditions for H.E.S.S.:

- Fermi-GBM GRBs are followed if the localisation uncertainty provided in the `Fermi-GBM-GND-POSITION` alert (see Sec. 2.1.2) is less than 2 deg and if the significance is larger than 10. The maximum allowed delay is 4 hours, and the maximum zenith angle is 45 deg. The final position provided in the `Fermi-GBM-FINAL-POSITION` notice is the one to be followed.
- All Fermi-LAT GRBs are followed provided the delay is less than 48 hours. The maximum zenith angle is 60 deg.
- All Swift-BAT GRBs are followed. The maximum allowed delay increases with smaller redshifts. For GRBs without redshit the maximum allowed delay is 4 hours. For GRBs with redshift less than 0.2 the maximum allowed delay is 12 hours. After the detection of GRB 180720B the maximum delay for all Swift-BAT was loosened to 12 hours. The maximum zenith angle is 45 deg.

If all the conditions above are met, 2 hours of GRB follow-up observations are scheduled, provided visibility and observation conditions are respected. The minimum observation time allowed is 10 minutes.

The observation of VHE emissions from three GRBs, the MAGIC detected GRB 190114C [21] and the H.E.S.S detected GRB 180720B [17] and GR190829A [158] (see Sec. 2.1.3) came with valuable lessons that changed the H.E.S.S. GRB follow-up procedure aspects. The three discoveries are presented in Sec. 2.1.3. To put these observations in context, Fig. 4.3 presents a sample of successfully performed

[3] Although the *prompt* and *afterglow* observation modes take the names of physical emission phases they are not directly related to them.

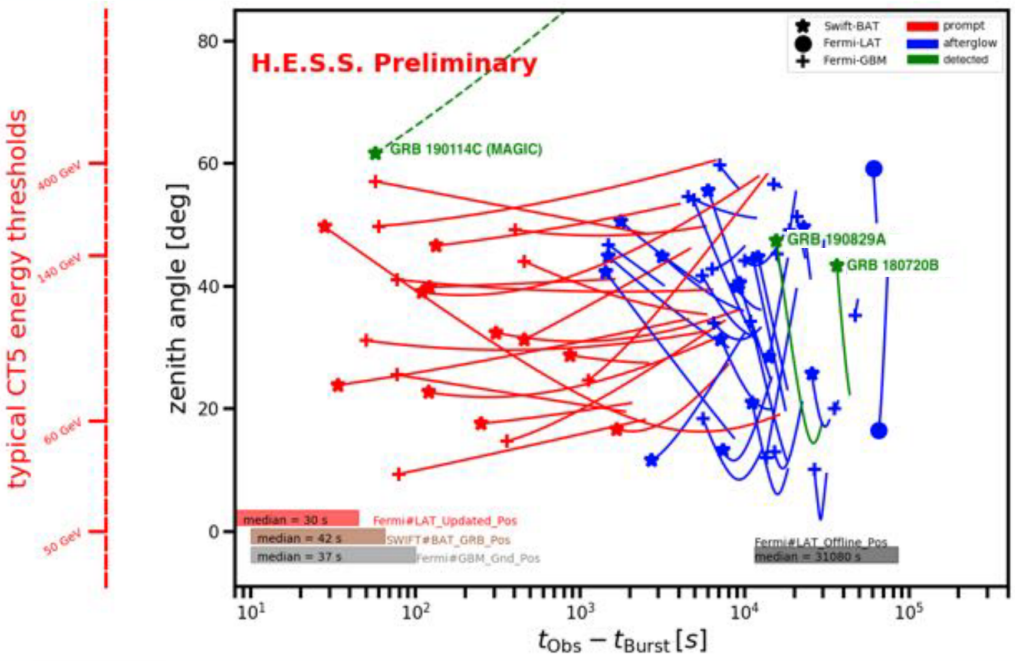

Figure 4.3: H.E.S.S. successful observation of GRBs detected by the Fermi-GBM, Fermi-LAT and Swift observatories. The plot shows the evolution of the zenith angle (y-axis) of the HR observations and therefore the variation of the energy threshold of the 28-m telescope with the observation time since the detection of the burst. Updated from [167].

H.E.S.S. follow-ups of GRBs. This plot shows that the VHE GRBs were detected at elevated zenith angle and therefore with high energy thresholds from IACTs. For the case of GRB 190114C the rapidity of the MAGIC follow-up (less than 1 minute latency) played a major role in the detection of the rapidly fading emission of the GRB that was observed in extreme conditions with elevated moon light levels and high zenith angle. This observation showed that VHE emission from GRBs could reach the TeV level especially in the early afterglow phase. The H.E.S.S. VHE GRBs were observed with large observation delays (several hours of latency) showing that GRB VHE emission could last for several hours/days.

I was fortunate to be part of the early team that made the GRB 190829A VHE emission discovery. I assisted in the MWL analysis that helped in the understanding of the GRB and its host galaxy. In the following I summarize my contribution to the discovery.

4.2.1 GRB 190829A, my contribution

Right after the detection of GRB 190829A, I had the opportunity to join the effort of a newly formed task group within the HESS GRB team by verifying that the detected VHE emission is in fact from the GRB and not from another source in the telscope's FoV, a check that must be done upon the detection of any

emission from GRB or GW transient events. For that, I explored known sources around the GRB region. After reconstructing the localisation of the GRB from the data of the first night of observations, I found that the host galaxy SDSS J025810.28-085719.2 [359] lies within the 2 σ contour of the localisation region of the emission. I note that the reconstruction of the source position is done with a log-likelihood maximization technique providing a source position with a better angular resolution than the instrument's PSF. The technique takes into consideration a source morphology shape estimation, here a point-like source, and the instrument's angular response to compute an expected number of events per bin, that will be compared to the observed number of events and the difference will be minimized against the morphological parameters. More details are provided in Sec.7.6 of [101]. Fig. 4.4 shows the excess, the high energy sources (AGNs) and the H.E.S.S. localisation of the emission around the region of the host galaxy. This map shows that the excess observed is not related to known VHE sources in the H.E.S.S. FoV.

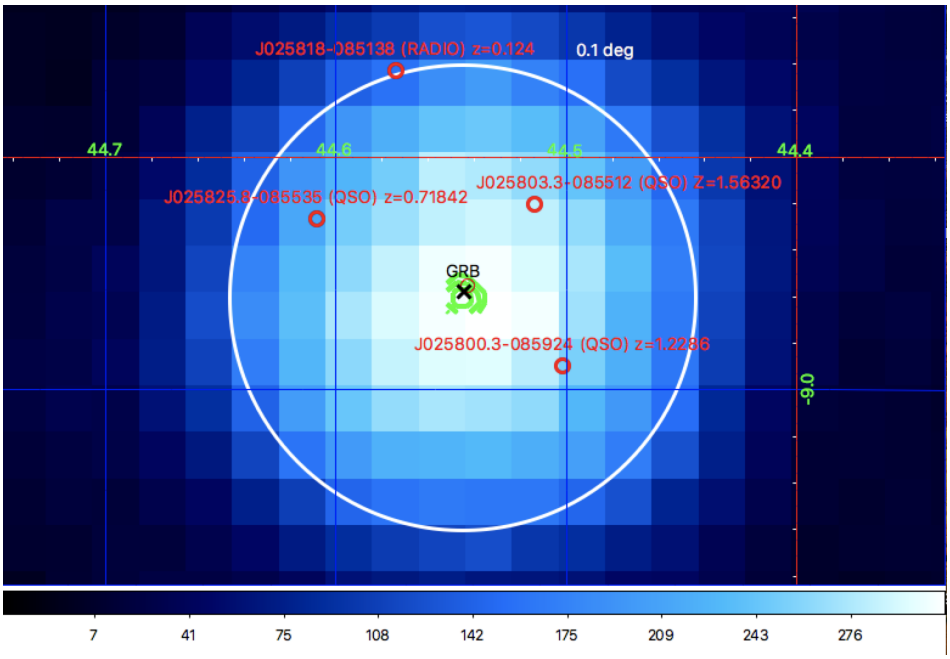

Figure 4.4: Preliminary excess map from the H.E.S.S. observations of GRB 190829A during the first night. The white circle represents 0.1 deg in the sky corresponding roughly to the H.E.S.S. PSF. The black X marks the GRB location [83]. The green contours represent the 68%, 95% and 99% localisation contours from the H.E.S.S localisation fit. The thin red circle is the host galaxy of GRB 190829A and the thick red circles represent the catalogued high energy sources in the region of interest [19].

The very high flux of the incoming VHE γ-ray photons of this GRB can be visualized in an animation that I created of the incoming gamma-like events detected by H.E.S.S. during the first night of observation. The animation can be found in: `https://www.dropbox.com/s/mh4jcovrtce22kr/GRB190829A_`

HESS_N1_FM.mov?dl=0. It shows a fraction of the incoming gamma-like events in the telescope's FoV by fast-forwarding through the first night of observation. The region around the GRB is highlighted and one can almost see without any background subtraction the excess of gamma-like events inside the region of the source.

The X-ray observations showed high levels of absorption from the GRB. Moreover, the GRB is located at the edge of its host galaxy which is in contrast with the usual trend where long GRBs are localised closer to the dense center of their host galaxies. I gathered information on the host galaxy to better understand the absorption in different wavelengths. I found relevant information in several galaxy catalogs. Amongst these information I find in the GSWLC catalog [323] the mass of the host galaxy $\mathrm{M} = 1.79 \times 10^{11} \pm 1.03 \mathrm{M}_{\odot}$, the star formation rate from mid-IR and UV/optical data (UV/optical data only) $\mathrm{SFR} = 1.64 \pm 1.256 \mathrm{M}_{\odot}/\mathrm{year}$ ($\mathrm{SFR} = 2.48 \pm 1.267 \mathrm{M}_{\odot}/\mathrm{year}$) [324] [322]. The host galaxy is in fact a spiral galaxy with similar properties (e.g. metallicity and age) to the Milky Way. To understand the high absorption in the X-ray band, I looked at X-ray, UV and IR images of the host galaxy overlaying the GRB localisation region in order to check if the GRB lies in a dense dust star forming region. The only publicly available images at the time came from wide FoV surveys, and showed no particular star forming regions around the GRB that is located in the outermost regions of the galaxy. This led us to believe that the absorption is probably not from the region around the GRB inside the galaxy. The GRB region was later on imaged with high resolution telescopes like the Hubble Space Telescope (HST). I also compare the host galaxy of GRB 190829A to a sample of SWIFT GRB host galaxies from [68]. In Fig. 4.5, I show that the mass and SFR of the GRB 190829A host galaxy lies within the normal range of other host galaxies and is in fact not exceptional.

I was also part of the team that was leading the UVOT UV and optical analysis for GRB190829A within H.E.S.S. The main purpose is to estimate the host galaxy flux from UVOT data to check for rising emission from the supernova (since the GRB was caused by a star core-collapse) at the time of the H.E.S.S. observation. I identified four symmetrical regions of the galaxy to check for excess emission. The four regions are presented in the left plot of Fig. 4.6. In order to determine these regions, I used a DSS image in the 535 nm band (green) and chose 3 circular regions of 5 arcsec diameter (R2, R3 and R4) which have the same distance as the GRB from the center of the host galaxy. The fourth region is centered on the GRB position (R1) with the same diameter. The emission levels from the four

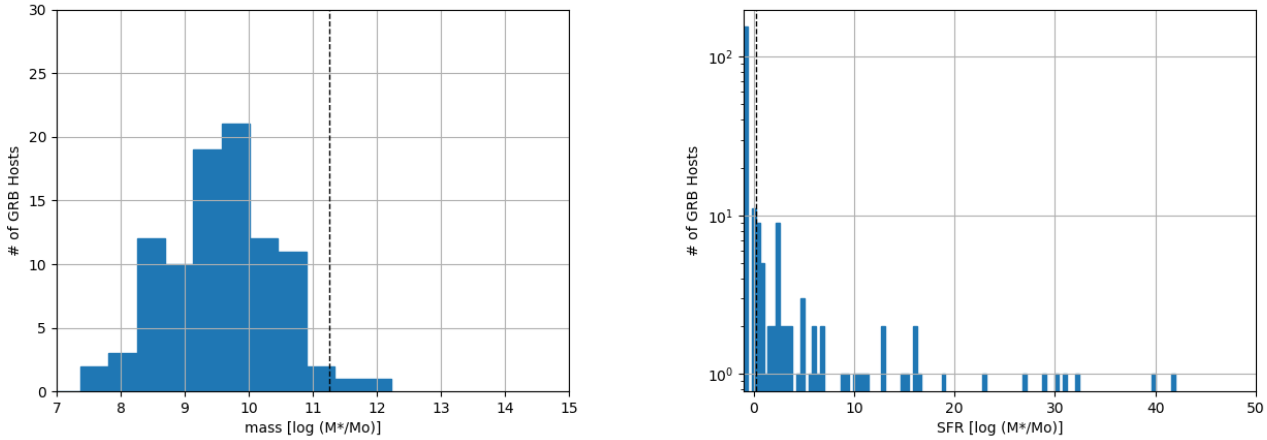

Figure 4.5: Mass (left) and star formation rate of host galaxies of GRBs detected by Swift. The dotted lines represent values for the GRB 190829A host parameters.

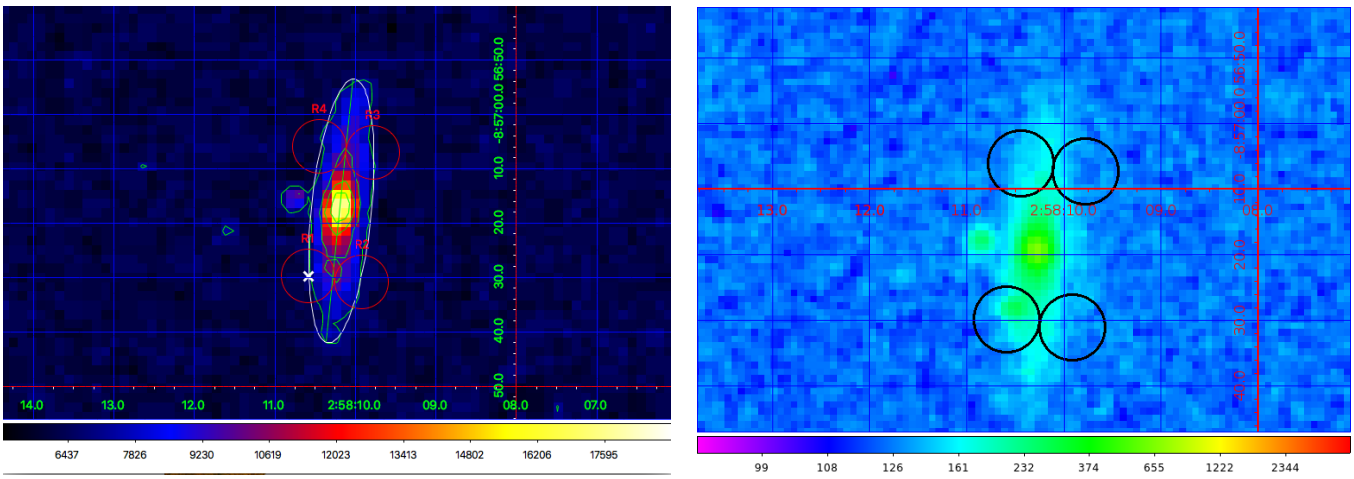

Figure 4.6: DSS image in the 535 nm band (left) and a summed Swift-UVOT image post GRB 190829A detection (right) with an overlay of the 4 regions where the Swift-UVOT flux is determined. R1 is the region of the GRB and the remaining three regions are symmetrically distant to the center of the host galaxy.

regions are: $\mathrm{R1} = 7.15 \times 10^{-13} \pm 1.40 \times 10^{-14}\, erg\, cm^2\, s^{-1}$, $\mathrm{R2} = 4.29 \times 10^{-13} \pm 1.91 \times 10^{-14}\,\mathrm{erg\,cm^2\,s^{-1}}$, $\mathrm{R3} = 3.51 \times 10^{-13} \pm 1.29 \times 10^{-14}\,\mathrm{erg\,cm^2\,s^{-1}}$ and
$\mathrm{R4} = 5.70 \times 10^{-13} \pm 1.48 \times 10^{-14}\,\mathrm{erg\,cm^2\,s^{-1}}$. The flux values from R1 and R4 are higher than that from R2 and R3. In R2 and R3 the levels agree within 3.4 σ and in R1 and R4 within 5.8 σ. It turned out that the differences in fluxes are due to the difference of the emission from the host galaxy within the analysis regions in the UVOT image shown in the right plot of Fig. 4.6. R2 and R3 are mostly centered on the background, while R1 and R4 include more emission from the host galaxy. The UVOT flux from R1 is shown in orange in Fig. 4.7. The UVOT flux level dropped then was constant during the H.E.S.S. observations. Even though it is approximate, the latter was enough to deduce that the emission in the GRB region is not due to the rise of a supernova during the first H.E.S.S. observation window, especially that the values agree with the overall plateau emission from the galaxy.

From the flux level contours in the DSS image of Fig. 4.6, the host galaxy appears as an ellipse. By applying $\sin \mathrm{i} = \sqrt{1 - (\mathrm{b/a})^2}$, where b and a are the minor and major axis respectively, I find that the galaxy is seen on-edge with an angle $\mathrm{i} \sim 77\,\mathrm{deg}$. Finally, after exploring several extinction lines in our own galaxy and considering several galaxy profiles for the host galaxy, we concluded that the extinction due to both the edge-on position of the host and the GRB material greatly affected the optical/UV data and we would need further expert analysis in order to use it in the modeling. A preliminary un-published light curve of the γ-ray, X-ray and UV data from GRB 190829A is shown in Fig. 4.7.

Interpretation of the GRB 190829A H.E.S.S data: The interpretation of the H.E.S.S. data is performed by other people in the GRB group and is presented in [158]. I give here a summary of this interpretation. Due to the proximity of GRB 190829A, EBL absorption effects that increase with distance (see Sec.1.1.2) are very small (see Fig.2 of [158]). The small absorption effects lead to a precise measurement of the flux with low levels of uncertainty. This lead, for the first time to precisely measure the intrinsic spectrum of the VHE emission from the GRB. The theoretical modeling of the GRB emission is shown in Fig. 4.8 for the first (top) and second (bottom) night of observations. The SSC modeling presented by the blue dashed lines does not fit well the data. In the standard GRB theory, synchrotron emission up to VHE γ-rays is not easily possible, since a maximum energy is placed on the electrons and it would require a high-efficiency process to accelerate multi PeV electrons in the magnetic fields [201]. However, by removing this maximum energy constraint, the synchrotron emission extended to VHE energies seems

to fit well ($> 5\,\sigma$) the observed spectrum as shown by the orange dashed lines in Fig. 4.8. These new results have revealed unexpected similarities/connection between the X-ray and VHE γ-ray emission, which were expected to have separate origins. This study highlights the need for further studies of VHE GRB afterglow emission.

Updates to the H.E.S.S. GRB program: In summary, five main lessons can be learned from GRB 1807209B, GRB 190114C and GRB 190829A:

- The VHE emission from GRBs can last several hours to days after the burst.
- The VHE and X-ray emission show similar temporal evolution and flux levels.
- VHE emission can be detected from GRBs up to several TeVs.
- For GRB 190829A, the X-ray light curve shows an unusual rise in the flux levels in the early afterglow (see Fig. 4.7). This means that even though the GRB is not particularly bright, the VHE flux level can still rise in the afterglow phase and might be detectable by IACTs.
- GRB 190829A VHE and MWL spectrum challenge the SSC paradigm.

Due to the lessons learned from the VHE GRBs detections with IACTs, the H.E.S..S GRB program got updated in 2019 and 2020. The main changes include:

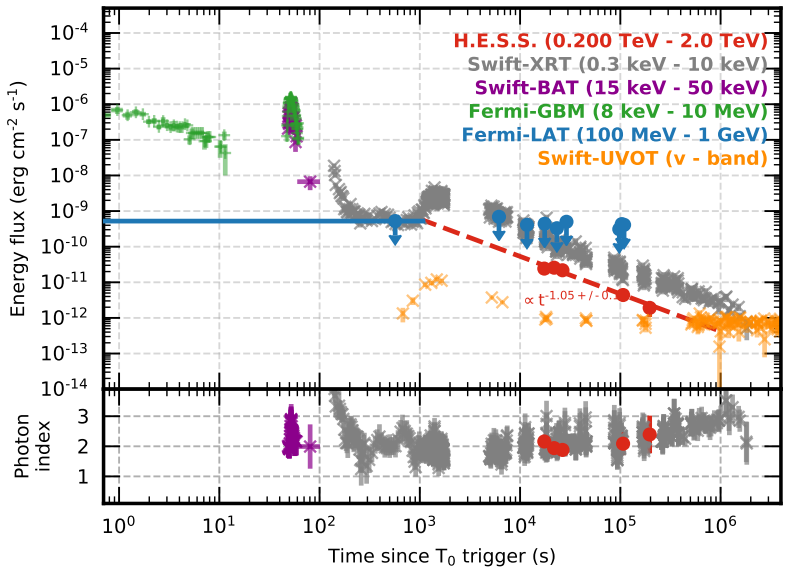

Figure 4.7: MWL light curve from GRB 190829a observations. The H.E.S.S. data was taken after the rise and drop of the UV emission from the GRB. From private communication with the GRB team.

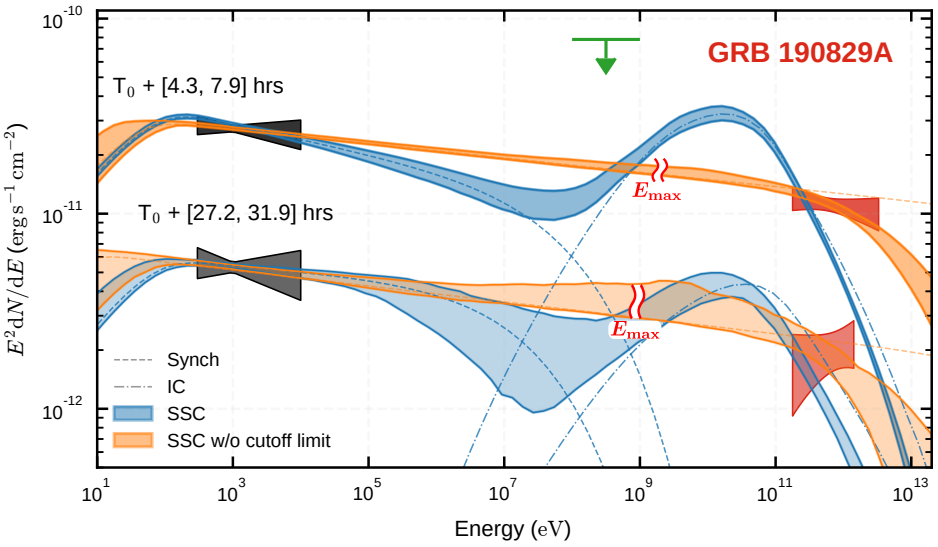

Figure 4.8: Theoretical multi-wavelength models of the first and second night data on GRB 190829A. The black region shows the spectrum and uncertainty of the Swift-XRT data, the green arrow upper limit is from Fermi-LAT (available only for the first night [290]), and the red region is the H.E.S.S. intrinsic spectrum and its uncertainty (statistical only). The shaded areas represent the 68% confidence intervals determined from the posterior probability distribution of the Markov chain MC parameter fitting for the standard SSC model (light blue) and for the synchrotron-dominated model (orange); the latter model does not impose a synchrotron cut-off energy (shown by $E_{\rm max}$). The synchrotron components of the two SSC models are indicated by dashed lines, while the dash-dotted lines show the IC components. These lines show the emission level when neglecting the internal gamma-gamma absorption. The upper curves are for the first night and the lower curves the second night. From [158].

- Relying on high levels of X-ray flux to trigger on potential VHE GRBs, extending the maximum observation delay to 24h for X-ray bright GRBs and extending the observation duration to the entire night for all GRBs instead of 2 hours.

- Creating a link between H.E.S.S. and ATCA to trigger radio follow-up observation on potential VHE GRBs detected by H.E.S.S in the real-time analysis.

- Implementing a tiling strategy on poorly localized Fermi-GBM GRBs in order to cover the localisation region.

These updates and my contributions to the program are detailed in Appendix A.

4.3 The H.E.S.S. GW follow-up plugin

From the fact that the emission in the afterglow phase in GRBs is showing a steady decrease in general, the need for rapid follow-up observations in order to detect electromagnetic counterparts of GWs at VHE energies in the early, bright phase becomes clear. In order to build the H.E.S.S. GW plugin[4] which is also described in [45], I focus on the the combination of rapidity and GW event coverage efficiency.

The GW follow-up algorithms introduced in Chap. 3 are provided in the GW follow-up plugin integrated into the H.E.S.S. transients follow-up system. This system reacts to all publicly available GW alerts. For each signal detected by LVC, the full sequence of notices is processed to find follow-up opportunities. During the run O3 these included *preliminary*, *initial*, *update* and *retraction* notices. In preparation of the run O4, an *Early Warning* notice has been added in June 2020 [337] (see Sec. 2.2.3).

The progress of an incoming event throughout the decision tree outlined in Fig. 4.9 is monitored via email alerts at all major decision points. This allows the expert on call (me) to follow all steps remotely.

As mentioned in Sec. 4.1, upon the arrival of an alert, the H.E.S.S. ToO alert system assigns a science case to it. For GW alerts, three science cases are currently available: BNS which also concerns all CBC mergers involving at least one NS (BNS, NSBH and MassGap), BBH and Burst alerts. Burst events are un-modelled GW events that can be caused by rare but interesting sources like nearby supernovae. Their reconstruction does not include a distance estimate of the event. Unlike for BNS mergers, most models do not predict a sizable EM emission associated to BBH mergers. Therefore, an order of decreasing priorities in the H.E.S.S. response system is: BNS, Burst then BBH. Each alert is evaluated respectively as a separate relevant science case in the `Alert identification` module. The H.E.S.S. ToO alert system will assess the alert using the cuts associated with the science case. The precise filtering criteria outlined here have been iterated several times during O2 and O3. I report the final values that were used during O3. These cuts are assessed in the `Filtering` and `Special cuts` modules using information stored in the `VoEvent` module against the values contained in the configuration files for each type of alert.

Science based decisions

The first step after the reception of a new alert is the definition of the relevant science case. The selection is done based on the information provided in the VoEvent message emitted by LVC starting with the GW

[4] The plugins mentioned here are not scripts or modules like the ones described in Sec. 4.1, they are instead additions to the overall Too follow-up system that include modifications and updates of all the modules.

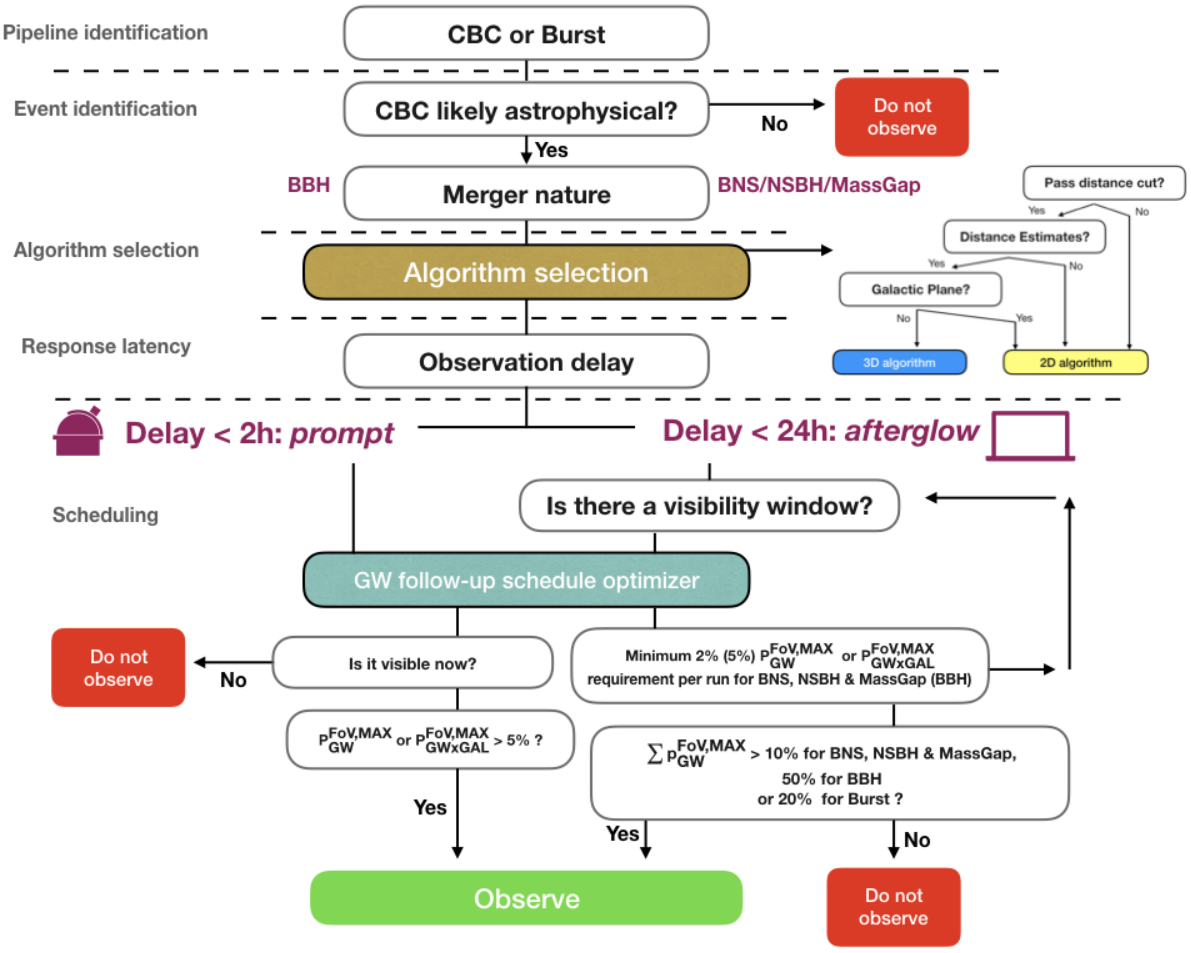

Figure 4.9: Schematic overview of the decision tree used in the automatic response of H.E.S.S to GW events.

detection pipeline to determine if it is a Burst or a CBC alert. CBCs are then evaluated based on their probability to be likely astrophysical in origin. At this step, events with high noise probability ($>$ 50%) that are less likely to be astrophysical are discarded.

Depending on the BBH probability parameter in the VoEvent alert message, the alerts are processed either as being emanating from a BBH merger ($\mathrm{probability\,BBH} > 50\%$), or a merger including at least one neutron star (BNS science case). The system then downloads the corresponding localisation map and proceeds with the selection of the optimal scheduling algorithm, i.e. the choice of a 2D or a 3D strategy (see Chap. 3).

Choosing a 2D or 3D strategy

Considering the completeness of the GLADE galaxy catalog (cf 3.3), only GW events having a mean distance $<$ 150 Mpc and having their GW map hotspot outside the *avoidance zone*, indicating the Galactic Plane, are analyzed using a 3D approach. Events lacking distance information or not fulfilling the mentioned criteria are treated with a 2D approach. Only in the case of a 3D approach the galaxy catalog is loaded. The localisation map is then forwarded to the GW follow-up schedule optimizer that derives suitable observational strategies using the algorithms described in Chap. 3.

For events selected for a 2D treatment, the `PGW-in-FoV` algorithm is used in the GW follow-up schedule optimizer for its better suitability for medium FoV instruments like H.E.S.S. For events that allow a full 3D analysis, the `PGalinFoV` algorithm is used due to its faster reaction time to small maps (see Sec.3.5.2 and Fig. 3.17). `PGalinFoV` is also better suited than `PGalinFoV-PixRegion` for single *prompt* reaction since it does not include the additional time consuming step of computing the 2D pixel observational seeds grid. These algorithms are based in the `Special cuts` module and use functions from the `GW tools` module. More information on the *prompt* reaction are given in the following.

Prompt alerts

For alerts that arrive during observation time and that would therefore allow for prompt observations, a rapid response is of utmost importance. Therefore, the GW follow-up schedule optimizer is divided into two modules: *prompt* and *afterglow*. The *prompt* module is available for low latency alerts (*preliminary* and *initial*), the *afterglow* module handles also *updates*. Instead of calculating the entire schedule for the available dark-time period, the *prompt* module only computes the first P_{GAL} or P_{GW} at the time of the arrival of the alert, taking into consideration the visible parts of the sky at that time. The obtained

observation direction is then assessed by considering zenith angle, darkness, coverage and time delay conditions in the `Visibility` module. If at the end of the decision making tree all observational criteria are met, observations are forwarded automatically to the data acquisition and slew control system of H.E.S.S. Without the need for time consuming human interventions the telescopes automatically stop the current data taking, slew to the derived pointing and start observations. Meanwhile, the *afterglow* module independently computes an entire schedule for the full available observation time of the current night by selecting the most probable position for each possible observation window in an iterative way.

Afterglow alerts

For alerts that arrive outside H.E.S.S. observation time, the *prompt* module will discard immediate automatic observation possibilities and the *afterglow* module will schedule observations for the upcoming night as described above. The observation schedule will be automatically distributed by email to the shifters and the experts on call, allowing human vetting if needed. At night the observations are added to the automatic observation scheduler

H.E.S.S.-related operational decisions

In addition to the scientific decisions described above, an alert has to pass H.E.S.S.-related operational cuts in order to be followed. In general, the aim of H.E.S.S. follow-up observations is to detect or constrain VHE emission associated to the observed GW events. Given that mergers including at least one neutron star are the most promising to show electromagnetic emission, I implemented rather loose filtering cuts to allow for exploratory searches aiming at the detection of a VHE counterpart associated to the GW event. The criteria within the H.E.S.S. GW program require a coverage of at least 10% of the localisation uncertainty region to trigger follow-up observations of a BNS, NSBH or MassGap event. This minimum coverage has to be reached within 24h of the detection of a GW event. These cuts automatically allow the follow-up of the most interesting events with good localisation and filter out the ones with large localisation uncertainties.

The aim of the follow-up in BBH mergers, for which electromagnetic emission is less probable, is mainly to constrain the VHE emission. This assumption leads to more stringent requirements on coverage achievable with the follow-up observations in order to be able to provide upper limits for most of the possible localisation/emission region. The minimum requirement used within H.E.S.S. for BBH follow-up is 50% of the GW localisation map.

Start time	Ra	Dec	PGAL	Observation window	Priority
2017-08-17 17:59	196.88	-23.17	0.72	2017-08-17 17:55 $\rightarrow$ 2017-08-17 18:39	0
2017-08-17 18:27	198.19	-25.98	0.16	2017-08-17 17:55 $\rightarrow$ 2017-08-17 18:48	1
2017-08-17 18:56	200.57	-30.15	0.05	2017-08-17 17:55 $\rightarrow$ 2017-08-17 19:01	2

Table 4.1: Example of the observation schedule of the GW170817 follow-up. The priority of the pointings is higher in ascending order.

Burst alerts fall between the two CBC categories and a minimum coverage threshold of 20% is chosen for their potential promising interest. Alerts that do not pass the filtering cuts are discarded.

In general a minimum requirement (2% for BNS and 5% for burst and BBH alerts) coverage per observation (P_{GAL} or P_{GW}) is applied for all GW alerts. For events arriving during the night and having observational delays $<$ 2h, the minimum GW coverage required in order to trigger an automatic *prompt* observation on a position in the sky without waiting for the full schedule to be computed has to be $> 5\%$ for the first pointing. If these values are not met, the observations will have to be performed in *afterglow* mode if the minimum requirements are reached. During testing (trials), I found that in general, if H.E.S.S. is not capable of covering the minimum requirements with the first pointing, it will not be able to reach the minimum allowed coverage of the entire map. This value will serve to limit the times where H.E.S.S. observations are interrupted due to the *prompt* follow-up of potentially "uninteresting" GW alerts that do not pass the full *afterglow* requirements.

Output of the H.E.S.S. GW module

Similarly to the offline schedule described in Sec. 3.4, the output produced by the implemented GW follow-up tools contains for each observational position the best time to observe and the available observational window throughout the night. This allows for some flexibility in the observations in case the best time could not be respected. All pointings are ranked according to their achieved coverage. The observers are presented with both a table like Tab. 4.1 summarizing the proposed scheduling as well as with graphics that illustrate for example the zenith angle evolution of all scheduled positions as illustrated in Fig. 4.10.

Experts on call are assigned to assist the observers. Their responsibility is to monitor and modulate the automatic response if needed. Offline tools are developed for rapid human intervention (see 3.4). In the case of a GW map *update* that arrives after GW ToO observations have already started, a new schedule is automatically computed. These *update* maps can also be correlated with external triggers (see RAVEN

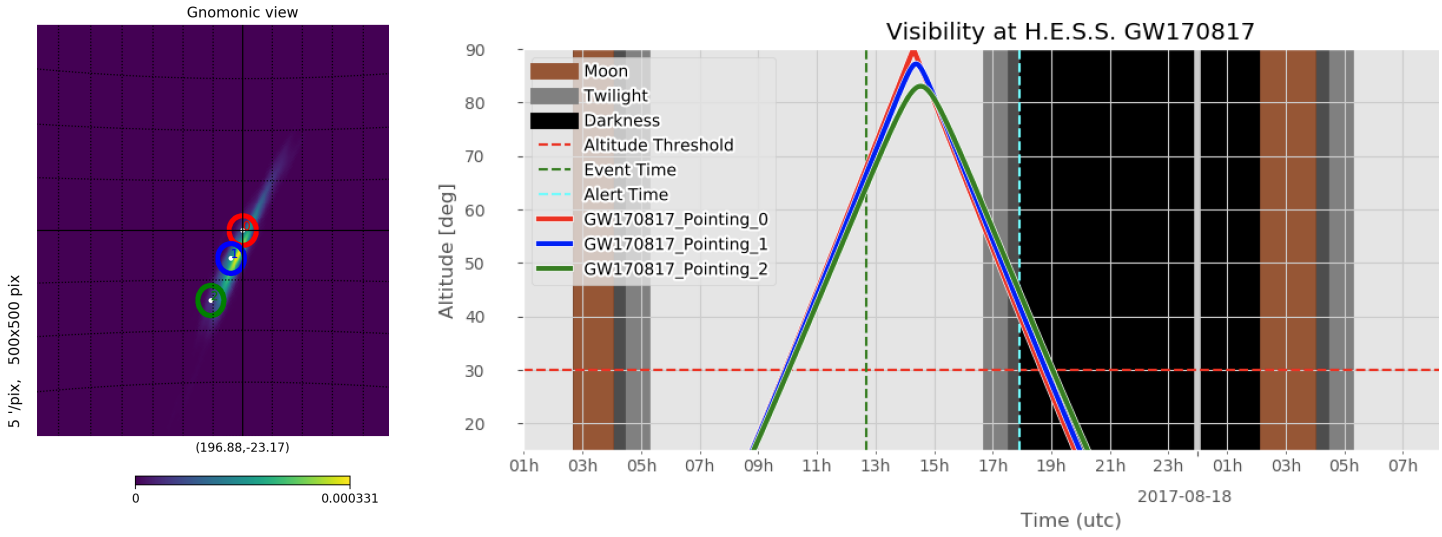

Figure 4.10: Example of the visual aid provided by the GW follow-up framework for the case of GW170817. On the **left** the scheduled pointings are superimposed on the GW map with their respective number and on the **right** the zenith angle evolution of their corresponding position throughout the night is shown.

in [213]). For example the localisation region of a GW alert can be cross-matched with the localisation region from a Fermi-GBM GRB occurring at the same time. An *update* of the GW localisation map is then distributed. The expert on call has the ability to modify this schedule and take into consideration previous observations occurring during the night. Additional tools are considered in order to monitor the detection of transients and summarize information of known γ-ray sources in the GW localisation area, like Astro-COLIBRI [301][5].

In case a signal with a significance of more than 5 σ is found by the real-time analysis, the observers will re-observe the corresponding position after making sure that the signal does not originate from known VHE sources. VHE sources can be found in the TeVCaT [367] catalog for example.

4.3.1 GW plugin response time

Since we did not have immediate, *prompt* H.E.S.S. GW follow-up during O2 and O3, I use simulated, *mock* alerts in order to quantify the speed of the response of the H.E.S.S. alert system to GW alerts. *Mock* alerts are distributed by LVC as test alerts of simulated GW events that can be used by observatories to commission their follow-up programs. From these *mock* alerts, I select *preliminary* and *initial* alerts of simulated nearby BNS events that arrive during the night and only consider alerts that pass all observation filtering criteria with a 3D coverage. The results presented in Fig. 4.11 show that the H.E.S.S. average response

[5] https://astro-colibri.com/#/

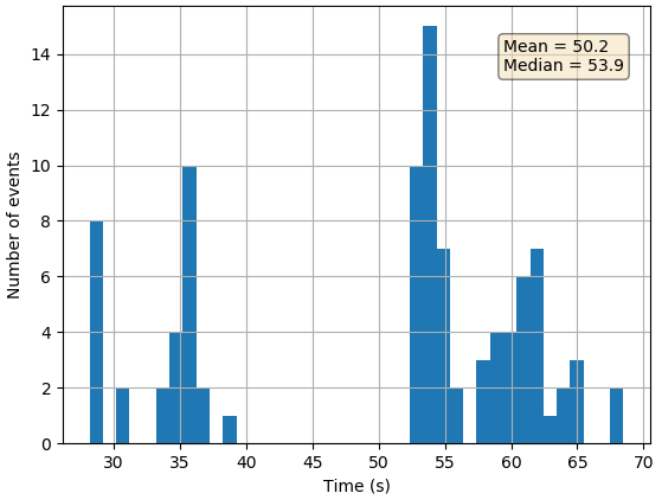

Figure 4.11: The H.E.S.S. *prompt* 3D response time to GW Mock alerts from July to October 2019 excluding telescope slewing time. Only alerts passing all filtering requirements are considered.

time is $\sim$50 seconds for this type of alerts, that corresponds to the most interesting alerts for H.E.S.S. This represents the time needed for all steps to be executed in the *prompt* decision tree shown in Fig. 4.9 since the reception of the alert to the distribution of the observational schedule to the shifters, the GW expert team and, most importantly, the DAQ system steering the telescopes. As expected, responses taking more than 50 seconds correspond to events with high resolution localisation maps (e.g. $N_{side} = 2048$). As explained in Sec. 3.5, these maps have a larger loading time. Low resolution skymaps with $N_{side} < 2048$ are clustered at short calculation times on the left side of the histogram ($< 40\,s$). The additional telescope slewing time is depending on the distance between the current observations and the target as well as the operation mode. Allowing tracking through zenith in *reverse mode*, the 28-m H.E.S.S.-II telescope can be on target in less than one minute [166]. We can thus expect that H.E.S.S. is able to start observations of a promising close-by GW target often within 1 minute and for the large majority of cases within less than two minutes after receiving the alert.

Taking into account additional effects that may delay the VHE emission, e.g. off-axis viewing angles as seen in GW170817, multi-wavelength information and dedicated long-term observations ranging from several hours to weeks are necessary. An example of such a campaign is presented in [18]. These campaigns are scheduled outside the automatic system presented here, and the experts rely on MWL information that can be distributed via ATels or GCN circulars.

4.4 H.E.S.S. follow-up of GW events

During O1 and O2 a total of 10 BBH and 1 BNS candidates were reported [4]. In O3, 80 alerts were issued including 24 events that were later classified as noise and retracted, 3 terrestrial non-retracted events, 52 CBC and 1 unmodeled Burst candidate [226]. Due to the relatively long time delays in the emission of the GW alerts and the large localisation uncertainties during O1 (only the LIGO detectors operated during O1) no observations were conducted by H.E.S.S. in this initial period. H.E.S.S. successfully performed follow-up observations of six GW events during O2 and O3. These follow-up observations are also presented in [45].

4.4.1 GW events observations during O2

The H.E.S.S. GW follow-up tools were first applied to real GW data in a technical trial run using the burst alert G284239 identified by LIGO (Hanford + Livingston) although with relatively low significance (e.g. a false alarm rate < 4 per year) at 2017-05-02 22:26:08 UTC. The four observation runs obtained during this ToO were influenced by bad weather conditions but allowed to streamline the follow-up procedures and the communication between offsite experts and the onsite crew that led to the introduction of the full available observation window for each observation to allow flexibility in scheduling when weather and technical difficulties delay observations. The obtained pointing pattern has been made available in GCN #21084 [151].

GW170814 is a binary black hole merger event that was detected by the two LIGO and the Virgo interferometers [9]. This was the first time that a GW event was detected by all three observatories and the added independent baselines from Virgo reduced the localization uncertainty significantly. H.E.S.S. started follow-up observations on the 16^{th} of August 2017. Observations were obtained during three consecutive nights as first science observations with H.E.S.S. following a GW event. The obtained 2D coverage using the `Best-pixel` algorithm is shown in Fig. 4.12. The pointing pattern shown in this figure has been derived assuming a circular FoV with a radius of 2.5 deg, corresponding to the 12-m telescopes. The observations were carried out as planned. The obtained observations cover 95% of the final localisation map of the event and therefore allowed for the first time to derive meaningful upper limits on the VHE γ-ray flux. As noted in Chap. 3, the used `Best-pixel` algorithm is causing significant overlap between the

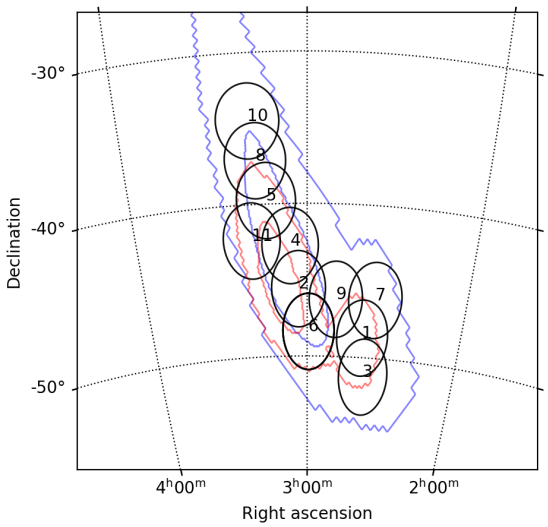

Figure 4.12: H.E.S.S. coverage of GW170814. The blue contours represent the 90% and 50% localization regions for the BAYESTAR maps that triggered the telescopes distributed initially. The red contours represent the 90% and 50% localization regions for the updated LALInference maps. The black circles represent the 2.5 deg FoV of performed observations by chronological order.

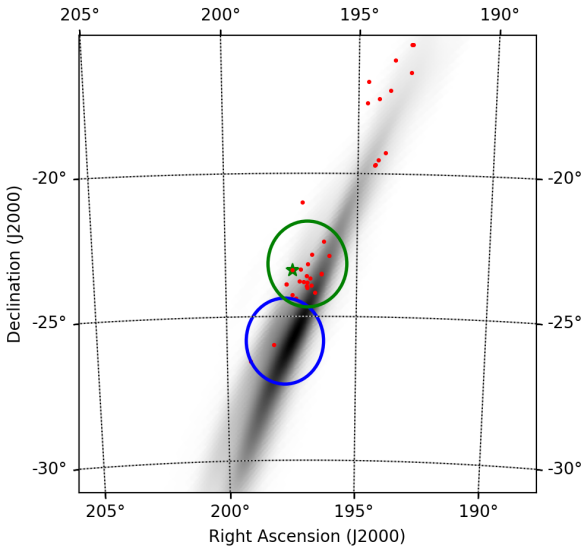

Figure 4.13: GW170817 first LALInference localisation map. The green and blue circles represents the 1.5 deg radius FoV of the first scheduled observation using 3D algorithms and 2D algorithm respectively. The green star represent the host galaxy NGC4993 (where the counterpart was found) and the red dots represent the highest ranking potential host galaxies in the region of the GW event.

different pointings, a drawback that is corrected by the `PGW-in-FoV` method. The related improvement is illustrated for example by the fact that a `PGW-in-FoV` scheduling would have been able to achieve a similar coverage with 2 fewer observations. I presented preliminary analysis results of the obtained H.E.S.S. data on GW170814 in [46]. In order to exploit the high sensitivity and low energy threshold, the preliminary analysis of the data is relying on data from the 28-m telescope. This leads to a reduction of the effective FoV available for the final results, a fact that has been taken into account subsequently by conservatively assuming a 1.5 deg FoV radius for scheduling GW follow-up observations during O3. Applying this value to GW170814, the VHE coverage of the final localisation area reaches 68%.

Multi-messenger astrophysics with GWs started with the detection of the binary neutron star merger GW170817 on August 17, 2017 [11]. The event identified by LIGO occurred at 12:41:04 UTC. Located at a distance of 40^{+8}_{-14} Mpc, it is still the only GW event that was located at a small enough distance for the efficient use of a galaxy catalog during the scheduling. A BAYESTAR-reconstructed 3D localisation map using data from all three interferometers was published by LVC at 17:54:51 UTC [214]. The 90% region

of the localization uncertainty had a size of 31 deg^2 and was used as input for the `PGalinFoV` algorithm. H.E.S.S. data taking started on August 17 at 17:59 UTC when the necessary darkness conditions were reached. This was only about 5 minutes after the publication of the localisation of the GW event. As illustrated in Fig. 4.13, the first pointing position generated by the 3D algorithm covered the host galaxy in spite of it being located at the edge of the skymap away from the GW hotspot. Demonstrating the superiority of the 3D galaxy based approach, a 2D `PGW-in-FoV` algorithm would naturally focus on the hotspot and would therefore have missed the location of the merger. Thanks to the efficient and rapid reaction, H.E.S.S. was the first ground based facility to get on target and take data of the BNS merger, several hours before the discovery of the optical counterpart. Observations of GW170817 with H.E.S.S. then continued over several days until the direction was not observable any longer. An extensive additional campaign covering the peak of the X-ray emission from the source started 4 months later in December 2017. Analysis and interpretations of these data are discussed in [16] and [18] respectively and in Chap 6.

4.4.2 GW events observations during O3

S190512at [215] is the first GW event detected during the physics run O3 to be well localised with a low zenith angle for H.E.S.S. Since the minimum required coverage was not achieved, follow-up observations were scheduled manually in *afterglow* mode for testing and commissioning purposes. A preliminary version of `PGW-in-FoV` algorithm has been used to determine the pointing pattern. The planned observations of S190512at covered 34% (P_{GW}) of the *initial* localisation map considering a FoV of 1.5 deg radius. Influenced by bad weather (clouds) and technical issues not all of the scheduled observations could be obtained, thus leading to a coverage of 21% of the *updated* map [216]. Both, the scheduled and the obtained pointing patterns are illustrated in Fig. 4.14.

S190728q is the second event followed by H.E.S.S. during O3. The *initial* alert [217] classifying this event as a NSBH merger was received on 2019-07-28 07:39:04 UTC. Within a minute, the H.E.S.S. ToO alert system, evaluated the possibility of a *prompt* reaction and sent out a notice and a schedule to the H.E.S.S. GW team, the expert on call, and the onsite shifters. Four observation runs were scheduled to be obtained later that night covering $\sim$32% of the *initial* skymap. At 2019-07-28 20:29:12 UTC an *update* [218] was received after the first follow-up observation had already started and a new schedule containing 6 new observational positions was automatically distributed to the people mentioned above. A

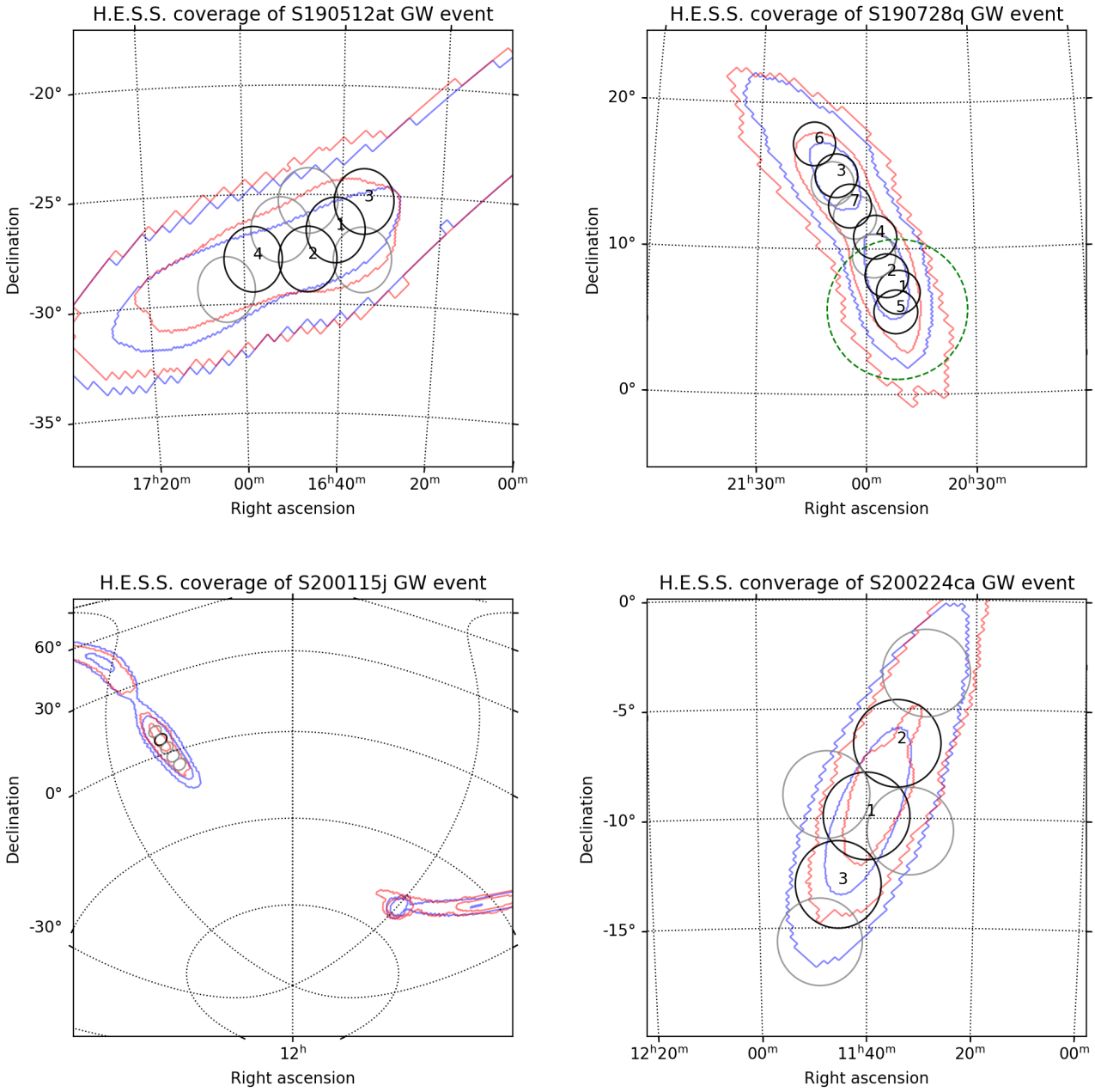

Figure 4.14: H.E.S.S. coverage of O3 GW events. The blue contours represent the 90% and 50% localization regions for the BAYESTAR maps distributed in the initial notices that triggered the follow-up. The red contours represent the 90% and 50% localization regions for the updated LALInference maps. The grey circles represent the H.E.S.S. FoV of scheduled observations covering the initially distributed maps and the black circles represent the FoVs of successful observations by chronological order. The FoVs have a radius of 1.5 deg for S190512at and S190728q and 2 deg for S200115j and S200224ca. For S190728q the green dashed circle represent the neutrino uncertainty region.

total of seven positions were observed during the night. The observations covered a part of the uncertainty region of a nearby neutrino candidate alert that was emitted by the IceCube collaboration during the same day [174]. The neutrino candidate is found within a -360 seconds time offset from the GW event time, has a localisation uncertainty of 4.81 deg and a significance of 1.8 σ. Moreover, a candidate optical transient was reported by ZTF, ZTF19abjethn [394]. Initially, we have foreseen to schedule four additional runs on the optical transient. They were cancelled after the dissociation [395] from the OT to the GW event. All scheduled positions were observed by H.E.S.S. [152] and allowed to cover 64% of the total P_{GW} of the *updated* GW localisation region considering a FoV of 1.5 deg radius. S190512at and S190728q are confirmed as BBH merger events and their properties can be found in the GWTC-2 catalog [13] under GW190512_180714 and GW190728_064510 respectively.

In the end of 2019, the large 28-m H.E.S.S. telescope underwent a camera upgrade and observations were carried out by the remaining four 12-m small telescopes that have a larger FoV of 2.5 deg radius. Taking this into consideration, the FoV parameter in the H.E.S.S. GW follow-up configuration has been changed from 1.5 to a conservative 2 deg radius for the remainder of O3. Moreover, following reassessement by the observations committee, responsible for the H.E.S.S. yearly observation schedule, the minimum allowed P_{GW} coverage per observation has been reduced to 2% for mergers involving a NS. With these new conditions H.E.S.S. managed to observe two additional GW events before the early stop of O3 on March 27, 2020.

S200115j is a NSBH merger detected on 2020-01-15 at 04:23:09 UTC [222]. Five observations were derived by the `PGW-in-FoV` algorithm. These would have allowed to cover 25% of the *initial* localisation region. Due to bad weather (clouds), only one run could be taken. It covers 2.4% of the *updated* map [223].

The last GW event observed by H.E.S.S. before the end of O3 is S200224ca [224], a BBH merger. The alert arrived during the night but because of rain the telescopes were parked in and *prompt* observations were not possible. The follow-up started $\sim$3 hours later, thus cutting short the schedule that had foreseen seven observations. Nevertheless, the three successful runs cover 72% of the *initial* and 70% of the *updated* localisation map [225].

The majority of GW events detected by LVC during O2 and O3 could not be followed due to their

large localisation regions or due to their location in the northern hemisphere. Only a few well localised events could not be followed due to weather conditions (rain, clouds and lightning) like in the case of the BBH merger S191204r [220] and the Burst alert S200114f [221]. Visibility constraints imposed by the full moon did not allow to observe the well localised NSBH merger S190814bv [219, 14] that arrived during the full moon period. From the 64 non-retracted alerts from astrophysical origin received during O2 and O3, H.E.S.S. scheduled observations for 8 events and was able to observe 6 of them (9.4%). The total number of GW follow-up observations with H.E.S.S. is expected to rise in the following observing runs. Prospects for O4 will be discussed in the end of Chap. 5.

4.5 The Large Size Telescope (LST) transient handler and prospects

The LST transient handler: LST is the first operational instruments designed for the CTA observatory. It is located in the northern hemisphere in La Palma next to the MAGIC site. The LST transient handler is under commissioning and it is capable of handling GRB and neutrino alerts from the GCN and 4PiSky networks. LST has a FoV of 4.3 deg in diameter and can perform observations up to a 75 deg zenith angle.

I am participating in the preparation of GW follow-up observations by developing the GW module that is triggered upon the reception of a GW alert from GCN. The transient handler parses the alerts and forwards to the GW module the link to the GW maps. An simplified overview of the system is illustrated in Fig. 4.15. The GW module of the LST resembles the GW offline scheduler described in Sec. 3.4 with specific configuration files with LST high level parameters like the FoV and the maximum allowed zenith angle. The parameters related to the GW algorithms (like the zenith angle weight parameter and the cuts on minimum galaxy probabilities) are the same as for H.E.S.S. for now. The location of the telescope is updated to match the location of LST.

Just like for H.E.S.S., I use the GW tools described in Chap. 3 to build the LST GW module that is a part of the LST transient handler. The practice becomes easier for the LST since these tools are already developed and tested for H.E.S.S. The LST GW module checks for distance information in the GW map, for the distance of the event and for the location of the hottest spot in the sky. Just like for H.E.S.S., if the event is close by and does not occur in the galactic plane a 3D strategy is chosen for the follow-up (`PGalinFoV`), otherwise a 2D strategy (`PGWinFoV`)is chosen to cover the GW localisation area.

Moreover, I implemented tiling strategies for Fermi-GBM GRBs. The treatment of the alert is similar to

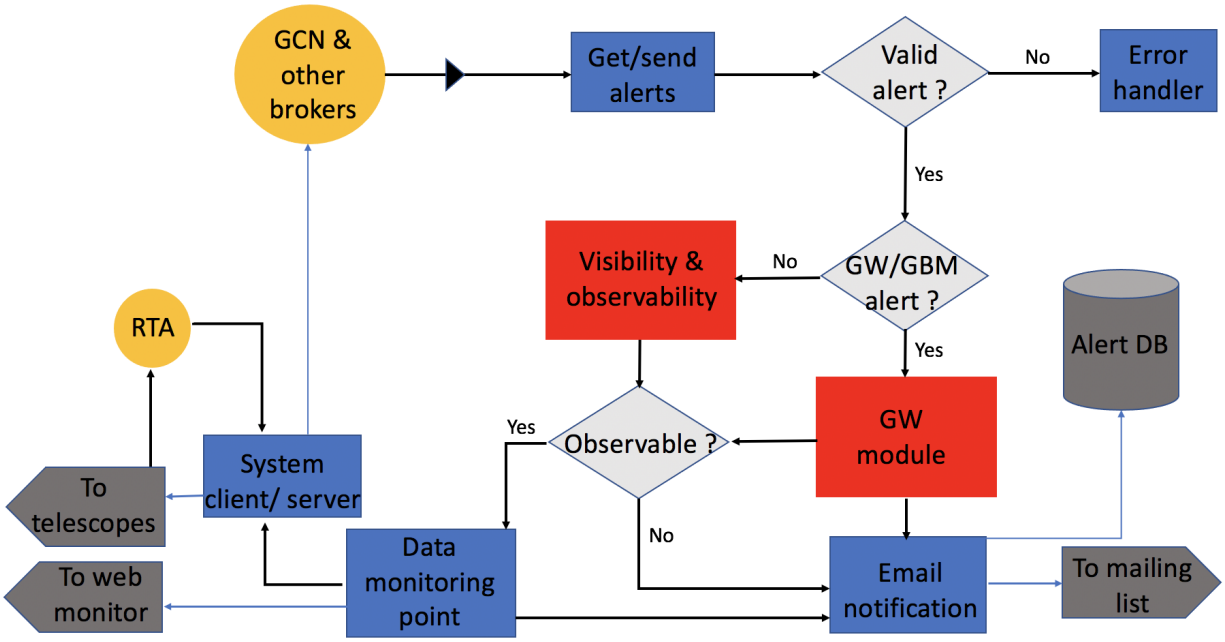

Figure 4.15: Schematic overview of the LST transient handler.

GW alerts. The usage of the GW follow-up tools presented in Chap. 3 for the LST collaboration for both GW and GBM alerts (like in H.E.S.S.) is a perfect example of the flexibility of the tools I developed that can be adapted for IACTs in order to cover localisation maps.

Prospects: For O4, both H.E.S.S and LST will be using the GW follow-up strategies described in Chap. 3 and 4 with possible further improvements. Together with MAGIC and VERITAS, they will be able to cover both hemispheres in order to maximize the chances of GW counterpart detection until the commissioning of the future CTA.

For *prompt* observations, some time could be saved by automatically slewing the telescope to the hotspot of the GW wave, while computing the best positions to observe using the GW follow-up algorithms. This is similar to the technique used in H.E.S.S. which consists in observing the first target before computing the whole GW follow-up schedule for the night but might be a few seconds faster. To efficiently assess this technique, one would have to take into consideration the time the telescope takes to slew from the hotspot to the best location of the GW map computed by the algorithms. For LST, *prompt* observations are still not implemented due to technical reasons. One can implement a follow-up for GW alerts for the 3D case that have a large localisation uncertainty using the `PGalinFoV-PixRegion` algorithm, since it has proven to be faster than `PGalinFoV` for large maps (see Sec. 3.5). In that case, large maps can be treated with `PGalinFoV-PixRegion`, while small maps, or maps that are detected with three interferometers or

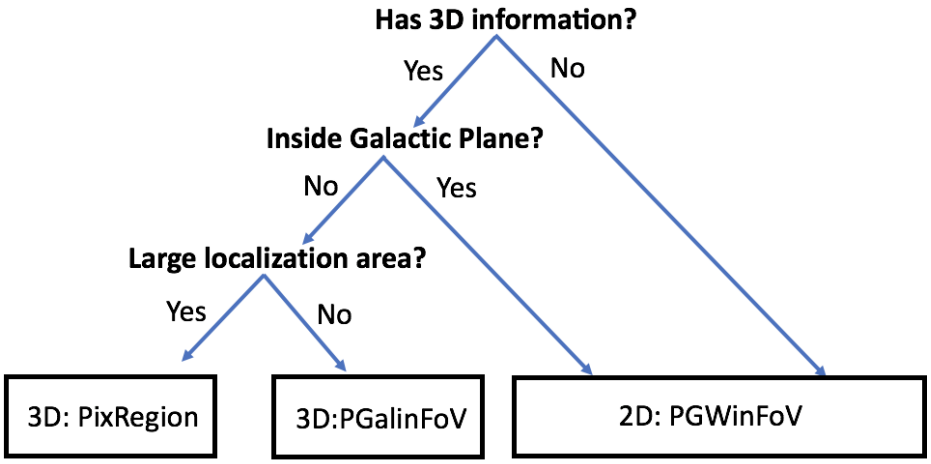

Figure 4.16: Schematic overview of a possible LST GW automatic handler.

more can be treated by `PGalinFoV` following the illustration in Fig. 4.16. Further time saving measures can be implemented. They include loading the galaxy catalog at the beginning of each night to save the time required by that step and general optimisation and parallelisation of the scheduling framework.

While the burst pipelines [195] are also sensitive to CBC events, the dedicated template based CBC pipelines typically provide better sensitivities and higher signal-to-noise ratios to these events. Out of the many events that could be caught primarily by the burst searches, nearby, i.e. galactic, supernovae are one of the most promising ones [139]. The pipelines searching for un-modelled signals provide only a 2-dimensional localisation. Taking into account the limited horizon of these searches, one could study the feasibility of correlating the GW localization uncertainty of burst alerts with the Galactic plane. Moreover, the general transient response systems of IACTs can be improved and follow-up observations of internal and external alerts can be improved by adding effective methods searching for MWL detection that might be occurring at the same time and might be counterparts to the GW alert. An example of such methods is the Astro-COLIBRI transient tool.

Part III

GW follow-up analysis

Chapter 5

Binary Black Hole (BBH) merger events follow-up with H.E.S.S.

5.1 VHE gamma-rays from BBH mergers ?

Generally speaking, electromagnetic emission from BBH merger is not highly anticipated due to the lack of tidally disrupted material like in the case of BNS or NS-BH mergers [283]. BBH systems are expected to be old enough to have swiped remnant material from previous supernovae around them or to have been kicked away from it. The existence of surrounding material around the merging binary system is the direct source for powering a jet, hence bright EM emission in the BBH merger scenarios is difficult to produce. Moreover, [387] explain that in the conventional way of describing the black hole growth process through matter accretion, even the strong EM emission from BBH merger can not escape the system due to infinite redshift caused by the event horizon of the black hole. The authors explain that compressed matter can extend the magnetic field to larger scales making EM emission possible to escape, but the usage of a time-dependent metric by considering the in-falling matter in the pre-existing black hole show that the time needed for the BHs to merge is much larger than the time needed to accrete all the matter around them. This means that by the time of the merger, all the remnant material around the BBH system would have disappeared inside the event horizons, making EM emission impossible and only GW radiation as a possible counterpart. Therefore, the existence of at least one neutron star in CBCs is required for EM emission to occur.

However, a weak transient event by Fermi-GBM [92] [91] detected 0.4 second after the GW150914 [5] BBH merger event sparked much interest and controversy, and inspired new models to explain the pro-

posed relation between BBH mergers and GRBs. [377] show that the γ-ray emission from the mentioned transient can be explained by a relativistic outflow with Lorentz factor larger than 10. They also argue the possible existence of synchrotron afterglow emission caused by debris outflow *pushes* forming shocks in the ambient gas. Extreme scenarios have also been suggested to explain the possible link between BBH merger and GRBs. One of the scenarios is the formation of a dumbbell configuration when the core of a rapidly rotating massive star collapsed where the BBH merger took place leading to possible EM emission [232]. A circumbinary disc around a merging BBH might get shocked and heated during the aftermath of the merger [249]. In the circumbinary disc case, the disk accretion can be slowed by the resonant torque from the binary forming a dead zone. The presence of the massive accretion disc combined with efficient escape of shock produced radiation, could lead to EM counterpart emission. Furthermore, [382] argue that if one of the BHs is charged, the evolving magnetic moment during the merging process would drive a Poynting flux with increasing wind power during the final phase of the merger and can generate a FRB and possibly a sGRB. Finally, EM emission, in particular optical transients, are expected if the BBH merger takes place in the accretion disk of an AGN. After a BBH merger, the system is kicked by the explosion. It enters the unperturbed gas and accrete matter into the newly formed black hole producing EM emission like in the case of the optical transient [140] detected by ZTF as a possible counterpart to S190521g [235]. The emission is expected to end when the BBH merger product exits the disk.

It is interesting to put all these theories to the test by actually observing and following-up on BBH mergers detected by Ligo and Virgo in the search for VHE γ-ray emission from a potential GRB related to these BBH mergers. Also, even if EM emission is not expected, BBH follow-up also are helpful for defining and improving GW follow-up strategies and analysis procedures for events where EM emission is expected. This is why, the H.E.S.S. collaboration has dedicated significant efforts and time to the follow-up of BBH mergers in the search for possible VHE γ-ray emission. As GW task leader, I am leading a publication on the results of the BBH mergers follow-up by H.E.S.S. [155].

5.2 Observation of BBH mergers with H.E.S.S. during O2 and O3

Following the procedures described in Chap. 4, H.E.S.S. observed 6 GW events during O2 and O3 (presented in Sec. 4.4): GW170814, GW170817, S190512at, S190728q, S200115j and S200224ca. GW170817 was observed during short and long-term follow-up observations. The analysis of these ob-

servations is treated in separate publications [16] and [18] and will be reported in Chap. 6. Due to cloudy sky, S200115j could not be observed with more than 1 run. The data of this run is heavily impacted by the weather conditions, therefore, this event is discarded from the discussion. After O3a, the CT5 camera was swapped with a new camera. The `M++` analysis from this camera is still under commissioning, therefore, the CT5 data of GW events follow-up that were observed after the camera exchange can not be analysed.

All the GW events that are treated in this chapter are BBH mergers. As explained in Chap. 4, BBH events are followed with 2D tiling strategies. More than 50% coverage was achieved for all these events except for S190512at that was observed in order to test the new follow-up scheme developed for O3. For this section I use analysis plots of the S190728q follow-up observations as an example and I provide the plots of the remaining three events in Appendix B. Here is an observational overview for each event:

- GW170814 [9] was observed on the third day after the merger due to the GW event falling during the full moon period. The zenith angle of the observations ranges between 30 and 50 deg. Observations were conducted with three 12-m telescopes (one of the four 12-m telescope was under maintenance) in addition to the 28-m telescope

- S190512at [215] with $\sim$7 hours delay after the merger. Observations started with a zenith angle of 14 deg and finished at 40 deg. Observations were conducted with three 12-m telescopes in addition to the 28-m telescope

- S190728q was observed with $\sim$11 hour delay at zenith angles ranging from 35 to 54 deg, with all five telescopes. A candidate neutrino was found by IceCube [174] near the localisation region. The H.E.S.S. observations cover a part of the neutrino candidate localisation uncertainty. A summary of these observations are provided in Tab. 5.1.

- S200224ca [217] is one of the best localised BBH events and one of the most followed (according to the Treasure Map[1] [374]). H.E.S.S. took three observation runs with $\sim$3 hours of delay. This is the smallest delay for H.E.S.S. GW follow-up observations so far. The zenith angles of the observations are between 20 and 30 deg. Observations were conducted with all five telescopes after the camera swap.

For the following, information (localisation maps and distance) from the latest publication for each events are considered. For GW170814 I consider the information published in the first GW catalog [4] and for

[1] `http://treasuremap.space`

S190512at and S190728q from the seconds GW catalog [13] containing the O3a event. S190512at and S190728q are published as GW190512_180714 and GW190728_064510 respectively. Finally since the O3b catalog is not yet released, I use latest information published in GCNs and GraceDB for S200115j and S200224ca.

Position	Start time (UTC)	RA J2000 (deg)	DEC J2000 (deg)	Duration (min)	Zenith angle (deg)
1a	2019-07-28 21:12	313.09	8.16	28	45
1b	2019-07-28 21:46	313.09	8.16	18	39
2	2019-07-28 22:23	317.11	15.02	28	43
3a	2019-07-28 22:59	314.39	10.81	14	35
3b	2019-07-28 23:18	314.39	10.81	28	34
4	2019-07-28 23:47	312.98	5.68	28	30
5a	2019-07-29 00:16	318.69	17.19	6	41
5b	2019-07-29 00:34	318.69	17.19	28	42
6	2019-07-29 01:03	316.14	12.94	28	42
7	2019-07-29 01:32	312.80	7.03	28	44

Table 5.1: H.E.S.S. observations of S190728q BBH merger GW event.

5.3 Data quality check and analysis configuration

The data quality check described in Sec. 1.3.2 is performed prior to the analysis of the GW follow-up observations. For each event I asses the quality of the data in order to remove runs with sub-optimal quality. During this check, I remove all observation runs under 10 minutes since they don't have the required statistics to be analysed. For GW170814, the data quality is acceptable for all the runs. For S190512at and S190728q, the CT5 camera showed some malfunctions and in-homogeneity in the CoG maps for some runs. These defects do not affect the preliminary offline analysis so they are kept. These data are eventually not used, as explained in the following. S200224ca was observed during a rainy/cloudy night and 1 run is removed due to important variability in the trigger rates.

The two questions to be addressed now are: which telescope data to use (CT1-4 or C1-5) and what configuration cuts to use (*standard* or *loose*)? S200224ca was observed after the CT5 camera exchange and no CT5 analysis was available at the time for `M++`. Moreover, a preliminary analysis shows that the sensitivity is not affected by the chosen configuration. The use of the CT5 telescope lowers the energy threshold, however this difference is just for few tens of GeVs. A comparison of CT1-4 and CT1-5 BBH follow-up analysis is provided in Appendix C.1. In order to have a homogeneous analysis only the data from the CT1-4 telescopes will be used for all events. As for cut configuration, I also find that the sensitivity will not be highly affected by the usage of *loose* or *standard* cuts. *Loose* cuts provide the advantage of

lowering the energy threshold. I find that like for the case above the difference would be only by few tens of GeVs. Even though the H.E.S.S. FoV is defined as 1.5 deg for CT5, and 2.5 deg for CT1-4, the effective FoV, which is the FoV where the number of events is statistically sufficient to perform analysis can vary with the observation conditions (especially the zenith angle). To ensure that we have enough events to perform the analysis, a requirement of $\alpha \mathrm{N}_{\mathrm{OFF}} > 5$ is imposed on each pixel of the map in order to consider it for analysis. This defines the edges of the FoV, or the effective FoV. An advantage brought by the usage of *loose* cuts is that the effective FoV will be larger. *Loose* cuts filter less background events and the statistics will be higher allowing wider edges. A comparison between *loose* and *standard* cuts for the analysis is provided in Appendix C.1. I find that the GW localisation coverage is only affected by less than 10% which is not enough to justify the usage of something other than standard analysis. Therefore, the more conservative *standard* cuts are used.

5.4 Analysis results of BBH merger follow-up

The analysis configuration used is `M++ HESS-I Stereo` (see Sec. 1.3.2) where the data from the CT1-4 telescopes are considered. The data is then analysed using the *standard* cuts of the semi-analytical *Model* analysis [103] (see Sec. 1.3.2). The background level in the FoV is determined from the data set itself using the "Ring background" technique [63] with 0.1 deg radius circular regions for the ON region. *Artificial* maps are created with a 0.02 deg pixel side. The "Ring background" technique is performed on each bin of the map. The edges of the maps are determined by the conditions: $\alpha \mathrm{N}_{\mathrm{off}} > 5$. All the bins fulfilling this condition will be considered, otherwise a "NaN" value will be assigned.

The excess in each pixel is determined by Eq. 1.31. I show in Fig. 5.1 the resulting excess map for the S190728q GW event. The excess values are then transformed into significance following the formalism described in [210] and in Eq. 1.33. A significance map is computed as shown in Fig. 5.1. No significant γ-ray emission is found above 5 σ. The significance distribution show in Fig. 5.1 follows a Gaussian distribution and is consistent with the background only hypothesis. The same is found for the other three GW events. Therefore, I conclude that the analysis resulted in no significant detection of any γ-ray counterparts to the BBH merger events. I proceed with the computation of upper limits.

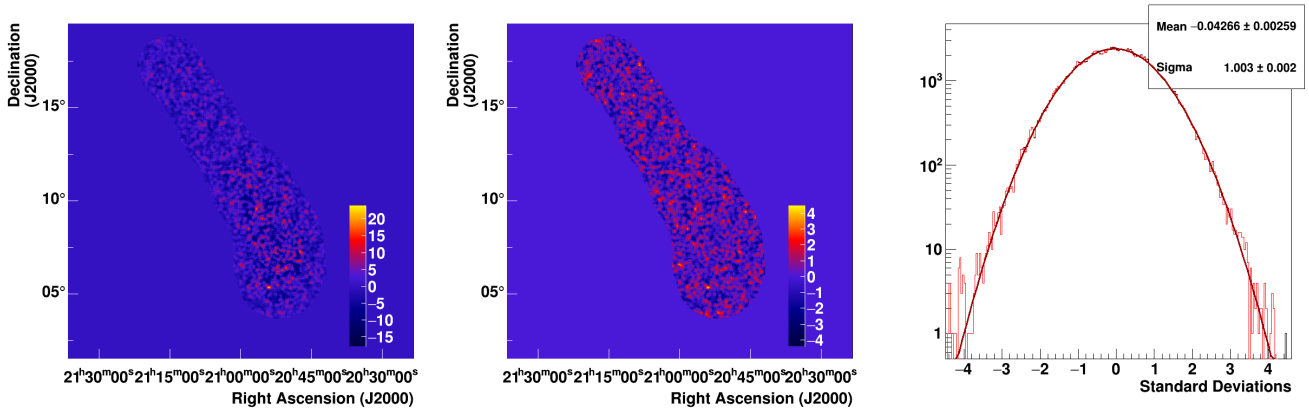

Figure 5.1: **Left:** Excess map computed from the H.E.S.S. observational data taken on S190728q presented in Tab. 5.1. **Middle:** Significance map computed from the H.E.S.S. excess map of S190728q. **Right:** Distribution of the H.E.S.S. significance map entries in red and a Gaussian distribution fit in black.

5.4.1 Upper limit maps 1-10 TeV

In order to constrain the VHE emission from these BBH mergers at the time of H.E.S.S. observations, I derive 95% confidence level integral upper limit maps for each GW event for a given energy interval [E_1, E_2] and a given spectrum shape following the procedure in [15] and in Eq. 5.1:

$$F = \frac{N_\gamma}{N_{\rm exp}} \int_{E_1}^{E_2} \phi_{ref}(E) dE \tag{5.1}$$

Where, in each position of the map N_γ is the measured excess computed with the Rolke method [320] by taking into consideration N_{ON}, N_{OFF} and α for each pixel. E_1 is the lower bound of the energy interval taken as 1 TeV here and E_2 is the upper bound taken as 10 TeV here. $N_{\rm exp}$ is the expected number of photons from MC simulations:

$$N_{\rm exp} = \sum_{R \in run} T_R \int_{E_1}^{E_2} \phi_{ref}(E_r) A_{eff}(E_r, q_R) dE_r \tag{5.2}$$

with E_r is the reconstructed energy, T_R is the observation live-time, q_R symbolizes the observation parameters for a specific run (zenith, off-axis, and azimuth angle; pattern of telescopes participating in the run; and optical efficiencies); A_{eff} is the effective area obtained from MC simulations, which is assumed constant during a 28 minutes run; and E_1 = E_{min} is the threshold energy appropriate for the observation. ϕ_{ref} is the assumed power law spectrum following:

$$\phi_{ref} = \phi_0 (E/E_0)^{-\gamma} \tag{5.3}$$

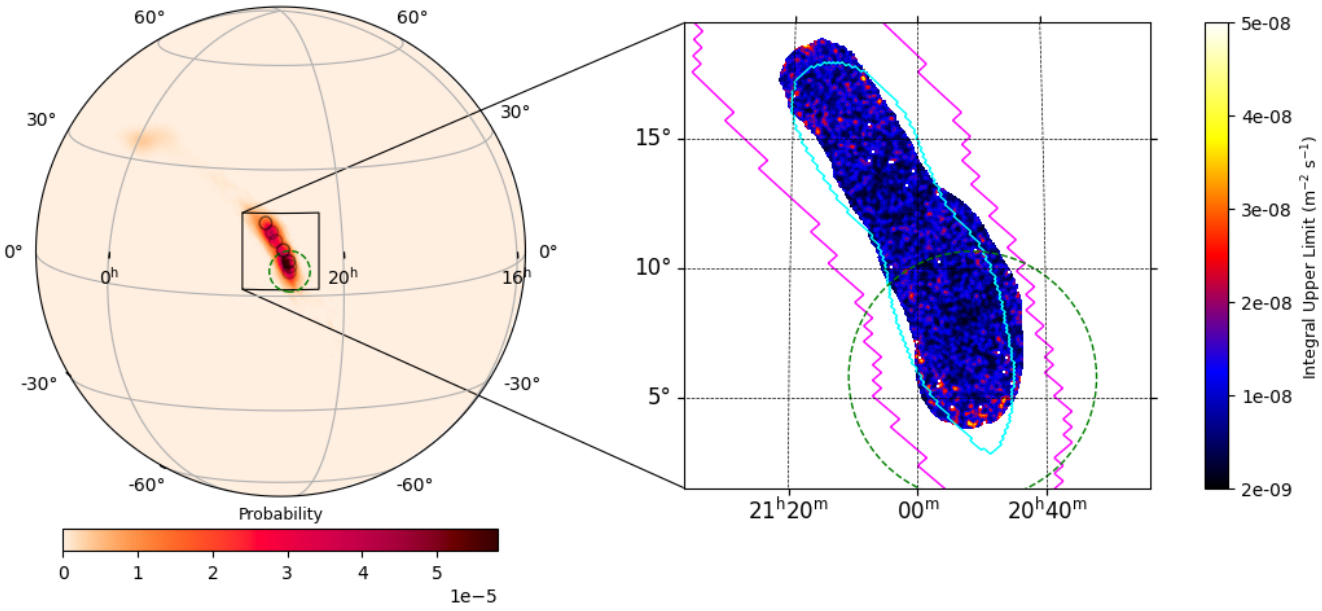

Figure 5.2: Integral upper limit maps computed from the H.E.S.S. observations of S190728q GW events presented in Tab. 5.1 assuming an E^{-2} source spectrum and a 1-10 TeV energy range. The magenta and cyan lines represent respectively the 90% and 50% localisation contours of the newest published GW map in [13]. The green dashed circle repreent the uncertainty region of an IceCube neutrino [174] candidate.

with $\gamma = 2$, E_0 the reference energy taken as 1 TeV and ϕ_0 the flux normalization which can be chosen arbitrarily since it will cancel out (It is chosen as $\phi_0 = 10^{-8}\,\mathrm{m}^{-2}\,\mathrm{s}^{-1}\,\mathrm{TeV}^{-1}$).

The resulting upper limit map is shown in Fig. 5.2 for S190728q and in Appendix B for the three remaining GW events. These upper limits constrain the emission from the BBH mergers in the core energy domain of H.E.S.S. without considering EBL absorption. The emission observed on Earth is however affected by EBL absorption. If we consider this time that the source has an intrinsic E^{-2} spectrum, the spectrum observed on Earth should be steeper. The maps computed in this section don't take into consideration propagation effects and therefore could be considered as from the source point of view (observer is at the source).

5.4.2 Specific Upper limit maps

Given the EBL absorption at the respective redshift of each event, I also compute integral upper limit maps considering this constraint. I also exploit the whole energy range that can be used for each specific event.

Specific energy range

Minimum energy E_{min}:

To determine the energy ranges in which the upper limit maps should be computed, theoretical and technical constraints should be taken into consideration. The technical constraints limit the instruments capabilities to provide usable data for upper limits to a certain range of energies, while the theoretical constraints determine the energy range at which the upper limits are meaningful and helpful to put constraint on the theoretical model. Due to the lack of VHE emission expectations from models of BBH mergers, in this section I only consider instrument energy range constraints. These constraints will allow to provide stringent and realistic integral upper limit over the whole energy range where:

- The γ ray is energetic enough to initiate a shower that can produce Cherenkov light detectable by the cameras.
- The shower is large enough to be detected by the cameras but small enough to be contained inside the FoV of the instrument. The shower size as seen from the cameras depends mainly on energy of the primary γ ray and the zenith angle.

To determine the best energy range for the upper limit maps I start by exploring the different options for the lower range or E_{min}. In the H.E.S.S. collaboration, E_{min} is usually taken as the energy threshold (E_{thr}) at an energy where the acceptance is at 10% of its maximum value, for the stereoscopic mode, because at very low energies, energy reconstruction shows some biases due to trigger selection effects [103] (see Sec. 1.3.2). To overcome these biases, a standard procedure would be to cut off the corresponding events. This energy threshold varies from run to run depending mainly on the zenith angle since the acceptance decreases with increasing zenith angle. Moreover, the energy threshold varies across the FoV since the acceptance is also dependant on the position in the FoV (off-axis angle).

Given that GW follow-ups consist of several runs taken at different directions, at different zenith angles and span large areas in the sky, in the following I show the method that I developed during the analysis of the GW follow-up observations to tackle this issue.

Initially, the problem seemed to choose a position in the skymaps at which an E_{thr} would be calculated and used for all the positions in the map. However, the choice of a common offset angle to all the positions at which E_{thr} is computed could lead to biases in the determination of E_{min} since any variation across the FoV and across the zenith angles would be neglected. This requires a more generalized solution that

would minimize the biases in calculation and would require a minimum number of assumptions to compute E_{th} maps.

To do that, a tool is created within the GW group and used/tested for the first time in this analysis. This tool will compute at each position of the map the energy at a certain x% (here 10%) of the maximum acceptance for each run separately. In that case, all the positions in the FoV of one run will be filled with the same value. The user can choose to have off-axis dependent values, meaning that at each position in the FoV, $E_{th,pos}$ will be chosen corresponding to its off-axis angle. In that case, inside the same run's FoV $E_{th,pos,run}$ will be dependent not only on the run configuration but also on the position in the FoV determined by the off-axis angle. A ψ_{cut} limiting the FoV radius at which $E_{th,pos,run}$ should be calculated is chosen. This process is done individually for each run then the threshold energies are merged together either by choosing the highest $E_{th,pos}$ coming from different runs following Eq. 5.4

$$E_{th,pos} = E^{MAX}_{th,pos,run} \tag{5.4}$$

or by taking the observation live time weighted average of the $E_{th,pos}$ that come from different runs following Eq. 5.5

$$E_{th,pos} = \frac{\sum_i^N E_{th,pos,run} t_{run}}{\sum_i^N t_{run}} \tag{5.5}$$

where N is the total number of runs covering the position, i is the corresponding run number and t_{run} is the livetime of the run.

I first choose a time weighted approach following Eq. 5.5 in order to account for different exposure times. I also prefer an off-axis dependent approach to explore and minimize the bias induced by any variation of $E_{thr,pos,run}$ across the FoV. I compare time weighted E_{thr} maps and maximum E_{thr} maps and don't find big differences in most cases. I show an example in Appendix C.2 for GW170814. Finally, for runs taken at high zenith angle (like in the case of S190827q), I notice that the E_{thr} values start to increase drastically at high ψ_{cut}, typically above 2 deg. Therefore, I choose a value of $\psi_{cut} = 2\,\mathrm{deg}$ knowing also that with the $\alpha.n_{off} > 5$ condition only few runs have an effective FoV $> 2\,\mathrm{deg}$ at high zenith angles due to reduced statistics. Not considering the edges of these runs affects the final E_{thr} at the percent level. I show an example in Appendix C.2 for GW170814 for a $\psi_{cut} = 2\,\mathrm{deg}$ and a $\psi_{cut} = 2.5\,\mathrm{deg}$. After the $E_{thr,pos}$ map is obtained, I correlate it with the significance map to obtain the same edges. This step is necessary to make sure that the $E_{thr,pos}$ computed corresponds to the data that will be used to compute the upper limit maps since the edges of the $E_{thr,pos}$ maps are defined by a ψ_{cut} while the edges of the significance

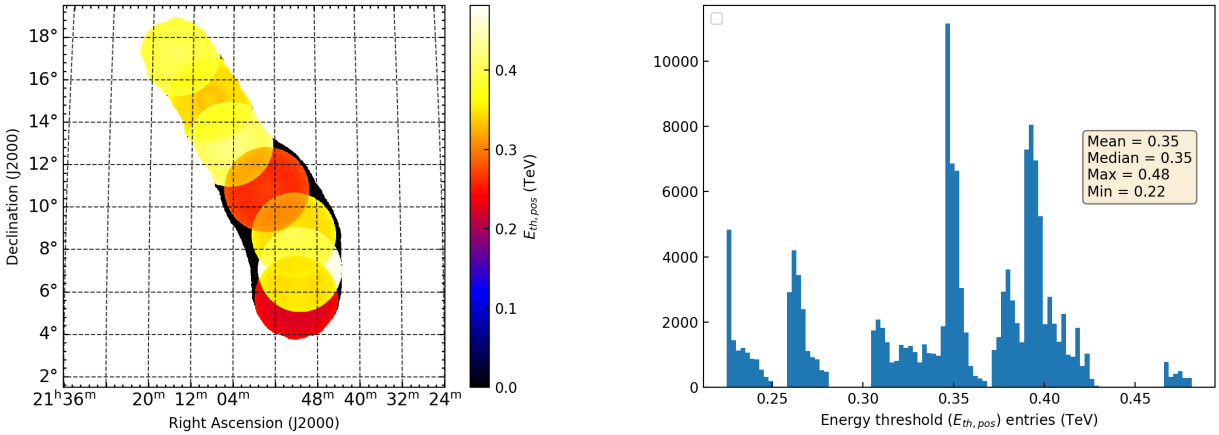

Figure 5.3: Energy threshold map (left) computed for $\psi_{cut} = 2\,\mathrm{deg}$ with time weighted off-axis $E_{thr,pos}$ and their distribution (right).

map is defined by the actual data with $\alpha.n_{off} > 5$. An example of the $E_{thr,pos}$ maps is given in Fig. 5.3.

The distribution of the $E_{thr,pos}$ values is then plotted (example in Fig. 5.3) and a E_{thr} value for the whole map is chosen. One could argue that the maximum value should be used to eliminate all energy estimation biases in all the regions. However the maximum value can be significantly affected for example by a single observation at a certain position taken late in the night at high zenith angle which will cause an overestimation of E_{thr}. Therefore we choose the median value.

Maximum energy E_{max}:

From previous GRB H.E.S.S. analysis, in order to derive differential upper limits at the location of a given source, a requirement of $N_{OFF} > 10$ per energy bin is set in order to have sufficient background events to compute the excess. However, for our analysis we derive integral upper limits maps. For that, all the events above a given energy threshold will be counted in the calculation, increasing the statistics for the calculation of the integral upper limits. Since events at very high energies are very rare and the systematic biases at high energies affect minimally the results we decide for the `M++` analysis to integrate to the maximum possible energy for which instrument response functions are available ($\sim$100 TeV). In fact, I study the difference between integral upper limit maps computed up to 10 TeV and 100 TeV respectively and I conclude that the difference in sensitivity is around $\sim$3% (100 TeV maps being more sensitive). An example for S190512at is given in Appendix C.3.

A cross-check analysis performed by another member of the task force is performed and the cuts on the energy threshold are based on the energy biased that can be determined by comparing reconstructed

energies versus true energies in simulations using the instrument response function.

In conclusion, the instrument limitations impose an energy range. One way to choose the energy range is to use cuts on energy reconstruction biases, another way is to rely on the maximum acceptance for an observation. The final E_{min} chosen for this analysis is the highest one provided by both techniques while E_{max} is chosen as the lowest values yielded by both techniques. The final energy range values used to compute the specific integral upper limit maps are shown in Tab. 5.3. I note that all E_{min} values used for the study are the ones computed considering the acceptance except for S200224ca where the cross-check analysis based on the minimization of energy biased yielded a higher E_{th}. All E_{max} values are also derived with the latter method.

Specific spectral index

In order to choose the type of analysis for the GW follow-up data, I explore potential EBL absorption effects on our sources.

I explore the effects of EBL absorption at the redshifts of the GW events within the energy range of 0.1 to 100 TeV. For that I consider a source with a standard power law spectrum with an index $\gamma = 2$, I show in Fig. 5.4 the effect of EBL absorption at the different GW redshifts on the flux. In practice, I use the function `AbsorbedSpectralModel` from `gammapy v0.17` [104] that takes as input the power law model, the Franceschini absorption model [126] and the redshift. EBL absorption effects on the spectral indices are considerable even at low energies. At the highest redshifts ($z = 0.29$), EBL absorption induces a drop in flux of an order of magnitude at 1 TeV, an effect that increases drastically at higher energies. I show in Fig.5.4 the variation of the spectral index in function of the energy.

I calculated the equivalent power law spectral index at the respective E_{th} of each event assuming a power law spectrum. The equivalent spectral index is the index of the power law tangent to the EBL absorbed spectrum at E_{th}. E_{th} is chosen due to the fact that low energy events are expected to be dominant for VHE GRBs. I also study the dependence of the equivalent spectral index to the EBL model used and the energy chosen. To do that I explore EBL absorption effects by considering three EBL models from [126], [108] and [121]. I also vary the energy at which I choose to compute the equivalent spectral index in the low energy range up to 1 TeV. I show the resulting spectral indices for the various EBL models for the S190728q GW event at 0.35 and 1 TeV in Tab. 5.2. The equivalent spectral index shows less than 14% dependence on the EBL model and the chosen energy in the lower part of the energy spectrum up

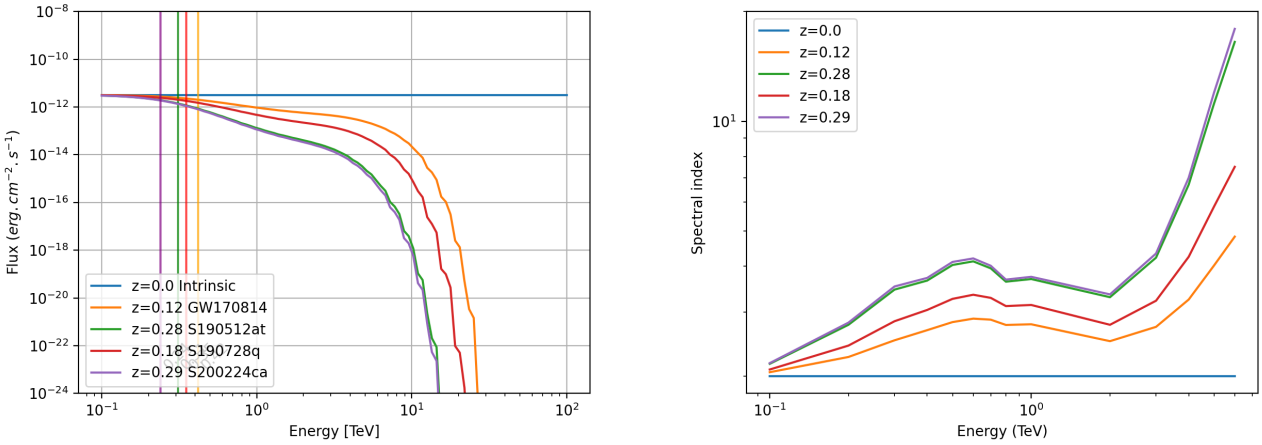

Figure 5.4: Comparison of the flux affected by EBL at $z = z_{GW}$ and $z = 0$ for a source with a power law spectrum and spectral index $\gamma = 2$ (left) and the equivalent spectral index EBL at $z = z_{GW}$ depending on the energy (right)

	Franceschini	Dominguez	Finke
at 0.35 TeV	2.98	3.01	3.26
at 1 TeV	3.31	3.39	3.26

Table 5.2: Equivalent spectral indices at 0.35 and 1 TeV and redshift for a redhsift of $z = 0.18$ for the Franceschini [126], Dominguez [108] and Finke [121] EBL models.

to 1 TeV. Propagating this dependency to the upper limit maps will result in less than 10% variation in the upper limit values. I show in Fig. 5.5 the distribution of the integral UL entries (Energy range 0.35 - 26.10 TeV) for S190728q assuming a power law spectral index of 2.98 and 3.39 (the minimum and maximum values from Tab. 5.2). The values show less than 10% difference. Varying the intrinsic spectral index between 1.5 and 2.5 leads to a variation of the equivalent spectral index between +16% and -16% for the absorbed emission. This affects the integral upper limits values between +19.4% and -10.7%.

The resulting power law indices used to consider EBL absorption and energy ranges are presented in Tab. 5.3. Integral upper limits are computed at each observed position of the map for all four BBH mergers following Eq. 5.1 with specific instrument constrained energy ranges for E_1 and E_2 and equivalent spectral index γ. These maps are presented in Fig. 5.6 for S190728q and in Appendix B for the remaining three GW events.

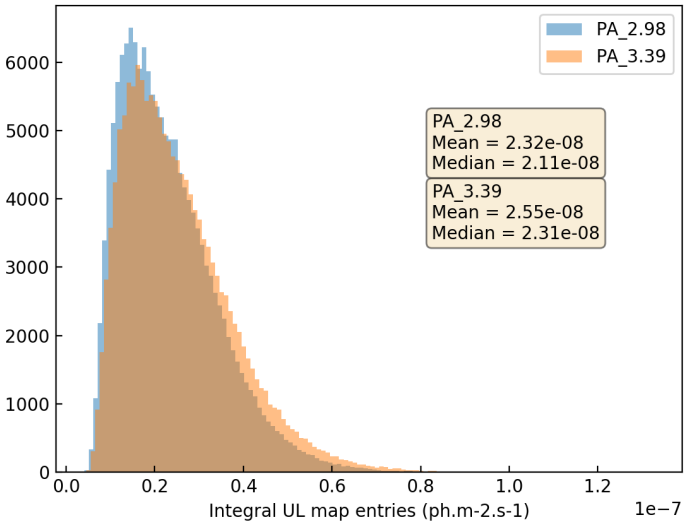

Figure 5.5: Integral UL map distribution for S190728q assuming a power law spectral index of 2.98 and 3.39 respectively. The energy range is 0.35 - 26.10 TeV.

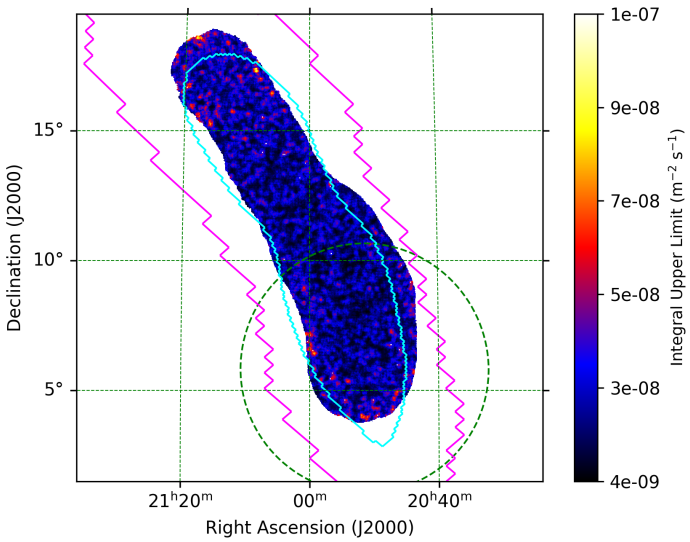

Figure 5.6: Integral upper limit maps computed from the H.E.S.S. observations of S190728q presented in Tab. 5.1. I assume an internal E^{-2} source spectrum taking into consideration EBL absorption effect and a specific energy range 0.35 TeV-26.10 TeV as shown in Tab. 5.3. The magenta and cyan lines represent respectively the 90% and 50% localisation contours of the GW map in [13]. The green dashed circle represent the uncertainty region of an IceCube neutrino candidate [174].

GW event	Final mass ($M_\odot$)	Redshift	$\gamma(E = E_{\text{th}}, z = z_{GW})$	Energy range (TeV)	Coverage	$T_{\text{start}}, T_{\text{stop}}$ (s)
GW170814	$53.2^{+3.2}_{-2.4}$	0.12	2.73	0.42-34.80	75.4%	$2.22 \times 10^5, 4.10 \times 10^5$
S190512at	$34.5^{+3.8}_{-3.5}$	0.27	3.50	0.31-38.31	34.5%	$1.84 \times 10^4, 2.82 \times 10^4$
S190728q	$19.6^{+4.7}_{-1.3}$	0.18	2.98	0.35-26.10	50.8%	$4.88 \times 10^4, 7.28 \times 10^4$
S200224ca		0.29	3.08	0.24-38.31	62.13%	$1.07 \times 10^4, 1.59 \times 10^4$

Table 5.3: Spectral indices (γ) at a GW event's corresponding redshift and at E_{th} assuming an intrinsic E^{-2} spectrum. The energy range used to derive the specific integral upper limit maps and the corresponding coverage are presented in columns 5 and 6 respectively. The second column indicates the final mass of the BBH event and the last column lists the start and end of the H.E.S.S. observations of the GW event, as calculated from the reported GW merger time.

5.5 Luminosity Upper limits

To compute luminosity upper limits from the previously derived integral upper limits I consider the variation of the distance estimation of the events across the observed parts of the GW map. The per-pixel distance information contained in the maps follow a Gaussian distribution as explained in Sec. 2.2.3. The per-pixel mean distance is considered here and it varies by few hundreds of Mpc across the map. I plot the per-pixel mean distance in Fig. 5.7 inside the regions observed by H.E.S.S. for S190728q. In some regions of the distance map the difference can reach more than 100 Mpc inside the observed H.E.S.S. region. I consider the 1-10 TeV integral upper limit maps in order to compute intrinsic luminosity upper limits in the rest frame of the source:

$$L = 4\pi D_{\text{L}}^2 F_e \tag{5.6}$$

$$= \frac{N_\gamma}{N_{\text{exp}}} 4\pi D_{\text{L}}^2 \int_{\frac{E_1}{1+z}}^{\frac{E_2}{1+z}} E \times \phi_0 \left(\frac{E}{E_0}\right)^{-\gamma} dE \tag{5.7}$$

For each pixel of the map, F_e is the integral energy flux upper limit:

$$F_e = \frac{N_\gamma}{N_{\text{exp}}} \int_{\frac{E_1}{1+z}}^{\frac{E_2}{1+z}} E \times \phi_0 \left(\frac{E}{E_0}\right)^{-\gamma} dE \tag{5.8}$$

where N_γ is the measured excess computed with Rolke [320], and N_{exp} is the total predicted number of excess events. D_{L} is the mean luminosity distance, E_1 is 1 TeV, E_2 is 10 TeV, z is the redshift computed from D_{L} using the cosmological paramteres in [26], E_0 is the normalization energy and is considered as 1 TeV, ϕ_0 is the flux normalization, and γ is the power law spectral index which is taken here as 2 (see Sec. 5.4.1).

The values are converted to erg s^{-1} and the results are shown in Fig. 5.8 for S190728q and in Ap-

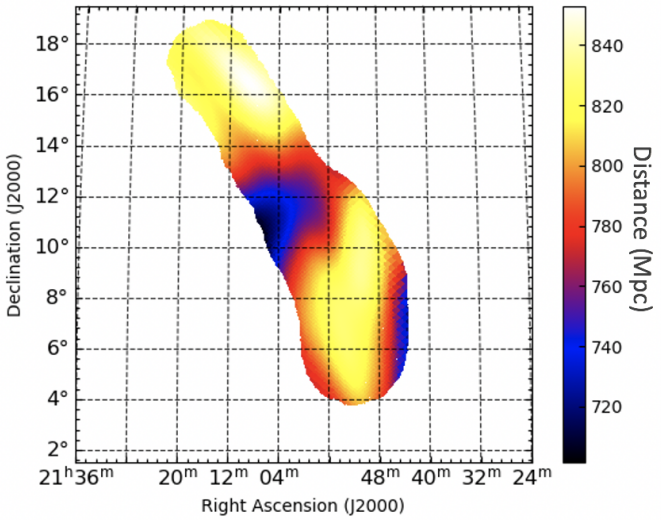

Figure 5.7: Mean distance estimate of the S190728q event restricted to the regions observed by H.E.S.S. The GW map used is from the latest release [13].

pendix B for the remaining GW events.

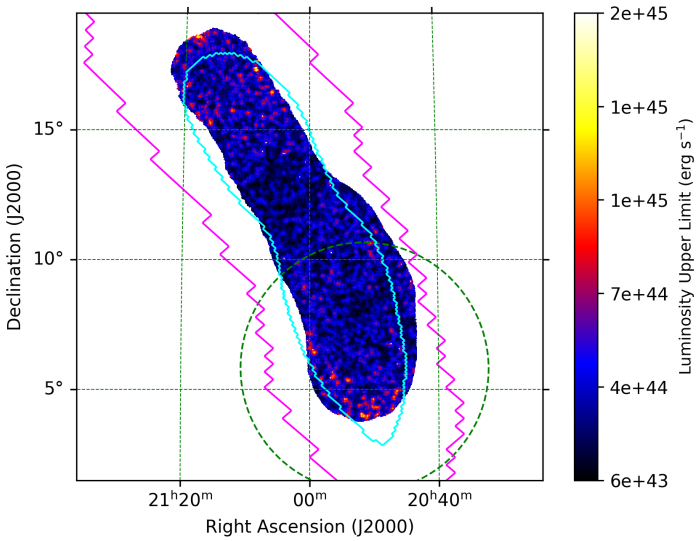

Figure 5.8: Luminosity upper limit maps computed from H.E.S.S. observations of S190728q. The magenta and cyan lines represent respectively the 90% and 50% localisation contours of the newest published GW map in [13]. The green dashed circle repreent the uncertainty region of an IceCube neutrino candidate [174].

5.6 Discussion

The H.E.S.S. observations presented in this chapter (and will be published in [155]) cover the most probable regions of the GW localisation uncertainties. The coverage determined from the effective FoV of the H.E.S.S. observations (determined by $\alpha N_O F F > 5$) are presented in the last column of Tab. 5.3. The computed upper limits constrain for the first time the VHE γ-ray emission from BBH mergers. No electromagnetic or neutrino counterpart have been confirmed for any of the H.E.S.S. observed events.

To facilitate comparisons with other physical phenomena, I derive per-pixel upper limits on the integral energy flux and luminosity in the observed regions as explained in Sec. 5.5. The luminosity upper limits are derived in the intrinsic emission that is considered EBL corrected[2] in the 1-10 TeV range assuming an internal E^{-2} spectrum as explained in Sec. 5.5. In order to compare the *observed* properties, I calculate the energy flux upper limits F_e using the EBL-attenuated spectra[3] in the specific energy ranges presented in Tab. 5.3. The spatially averaged upper limits on the energy flux and luminosity are provided in Table 5.4 as a reference.

GW event	energy flux, event-specific (erg cm^{-2} s^{-1})		luminosity, standard (erg s^{-1})	
	mean	standard dev	mean	standard dev
GW170814	3.7×10^{-12}	1.8×10^{-12}	1.3×10^{44}	9.8×10^{43}
S190512at	3.1×10^{-12}	1.5×10^{-12}	9.9×10^{44}	4.7×10^{44}
S190728q	2.6×10^{-12}	1.3×10^{-12}	3.2×10^{44}	1.6×10^{44}
S200224ca	2.7×10^{-12}	1.2×10^{-12}	1.9×10^{45}	8.8×10^{44}

Table 5.4: The energy flux and luminosity upper limits for the four GW events are calculated individually for each pixel in the sky region observed by H.E.S.S. The energy flux upper limits here are not EBL attenuated, and are calculated over the event-specific energy ranges (Tab. 5.3). The luminosities are calculated from EBL-corrected energy fluxes assuming an E^{-2} source spectrum over a 1–10 TeV energy range, and using the per-pixel luminosity distances. These values are also plotted in Fig. 5.9 and 5.10.

As explained in Sec. 5.1, there are some models that predict electromagnetic emission from BBH mergers, often by invoking a remnant disk around one of the two BHs or the binary system itself [284, 263, 197, 249], or a more exotic scenario such as charged black holes [382, 211, 127]. These models focus on producing synchrotron emission in jets which, assuming conditions similar to GRBs, peaks in the X-ray and low energy γ-ray energy ranges, especially at late times. They do not make many statements about VHE

[2]EBL corrected means here that the upper limits (as if the observer is at the source) are computed without taking into consideration EBL absorption effects.

[3]EBL attenuated refer to the upper limits (as observed from Earth) that are derived by adding the EBL absorption effects resulting in a steeper power law spectrum index as indicated in Tab. 5.3

emission. For instance, the scenarios involving a remnant disk make predictions on the emission based on synchrotron from the relativistic jets that are launched after the merger. Assuming that the acceleration and radiation of the charged particles occur in the same region, and by equating the acceleration and emission timescales there is a maximum synchrotron photon energy that can be estimated for GRB-like conditions at the order of 1 GeV after few hours [e.g. 158]. This is more than an order of magnitude below the H.E.S.S. energy range and two orders of magnitude below the event-specific energy ranges shown in Tab. 5.3. Interpreting the H.E.S.S. upper limits in the context of these models would require an additional photon production mechanism at high energies, such as IC emission, or some other assumptions about the acceleration and/or cooling processes. This is beyond the scope of this work given the amount of uncertainties involved in the prediction on the production of VHE emission.

At the same time, we can still compare the energy flux and luminosity upper limits to those of GRBs, as the energy released in both cases comes from the destruction of stellar objects. The computed upper limits are compared to GRBs that were detected by H.E.S.S. in the VHE range [17, 158], as well as extrapolations of GRBs that were detected at GeV energies by Fermi-LAT [30] and are used to derive prospects for the upcoming GW observation runs (see Sec. 5.7).

The work on the GRB extrapolations is lead by Sylvia Zhu (co-author of our BBH follow-up paper) and will be published in [155]. To do so, we take the set of Fermi-LAT GRBs with known redshifts and temporally extended emission [30]. For each LAT GRB, we take the energy flux at late times measured in the 100 MeV – 100 GeV energy range and using the spectral index measured by Fermi-LAT at these times, extrapolate it into 1 TeV – 10 TeV energy band. The emission is then extended in time using the power-law decay index measured by LAT at late-time. The energy flux is then converted to isotropic luminosity at the GRB redshifts. Note that these are simplistic extrapolations and they result in overpredictions on the VHE flux of the LAT GRBs. Some of these GRBs have spectral indices of -2 suggesting that the spectrum turns over above the LAT energy range. In addition, the peak of the γ-ray emission shifts to lower energies as the blast wave decelerates, reducing the flux at VHE γ-rays, whereas we have essentially assumed that there is no spectral evolution above the LAT range. To estimate the effect of our assumption, we found that if the spectrum softens from $\gamma_{\rm LAT} \rightarrow \gamma_{\rm LAT} + 0.5$ (and from $\gamma_{\rm LAT} \rightarrow \gamma_{\rm LAT} + 1$) when going from the LAT to the H.E.S.S. energy range, the luminosity drops by a factor of around 50 (and to about three orders of magnitude for $\gamma_{\rm LAT} + 1$).

The observed energy flux calculation of the GRBs is also performed by Sylvia Zhu. For the VHE-

detected GRB 180720B, we calculate the energy flux of the observed spectrum using the power law fit to the data (i.e., the fit that is EBL absorbed). For GRB 190829A, this information is not provided for the third night on its own, so we calculate the EBL-attenuated energy flux for each of the three nights separately using the constant intrinsic photon index of 2.07 derived by combining the data from all three nights. For the LAT GRBs, we take the extrapolated spectra and calculate the effect of the EBL on these spectra as if the LAT GRBs are all at the redshift of S190728q and over the specific energy range of S190728q. Using one of the other BBH events results in a decrease in the energy flux extrapolations by at most 50% for the "distant" S190512at and S200224ca, and an increase of less than 75% for the "nearby" GW170814.

Moreover, the temporal extrapolation assumes that the temporal evolution remains unchanged and that all the LAT GRBs are on-axis events. The latter is an assumption that holds given that the light curves of these GRBs decays with time and no subsequent re-brightening was observed like in the case of GW170817. In fact, due to the degeneracy between the inclination angle and the source distance the viewing angle remains unconstrained for the GW events. Constrains on the viewing angle can be placed by knowledge of the host galaxy, for instance, which is difficult to ascertain without an electromagnetic counterpart. Because of this, the inclination angles of the events discussed here are unconstrained, and cannot be used to further predict the behavior of any potential electromagnetic emission. In addition, all except one of the LAT GRBs (and both of the H.E.S.S. GRBs) are long GRBs, whereas short GRBs are the ones associated with merger events. Therefore, the LAT extrapolations should be considered as simply representing a "range" of potential behavior and should not be considered very strictly.

The luminosity comparisons are shown in Fig. 5.9. We see that the upper limits derived from the H.E.S.S. observations lie below some of the extrapolated LAT GRB level — given that the GRBs in general are located at large distances. They are also at the same level of the GRB 190829A which is at a similarly low redshift and below the GRB 180720B level which is at a relatively high redshift. This suggests that if the studied GW events produced GRBs similar to the ones shown in the plot, H.E.S.S. would have a good chance of detecting the VHE emission. It can be seen that the two closer events (GW170814 and S190728q) have the most constraining luminosity upper limits. The level of the upper limit is not greatly affected by the observation duration, due to the tiled nature of the observations. In comparison, the upper limit for GW170817 taken over the entire observation duration is three orders of magnitude lower, primarily because of this event's proximity but also due to the deeper observations of this well localized source (3.2 hours) [46].

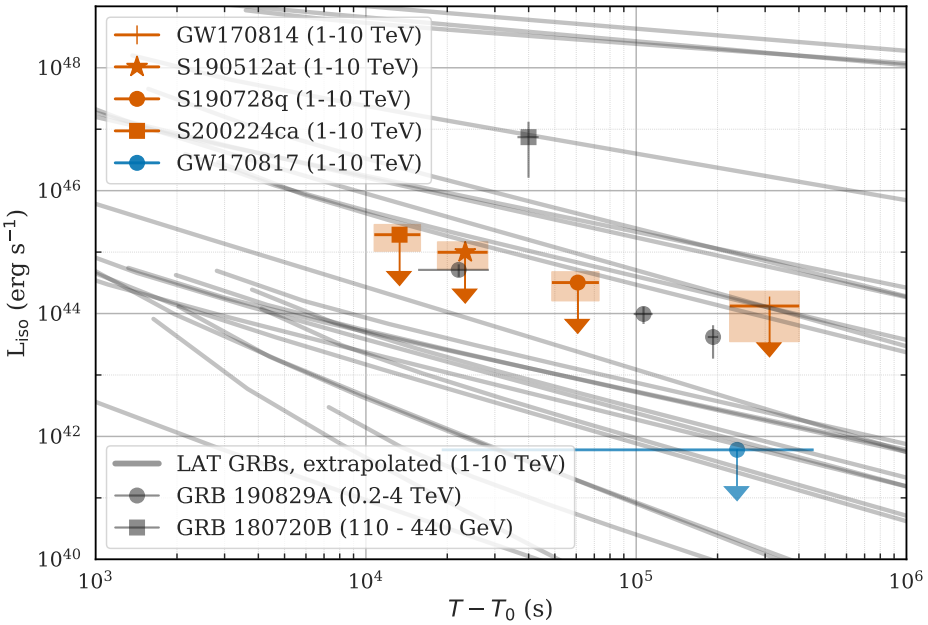

Figure 5.9: Mean (range points) and standard deviation (orange bands) of the per-pixel luminosity upper limits for the four BBH events in the 1-10 TeV energy range. The grey lines represent the extrapolated luminosity for the Fermi-LAT GRBs with knows redshifts and extended emission, and the blue points represent the H.E.S.S. detected VHE GRB luminosities. The luminosity upper limit for GW170817 derived from the H.E.S.S. observations [16] is shown in black. All five GW upper limits are calculated assuming an intrinsic E^{-2} spectrum. See text for details. From [155].

The average energy flux upper limits for the GW events are shown in Fig. 5.10, along with the LAT GRB extrapolations as well as the measured values for the H.E.S.S.-detected GRBs. The upper limits for the four BBH merger events studied here span a large range in observation delays, but lie at similar levels. The upper limits for the BBH events lie over an order of magnitude above the expectations for almost all of the GRBs. We can see that in this case, the H.E.S.S upper limits would have to have happened at a much earlier phase (with smaller $T - T_0$) or with much lower sensitivities. For the latter, longer observations per target would be required. I remind the reader that unlike for GRBs, during GW follow-up observations no single sky position gets as much exposure as it would in a standard single-position multi-hour follow up. However, looking at the levels of the GW170817 upper limits, which were derived with 3.2 hours of observation, we can see that they lie below the level of the H.E.S.S. sensitivity presented here but is still not at the level of the extrapolated LAT GRBs. Therefore, focusing on minimizing $T - T_0$ would result in better results. We note that assuming the measured GRB 190829A spectrum extends up to 40 TeV increases the absorbed energy flux by only 7%, and the increase is negligible for GRB 180720B given its farther distance)

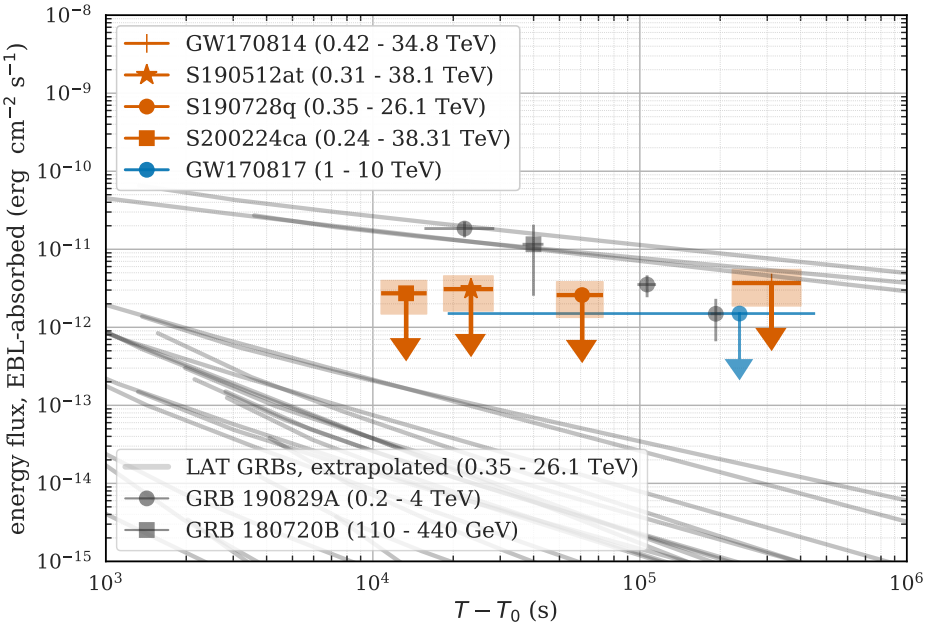

Figure 5.10: Mean (range points) and standard deviation (orange bands) of the per-pixel integral energy flux upper limits for the four BBH events from the per-pixel EBL-absorbed integrated energy flux upper limit maps. These are calculated using the specific energy range and index for each event, based on the redshift (Table 5.3). The grey lines represent the extrapolated flux for Fermi-LAT GRBs with known redhsift and extended emission into the specific energy band of S190728q. The EBL absorption for the LAT GRBs is calculated based on the redshift of S190728q. The blue points represent the energy flux for the H.E.S.S. VHE detected GRBs. The measurements for the GW170817 [16] energy flux upper limits is shown in black. See text for details. From [155].

5.7 Prospects for O4

For the GW events included in this study, the delay between merger and H.E.S.S. detection is of the order of hours (days for GW170814) due to the necessity of waiting for observation conditions to be fulfilled (*darkness* and zenith angle constraints mainly). The low rate of well localized events in the previous Advanced LIGO and Virgo runs meant that H.E.S.S. was unlikely to have observed an event with a favorable time and position. In the following, the detection expectations are taken from [7] keeping in mind that these numbers are regularly updated. In fact, for O3, 25% of events were expected to have 90% localisation region similar to the four events studied here and the expected rate was 18^{+53}_{-12} event per year. From [1], it can be seen that this prediction was more or less accurate. Taking into consideration these expectations, the number of events that would be well localised to be considered for observations by H.E.S.S. during O3 is approximately 4^{+13}_{-3}. Considering an isotropic distribution in the sky and the fact that half the sky is reachable by H.E.S.S. this number drops to only 2^{+7}_{-2}. Taking into account that on average H.E.S.S. can observe for 6 hours a night (averaging over a year), the number of expected *prompt* follow-ups by H.E.S.S.

for O3 is 1^{+2}_{-1}. This number turns out to be accurate given that H.E.S.S. had the possibility to observe only one GW event (S200224ca) promptly but couldn't due to bad weather (see Sec. 4.4.2).

The number of events expected to have good localisation increases to 75% for the four-interferometer network in O4, and with an estimated event rate of 90^{+232}_{-55} per year, this means around 67^{+174}_{-41} mergers per year would pass the requirements for H.E.S.S. follow up. Given that around half the sky is observable by H.E.S.S., and taking into account that on average H.E.S.S. can observe for 6 hours a night again, this results in approximately 8^{+22}_{-5} events per year occurring during *dark* time with a possibility of *prompt* observation. This would mean the upper limit in Figure 5.10 moving to much smaller values of $T - T_0$ — depending on the alert latency — for around 8 events a year (not accounting for bad weather).

Additionally, given the more precise localisations expected in O4, H.E.S.S. could instead choose to spend time on deeper observations of well localized GW events. In O4, around 35% of mergers observed by the four-interferometer network are expected to have 90% credible areas of less than 20 deg^2 comparable to the H.E.S.S. FoV. For an expected rate of 90^{+232}_{-55}, the number of events with very good localisation is 35^{+81}_{-19} per year. Considering a uniform distribution in the sky, and taking into account the events that will be located "behind the sun" during H.E.S.S. *dark* time, this translates to around 8^{+20}_{-5} events per year for which at least the 50% credible region could be observed with only one pointing. This would then allow the energy flux upper limit in Figure 5.10 to improve by a factor of ~ 5 depending on the amount of observation time and assuming a maximum continuous observation time of 12 hours. I note that the number of events occurring during *dark* time and that could be observed with only one pointing is in that case 4^{+10}_{-2}.

In conclusion, improving the chances of a VHE detection would require reducing the delay of follow-up observations, and/or spending more time observing single sky regions. Minimizing the observation delay (i.e., following up GW events that are immediately observable by H.E.S.S.) would have a greater effect on the detectability than reducing the sky coverage and spending more time observing single positions. As described in this section, this will naturally happen in the next observing runs, with the increased rate of GW detections. Therefore, we do not expect to fundamentally alter our observing strategy, and will continue to prioritize sky coverage.

Chapter 6

GW/GRB 170817 long-term follow-up with H.E.S.S.

6.1 GW/GRB 170817 models

The X-ray emission detected from GW170817 $\sim$9 days after the merger provides the observational link that was missing to related BNS mergers to the afterglow of sGRBs. These late emissions are typical synchrotron radiation that indicates the existence of electron acceleration in the merger remnant in the ejecta magnetic field [345]. The delayed afterglow onset of the radio and X rays could indicate that GW170817 is seen at an off-axis angle. However, [354] and [185] argue that the observed emission could not account for the observed γ-ray signal and proposed alternative models, a structured jet or a choked jet. A structured jet is a jet with an angular profile of Lorentz factors [187], while a chocked jet is a jet enveloped in a mildly relativistic isotropic expanding cocoon, with a possibility that the jet might emerge from the cocoon [206]. The cases of a uniform jet and the simple cocoon models predict a sharp rise in the afterglow, but the subsequent re-brightening ruled out these two models. As shown in Fig. 6.1 the synchrotron emission started to plateau after 160 days after the merger and then faded. The fading of the emission is related to the Sedov phase where the adiabatic expansion of the remnants decelerates, ceasing the non-thermal emission from the merger. Extensive X-ray and radio observations of the source are presented in [143]. Later on, [356] using radio, optical and X-ray observations show that the afterglow emission shows a rapid decline that is faster than cocoon-dominated/choked jet models.

The early optical emission is from the kilonova and is not directly related to the GRB afterglow. The GRB optical afterglow is much fainter and is visible 100 days after the merger [236]. Today the best

explanation of the afterglow emission seen from GW/GRB 170817 is a structured jet misaligned with our line of sight i.e. seen at an off-axis angle (at around 21 deg), with a possible continued energy injection by a long-lived central engine [355]. The delayed subsequent brightening of the afterglow emission is explained by the fact that the jet opening angle starts to increase until it becomes in the line of sight of an observer on Earth, similar to the case illustrated in Fig. 2.2. Furthermore, in the upcoming months/years we might observe the onset of a non-thermal kilonova afterglow, produced by the interaction of the sub-relativistic merger ejecta with the ambient medium, marked by the flattening and further re-brightening of the X-ray curve depending on the velocity of the ejecta.

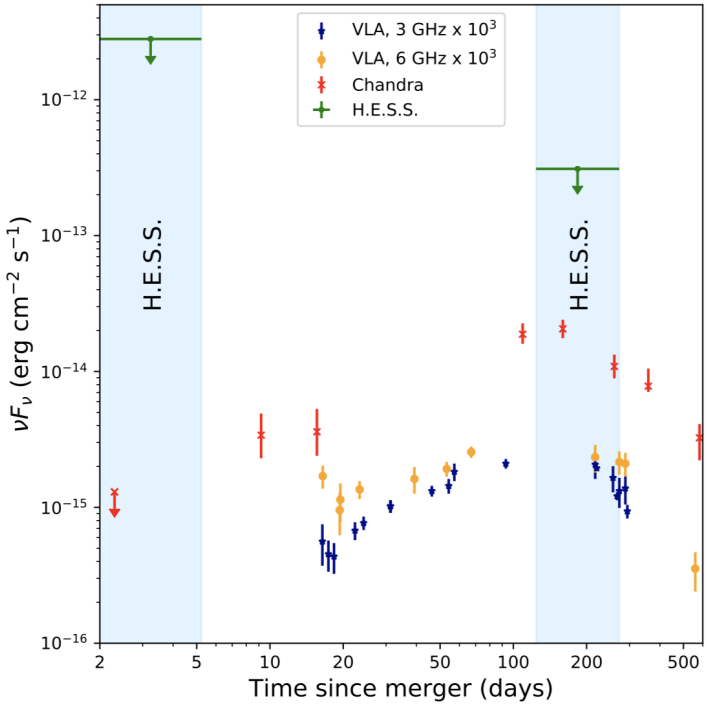

Figure 6.1: VLA radio data at 3 GHz (blue stars) and 6 GHz (orange circles) [144] [33] [248] [106] [34], [262] [143], Chandra X- ray data [269] [143] (red crosses) and the H.E.S.S VHE γ-ray observation windows (blue areas) and the derived 1-10 TeV upper limits (green arrows) with CT1-5 discussed in the following sections. From [18].

6.2 Short-term follow-up by H.E.S.S.

The short-term rapid follow-up of GW170817 is presented in [16]. H.E.S.S. observed the GW counterpart from 5.3 h to 126 h after the merger with 7 runs. The analysis is performed with `H.E.S.S.II Mono` using data from the 28-m large telescope only with *loose* cuts in order to lower the energy threshold. The

average zenith angle of the observations is relatively high ($\sim 60\,\mathrm{deg}$) leading to an energy threshold of 270 GeV. No significant VHE emission is detected. The upper limits shown in Fig. 6.2 computed from these observations are the first stringent upper limits on VHE emission from BNS merger. Due to the proximity of the event ($z = 0.0097$) no EBL absorption correction is applied.

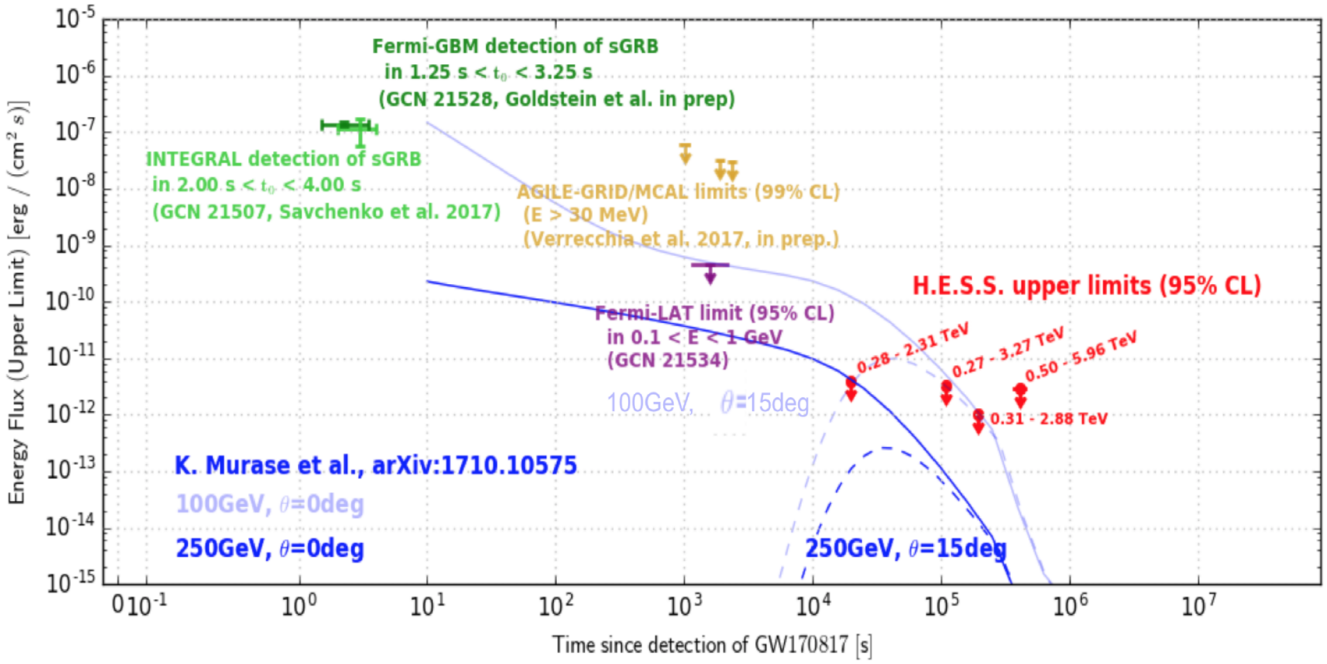

Figure 6.2: γ-ray lightcurve generated by external inverse Compton radiation for emission at $E = 100\,\mathrm{GeV}$ and $E = 250\,\mathrm{GeV}$ considering viewing angles $\theta = 0\,\mathrm{deg}$ and $\theta = 15\,\mathrm{deg}$ with upper limits on the VHE spectrum derived from H.E.S.S. observation on GW170817. From [331], adapted from [264].

[264] investigated the GeV-TeV γ-ray emission that involves a short GRB-like jet generated by a BNS merger, for both on-axis and off-axis observers, by considering Inverse-Compton emission from the up-scattering of X-ray photons by relativistic electrons in the jet. The simulated lightcurves from their models by external inverse Compton radiation, for $E = 100\,\mathrm{GeV}$ and $E = 250\,\mathrm{GeV}$ for observer angles $\theta = 0\,\mathrm{deg}$ and $\theta = 15\,\mathrm{deg}$ are overlaid on the lightcurve from H.E.S.S. shown in Fig. 6.2. The H.E.S.S. upper limits show that if the jet was viewed at an angle $\theta = 0\,\mathrm{deg}$, VHE emission would have been detected. The H.E.S.S. upper limits are consistent with the off-axis interpretation of a canonical jet observed at a viewing angle which is larger than $\theta = 15\,\mathrm{deg}$. Moreover, the simulated spectrum of VHE emission generated by IC radiation at 4.4 hours and 7 hours for viewing angle $\theta = 0\,\mathrm{deg}$ and at 5.5 hours for viewing angle $\theta = 15\,\mathrm{deg}$ are compared to the H.E.S.S. upper limits in Fig. 6.3. The non-detection by H.E.S.S. and the derived differential upper limits are consistent with the viewing angle at $\theta = 15\,\mathrm{deg}$ model. This is an example of how upper limits from VHE observations can constrain the parameters of the GRB jet.

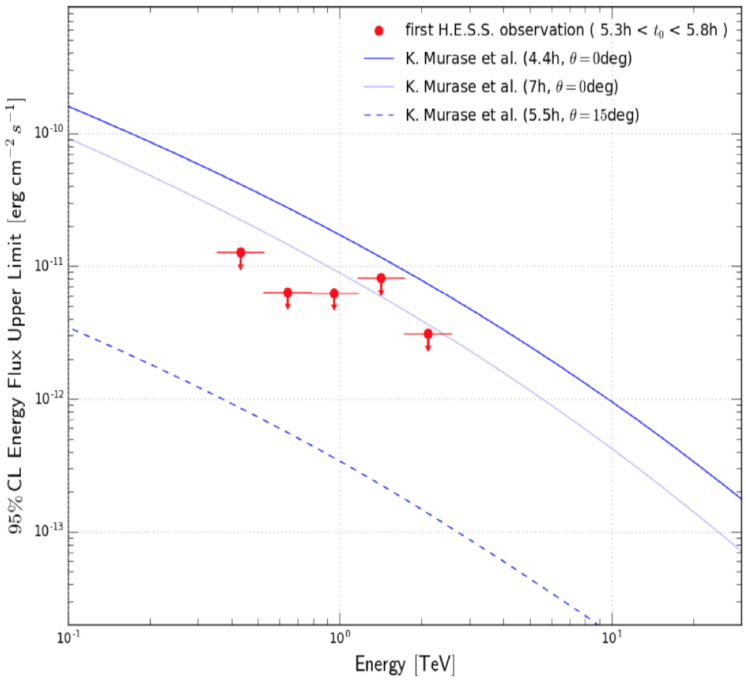

Figure 6.3: γ-ray spectra generated by external inverse Compton radiation for emission at different times considering viewing angles $\theta = 0\mathrm{deg}$ and $\theta = 15\mathrm{deg}$ with differential upper limits on the VHE spectrum derived from the first H.E.S.S. observation on GW170817. From [331], adapted from [264].

6.3 Long-term follow-up motivation

[319] (see also [345]) show that radio and x-ray observations can be used to constrain the magnetic field in the ejecta. The authors constrain the magnetic field strength in the source:

$$0.03\,\mathrm{mG} < \mathrm{B} < 2\,\mathrm{mG} \tag{6.1}$$

In the same paper, the authors also argue that γ-ray observations provide better constraints on the magnetic field. In the BNS merger environment embedded with radiation and non-thermal accelerated particles, inverse-Compton scattering of the photons by the electrons is expected, leading to IC emission in the γ-ray domain. The non-thermal emission spectrum would have two main components: the synchrotron and the IC components. Observational evidence of GW170817 show that at early times, the kilonova provides the dominant target radiation field in the remnant for IC scattering. However, the kilonova is rapidly fading with a flux that falls with $t^{-2.3}$, which will result in late-time dominance of the synchrotron radiation. In that case it is expected that SSC will dominate the IC emission since the same electron population that is producing synchrotron emission is scattering the emitted photons. While the radio and

X-ray observations (synchrotron emission) provide information on the product of the energy density in electrons and in the magnetic field $\mu_e \mu_B$, the SSC component itself is proportional to $\mu_e^2 \mu_B$. When the magnetic field is weaker in order to maintain the synchrotron level of emission it means that the energy density in electrons is higher and vice-versa (i.e. Fig. 6.4), and radio and X-ray observation cannot break this ambiguity by themselves. By modeling the IC emission at later times after the thermal emission fades (because at early times thermal emission still provides considerable target for inverse-Compton scattering electrons), [319] show that H.E.S.S. observations of the source can provide upper limits in the TeV emission domain ($\sim$1 TeV) that will be used to place a more constraining lower limit on the magnetic field and break the ambiguity. The calculations are shown in Sec. 6.6.

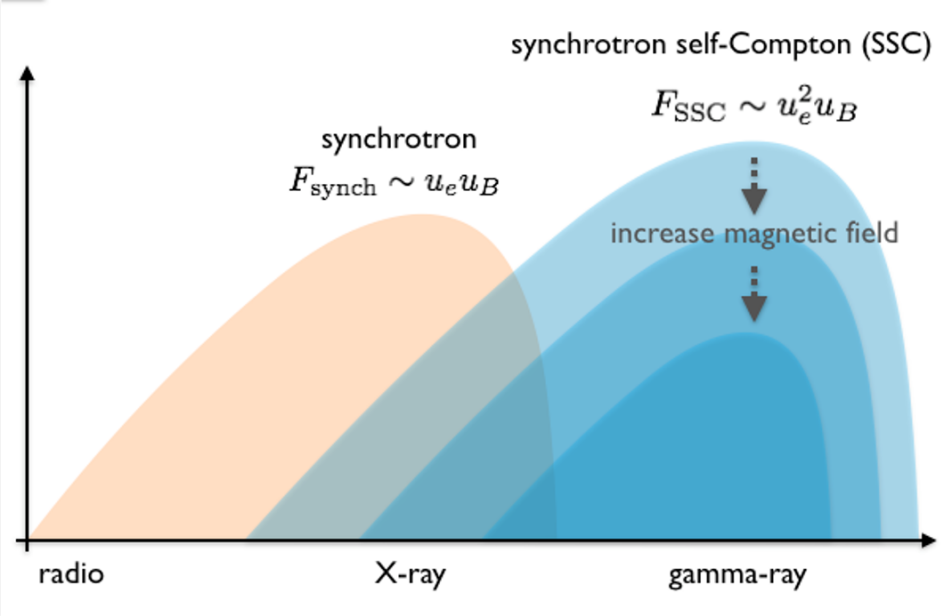

Figure 6.4: Spectral Energy Distribution representation of EM170817. The value of the IC flux allows to determine the strength of the magnetic field. The magnetic field increases when the IC emission decreases to keep $\mu_e \mu_B$ constant. From internal communication with Stefan Ohm.

6.4 Long-term observations and data selection

During the peak and the fading of the sycnchrotron emission, H.E.S.S. was probing the VHE γ-ray emission from the source as shown in Fig. 6.1. The H.E.S.S. long term follow-up observations started on 16 December 2017 (124 days after the merger) and lasted until 17 May 2018 (272 days after the merger). All available telescopes including the four 12-m small telescope and the large 28-m telescope were used when possible. Before starting with the analysis we perform a data selection and a data quality check.

The entire analysis procedure, results and interpretation are presented in the following sections.

Data selection: The preliminary data selection for the analysis is performed by searching in the H.E.S.S. database for observations fitting the follow-up analysis criteria. To do that for the *mono* analysis (`std`), I select the observation runs that fit the following criteria:

- The run should include the EM170817 position in the FoV.
- The run should be taken in the period after the detection of GW170817 until the end of the long-term follow-up campaign.
- Runs that have a duration less than 5 minutes are discarded.
- The observations should be performed with the CT5 telescope.

I find in the H.E.S.S. database 104 runs that the fit these run selection criteria.

Data quality check: The data quality check (detailed in Sec. 1.3.2) is performed before each analysis. After a thorough check, any hardware issues will be identified and biased runs will be discarded. The analysis in done with the remaining runs.

I perform the data quality check for all the 104 CT5 observation runs of this source during the campaign. Here, I will not go through all the details, I will instead provide a short summary of the outcome of this data quality check. From the 104 selected runs, 1 run is removed due to a hotspot in the CoG map, and three other runs where removed due to inhomogeneous CoG maps; 4 runs where removed due to unstable pedestal levels and a high bad pixel fraction. Finally 12 runs are discarded due to high variability in the trigger rates caused mainly by bad weather conditions (clouds mainly). This leaves 32.2 hours of CT5 data for the analysis.

6.5 Analysis, results and upper limits

The data from the other four telescopes is also analysed. The overall analysis is divided into three data sets. The first data set includes observations from all five telescopes during the GW170817 short-term follow-up that was not analysed in [16]. The second data set includes the CT5 *mono* observations during the long-term follow-up of EM170817 presented above. The third data set includes CT1-5 (all five telescopes) *stereo* observations during the long-term follow-up of EM170817 analysed in this section. My

advisor and I were responsible for the CT5 *mono* analysis (`M++ H.E.S.S.II Mono`), the analysis from the other four telescopes is done by other members of the task force. In this section, I first show the final results of `M++` *mono* analysis, then the final results of the analysis done by combining data from all five telescopes. The results of the latter gives in total $\sim$53.9 hours of data with CT1-5 used to constrain the magnetic field [18].

For the *mono* `std` standard analysis, the events from the CT5 telescope are selected and their direction and energy reconstructed using the log-likelihood optimization [103] described in Sec. 1.3.2. After this, the background subtraction is performed using the "Ring background" method described in Sec. 1.3.2. A circular region-of-interest centered on the position of SSS17a with a radius of 0.1 deg is defined. The Excess is determined following Eq. 1.31. The excess map is presented in the left side of Fig. 6.5. Using [210] the excess map is transformed into significance map (right side of Fig. 6.5) using Eq. 1.33.

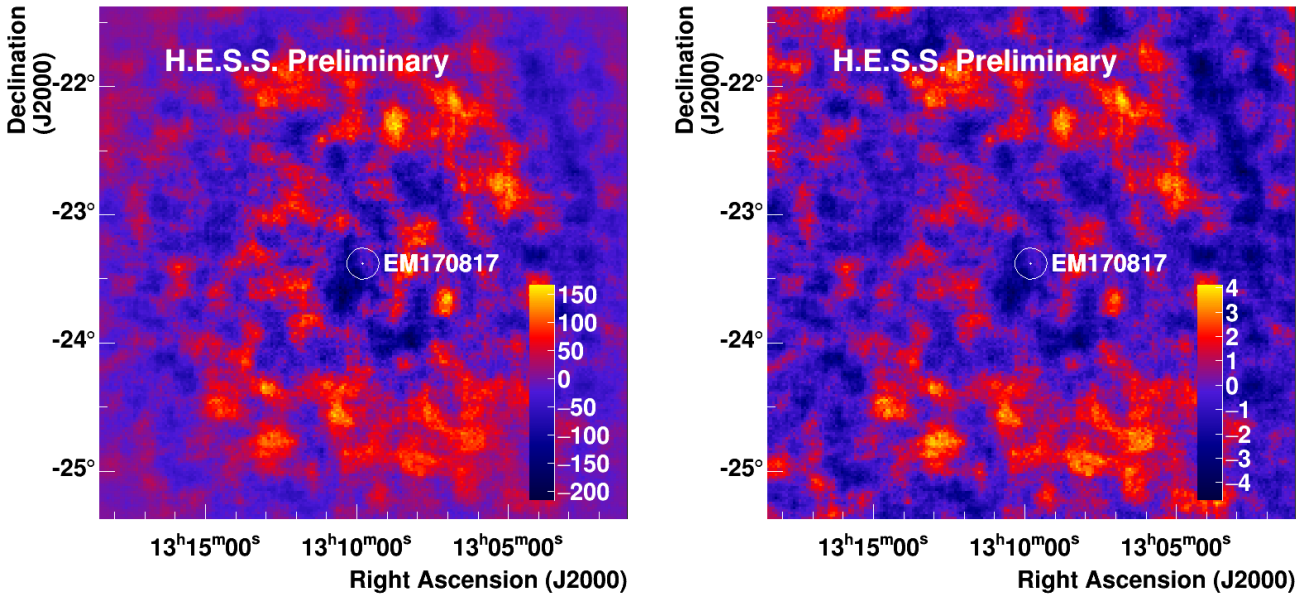

Figure 6.5: Excess (left) and significance (right) map computed from the `H.E.S.S.II mono` long-term observations of EM170817

No significant signal above 5 sigma is detected at the position of the source or anywhere in the map. The θ^2 histogram (shown in Fig. 7.4 shows the distribution of the square of the angular distance (θ^2) of gamma-like events to the center of the source region. For that the multiple off method is used (see Sec. 1.3.2). If a signal is detected we would expect to have a rise in the θ^2 values around 0 deg^2 followed by a decrease further away from the center of the source, which is not the case in Fig. 6.6.

Considering an energy threshold for the *mono* dataset where the acceptance is at 15% of its maximum

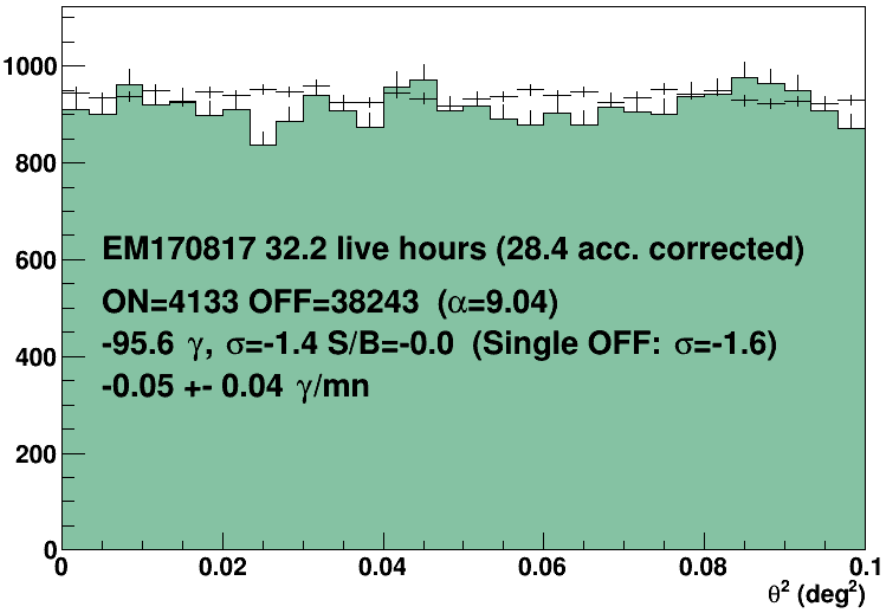

Figure 6.6: θ^2 distribution of gamma-like events around the GW/GRB 170817 region. The values of the number of ON and OFF events, the significance σ and the signal to noise (S/N) computed with the multiple-off method are displayed.

value, leading to a value of 107 GeV and a source with a E^{-2} spectrum with no EBL absorbtion, 95% confidence level differential upper limits above the energy threshold are computed following Eq. 6.2.

$$F^{UL}_{(E_1,E_2)} = \frac{\frac{N_\gamma}{N_{exp}} \int_{E_1}^{E_2} \phi_r e f dE}{\Delta E} = \frac{\frac{N_\gamma}{N_{exp}} \int_{E_1}^{E_2} \phi_0 (\frac{E}{E_0})^{-\gamma} dE}{\Delta E} \tag{6.2}$$

For each energy bin E_2–E_1, ΔE is the width of the bin, N_{exp} is the expected number inside the energy bin (integration within the bin bounds) and the remaining variables are defined in Sec.5.4.1. In each energy bin above the energy threshold, the differential flux is calculated following Eq. 6.2.

The same analysis is done for the entire dataset with the CT1-5 telescopes (*stereo*`std`) with no significant detection. The energy threshold is defined at the position of the source where the acceptance is at 10% of its maximum value for the *stereo* analysis and differential upper limits are computed. The upper limits of the `M++` CT5 *mono* and the final CT1-5 *stereo* analysis are shown in Fig. 6.7. As expected the *mono* analysis has a lower energy threshold ($\sim$ 107 GeV) than the stereo analysis ($\sim$ 133 GeV), however the *stereo* analysis is usually more constraining (depending on the energy range). The latter is used to constrain the magnetic field in the following section.

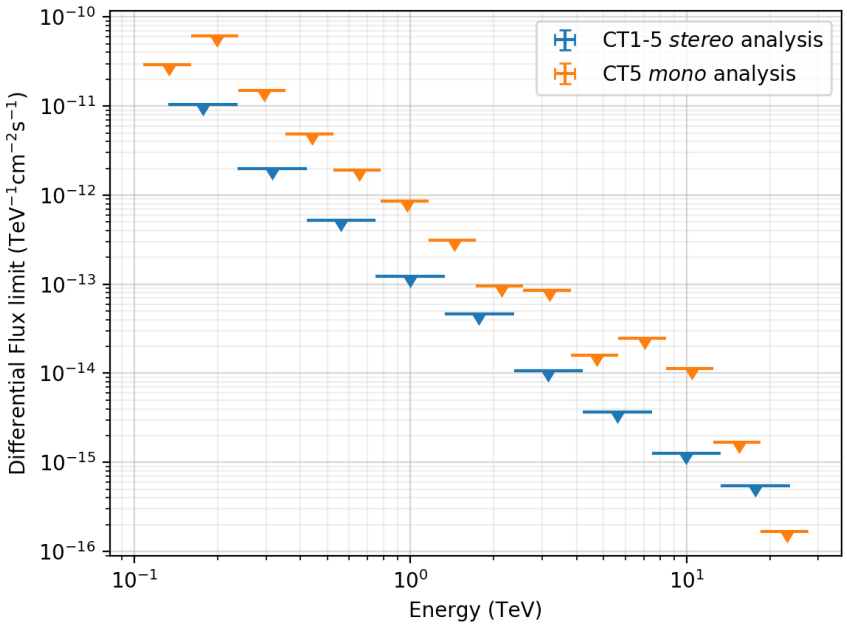

Figure 6.7: Differential upper limits computed from the H.E.S.S. CT5 *mono* and CT1-5 *stereo* long-term observations of EM170817.

The final published results of the analysis of the short-term follow-up *mono* analysis, the CT1-5 *stereo* analysis for the same dataset and the CT1-5 *stereo* analysis of the long-term follow-up are summarized in Tab. 6.1. Integral upper limits are derived in the 1-10 TeV range following the method defined in Chap 5.4.1. Moreover, the upper limits are also derived above an energy threshold E_{th} defined for each data set as explained in Chap 5.

Config	$T - T_0$ (days)	Exposure (h)	Energy range (TeV)	$F(> \mathrm{E}_{th})$ erg cm^{-2} s^{-1}	F(1-10TeV) erg cm^{-2} s^{-1}	zenith angle (deg)	Reference
CT5	0.22 - 5.23	3.2	0.27 - 8.55	$< 1.5 \times 10^{-12}$		58	[16]
CT1-5	0.22 - 5.23	3.2	0.56 - 17.8	$< 4.7 \times 10^{-12}$	$< 2.8 \times 10^{-12}$	58	[18]
CT1-5	124 - 272	53.9	0.13 - 23.7	$< 1.6 \times 10^{-12}$	$< 3.2 \times 10^{-13}$	24	[18]

Table 6.1: Properties of the H.E.S.S. data sets on GW170817 / GRB 170817A and analysis results.

6.6 Interpretation: constraining the magnetic field

Although I did not work on the modeling of the source, I report here on the work done to constrain the magnetic field in the source, using the upper limits derived in the previous section. The long-term GW170817 H.E.S.S. follow-up findings are published in [18].

Two geometric models are considered: an isotropic non-relativistic expansion of the remnant and a relativistic jet. the following entities are defined:

- β is the value of the expansion speed. It is taken as $\beta = 0.2$ in the isotropic scenario (based on photospheric velocity measurements of the remnant [289] and $\beta = 0.94$ in the jet scenario. The jet opening angle is $\theta'_{jet} = 5\,\mathrm{deg}$ and is observed at an angle $\theta_{obs} = 20\,\mathrm{deg}$. These values for the jet scenario are motivated by radio observations of superluminal motion of the source [262].

- δ is the doppler factor. We have

$$\theta_{obs} = 20^\circ = 180^\circ/\pi\tau \tag{6.3}$$

  with τ as the Lorentz factor. Therefore $\delta = \tau = 3$.

- Δt is the time since the merger and is taken as $\Delta t = 110\,\mathrm{days}$ for which there are simultaneous flux measurements in both radio and X ray bands. Moreover, in Fig. 6.1 we see that the flux levels at this time are comparable to the flux levels throughout the H.E.S.S. observation period.

- R' is the size of the emitting region in the source frame. In the jet scenario the emitting region is assumed to be a spherical blob at the front edge of the jet with $R'_{blob} \sim \delta\beta c\Delta t\theta'_{jet}$. In the isotropic scenario $R'_{iso} = \beta c\Delta t$

- B and B' are the magnetic field strength in the source in the observer frame and the source frame respectively.

- E_e and E'_e are the maximum electron energy of the emitting electrons in the observer frame and the source frame respectively.

- N_e and N'_e are the number of X-ray emitting electrons in the observer frame and the source frame respectively.

- τ'_{syn} and τ'_{IC} are the synchrotron and IC cooling times respectively.

The X-ray observations fix the maximum synchrotron observed energy $E_X = 10\,\mathrm{keV}$ [269]. This is related to the magnetic field strength in the source and the maximum electron energy of the emitting electrons

$$E'_X \sim E'^2_e B' \tag{6.4}$$

with $E'_e = \delta^{-1} E_e$ for the relativistic scenario. This means that for the relativistic jet scenario for a given value of B', $E'_e \propto \delta^{-0.5}$.

Moreover, the X-ray luminosity L'_X relates to the total number of electrons emitting X rays through

$$L'_X = N'_e E'_e / \tau'_{syn}(E'_e) \propto N'_e E'^2_e B'^2 \tag{6.5}$$

knowing that for the relativistic scenario $L'_X = \delta^{-4} L^{iso}_X$ (since the jet emits isotropically in its own rest frame). For a given value of B' and a measured X-ray flux $N'_e \propto \delta^{-3}$ in the relativistic jet scenario.

Furthermore, the γ-ray luminosity in the rest frame is:

$$L'_{IC} = N'_e E'_e / \tau'_{IC}(E'_e) \propto N'_e (L'_X / (4\pi R'^2 c)) E'^{0.5}_e \tag{6.6}$$

For a relativistic jet scenario, from the obtained relations defined above for L'_X, N'_e and E'_e in function of δ, the definition of R' for a relativistic jet and by fixing the X-ray luminosity from the X-ray observations we get for a given value of the magnetic field B':

$$L'_{IC} \propto \theta'^{-2}_{jet} (\beta \Delta t)^{-2} \delta^{-9.25} \tag{6.7}$$

In the observer's frame $L'_{IC} = \delta^{-4} L_{IC}$ and we get:

$$L_{IC} \sim 10^{46} (\frac{\theta'_{jet}}{5^\circ})^{-2} (\frac{\beta \Delta t}{0.94 \times 110 days})^{-2} (\frac{\delta}{3})^{-5.25} \mathrm{erg.s}^{-1} \tag{6.8}$$

All the variables are known in Eq. 6.8, therefore, by fixing the value of the magnetic field and for a measured X-ray flux one can predict the IC (γ-ray) luminosity. Inversely, by fixing the value the γ-ray emission and for an observed X-ray flux, one can predict the value of the magnetic field.

The upper limits derived in Sec. 6.5 translate into integral energy flux limit $\nu F\nu$ which will be used to constrain the magnetic field. To compute $\nu F\nu$ we follow: $\nu F\nu$ = $E^2 dN/dE$ where dN/dE is the spectrum which in the case of upper limits becomes $\nu F_\nu = E^2 F^{UL}_{(E_1,E_2)}$. Knowing the distance of the source the luminosity (upper limits on L_{IC}) can be deduced from the flux.

The final results are presented in Fig. 6.8. The solid and dashed curves correspond to the modelled emission considering the minimum and maximum flux values allowed by the X-ray measurements. The modelled IC flux is adjusted so it does not exceed the upper limits derived by H.E.S.S. In the relativistic

jet scenario, the magnetic field is constrained to $> 24\,\mu\mathrm{G}$ while in the isotropic outflow scenario the limit is $> 210\,\mu\mathrm{G}$. This is due to the fact that the more relativistic the jet is, N'_e should be higher in order to reach flux limits. This implies a lower B' in order to maintain the X-ray flux.

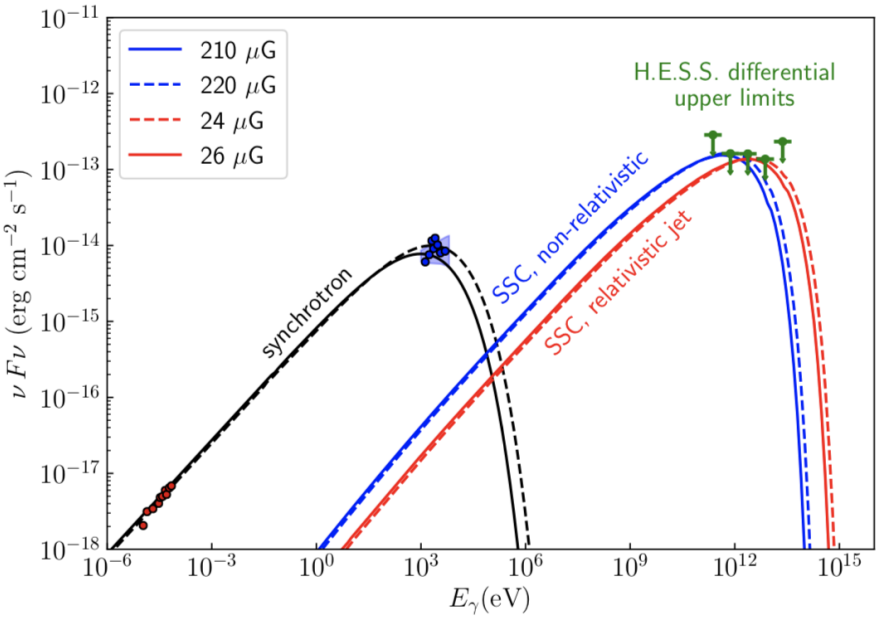

Figure 6.8: Spectral energy distribution of EM170817 for the non-relativistic (blue lines) and relativistic (red lines) scenarios. The blue and red dots correspond respectively to the X-ray and radio measurements. The green dots represent the H.E.S.S. derived upper limits. The solid and dashed lines correspond respectively to the minimum and maximum X-ray emission. From [18].

6.7 Conclusion

The study presented here certainly sheds the light on the advantages that multi-messenger and multi-wavelength observations have to offer. In a nutshell, the BNS merger itself is detected by the GW interferometers and the short GRB is promptly detected by the Fermi GBM and INTEGRAL space observatories triggering the widest follow-up campaigns around the globe. Optical observations lead to the detection of the counterpart SSS17a located in the NGC 4993 galaxy [95]. Afterglow monitoring of the source with H.E.S.S. constrained the short-term VHE emission, while the optical and infrared observations allowed the characterisation of the kilonova. The non-thermal spectrum is probed by the X-ray and radio observations that constrain the synchrotron part of the spectrum. Interferometric radio and X-ray observations are also crucial for inferring the jet properties. Finally, γ-ray observations, allow to directly probe the magnetic field by breaking the ambiguity between the magnetic field and the electron energy density.

In the H.E.S.S. collaboration, unlike short-term follow-ups of GW waves, this campaign was mainly motivated by the monitoring of MWL data (X rays and radio). No significant VHE long-term emission is detected by H.E.S.S. in the short and long term follow-ups. Upper limits on the VHE γ-ray flux are derived. These limits are interpreted as lower limits on the magnetic field in the remnant of the merger of $> 24\,\mu\mathrm{G}$ for the relativistic jet scenario and $> 210\,\mu\mathrm{G}$ for the isotropic outflow scenario.

With $\sim$ 54 hours of observations, H.E.S.S. is able to reach sensitivities in the order of 10^{-13} erg cm^{-2} s^{-1}. The future Cherenkov Telescope Array will be an order of magnitude more sensitive than H.E.S.S. CTA observations of such events will allow to place even more stringent limits on the magnetic field of BNS mergers.

Part IV

FRBs

Chapter 7

Searches for VHE gamma-rays associated to FRBs with H.E.S.S

7.1 Introduction to FRB follow-up with IACTs

As mentioned in Sec. 2.3, FRBs are characterized by their fast transient emission that is in the order of the millisecond. Several FRB models predict the emission of γ rays with the radio emission while others don't. In order to put the emission of γ rays from FRBs to the test, H.E.S.S. dedicates several hours per year ($\sim$10 hours) to the follow-up observations of FRB events. FRBs are discovered serendipitously by radio instruments and the follow-up of such fast events with medium to small FoV telescopes is challenging. In the H.E.S.S. collaboration we rely on two methods in order to attempt to find VHE γ-ray counterparts for FRBs. The first method consists in creating links between radio telescopes and H.E.S.S. using the VoEvent protocol in order to observe an FRB as quickly as possible after its detection. Since the emission of FRBs is in the order of the millisecond, this method aims mainly to probe the afterglow emission. The second method consists in observing simultaneously with radio telescopes the same region in the sky. The idea is that an FRB would be discovered during these simultaneous observations. I start with an overview of past observations of FRBs with IACTs.

In 2015, H.E.S.S. followed two FRB events that were detected by the Parkes SUrvey for Pulsars and Extragalactic Radio Bursts (SUPERB) project[1] [189]. FRB 20150418 was detected by the SUPERB project on 2015-04-18. A fading transient radio emission was detected from the FRB for 6 days which led to its association to a host elliptical galaxy at $z = 0.492 \pm 0.008$ [190]. The isotropic energy of the explosion was

[1] https://sites.google.com/site/publicsuperb/home

estimated to be in the order of a few 10^{50} erg. H.E.S.S observations of the FRB started at 17:55 UTC after the reception of the alert from the SUPERB team during day time. The H.E.S.S. observations have a delay of $\sim$14.5 hours after the detection of the event. The H.E.S.S results are presented in [157]. No significant VHE emission was detected. H.E.S.S. observations of FRB 20150418 provide the first upper limits on the emission in the VHE domain in the afterglow of a FRB. FRB 20150215 [285] was detected in the Parkes multibeam receiver at 20:41:41.146 UTC with a fluence of $\sim$2.1 Jy ms. The burst was localised at 20 deg from the galactic center with coordinates RA 18:17:27 and Dec 04:54:15. The DM measurement suggests an extragalactic origin with z $<$ 1. H.E.S.S. observed FRB 20150215 during two nights on 2015-02-22 at 02:53 UTC and 2015-02-25 starting at 02:49 UTC with a delay of several days. No significant detection was found. The FRB was also observed in the X-ray bands with Chandra and Swift-XRT with no significant transient emission detection. Several optical and radio instruments also observed the FRB with no significant detection. No neutrino counterparts were detected by ANTARES.

Several observation campaigns with IACTs were also held on other FRBs like the campaigns on the repeating FRB 20121102 and FRB 20180814 with the MAGIC and VERITAS telescopes. During the MAGIC campaign on FRB 20121102 five radio bursts were detected by Arecibo and no significant VHE γ-ray counterparts were found [165]. MAGIC is also able to detect short optical pulses through the modification of the central PMT to be able to increase its bandwidth and take advantage of the large collecting mirror surface. MAGIC is able to detect pulses with duration in the order of 1 milliseconds to 1 second and can detect Crab-like optical pulses with 10 seconds of observations [147]. No optical pulses were detected during the MAGIC observation campaign. During the VERITAS campaign on FRB 20121102 several FRBs were detected contemporaneously to VERITAS observations, however no significant VHE emission was detected. No FRBs were detected during the observations on FRB 20180814. VERITAS also searched for optical transient using their optical photometry hardware on one of their telescope with no successful detection either [169].

7.2 The H.E.S.S. rapid follow-up program of UTMOST FRBs

7.2.1 Automatic response to UTMOST FRB alerts

The FRBs previously observed by H.E.S.S. have several hours to days delays after the detection of the event. In order to decrease the follow-up delay of FRBs, I implement an automatic response in the H.E.S.S. ToO follow-up system (see Sec. 4.1) to UTMOST FRBs. UTMOST is the first radio telescope to issue

VoEvent alerts upon the detection of an FRB. The data is analysed in real time and an alert is issued upon the detection of a potential FRB. Three main parameters are used as follow-up criteria:

- The signal to noise ratio S/N. S/N is defined in [80] as the ratio of the sum of the on-pulse flux I_{ON} to the product of the RMS of the off-pulse flux I_{OFF} and square root of number of on-pulse bins n_{bin}.

$$S/N = \frac{I_{ON}}{\sqrt{n_{bin}}\, I_{OFF}} \tag{7.1}$$

  The minimum S/N values required to follow an UTMOST FRB with H.E.S.S. is 10.

- The dispersion measure DM (see Eq. 2.8 and 2.9). The DM can be used to place an upper limit on the redshift of the event. A maximum requirement of $\mathrm{DM} = 1000\,\mathrm{pc\,cm^{-3}}$ is imposed by H.E.S.S. This will limit observations to FRBs with $z <\sim 1$ (see Sec. 2.3). This is motivated by EBL absorption effects that increase with the redshift.

- The $importance$ parameter. The $importance$ parameter is specific to UTMOST and indicates if the event was vetted by a human. If the importance is 1, it means that the FRB event is vetted by a person. The importance parameter is an indication of the false alarm ratio of the event. I implement a condition requiring $importance > 0.99$ for H.E.S.S. follow-up in order to achieve a negligible false alarm rate.

If an FRB alert passes the three criteria mentioned above, the H.E.S.S. ToO follow-up system will assess the position of the FRB and will try to find an observation window where visibility and observation conditions are met (defined in Sec. 3.1). This means that the FRB should be visible with a zenith angle $<$ 60 deg during *dark* time or with low levels of moon light (*moonlight* observations defined in Sec. 3.1). Finally the observation delay will be assessed and the FRB will be observed only if a maximum delay of 2 hours is respected. This maximum observation delay was initially 6 hours but was lowered to 2 hours because we only want to prioritise *prompt* follow-up observation of FRBs (more details in Sec. 7.2.2). The schematics of the FRB module decision making tree is illustrated in Fig. 7.1.

7.2.2 H.E.S.S. follow-up of FRB 20190806

The first alert received from UTMOST that passed the H.E.S.S. filtering criteria with a maximum 6 hours delay is FRB 20190806 that was detected by UTMOST at 2019-08-06 17:07:58.0 UTC with a $\mathrm{DM} = 388.5\,\mathrm{pc\,cm^{-3}}$. Fig. 7.2 shows the Frequency versus time behaviour of the first FRB detected by UTMOST, FRB 20190806.

The upper limit on the DM-inferred redshift is $z \sim 0.32$. The H.E.S.S. ToO response system automatically triggered observations of this event for the following night with an observation delay of $\sim$4.5 hours, which is to this time the smallest FRB observation delay for H.E.S.S. Observations lasted for 2 hours with the CT1-4 telescopes (CT5 was undergoing the camera swap mentioned in Sec. 5.2). This observation is the first successful automatic FRB ToO follow-up scheduled by H.E.S.S.

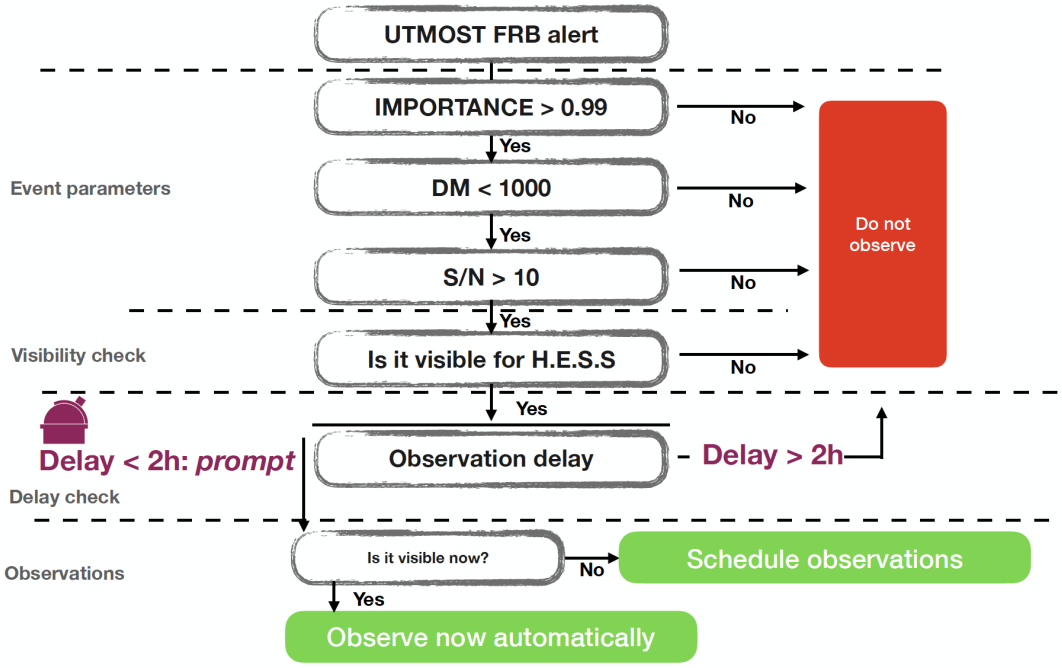

Figure 7.1: Schematic overview of the decision tree used in the automatic response of H.E.S.S to UTMOST FRB events.

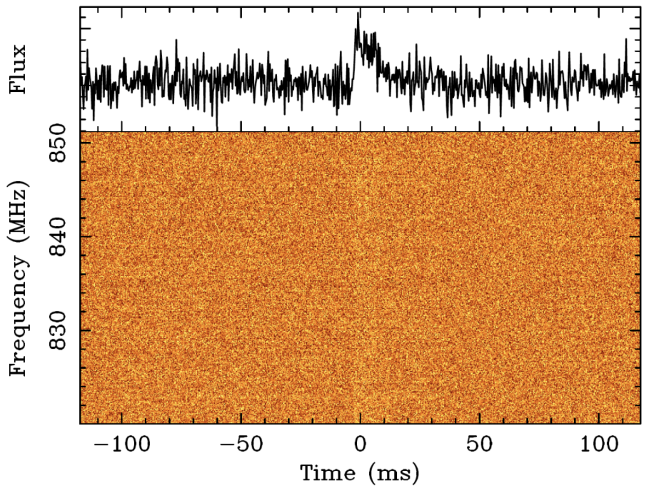

Figure 7.2: Frequency versus time behaviour of FRB 20190806 detected by UTMOST. The lower panel is a frequency-time plot of spectral brightness and the upper panel shows the frequency-averaged pulse profile. From `https://astronomy.swin.edu.au/research/utmost/?p=1664`.

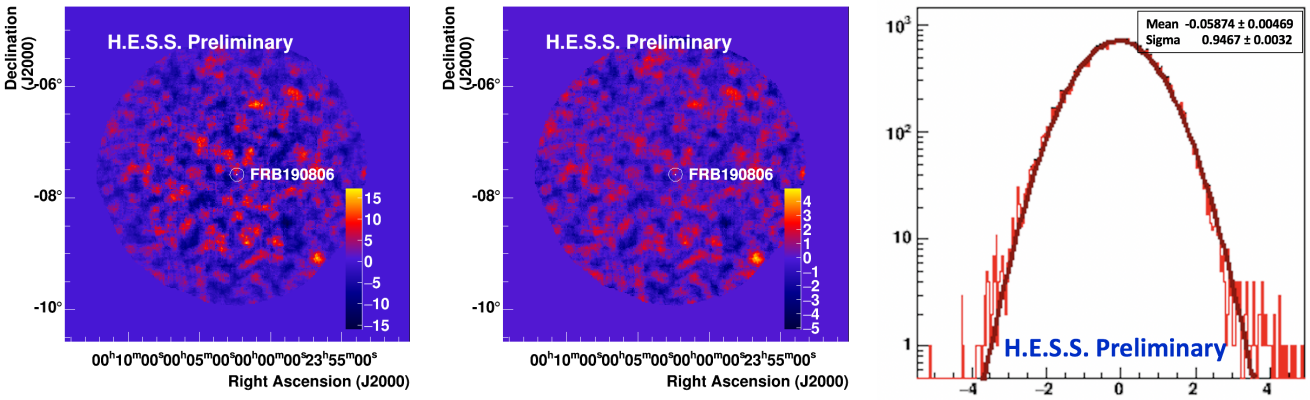

Figure 7.3: **Left:** Excess map computed from the H.E.S.S. observational data taken on FRB 20190806. **Middle:** Significance map computed from the H.E.S.S. excess map of FRB 20190806. The hotspost in the bottom right of the maps could not be matched with any source and did not show in the cross-check analysis. It is probably a statistical fluctuation. **Right:** Significance distribution of the H.E.S.S. significance map entries in red and a Gaussian distribution fit in black.

After this event we changed the H.E.S.S. strategy for FRB *prompt* observations. The new strategy relies on lowering the maximum observation delay to 2 hours and observing the FRB with only 1 run. The observations are extended if a significant signal is detected in the real-time analysis.

H.E.S.S. analysis and preliminary results

Using the *model* [103] analysis described in Sec. 1.3.2 with *loose* cuts and the "Ring Background" method [63] with a 0.122 deg radius source region centered on the FRB position, I compute the excess, significance and significance distribution plots presented in Fig. 7.3.

No significant VHE γ-ray signal is detect above the 5 σ level. The θ^2 histogram (see Sec. 6.5) computed with the multiple off method is used (see Sec. 1.3.2) is shown in Fig. 7.4. As explained in the last chapter, if a signal is detected we would expect to have a rise in the θ^2 values around 0 deg^2 followed by a decrease further away from the center of the source, which is not the case in Fig. 7.4.

VHE gamma-ray variability search

Given the fast nature of FRB emission, I also want to search for a transient VHE signal like a sudden rise of the emission (or pulse). In case they exist, fast γ-ray pulses from the source with high variability would be embedded in the background and difficult to detect if the entire data set is analysed and significance is considered over extended period of time. Therefore I search for variable transient signals in the data set using the tools provided in [76]. These tools use the arrival times of the gamma-like (gamma

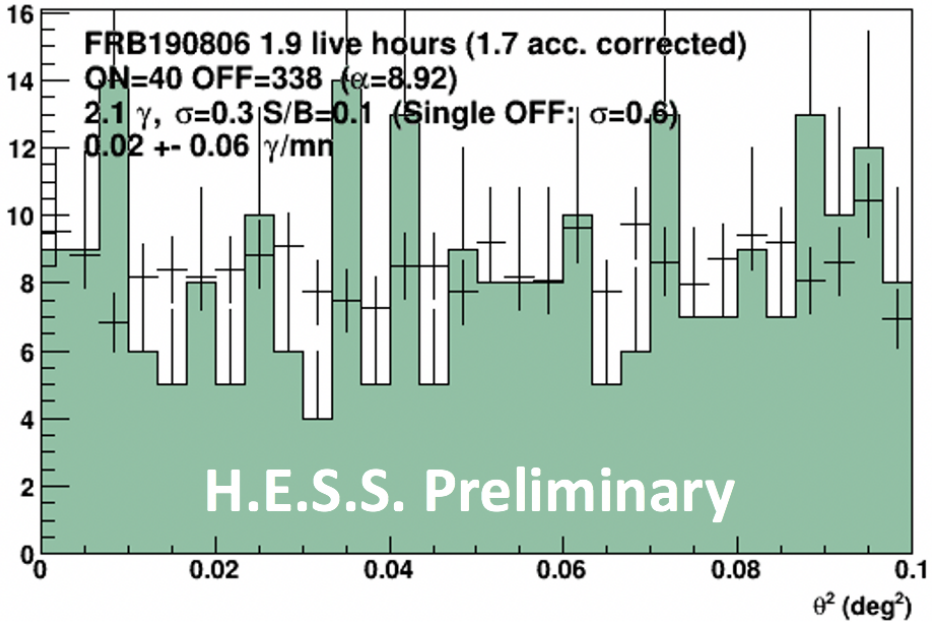

Figure 7.4: θ^2 distribution of gamma-like events around the FRB 20190806 region. The values of the number of ON and OFF events, the significance σ and the signal to noise (S/N) computed with the multiple-off method are displayed.

candidate) events that pass the selection cuts by the *model* analysis in the source region. In order to do that, the arrival times should be corrected for the instrumental induced variations. This is done by computing new arrival acceptance-corrected times. This step is described in Sec. 2.2 of [76]. The normalized acceptance-corrected times of arrival of gamma-like events can be used in order to perform several tests to search for emission variability.

Cumulative sum test: The cumulative sum test was first developed in [273]. The statistics of the arrival time of the background events is based on a Poisson behavior. The test consists in calculating the cumulative sum variable χ_i for a time i. For a set of N time intervals ΔT, $\chi_i = \sum_{k=1}^{i}(\Delta T_K - < \Delta T >)$ with $< \Delta T >= 1/N \sum_{i=1}^{N} \Delta T_i$. It has a null mean. The detailed steps and definitions are shown in Sec. 3.3 of [76]. For each normalized acceptance-corrected arrival time the cumulative sum test will calculate how close the variable χ_i is to a Poisson distribution. This test does not require any assumption regarding the time- scale to probe and requires a minimum of 20 gamma-like events in the studied sample. The estimator is bound to be null for the first and the last event.

I show in Fig. 7.5 the cumulative sum test results for FRB 20190806. The gamma-like events inside the source vary within $\sim 2\sigma$ from a Poisson behaviour and therefore no significant variability is detected.

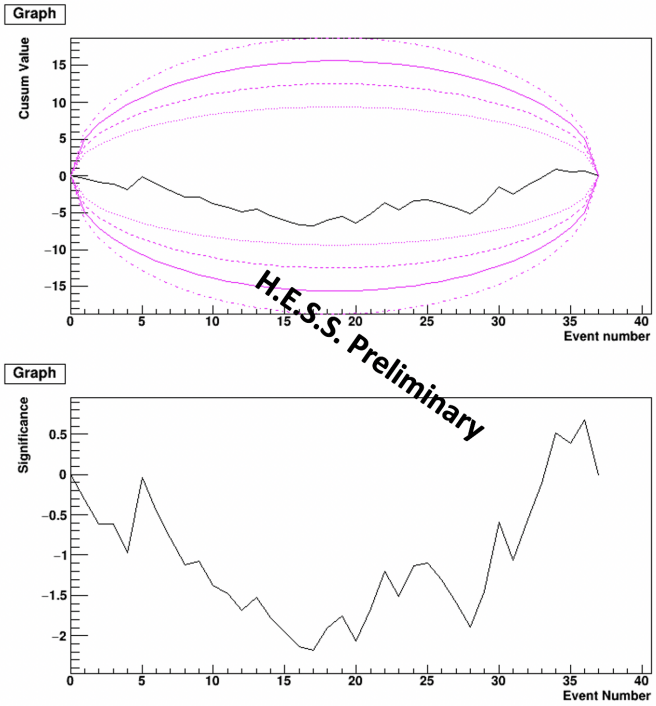

Figure 7.5: Cumulative sum variable (upper panel) and its significance (lower panel) computed for each gamma-like event inside the source (FRB 20190806) region with normalized acceptance-corrected arrival times. The magenta lines correspond to the 3 σ, 4σ, 5 σ and 6 σ levels variation from a Poisson behaviour.

ON-OFF test: The ON-OFF test is performed with the real arrival time without taking into consideration the acceptance-correction. The arrival times are divided into bins with a binning size being the probed time scale. The gamma-like events inside each bin are possibly composed of γ rays and background events. In order to compute the excess of γ rays inside the bins, the number of events inside each bin is compared to the estimated number of background events using all the other bins following. The excess and the significance are calculated following Eq. 1.31 and Eq. 1.33 respectively. I note that the bins showing an excess of variable emission ($> 5\sigma$) are not considered in the background. Since several numbers of bins are tested, a trial factor should be taken into consideration. The pre-trial probability can be converted into a probability corrected for a trial factor. The details of this test are shown in Sec. 3.2 of [76]. the ON-OFF test permits to determine if an increase in the source activity occurs or if a transient emission happens. If a γ-ray source observed is steady, the ON-OFF test will not show significant excess. As prescribed in [210] the ON and OFF regions should have at least 10 gamma-like events. The probed time scale should be chosen accordingly. I run the ON-OFF test on the H.E.S.S. available data set from FRB 20190806 observations and don't find any significant variability on the scale of few minutes. An example of the output of this test is shown in Fig. 7.10 for another analysis.

Additional tests like the Exp test [298], the Bayesian block test [327] and the Poisson probability test can also be applied. In a nutshell, the Exp test uses an estimator that will be equal to 1/e for Poisson behaviour, smaller for a burst like behaviour and larger for a periodical behavior. The Exp-Test for FRB 20190806 gives a significance of 0.877646 σ that the distribution of the arrival times diverges from a Poisson distribution. The Bayesian block test will search for localized structures of pulses and variation in the data set independent of any pulse-shape model. The Bayesian block test does not reveal any pulsed structure in the case of FRB 20190806 H.E.S.S. data. The Poisson probability test is detailed in Chap. 8. The aim of this test is to compute the deviation of the gamma-like event's arrival from a Poisson behaviour, by considering the acceptance-arrival times and a pre-defined number of expected gamma-like events arrival intervals. This test also does not show any significant deviation above 2 σ.

7.3 MWL observation campaigns

7.3.1 H.E.S.S., MeerKAT and Swift campaign on FRB 20171019A

The H.E.S.S., MeerKAT and Swift campaign on FRB 20171019A is in the context of a study that aims to search for persistent radio emission and MWL counterparts of three ASKAP detected FRBs: two non-repeating FRBs, FRB 20190711 and FRB 20190714, and the repeating FRB 20171019A. The campaign was held with MeerKAT from August to September 2019. The findings will be published in [86].

H.E.S.S. joined the campaign later on and participated in the observations of FRB 20171019A only. Swift observations were also triggered contemporaneously to H.E.S.S. and MeerKAT observation on this FRB. I was responsible for the H.E.S.S. and Swift analysis for this campaign.

FRB 20171019A was first detected by ASKAP [335], with two additional bursts detected by Green Banks [204] and CHIME [277]. FRB 20171019A is localised with an uncertainty region of $10' \times 10'$. The host galaxy of FRB 20171019A is not identified. FRB 20190711 [241] and FRB 20190714 [149] are localised to galaxies with redhsift $z = 0.2365$ and $z = 0.5220$ respectively. FRB 20190711 and FRB 20190714 are localised at 2 kpc and 3 kpc from the center of their hosts respectively.

The search for persistent radio emission from FRBs with MeerKAT.

The radio observations were analysed by other people in the task group. I present here the main results of their analysis. The data analysis and results of the MeerKAT observations of FRBs 20190711A,

20190714A, and FRB 20171019A is detailed in [86]. From the targeted FRB fields reported, only FRB 20190714A is observed to be spatially coincident with a persistent radio source. The MeerKAT observations detected diffuse radio emission with a peak flux density of $\sim 53\,\mu\,\mathrm{Jy}$ associated with FRB 20190714A at $z = 0.2365$.

The flux density detected from FRB 20190714A is ~ 3 times less than that of the persistent source associated with FRB 20121102A. One of the leading models to explain the bursts from, and the radio counterpart to FRB 20121102A is a young nebula powered flaring magnetar embedded in a 20–50 year-old supernova remnant [61, 260]. The nebula is suggested to contribute significantly to the persistent radio luminosity that is expected to decrease on a timescale of a few decades to centuries. On the other hand, the lack of a bright persistent radio source associated with FRB 20180916A suggests that it is comparatively older at $\gtrsim$ 200–500 years and the persistent radio source may have faded. Given the association of a ~ 3 times fainter persistent source than FRB 20121102A, FRB 20190714A may be a repeating FRB whose age lies between that of FRB 20121102A and FRB 20180916A.

Swift XRT and UVOT observations of FRB 20171019A and results

Here I use data from XRT [79] which operates in the soft X-ray domain of 0.2 - 10 keV as well as data taken by UVOT [321] operating in the UV to optical domain (170 - 600 nm). During the FRB 20171019A MWL observation campaign, two ToO observations were performed with *Swift* from 2019-09-28 18:37:02 to 2019-09-28 21:52:54 and 2019-10-18 18:03:00 to 2019-10-18 20:03:00 on the FRB 20171019A localisation region with a total of 2ks of observations for each epoch.

UVOT analysis: The UVOT images taken in UVM2 filter (central wavelengh = 2246 Å) are aspect corrected and summed with the `uvotimsum` tool (`HEASOFT 6.26` [2]). The UVOT FoV corresponds roughly to the uncertainty of localisation of FRB 20171019A. With `uvotdetect`, I find 30 sources above the 5σ level and within the FRB 20171019A uncertainty region. Using a 3 arcsec maximum separation which is slightly larger than the UVOT PSF [75] I cross-match these sources with known catalog sources. I find that out of the 30 sources detected by UVOT, 28 are spatially coincident with stars catalogued in the SDSS catalogue (DR12) [31] and 1 source is coincident with a galaxy (AGN broadline SDSS ID: 1237652599570890948 at $z \sim 0.156$). This galaxy is also detected by the MeerKAT radio observations.

I use the NASA/IPAC Extragalactic Database (NED[3]), to search for known galaxies in the FRB 20171019A

[2] `https://heasarc.gsfc.nasa.gov/docs/software/lheasoft/`
[3] `https://ned.ipac.caltech.edu`

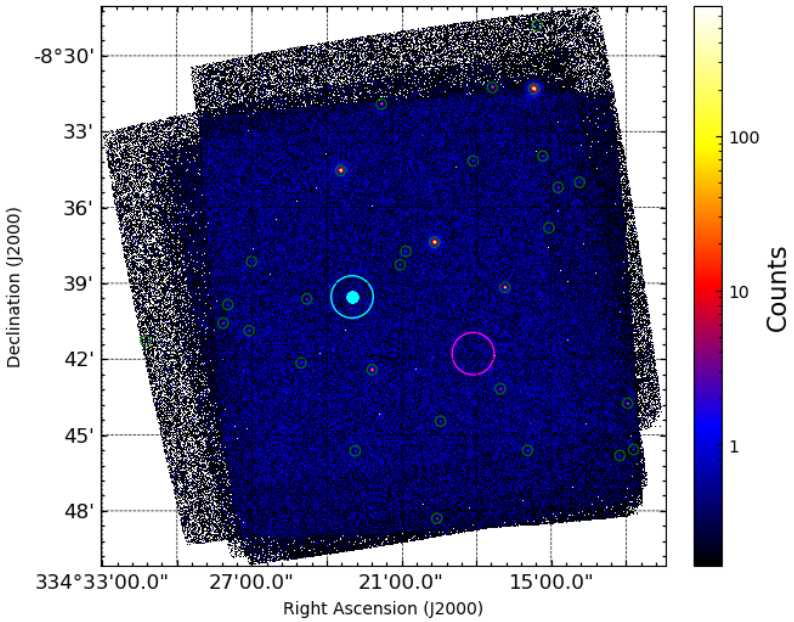

Figure 7.6: UVOT summed image of the FRB 20171019A region taken during the MWL observation campaign in September - October 2019. The green circles indicate the sources detected above 5σ. The cyan dot indicates the centre position of FRB 20171019A. The cyan circle around it indicates the source region used to derive the upper limits and the magenta region indicates the background region.

uncertainty region. I find tens of galaxies with unknown redshifts, therefore I cannot draw conclusions on the host galaxy from our observations. I use the count rate to flux conversion factor for GRB models corresponding to the UVM2 filter from [293] to get the UVOT flux image shown in Fig. 7.6. Using a 50 arcsec circular ON region centred on the position of FRB 20171019A and a 50 arcsec OFF region that does not contain any of the detected sources I run the `uvotsource` tool with a 5σ background threshold and obtain a flux upper limit of 1.39 $\times$ 10^{-16} erg s^{-1} cm^{-2} Å^{-1}.

XRT analysis: The photon-counting (PC) XRT data are processed with `xrtpipeline` (`HEASOFT 6.26`). I extract a summed image with `xselect` as shown in Fig. 7.7. At the edge of the FoV, I detect an emission spatially coincident with the Wolf 1561 star. As I consider this source unrelated to the FRB, I use the online Swift-XRT data products generator [115] [114] to derive upper limits on the count rate of 0.001885 counts s^{-1}. Using `WebPIMMS`[4] (v4.11a) and assuming $N_H = 5.12 \times 10^{20}$ and a power law model with a photon index $\tau = 2$, this upper limit translates to a flux of 6.632 $\times$ 10^{-14} erg s^{-1} cm^{-2} (8.269 $\times$ 10^{-14} erg s^{-1} cm^{-2} unabsorbed).

[4] `https://heasarc.gsfc.nasa.gov/cgi-bin/Tools/w3pimms/w3pimms.pl`

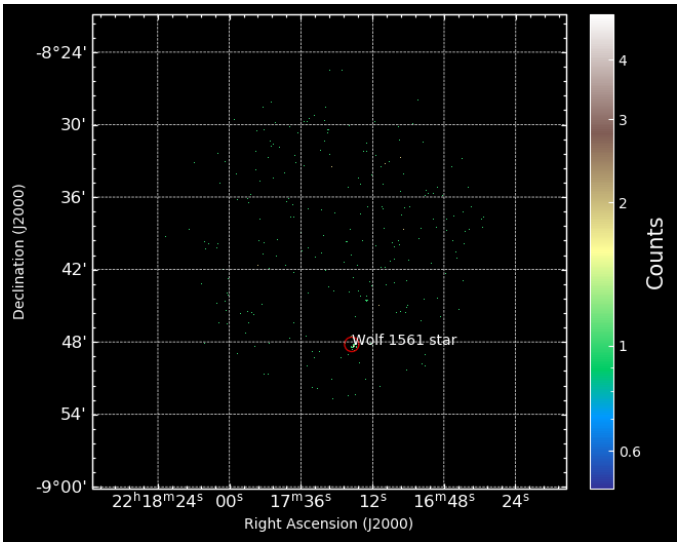

Figure 7.7: XRT summed image of the FRB 20171019A region taken during the MWL observation campaign in September - October 2019. The position of the Wolf 1561 star is shown in red.

H.E.S.S. observations of FRB 20171019A and results

Observations on FRB 20171019A were held during two nights when H.E.S.S. observations were possible with a zenith angle $<$ 30 deg and for a duration of 2 hours. The first night of observations was on 2019-09-28. Due to weather issue (clouds), H.E.S.S observations started 1 hour late. The observations during this night have 1 hour of overlapping observation time with MeerKAT. The second night of observations was on 2019-10-18. Due to light rain and lightning no observations could be performed by H.E.S.S.

For the first night, the data set was obtained with the entire H.E.S.S. array. A standard data quality selection is applied [28] (see Sec. 1.3.1). The events have then been selected and their direction and energy reconstructed using the *model* analysis [103] (see Sec. 1.3.2).

I define a circular region-of-interest centered on the position of FRB 20171019A with a radius of 0.122 deg. The background subtraction is done with the "Ring background" technique [63] (see Sec. 1.3.2). As depicted in Fig. 7.8, no significant γ-ray excess above the expected background is detected from the direction of FRB 20171019A. A second analysis using an independent event calibration and reconstruction [275] confirms the result. The θ^2 histogram (see Sec. 6.5) computed with the multiple off method (see Sec. 1.3.2) is shown in Fig. 7.9. It shows no detection of a signal.

I also search for variable emission on timescales of several minutes using the cumulative sum and ON-OFF tests (see Sec. 7.2.2) and don't find any significant variability. I show in Fig. 7.10 the results from the ON-OFF test that I performed using a 900 seconds binning window. The top left panel shows the N_{ON}

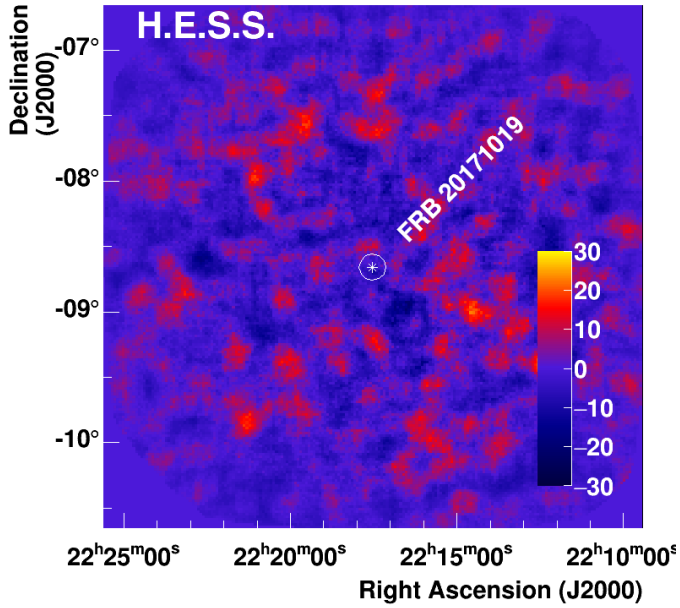

Figure 7.8: Map of VHE γ-ray excess events as observed by H.E.S.S. during contemporaneous observations with MeerKAT illustrating the absence of significant γ-ray emission from the region around FRB 20171019A (indicated by the white circle).

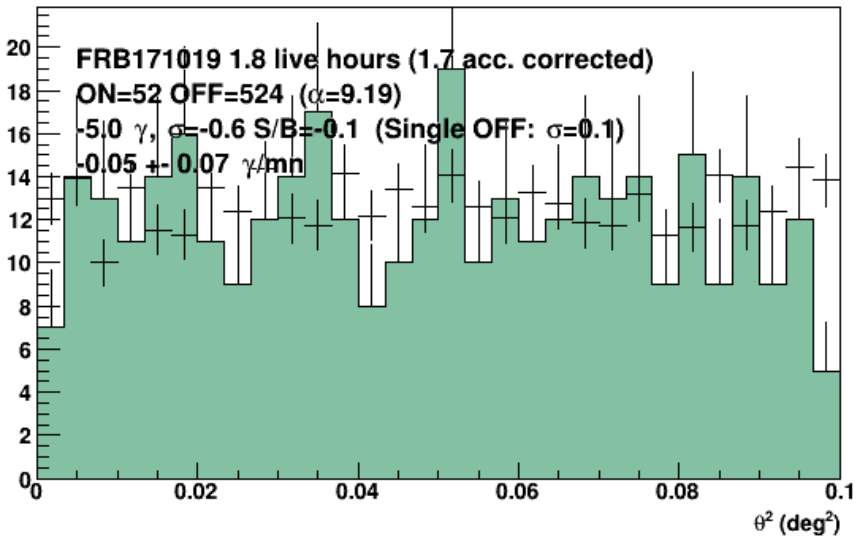

Figure 7.9: θ^2 distribution of gamma-like events around the FRB 20171019 region. The values of the number of ON and OFF events, the significance σ and the signal to noise (S/N) computed with the multiple-off method are displayed.

and the αN_{OFF} values for the bins tested for variability. The top right panel shows the excess computed with Eq. 1.31. The bottom left panel shows the significance of the excess computed with Eq.17 from [210] and the bottom right panel shows the significance distribution with a Gaussian fit. As can be seen from

the plot, no significant variability in the emission is detected above 1.7 σ. I also perform the test for a 300 seconds and a 600 seconds binning size and don't find any significant variability detection. For a binning size less than 300 seconds the bins will not have enough N_{ON} and N_{OFF} in order to respect the minimum requirement set by [210] ($N_{ON} > 10$ and $N_{OFF} > 10$).

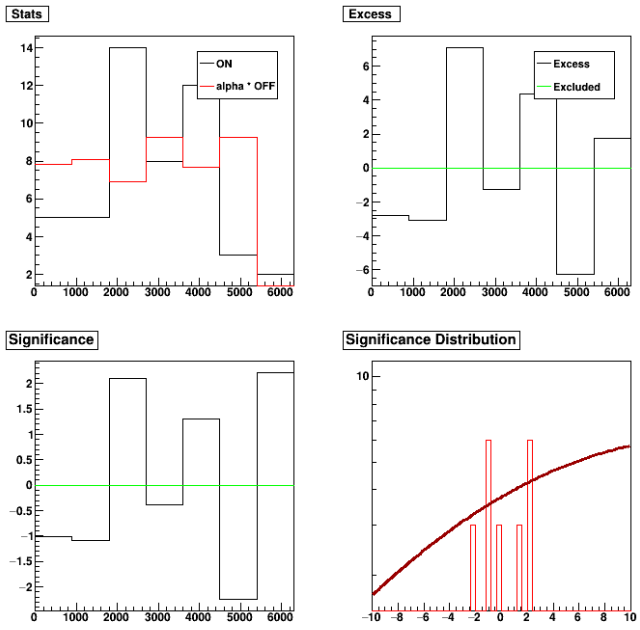

Figure 7.10: ON-OFF test results for a binning size of 900 seconds. **Top left:** Statistics per bin. **Top right:** Excess per bin. **Bottom left:** Significance per bin. **Bottom right:** Significance distribution. The green line shows the excluded signal (here none).

For the total data set of 1.8 h, 95% confidence level (C. L.) integral upper limits on the photon flux are derived using the method described by Rolke et al. [320] and Eq. 5.1 and assuming an underlying power-law spectral index of the γ-ray emission of $\gamma = 2.0$. For these observations, the zenith angles range from 15 to 25 deg, which leads to an energy threshold for the stacked data set of $E_{\mathrm{th}} = 120\,\mathrm{GeV}$. The upper limit on the VHE γ-ray flux above that threshold in the source region and assuming an energy dependence following E^{-2} is $\Phi(E > 120\,\mathrm{GeV}) < 2.1 \times 10^{-8}\,\mathrm{m}^{-2}\mathrm{s}^{-1}$. A map of flux upper limits covering the full region accessible within the H.E.S.S. FoV is given in Fig. 7.11.

7.3.2 Deeper Wider Faster campaign

The Deeper Wider Faster (DWF) program is a multi-wavelength and multi-messenger "proactive" chase of the fast transients (milliseconds-to-hours scale) in the sky with a special interest for FRBs. The program coordinates simultaneous observations between ground-based and space-based facilities. The in-

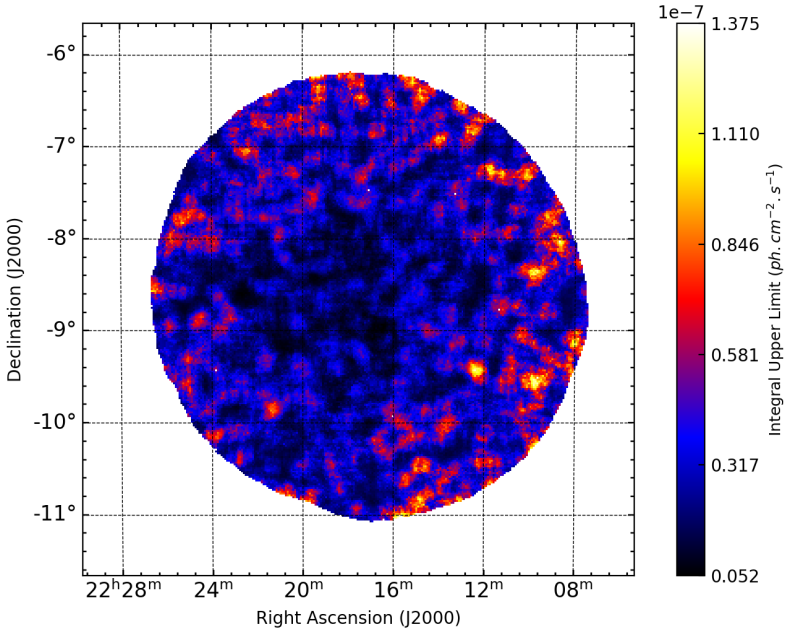

Figure 7.11: Map of upper limits on the VHE γ-ray flux derived from the H.E.S.S. observations on FRB 20171019A. The limits are valid in the interval $120\,\mathrm{GeV} < E < 125\,\mathrm{TeV}$ and assume a E^{-2} energy dependence.

volvement of facilities from around the globe lead to the division of the DWF program into two parts: DWF–Pacific and DWF–Atlantic. A list of the observatories involved and a description of the DWF program can be found in [40].

H.E.S.S. took part of a DWF observation campaign that was held during 6 observation nights from 24 to 29 June 2019. The observations targeted three fields in the sky: a field around NGC6101 with RA: 16h26m00s and Dec: 73d00m00s, a field around NGC6744 with RA: 19h08m00s and Dec: 64d30m00s and a field containing the host galaxy of FRB 20180924 [56]. H.E.S.S. dedicated its first moonlight observations (that were under commissioning at that time) to participate in this observational campaign. A total of 9 telescopes including H.E.S.S. observed the same fields simultaneously while other optical facilities from the other side of the globe were prepared for follow-up observation in the case of a FRB detection.

Several channels (ZOOM[5] room, slack[6] channel, email list) were dedicated to the communication between the observatories and I was one of the contact people from H.E.S.S. that participated in this campaign.

[5] https://zoom.us
[6] https://slack.com/intl/en-fr/

Moonlight commissioning test for H.E.S.S: The pixel threshold is the minimum amount of p.e. detected in the PMTs in order to trigger it. Operations during *dark* time are held with an average of ~ 4 p.e. threshold. During *moonlight* observation, the high level of diffuse light requires a higher threshold. A total of 44 observation runs were taken with H.E.S.S under *moonlight* except for 4 runs in the fifth night that were taken under *dark* time. The pixel threshold was altered between 5.5 and 6.5 p.e. The threshold is chosen by monitoring the trigger rates of the telescopes. When the trigger rates are elevated due to diffuse light falling into the PMTs, the threshold is increased.

I monitored the data quality for these runs. During the first night, the moon phase was 63% which is above the maximum allowed (60% at the time) and a threshold of 5.5 p.e. was used (the 6.5 p.e. threshold was not tested yet). The high brightness of the moon reflected on the trigger rates that rose drastically leading to the interruption of the observations. During the second night, the moon phase was 54%. Even-though the moon phase was below the maximum allowed value it was still high enough to be reflected on the pedestal levels. I show in Fig. 7.12 an example of the NSB map (see Sec. 1.3.2) for the runs taken on NGC 6101 during that night. On the edge of the FoV, the high pedestal levels are not related to stars in the sky. They are caused by the reflection of the moonlight on the telescope. High pedestals were found also for the runs taken on the FRB 20180924 field during that night. The high pedestals do not reflect in the CoG maps and do not affect the analysis.

Several optical transients were detected during this DWF campaign, however no FRBs were detected due mainly to technical and weather problems encountered by the radio telescopes (MeerKAT and Parkes). I analyse all the H.E.S.S. data taken during the DWF campaign with the *model* analysis and I do not find any significant persistent VHE emission.

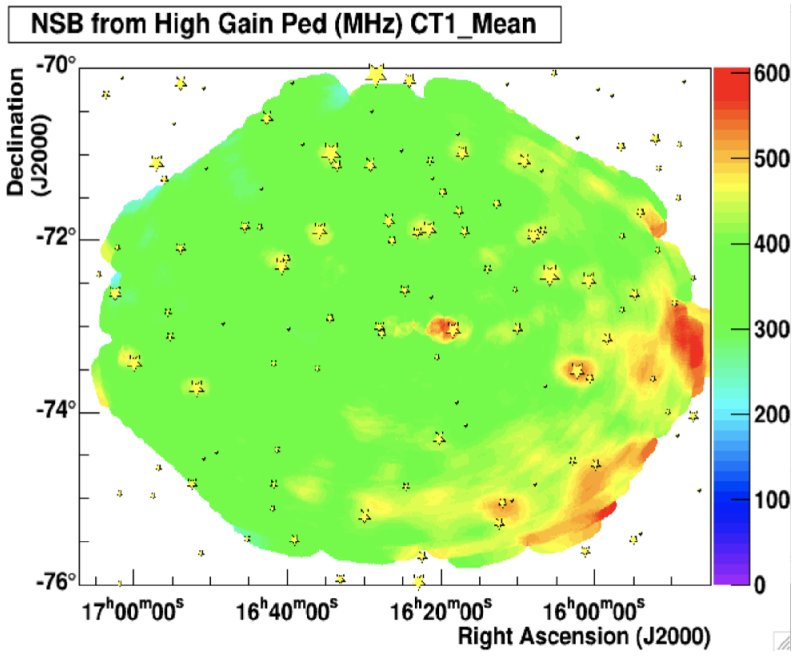

Figure 7.12: NSB map of the H.E.S.S. CT1 telescope whole observing the NGC 6101 field taken under *moonlight* conditions.

7.4 Prospects with archival searches

Simultaneous MWL observations of a sky region could lead to the detection of an FRB simultaneously to other observations like in the case of the VERITAS [169] and MAGIC [165] campaigns. These campaigns are limited by the small to medium FoV of the telescopes involved. The chances of FRB detection during MWL FoV increases with larger FoVs. In the search for counterparts to FRBs we can exploit the large FoV and large duty cycle of space based γ-ray observatories such as Fermi-GBM and Swift-BAT or ground based detectors such as water Cherenkov tanks (HAWC).

I search the archival data in order to find coincident FRB and GRBs. GRBs with small localisation uncertainties are easier to match with corresponding FRBs, therefore I consider the Swift-BAT GRB catalog for now since BAT has a localisation uncertainty in the order of few arcmin. FRBs found on the TNS database until the end of 2020 and Swift-BAT GRBs from the third Swift-BAT catalog [212] are plotted on a skymap in Fig. 7.13.

Due to their extragalactic origin, both FRBs and GRBs have an isotropic distribution in the sky. Considering different time scales, I search for coincident FRBs and GRBs. I consider FRBs and GRBs that arrived together within a 12 hours window. For those I consider the distribution of their arrival times differ-

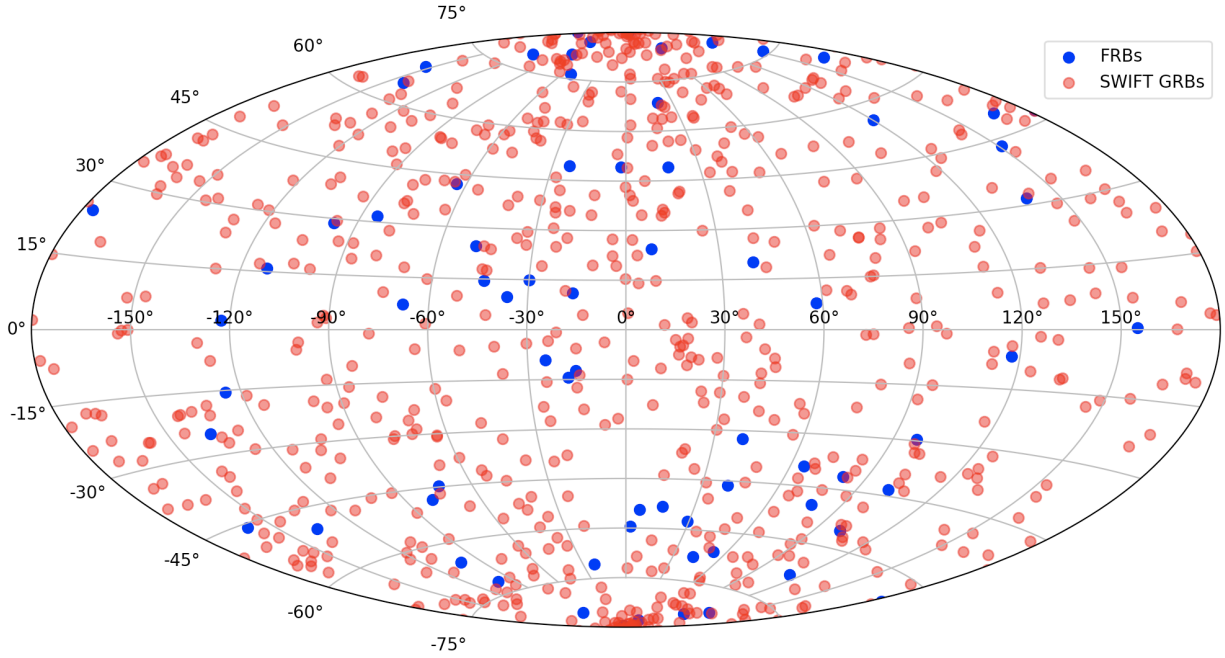

Figure 7.13: All sky sky search for FRBs from TNS and Swift-BAT GRBs.

ence ΔT and their separation in the sky. No clear spatial and temporal association between any FRB and GRB is found.

This search should be extended to other GRB catalogs and transients. A probabilistic association of GRBs to FRBs should be performed in order to get a clearer picture if there is an association between detected FRBs and GRBs, but this is the work for future project. This could be done following [27]. The search also can be extended to include GRB catalogs detected by other observatories like Fermi.

For the VHE domain, we can search for a spatial and temporal coincidence between FRBs and clusters of γ-ray photons detected by IACTS or water Cherenkov tanks. A search for the association of photon clusters to emissions from the evaporation of primordial black holes is currently lead by another team in the CEA-Irfu H.E.S.S. group. The study is not public yet. The detected photon cluster list from this study can be used (when published) to test their potential association to FRBs.

Chapter 8

H.E.S.S. follow-up of SGR 1935+2154

8.1 SGR 1935+2154 and fast radio bursts

Following its discovery in 2014 [96], SGR 1935+2154 has become probably the most burst-active SGR, emitting dozens of X-ray bursts over the past few years [227]. SGR 1935+2154 has been associated with the middle-aged SNR G57.2+0.8 at a distance of about 6.6 kpc [391]. In late April 2020, SGR 1935+2154 showed renewed X-ray burst activity culminating with a "forest of bursts" as detected by Swift-BAT. Many other X-ray and soft-γ-ray telescopes (Fermi-GBM, INTEGRAL, Super-AGILE, HXMT, Konus-Wind, NICER) also reported multiple bursting activity over this period into late May.

This situation became considerably more interesting with the detection of short, intense radio bursts from the direction of SGR 1935+2154. Two millisecond-duration radio bursts (FRB 20200428) were detected, the first burst being a double-peaked one detected by CHIME and STARE2 [88, 72] on April 2020, at 14:34:33 UTC and the second burst by FAST [384] on April 30 2020, at 21:43:00 UTC. The radio energy released under the assumption of an isotropic emission of the bursts at 6.6 kpc is about 10^{34}-10^{35} erg, just below the low end of the extra-galactic FRB distribution observed so far as shown for a sample in Fig. 8.1. This coincidence is the first evidence that magnetars are linked to fast radio bursts (FRBs), or at least a subset of (repeating) bursts.

The source became even more interesting when it turned out that FRB 20200428 is coincident with an X-ray burst from the source seen by AGILE [349], Konus-Wind [314], INTEGRAL (burst G in[256]) and Insight-HXMT [177, 389]. I show in Fig. 8.2 the light curve detected in the INTEGRAL IBIS/ISGRI instrument of the pulses of burst G that are coincident with the radio pulses from the FRB 20200428. After removing the radio dispersion delay, the timing of the first radio burst appears to line up very well

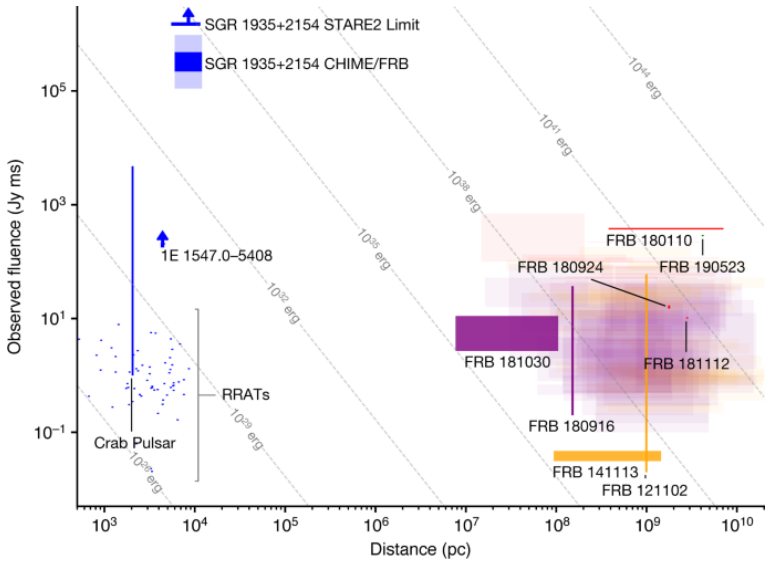

Figure 8.1: The observed burst fluences and uncertainty at radio frequencies from 300 MHz to 1.5 GHz for Galactic neutron stars and extragalactic FRBs with their estimated distances and isotropic energy. Objects with accurately measured distances (parallax or host galaxy redshift) are indicated with vertical lines. RRAT, rotating radio transient. From [88].

with the bright X-ray bursts seen by INTEGRAL. This can be considered as the first counterpart of a FRB ever detected. It was also shown that the X-ray bursts overlapping the double-peaked CHIME radio burst have an unusually hard spectrum, suggesting that the X-ray and the radio bursts arise from a common scenario [314]. Furthermore, the non-thermal nature of the Insight-HXMT burst [209] points to the presence of multi-TeV electrons. Multi-GeV to TeV γ-ray emission via the inverse-Compton process may then accompany this X-ray emission.

Various theoretical emission and source models link FRBs to magnetars. Some of these models are introduced in Sec. 2.3.2. A model by [238] predicts strong millisecond bursts in the TeV band from accompanying FRBs. The proposed model suggests that the energy released during the hard spike of a magnetar burst is too strong to be confined by the magnetic field leading to a mildly relativistic outflow. Due to strong magnetohydrodynamic waves emerging at the onset of the spike, this outflow is propagated into the non-perturbed magnetosphere through the magnetized magnetar wind in a magnetic piston. When the pulse reaches the wind termination shock, a forward shock is created when the pulse pushes the plasma outwards through the magnetized relativistically hot plasma of the nebula and a reverse shock propagates back into the magnetic piston. In the forward shock, relativistic particles are boosted to very high Lorentz factors and lose their acquired energy to synchrotron emission that is Lorentz shifted into the TeV band. Therefore, magnetar hyper flares are supposed to be accompanied by millisecond TeV

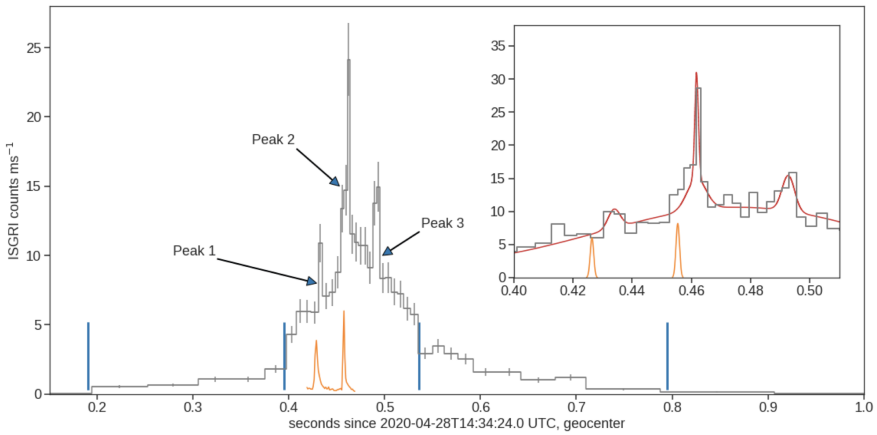

Figure 8.2: Background subtracted and deadtime-corrected light curve of burst-G in the 20-200 keV range obtained with the IBIS/ISGRI instrument. The blue lines indicate the time intervals used for the spectral and imaging analysis. The orange line (adapted from [87]) marks the position of the radio pulses. The inset shows the brightest part of the burst, binned with a minimum of 25 counts per bin. The red line is the fit to the ISGRI unbinned data with a combination of Gaussian curves. From [314].

emission (see Eq. 12 and 15 in [238]). This motivates a search for VHE emission down to the millisecond scale presented in Sec. 8.3.2. H.E.S.S. observed SGR 1935+2154 during its active phase in April 2020 and the findings will be published in [156] and in the following sections.

8.2 H.E.S.S. and other MWL observations of SGR 1935+2154

In order to put the H.E.S.S. observations into perspective, I gather MWL information on bursts and observations of SGR 1935+2154, especially during its high period of activity on April and May 2020. The sources that I use are cited in the caption of Fig. 8.3. I summarize the main MWL observations and detections in the following by decreasing energy bands.

VHE gamma-rays: The H.E.S.S. transients follow-up system automatically triggered Target of Opportunity (ToO) follow-up observations on SGR 1935+2154 after the reception of a first Swift-BAT alert indicating a high-intensity X-ray burst from a known SGR source at 2020-04-27 18:26:19.95 UTC (58966.76828646 MJD). A second Swift-BAT alert arrived $\sim$6.5 minutes later [57]. Darkness and visibility constraints only allowed follow-up observations to commence $\sim$7.5 hours later at a relatively high zenith angle. The observations lasted 2 hours consisting of 4 runs taken with *wobble* offsets whereby the source is alternately offset by 0.5 deg in opposite directions of the right ascension and declination. The position reported by Swift-BAT has a 3 arcmin uncertainty and is thus fully comprised within the H.E.S.S. FoV of 2.5 deg ra-

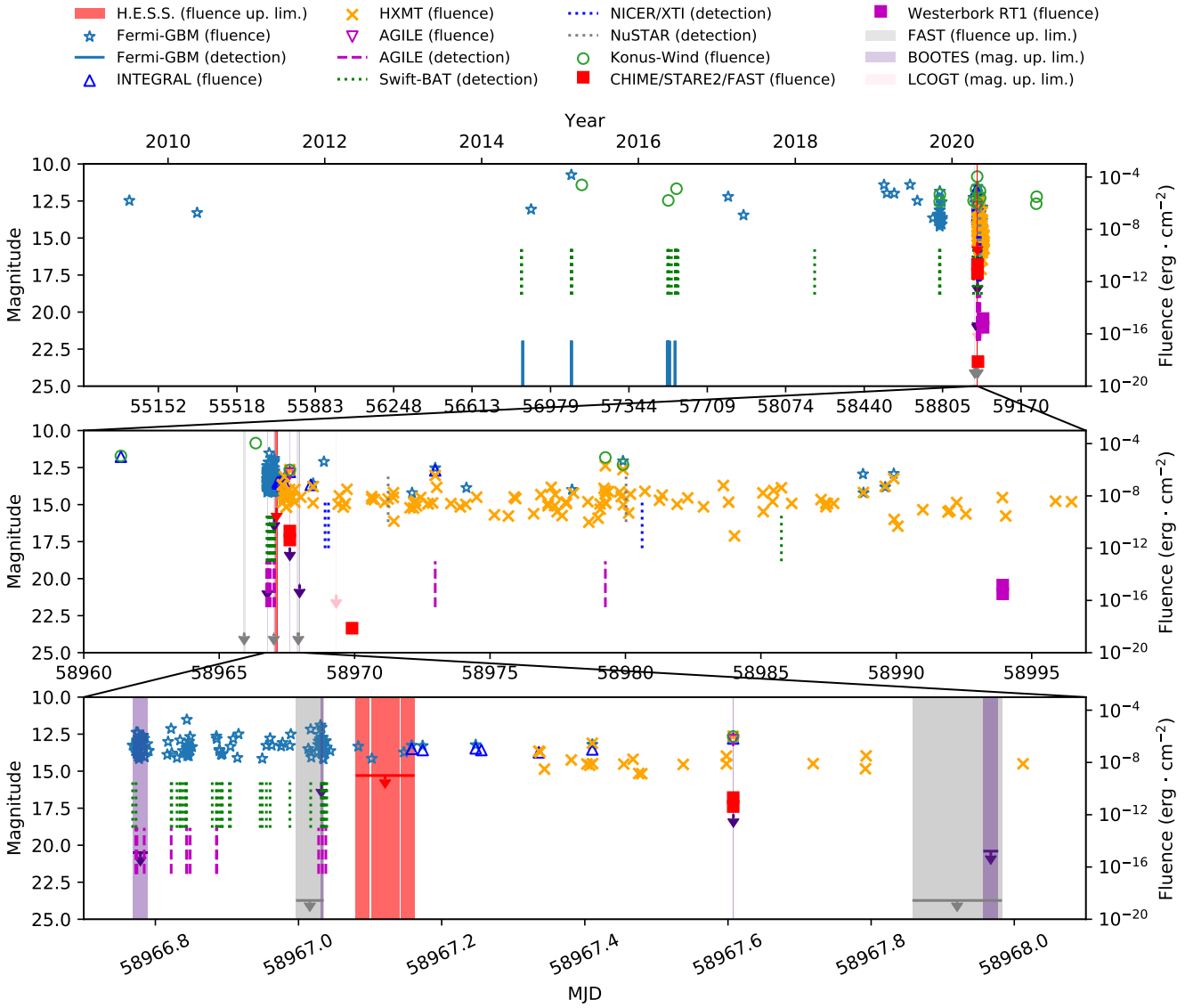

Figure 8.3: SGR 1935+2154 observations with γ-ray, X-ray optical and radio telescopes. I present in this plot X-ray bursts from the source detected by Fermi-GBM [228, 183, 78, 381, 380, 378, 379, 366, 142, 365, 66], Swift-BAT [352], NICER/XTI, NuSTAR [74], INTEGRAL [256], HXMT [388, 177], AGILE [358, 349] and Konus-Wind [314, 307, 311, 308, 312, 306, 309, 310, 199, 136, 198, 128]; radio burst from CHIME [88, 329], STARE2 [72], FAST [384] and the Westerbork (RT1), Onsala (25m), Toruń (30m) dishes [192]. I also show the H.E.S.S., FAST, BOOTES and LCOGT [229] observations with upper limits from these instruments.

dius. A summary of the observations is presented in Tab. 8.1 and I put them in context with the MWL observations of the bursting activity of SGR 1935+2154 in Fig. 8.3 (References therein).

Gamma rays and X rays: Fig. 8.3 shows detected bursts with γ-ray and X-ray instruments like AGILE,

Start time	Duration	Average zenith angle
2020-04-28 01:55:00 UT	28 min	55.0 deg
2020-04-28 02:26:55 UT	28 min	51.0 deg
2020-04-28 02:56:08 UT	28 min	48.1 deg
2020-04-28 03:25:24 UT	28 min	46.2 deg

Table 8.1: Summary of the H.E.S.S. observations of SGR 1935+2154. The observations overlapped with magnetar bursts detected by INTEGRAL and Fermi-GBM.

Fermi-GBM, INTEGRAL, Konus-Wind, HXMT, NuSTAR, NICER/XTI and Swift-BAT since the detction of the SGR until the end of 2020. Fig. 8.3 illustrates clearly the striking number of bursts detected during the high activity phase in April/May 2020. Around the time of the SGR bursting activity, I highlight the Konus-Wind detected burst clusters on April 27 by showing only the most intense bursting activity that occurred around 18:33:01 (58965.77293 MJD) with a duration of $\sim$23 seconds and a very high fluence of 1.09×10^{-4} erg cm^{-2} [310].

Four Fermi-GBM detected bursts occurred during the H.E.S.S. follow-up observations of the source [228]. Moreover, INTEGRAL reported the detection of an X-ray burst at 03:47:52.2 UTC (burst A in [256] at 58967.15824306 MJD) that coincides with the fourth Fermi-GBM burst during the last data taking run by H.E.S.S. Therefore the H.E.S.S. observations provide for the first time simultaneous VHE gamma-ray observational data with X-ray bursts emanating from a SGR.

The coincidence of bursts detected by INTEGRAL, Konus-Wind, AGILE with the radio bursts from CHIME and STAR2 (indicated by a red box) can be seen on the lower panel of Fig. 8.3.

Optical: No optical emission has been seen by the Bootes telescopes. The observations of Bootes-2 (Malaga, Spain) are contemporaneous with the first FRB. No optical emission from the FRB was detected and 3σ upper limits in the Z-band are given as $>$15.9 mag during this epoch. No optical emission was seen by LCOGT (California, USA) nor by the MeerLICHT (not shown in Fig. 8.3) and the other Bootes optical telescope.

Radio: The H.E.S.S. observations precede FRB 20200428 associated with SGR 1935+2154, detected by CHIME at 2020-04-28 14:34:33 UTC [88, 329] and STARE2 at 2020-04-28 14:34:25 UTC [72] ($\sim$58967.60733 MJD). Several X-ray instruments detected coincident X-ray bursts as shown in Fig. 8.3. Follow-up observations by the FAST radio telescope (Pingtang, China) in the 1.25 GHz band, did not re-

veal radio bursts down to a fluence of $<$22 mJy ms, however, a weak, highly linearly polarised radio burst was detected on April 30 [384] (58969 MJD). Moreover, no radio bursts were detected in the observation campaigns by the Arecibo, Effelsberg, LOFAR, MeerKAT, MK2 and Northern Cross radio telescopes (not shown in Fig. 8.3) reported in [53]. The upper limits derived from these observations are between 18 mJy - 25 mJy. Two additional radio bursts separated by $\sim$ 1.4 s on May 24, 2020 [192] (58993 MJD) were detected following an X-ray burst detected by HXMT during a joint campaign between the Westerbork (RT1), Onsala (25m), and Toruń (30m) radio dishes. The burst fluences are several orders of magnitude lower than the two bursts detected by CHIME and STARE2 with values of 112 $\pm$ 22 Jy ms and 24$\pm$ 5 Jy ms, respectively. The four FRBs detected from SGR 1935+2154 thus span around seven orders of magnitude in fluence. No FRBs were detected during the time of the H.E.S.S. data acquisition.

I note that SGR 1935+2154 renewed its activity in the beginning of 2021 with bursts detected by INTEGRAL [255], Fermi-GBM [316] [317], CGBM [305] and Konus-Wind [313].

8.3 H.E.S.S. data analysis and transient emission searches

8.3.1 H.E.S.S. analysis results

After the exchange of the CT5 camera, the data from the CT5 telescope is currently unavailable for `M++` analysis. The quality of the data from the four 12-m telescopes is first verified by applying the data quality selection [28] described in Sec. 1.3.2. I then analyse the data using the *standard* cuts of the semi-analytical *model* analysis [103].*Standard* cuts are used because this is a galactic source in a high background region. Using the "Ring background" [63] technique to determine the background and using a radial acceptance with a 0.1 deg source region and following [210], I derive excess, significance, and significance distribution plots shown in Fig. 8.4 (see Chap. 1 for details.). From the results shown, I conclude that no significant VHE emission was detected. The θ^2 histogram (see Sec. 6.5) computed with the multiple off method (see Sec. 1.3.2) is shown in Fig. 8.5. It shows no detection of a signal. I note that, using the the "Ring background" method, the total number of ON events is $\mathrm{N_{ON}} = 26$ and OFF events is $\mathrm{N_{OFF}} = 270$ in the source region with $\alpha = 0.0813$ leading to an excess value of 4.0. These numbers are slightly different with the "Multiple-off" method as shown in Fig. 8.5.

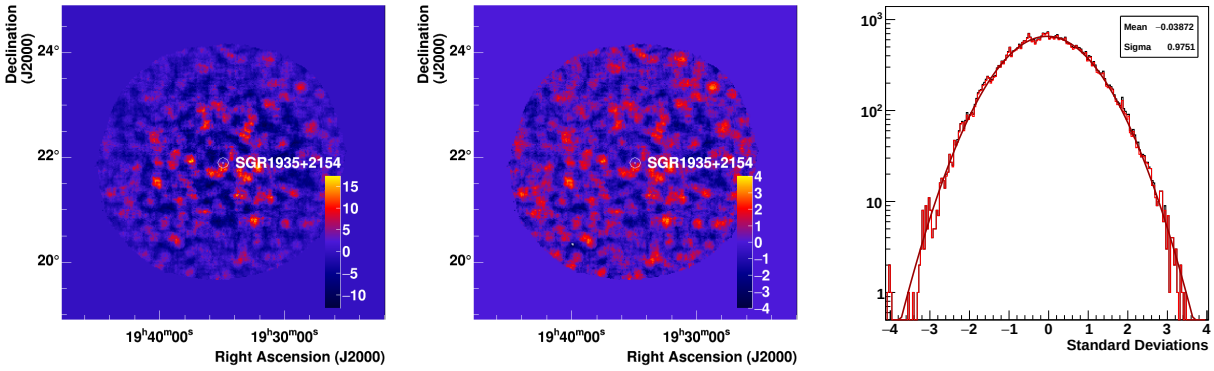

Figure 8.4: **Left:** Excess map computed from the H.E.S.S. observational data taken on SGR 1935+2154 presented in Tab. 8.1. **Middle:** Significance map computed from the H.E.S.S. excess map of SGR 1935+2154. **Right:** Significance distribution of the H.E.S.S. significance map entries in red and a Gaussian distribution fit in black.

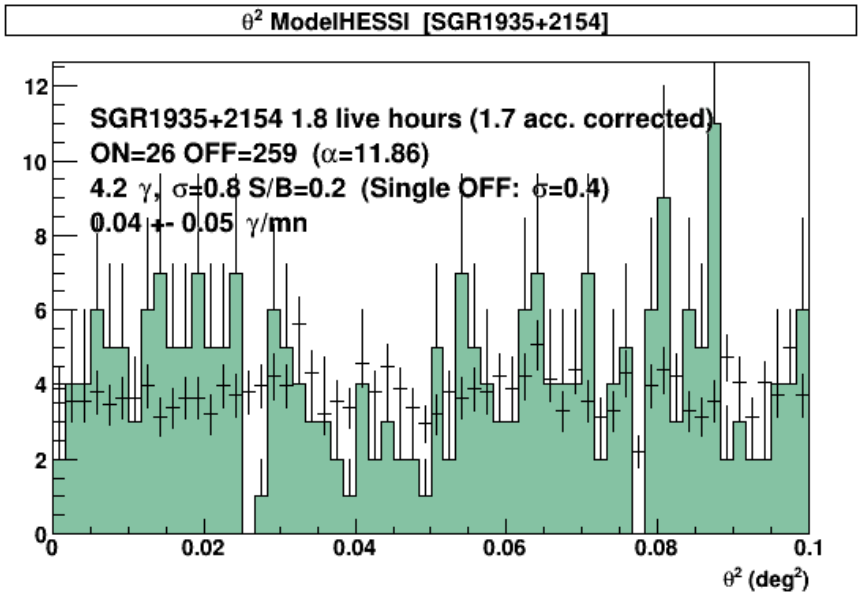

Figure 8.5: θ^2 distribution of gamma-like events around the SGR 1935+2154 region. The values of the number of ON and OFF events, the significance σ and the signal to noise (S/N) computed with the multiple-off method are displayed.

8.3.2 Search for transient VHE emission

Search for transient VHE emission on the minutes scale: I search for variability in the arrival times of the gamma-like events during the H.E.S.S. observations. I use *loose* cut criteria for the event selection in order to increase the number of gamma-like events after selection cuts. I search for a transient signal in the data set using the variability tools described in Sec. 7.2.2. I run the cumulative sum and don't find any significant variability above 5 σ. I run the ON-OFF test with several timescales ranging from 200 to 1000s, with no successful detection either. I show in Fig. 8.6 the ON-OFF test results for a 1000 seconds

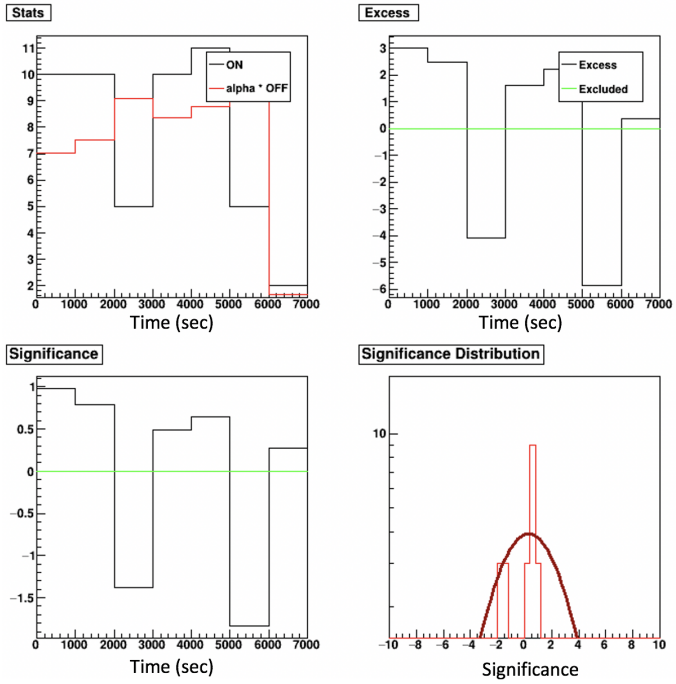

Figure 8.6: ON-OFF test results from H.E.S.S. observations of SGR 1935+2154 for a binning size of 1000 seconds. **Top left:** Statistics per bin. **Top right:** Excess per bin. **Bottom left:** Significance per bin. **Bottom right:** Significance distribution. The green line shows the excluded signal (here none).

time scale. The bins have the required number of ON and OFF events (> 10), however the significance is below 1 σ for all the bins.

Search for VHE variability on the sub-second scale: In order to study the number of events around the X-ray bursts coincident with H.E.S.S. observations, and to search for a potential rise or pulse in the VHE emission around this time, I consider their arrival times and see how much they deviate from a Poisson behaviour that is expected from background or stable sources. Within the H.E.S.S tools for the detection of variability, one particular function, the Poisson probability function, is developed to compute how many standard deviations a data set is away from an expected Poisson behaviour. As shown in Fig. 8.7 it uses a sliding window, iterating through the acceptance-corrected arrival times (see Sec. 2.2 of [76]) to calculate:

$$\sigma = \sqrt{2}\, erfc^{-1}(P(N, \Delta\tau') = \sqrt{2}\, erfc^{-1}(\frac{1}{\tau(N)} \int_0^{\Delta\tau'} t^{N-1} e^{-t} dt) \tag{8.1}$$

where $efrc^{-1}$ is an inverse complementary error function (to get a σ value), N is the width of the window to be considered or the number of arrival time intervals inside one window (e.g. if $N = 2$ the function will consider two arrival time intervals), $\Delta\tau'$ is the acceptance-corrected time interval, $P(N, \Delta\tau')$, the

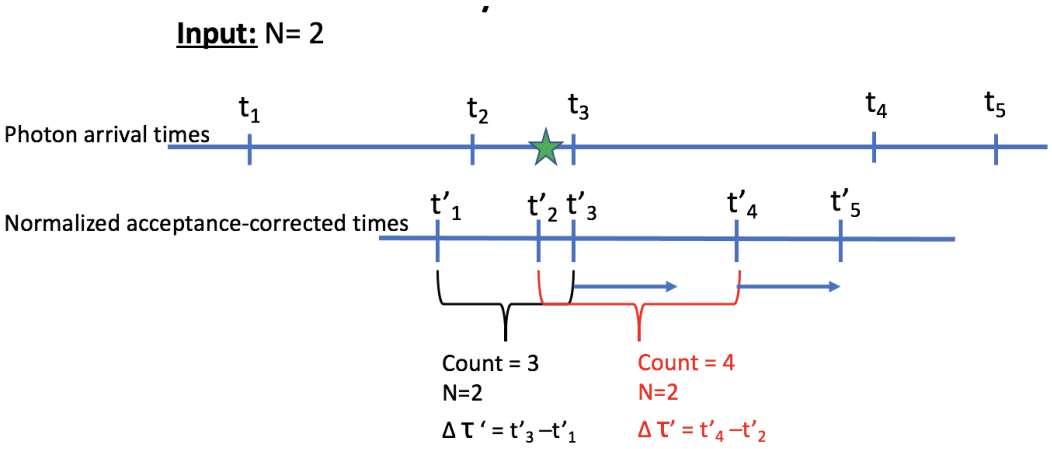

Figure 8.7: Schematics of the Poisson probability function. The arrival times of the event are designated by t_1, t_2... The acceptance-corrected arrival times are designated t'_1, t'_2. The green star designates an coincident X-ray burst. N is the number of arrival time intervals inside a window (here $N = 2$). The function will use a sliding time window to compute the acceptance-corrected time interval $\Delta\tau'$ and will compute the significance of deviation from a Poisson behaviour following Eq. 8.1.

cumulative distribution function (to get a probability value), is a normalized gamma function and $\tau(N)$ is a gamma function evaluated at N. N is given as an input to the function. The accumulated event arrival times are modelled by a Poisson process.

I run this test on the SGR 1935+2154 H.E.S.S. data using $N = 2$ (3 gamma-like events with 2 arrival intervals in between) in order to search for clusters of γ rays from the source region. The results are shown in Fig. 8.8. The arrival times of the events is consistent with a Poisson behavior since no significance deviation was detected above 2 σ. Since the search for variability is performed several times the post-trial significance should be taken in consideration. This is done by converting the pre-significance value to a probability P_{pre} that can be corrected for trial factors by applying $P_{post} = 1 - (1 - P_{pre})^{n_{trials}}$ and converted back to a post-significance values.

Instead of choosing N, which is related to the expected number of photons coming from a burst during a time window, it would be easier to choose a time interval in which we want to search for variability. Therefore, I create a new function based on the one described above in order to let the user input the non-corrected interval time Δt in which they want to search for variability instead of the expected number of arrival intervals N. The steps of this function are illustrated in Fig. 8.9. Instead of sliding through the window, the function will calculate the significance following Eq. 8.1 inside the defined time interval by counting the number of gamma-like events arrival intervals inside this pre-defined interval and by considering their acceptance-corrected times $\Delta\tau'$. In case of no significant variability, the two numbers

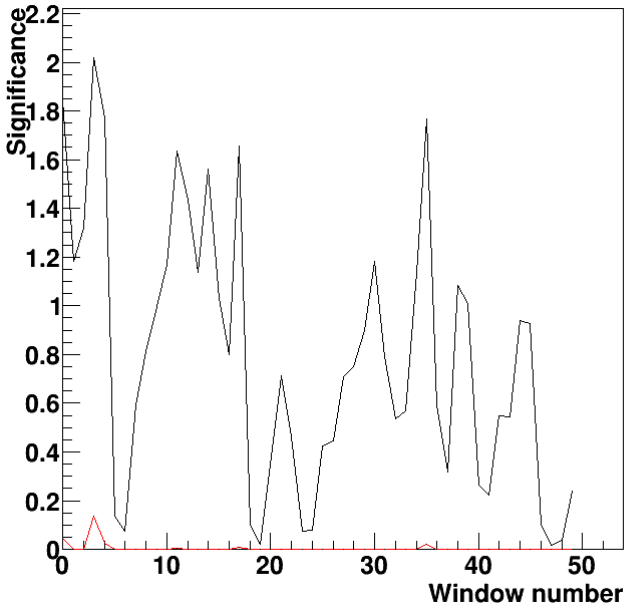

Figure 8.8: Significance computed from Eq. 8.1 for each acceptance-arrival window number with $N = 2$ for the H.E.S.S. observations of SGR 1935+2154. The red line represents the post-trial significance.

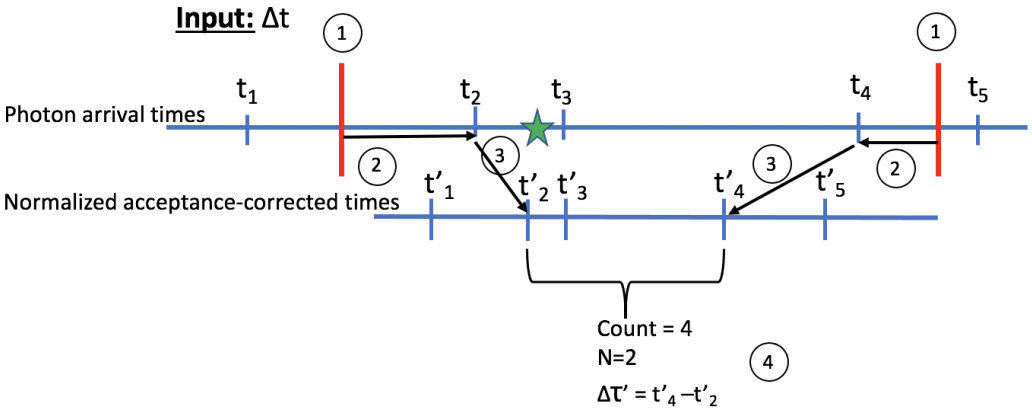

Figure 8.9: Schematics of the Poisson Probability function. The arrival times of the events is designated by t_1, t_2... The acceptance-corrected arrival times are designated t'_1, t'_2... The green star designates a coincident X-ray burst. 1: The input to the function is the time interval in which the variability test should be performed Δt (designated in red). 2: The function locates the nearest events inside this time interval. 3: The arrival times of these events are associated to their acceptance-corrected times. 4: The function will count the number of event arrival intervals N (here $N = 2$), the number of gamma-like events inside the interval, the total counts of events until the end of the interval, the new acceptance corrected time interval $\Delta\tau'$ and will use N and $\Delta\tau'$ to compute the significance following Eq. 8.1.

are expected to be similar. In case of a pulse of γ rays, like in the case of burst, $\Delta\tau'$ is expected to be significantly smaller than N.

I use this function to determine the significance of the arrival of the gamma-like events coming from a 0.122 deg radius circular region around SGR1935+2154 position and around the four X-ray bursts

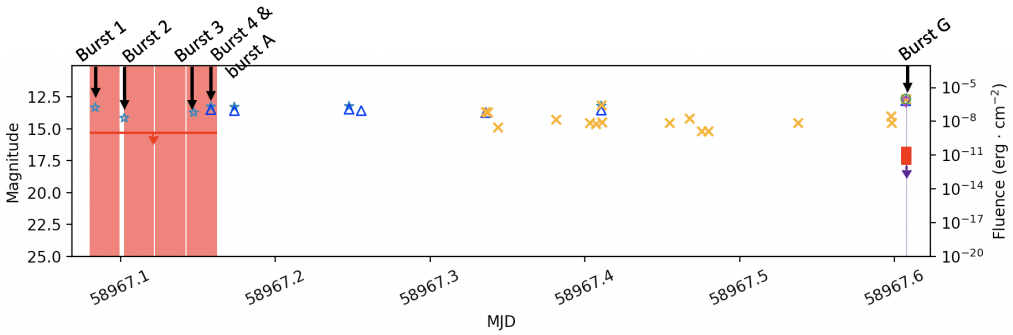

Figure 8.10: Close up from Fig. 8.3 of the SGR 1935+2154 observations with γ-ray, X-ray optical and radio observations around the time of the H.E.S.S. follow-up.

coincident with H.E.S.S. observations. I also show in Fig. 8.11 the gamma-like events coming from the location of the source at the time of the X-ray bursts in function if their arrival time and their reconstructed energy. I show in the middle the four bursts (two bursts from INTEGRAL and GBM are overlapping) that are coincident with the H.E.S.S observations. To perform the test, I use a real time window of 2 minutes like shown in Fig. 8.11 and a search for gamma-candidate events from a region of radius 0.122 deg around the location of SGR1935+2154. For reference I show a close up from Fig. 8.3 around the H.E.S.S. observations in Fig. 8.10.

The results of the test are:

- For the first X-ray burst (upper left panel of Fig. 8.11), 2 gamma-like events arrived within a 2 minutes interval. $\Delta\tau'$ is 0.091 and N = 1. Following Eq. 8.1, $\sigma = 1.71$

- For the second X-ray burst (lower left panel of Fig. 8.11, only one gamma-like events arrived within a 2 minutes interval. In fact, the second X-ray burst occurred few seconds before the start of the second H.E.S.S. observation run, therefore, there are no coincident gamma-like events around the time of the burst on the seconds scale.

- For the third X-ray burst (upper right panel of Fig. 8.11: only 1 gamma-like events arrived within a 2 minutes interval.

- For the fourth X-ray burst (lower right panel of Fig. 8.11: only 1 gamma-like events arrived within a 2 minutes interval.

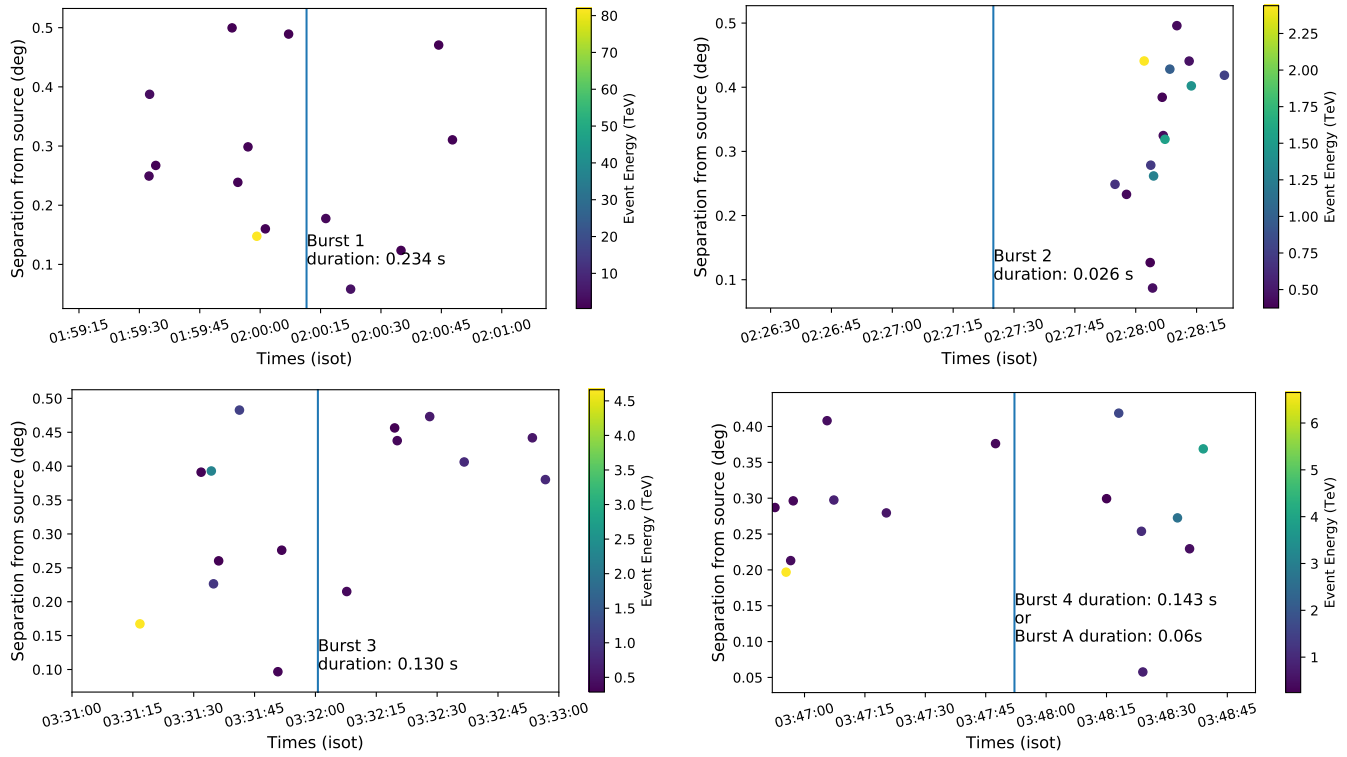

Figure 8.11: Gamma candidate events around the position of SGR 1935+2154 at the time of the GBM and INTEGRAL bursts. The X-ray bursts are show as vertical lines.

8.3.3 Upper limits from the H.E.S.S observations

I define a lower energy threshold where the acceptance is at 10% of its maximum value, leading to a value of 600 GeV and assuming a generic E^{-2} energy spectrum I compute 95% confidence level differential upper limits shown in Fig. 8.12 at the position of SGR 1935+2154 using the Rolke method described in [320] (see also Sec. 6.5). Integrating above 600 GeV gives a value of $\Phi_\gamma(\mathrm{E} > 600\,\mathrm{GeV}) < 1.5 \cdot 10^{-12}\,\mathrm{cm}^{-2}\,\mathrm{s}^{-1}$. If we consider a E^{-2} spectrum this value drops by $\sim$ 13% and for a E^{-3} spectrum it increases by $\sim$ 7%.

The transient emission in the form of a burst can be constrained by considering the H.E.S.S. effective area. At the TeV energy levels this effective area is in the order of 10^5 m^2 (see Sec. 1.3.2). The H.E.S.S. sensitivity for fast transient phenomena, i.e. assuming detection of γ-ray multiplets at millisecond-scale time windows, is at the order of $\sim 10^{-9}\,\mathrm{erg\,cm}^{-2}$ (dividing the energy from two photons at E_{th} by the effective area) depending on the zenith angle of the observations. This level makes H.E.S.S. sensitive to the very bright FRBs on extragalactic scales [238].

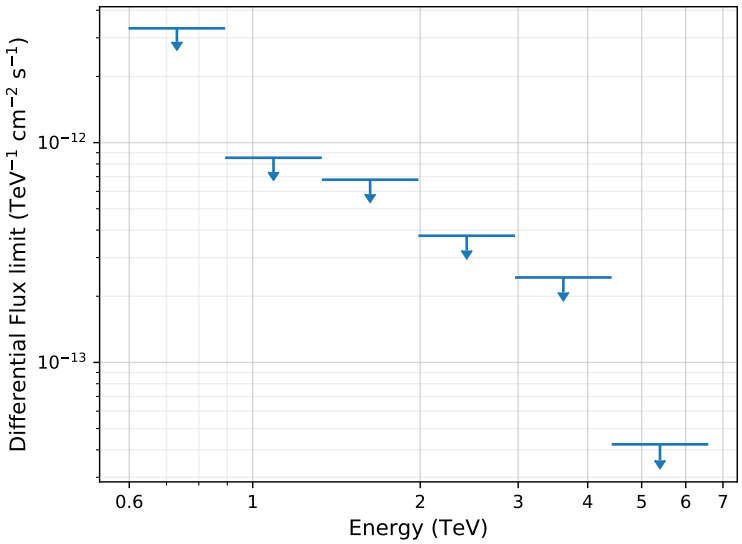

Figure 8.12: Differential 95% C.L. upper limits derived from the H.E.S.S. observational data taken on SGR 1935+2154 in the VHE domain.

8.4 Interpretation of H.E.S.S. and MWL observations and conclusion

The H.E.S.S. observations described here present the first VHE γ-ray observations of a magnetar during a high activity phase. Our observations are coincident with four X-ray bursts detected by two instruments (Fermi-GBM and INTEGRAL) and put stringent upper limits on the VHE emission during the active phase of the magnetar. The results will be published in [156].

The coincident INTEGRAL burst (Burst G from [256]) with the FRB detected by CHIME and STARE2 has a harder spectrum shape (-2) from the burst occurring during the H.E.S.S. observations (Burst A) and is more energetic: the ratio of the fluence from Burts A and G is $F_G/F_A = 5.308$. Assuming that Burst A could be connected to another coincidental FRB half an order of magnitude less energetic than the detected radio burst FRB 20200428, the hypothetical FRB is still within the sensitivity of radio instruments. The fact that several X-ray bursts happened during FAST radio observations and the lack of radio burst detection with $\mathrm{UL} \sim 2.75 \times 10^{-19}\,\mathrm{erg}\cdot\mathrm{cm}^{-2}$ drives me to believe that these ordinary SGR bursts (including Burst A) are different than Burst G in nature. A similar burst to Burst G occurred on April 12 few days before the H.E.S.S. observations. Unfortunately, this period of time is not covered by any radio or VHE observations. Moreover, the HXMT burst associated to the FRB is primarily non-thermal in nature (with a power law spectrum) [209] which is very rare for SGRs (6% of SGR bursts as per [209]).

The lack of VHE γ rays is consistent with expectations from regular bursts [186] when thermal emission mechanism are involved. The integral upper limits derived from the two hours of H.E.S.S. observation can be used to place limits on the persistent VHE emission from the source during these observations. Assuming an $E^{-2.5}$ spectral index, the upper limits can be translated into upper limits on the energy flux $F(\mathrm{E} > 600\,\mathrm{GeV}) < 2.4 \times 10^{-12}\,\mathrm{erg\,cm^{-2}\,s^{-1}}$. Assuming a distance of 6.6 kpc, the luminosity upper limit is

$$\mathrm{L}(\mathrm{E} > 600\,\mathrm{GeV}) < 1.3 \times 10^{34}\,\mathrm{erg\,s^{-1}}$$

Moreover, the H.E.S.S. sensitivity to gamma multiplet can be transformed into a sensitivity to the isotropic energy from a VHE burst on the millisecond timescale

$$\mathrm{E_{VHE,iso}}(\mathrm{E} > 600\,\mathrm{GeV}) \leq 5.2 \times 10^{36}\,\mathrm{erg}$$

This upper limit is higher than the isotropic energies of FRB 20200428 which has an isotropic energy of 10^{34} erg - 10^{35} erg. However, the upper limits derived from H.E.S.S observations are comparable to the energy suggested by the coincident Fermi-GBM and INTEGRAL bursts with energies 10^{38} erg - 10^{39} erg, indicating that if there was an isotropic VHE emission and with the same amount of energy release in the X-ray during the time of H.E.S.S. observations it would have been detected. This conclusion can also be deduced from the fluence values of the mentioned bursts and H.E.S.S. upper limit in Fig. 8.3 and 8.10.

The non-detection by H.E.S.S. may suggest that the Inverse Compton process is weak in the magnetar surroundings, making the VHE emission too weak to be detected. The γ-ray emission is possibly happening too close to the magnetar surface and pair production could result in significant energy losses for the VHE γ rays leading to cutoffs in the MeV to GeV energy range, like it is mentioned for the trapped fireball scenario in Sec. 2.3.2. This flux suppression could be avoided in scenarios where the gamma rays are generated away from the magnetar's intense magnetic field [171]. The H.E.S.S. observations could therefore probe the particle transport aspects such as outflows in the vicinity of SGR 1935+2154 during the recent flaring episode. I cannot conclude on VHE counterpart emissions from FRBs since the H.E.S.S. data presented here are not coincident with any radio burst and the coincident X-ray bursts seem to be different in nature to the bursts coincident with FRB 20200428. However, the predicted energy released during a VHE pulse from magnetar nebulae by [238] should be detectable at distances of hun-

dreds of Mpc. The derived sensitivity of H.E.S.S. to TeV photons suggests that such VHE bursts would be detectable by H.E.S.S. This motivates further observations of magnetars and FRBs in the VHE domain.

In conclusion, the details of the underlying emission mechanism are still unclear and further MWL observations of these objects are necessary. As mentioned in Sec. 8.2, SGR 1935+2154 renewed its activity in the beginning of 2021 and H.E.S.S. will continue to monitor SGR and FRB sources in the aim of providing additional pieces to the puzzle of the origin of FRBs and the mechanisms of magnetar flares.

Summary

My research is dedicated to the study of the transient VHE non-thermal Universe. I focus my study on GWs and FRBs and on the search for possible VHE counterparts to these events.

- My main work is focused on the optimization of the GW follow-up observations. This optimization can be achieved either by using 2D strategies or 3D strategies. 2D strategies can either consider the individual probability inside the pixels or use the integral probability inside the FoV. 3D strategies can consider the probability of individual galaxies (with or without galaxy parameter weighting) or integrate the galaxy probabilities inside the telescope's FoV. I introduce a new algorithm feature which is the usage of a low and high resolution map in parallel to create a seed coordinate grid that can follow the spatio-temporal changes of the GW map in the sky. An easily adaptable GW scheduler and a testing pipeline are developed. I find that the integration of the probability in the FoV improves the coverage by 6% after 10 pointings for 2D strategies. I also find that the usage of a low and a high resolution map in 3D strategies keeps the computation time constant for large maps while maintaining coverage efficiency.

  I also contribute to the H.E.S.S. GRB follow-up program on the follow-up technical level and on the VHE GRB 190829A MWL analysis level. I build the GW plugin of the H.E.S.S. and LST transient systems which allows them to automatically filter and respond to GW events and schedule prompt and afterglow observations without human intervention. I assess the latency of the H.E.S.S. response to GW alerts and find that in most cases, H.E.S.S. can be on target in less than 1 minute. H.E.S.S. observed 6 GW events during O2 and O3 with the help of the GW follow-up tools and the upgrades to the H.E.S.S. Transients Follow-up System.

  The H.E.S.S. GW rapid follow-up program is presented in [45]. One of the ongoing projects is the generalisation of GW follow-up strategies for observatory with two or more sites like CTA. Other future studies can include the usage of more galaxy parameters in the galaxy weighting process, the correlation of burst GW event maps with the galactic plane to limit the search to galactic events and the implementation of further steps for the minimization of the computation time, like code parallelisation.

- The H.E.S.S. GW follow-up observations are analysed. From these, 4 BBH mergers follow-ups do

not result in significant VHE γ-ray emission. I derive upper limits on the emission, the energy flux and the luminosity in the VHE domain which are then compared to a range of VHE GRB emissions. I find that considering only the observed flux, the H.E.S.S. observations would have to happen at an earlier stage and/or with deeper observations per pointing. However, the derived intrinsic luminosity upper limits show that the observations are constraining in case the BBH events generated GRBs in the VHE domain. The isotropic VHE luminosity of the BBH events is below 10^{45} erg s^{-1}, around the level of the low luminosity GRB 190829A. These results will be published in [155].

Moreover, H.E.S.S. observed the BNS merger, GW170817, with a long-term follow-up campaign consisting of 54.9 hours of observations. No detection is found and upper limits are derived. Adding VHE γ-ray observations to the X-ray and radio observations helps disentangling the energy density in the electrons and the magnetic field components and place stringent lower limits on the magnetic field. In a relativistic jet scenario, the magnetic field is constrained to $> 24\,\mu$G while in an isotropic outflow scenario the limit is $> 210\,\mu$G. The findings are published in [18].

None of the GW events was observed in *prompt* mode during O2 and O3. I derive prospects for O4 and find that H.E.S.S. will be able to observed 8^{+21}_{-5} GW events promptly and will be able to have deeper observation lasting for an entire night for 8^{+20}_{-5} events. The minimization of the observation delay and the chance to observe more deeply will occur naturally in O4 with the increase in GW detection rate, therefore, I do not expect that the H.E.S.S. observation strategies will be fundamentally altered.

- On the FRB side, I establish a H.E.S.S. automatic response to UTMOST FRBs. I analyse the data of the first FRB automatically followed by H.E.S.S., FRB 20190806, and don't find any significant emission. I also participate in two MWL campaigns. The first one is a joint H.E.S.S., MeerKAT and Swift campaign on three FRBs. I analyse the H.E.S.S, Swift-XRT and Swift-UVOT data taken on FRB 20171019A and don't find any emission that can be clearly associated to the FRB. For the H.E.S.S. analysis, I also search for a transient emission on the minutes to seconds scale and don't find any significant detection. I present the findings from the radio search for persistent emission that possibly constraint the age of the remnant system of FRB 20190714A (between 20 and 500 years).

The findings from this campaign will be published in [86]. The second campaign is the DWF campaign for which H.E.S.S. dedicated its first moonlight science runs and observed simultaneously with 8 other facilities three regions in the sky without clear high energy discoveries until now. As a third possible method for searching for VHE counterparts of FRBs, one could search for spatial and temporal coincidences between archival cataloged transients or photon cluster from VHE instruments and FRBs. However, this project is just introduced in this thesis and could be potentially a work for the future.

Finally H.E.S.S. observed SGR 1935+2154 during its active phase in April 2020 around the time of the discovery of the first X-ray counterpart to the first galactic FRB (both associated to the source). The H.E.S.S. observations are coincident with four X-ray bursts from the source detected by Fermi-GBM and INTEGRAL. I analyse the data and don't find any significant persistent or transient VHE emission on the minutes to millisecond scale associated to the bursts. I derive upper limits on the persistent and transient VHE emission from SGR 1935+2154 and interprete them in their MWL context. While I cannot conclude on the emission from FRBs, I constrain, for the first time the VHE emission from regular SGR bursts: $\mathrm{L}(\mathrm{E} > 600\,\mathrm{GeV}) < 1.3 \times 10^{34}\,\mathrm{erg\,s^{-1}}$ for persistent emission and $\mathrm{E_{VHE,iso}}(\mathrm{E} > 600\,\mathrm{GeV}) \gtrsim 5.2 \times 10^{36}\,\mathrm{erg}$ for transient emission on the sub-second scale. The findings are published in [156]. SGR 1935+2154 renewed it activity in the beginning of 2021 and further observations with MWL facilities are encouraged.

Finally, I would like to mention my one month shift on the site of the H.E.S.S. telescopes where I got accustomed to the instruments and to ToO observations in general. This shift helped me understand the situation from an observer's point of view and helped me improve communication with the shifters during my expert on call shifts for the GW ($\sim$ 1 year during O3 as GW task leader), GRB ($\sim$ 5 months as member of the GRB group) and FRB (still ongoing as FRB task member) programs.

My publications during the thesis period:

	Peer reviewed	Proceedings
Publications (corr. author)	[18] [45] [156]	[46] [43] [48] [47]
Upcoming (corr. author)	[155] [86]	
Contributor	[158]	

Bibliography

[1] 2020, GraceDB (LIGO/Virgo O3 Public Alerts), https://gracedb.ligo.org/superevents/public/O3/, accessed: February 2021

[2] Aartsen, M., Ackermann, M., Adams, J., et al. 2018, Science, 361, 147–151

[3] Abadie, J., Abbott, B., Abbott, R., et al. 2012, A&A, 539, A124

[4] Abbott, B., Abbott, R., Abbott, T., et al. 2019, Phys. Rev. X, 9, 031040

[5] Abbott, B. P., Abbott, R., Abbott, T. D., et al. 2016, Phys. Rev. Lett., 116, 061102

[6] Abbott, B. P., Abbott, R., Abbott, T. D., et al. 2019, ApJ, 875, 161

[7] Abbott, B. P., Abbott, R., Abbott, T. D., et al. 2020, Living Rev. Relativ., 23, 3, version 58

[8] Abbott, B. P., Abbott, R., Abbott, T. D., et al. 2017, ApJL, 848, L13

[9] Abbott, B. P., Abbott, R., Abbott, T. D., et al. 2017, Phys. Rev. Lett., 119, 141101

[10] Abbott, B. P., Abbott, R., Adhikari, R., et al. 2009, Rep. Prog. Phys., 72, 076901

[11] Abbott, B. P. et al. 2017, Phys. Rev. Lett., 119, 161101

[12] Abbott, B. P. et al. 2017, ApJL, 848, L12

[13] Abbott, R., Abbott, T. D., Abraham, S., et al. 2020, arXiv e-prints, arXiv:2010.14527

[14] Abbott, R., Abbott, T. D., Abraham, S., et al. 2020, ApJ, 896, L44

[15] Abdalla, H., Abramowski, A., Aharonian, F., et al. 2018, A&A, 612, A1

[16] Abdalla, H., Abramowski, A., Aharonian, F., et al. 2017, ApJL, 850, L22

[17] Abdalla, H., Adam, R., Aharonian, F., et al. 2019, Nature, 575, 464

[18] Abdalla, H., Adam, R., Aharonian, F., et al. 2020, ApJL, 894, L16

[19] Abdollahi, S., Acero, F., Ackermann, M., et al. 2020, ApJS, 247, 33

[20] Accadia, T., Acernese, F., Alshourbagy, M., et al. 2012, J. Instrum., 7, 3012

[21] Acciari, V., Ansoldi, S., Antonelli, L. A., et al. 2019, Nature, 575, 455

[22] Ackermann, M., Ajello, M., Asano, K., et al. 2014, Science, 343, 42

[23] Ackermann, M., Ajello, M., Asano, K., et al. 2013, ApJS, 209, 11

[24] Ackermann, M., Asano, K., Atwood, W. B., et al. 2010, ApJ, 716, 1178

[25] Adams, T., Buskulic, D., Germain, V., et al. 2016, CQG, 33, 175012

[26] Ade, P. A. R., Aghanim, N., Arnaud, M., et al. 2016, A&A, 594, A13

[27] Aggarwal, K., Budavári, T., Deller, A. T., et al. 2021, arXiv e-prints, arXiv:2102.10627

[28] Aharonian, F., Akhperjanian, A. G., Bazer-Bachi, A. R., et al. 2006, A&A, 457, 899–915

[29] Aharonian, F., Buckley, J., Kifune, T., & Sinnis, G. 2008, Reports on Progress in Physics, 71, 096901

[30] Ajello, M., Arimoto, M., Axelsson, M., et al. 2019, ApJ, 878, 52

[31] Alam, S., Albareti, F. D., Prieto, C. A., et al. 2015, ApJS, 219, 12

[32] Albert, A., Alfaro, R., Ashkar, H., et al. 2019, arXiv e-prints, arXiv:1902.08429

[33] Alexander, K. D., Berger, E., Fong, W., et al. 2017, ApJ, 848, L21

[34] Alexander, K. D., Margutti, R., Blanchard, P. K., et al. 2018, ApJ, 863, L18

[35] Alexeyev, E. N., Alexeyeva, L. N., Krivosheina, I. V., & Volchenko, V. I. 1988, Physics Letters B, 205, 209

[36] Altschuler, D. R. 2002, in Astronomical Society of the Pacific Conference Series, Vol. 278, Single-Dish Radio Astronomy: Techniques and Applications, ed. S. Stanimirovic, D. Altschuler, P. Goldsmith, & C. Salter, 1–24

[37] Amiri, M., Bandura, K., Berger, P., et al. 2018, ApJ, 863, 48

[38] Anderhub, H., Backes, M., Biland, A., et al. 2013, Journal of Instrumentation, 8, P06008

[39] Anderson, G. E., Staley, T. D., van der Horst, A. J., et al. 2017, MNRAS, 473, 1512–1536

[40] Andreoni, I. & Cooke, J. 2019, in Southern Horizons in Time-Domain Astronomy, ed. R. E. Griffin, Vol. 339, 135–138

[41] Antier, S., Agayeva, S., Aivazyan, V., et al. 2019, MNRAS, 492, 3904–3927

[42] Aptekar, R. L., Frederiks, D. D., Golenetskii, S. V., et al. 1995, SSR, 71, 265

[43] Armand, C., Ashkar, H., Bai, B., et al. 2020, JRJC 2019. Book of Proceedings

[44] Artale, M. C., Mapelli, M., Giacobbo, N., et al. 2019, MNRAS, 487, 1675

[45] Ashkar, H., Brun, F., Füßling, M., et al. 2021, JCAP, 2021 (03), 045

[46] Ashkar, H., Schüssler, F., & Seglar-Arroyo, M. 2019, Mem. S.A.It., 90, 49

[47] Ashkar, H., Seglar Arroyo, M., Abdalla, H., et al. 2021, Proceedings of 37th International Cosmic Ray Conference — PoS(ICRC2021), 395, 943

[48] Ashkar, H., Zhu, S., Brun, F., et al. 2021, Proceedings of 37th International Cosmic Ray Conference — PoS(ICRC2021), 395, 936

[49] Ashton, T., Backes, M., Balzer, A., et al. 2020, Astropart. Phys., 118, 102425

[50] Aso, Y., Michimura, Y., Somiya, K., et al. 2013, Phys. Rev. D, 88

[51] Axford, W. I. 1981, Ann. N. Y. Acad. Sci., 375, 297

[52] Bai, X., Bi, B. Y., Bi, X. J., et al. 2019, arXiv e-prints, arXiv:1905.02773

[53] Bailes, M., Bassa, C. G., Bernardi, G., et al. 2021, MNRAS, 503, 5367

[54] Bailes, M., Jameson, A., Flynn, C., et al. 2017, PASA, 34

[55] Baker, J., Bellovary, J., Bender, P. L., et al. 2019, arXiv e-prints, arXiv:1907.06482

[56] Bannister, K. W., Deller, A. T., Phillips, C., et al. 2019, Science, 365, 565–570

[57] Barthelmy, S. D., Bernardini, M. G., D'Avanzo, P., et al. 2020, GCN circ 27657

[58] Bartos, I., Brady, P., & Márka, S. 2013, CQG, 30, 123001

[59] Bassa, C. G., Tendulkar, S. P., Adams, E. A. K., et al. 2017, ApJL, 843, L8

[60] Bell, A. R. 1978, MNRAS, 182, 147

[61] Beloborodov, A. M. 2017, ApJL, 843, L26

[62] Beloborodov, A. M. 2020, ApJ, 896, 142

[63] Berge, D., Funk, S., & Hinton, J. 2007, A&A, 466, 1219

[64] Bernlöhr, K. 2003, Astropart. Phys., 20, 111–128

[65] Bernlöhr, K. 2008, Astropart. Phys., 30, 149–158

[66] Bhat, P. N., Meegan, C. A., von Kienlin, A., et al. 2016, ApJS, 223, 28

[67] Bionta, R. M., Blewitt, G., Bratton, C. B., et al. 1987, Phys. Rev. Lett., 58, 1494

[68] Blanchard, P. K., Berger, E., & Fong, W.-f. 2016, ApJ, 817, 144

[69] Blandford, R. D. & Ostriker, J. P. 1978, ApJL, 221, L29

[70] Bloom, J. S., Djorgovski, S. G., & Kulkarni, S. R. 2001, ApJ, 554, 678

[71] Boch, T. 2019, in Astronomical Society of the Pacific Conference Series, Vol. 521, Astronomical Data Analysis Software and Systems XXVI, ed. M. Molinaro, K. Shortridge, & F. Pasian, 487

[72] Bochenek, C., Kulkarni, S., Ravi, V., et al. 2020, The Astronomer's Telegram #13684

[73] Bolmont, J., Corona, P., Gauron, P., et al. 2014, Nucl. Instrum. Methods Phys. Res. A, 761, 46

[74] Borghese, A., Zelati, F. C., Rea, N., et al. 2020, ApJ, 902, L2

[75] Breeveld, A. A., Curran, P. A., Hoversten, E. A., et al. 2010, MNRAS, 406, 1687

[76] Brun, F., Piel, Q., de Naurois, M., & Bernhard, S. 2020, Astropart.Phys., 118, 102429

[77] Burns, E., Svinkin, D., Hurley, K., et al. 2021, ApJL, 907, L28

[78] Burns, E. & Younes, G. 2015, GCN circ. 17496

[79] Burrows, D. N., Hill, J. E., Nousek, J. A., et al. 2005, Space Sci. Rev., 120, 165

[80] Caleb, M., Flynn, C., Bailes, M., et al. 2017, MNRAS, 468, 3746

[81] Cecchi, C. & the GLAST LAT Collaboration. 2008, Journal of Physics: Conference Series, 120, 062017

[82] Chatterjee, S., Law, C. J., Wharton, R. S., et al. 2017, Nature, 541, 58

[83] Chen, T.-W., Bolmer, J., Guelbenzu, A. N., & S.Klose. 2019, GCN circ. 25569

[84] Cheng, K. S. & Wang, X. Y. 2003, ApJL, 593, L85

[85] Cherenkov Telescope Array Consortium, Acharya, B. S., Agudo, I., et al. 2019, Science with the Cherenkov Telescope Array

[86] Chibueze, J. O. et al. 2021, in preparation from MNRAS

[87] CHIME/FRB Collaboration, Amiri, M., Bandura, K., et al. 2019, Nature, 566, 235

[88] CHIME/FRB Collaboration, Andersen, B. C., Bandura, K. M., et al. 2020, Nature, 587, 54

[89] Cline, T. L., Desai, U. D., Klebesadel, R. W., & Strong, I. B. 1973, ApJL, 185, L1

[90] Connaughton, V., Briggs, M. S., Goldstein, A., et al. 2015, ApJS, 216, 32

[91] Connaughton, V., Burns, E., Goldstein, A., et al. 2018, ApJL, 853, L9

[92] Connaughton, V., Burns, E., Goldstein, A., et al. 2016, ApJL, 826, L6

[93] Cordes, J. M. & Wasserman, I. 2016, MNRAS, 457, 232

[94] Cortina, J. 2019 [[arXiv]1907.10146]

[95] Coulter, D. A., Foley, R. J., Kilpatrick, C. D., et al. 2017, Science, 358, 1556–1558

[96] Cummings, J. R., Barthelmy, S. D., Chester, M. M., & Page, K. L. 2014, The Astronomer's Telegram #6294

[97] Dai, Z. G., Wang, J. S., & Yu, Y. W. 2017, ApJL, 838, L7

[98] Dálya, G., Galgóczi, G., Dobos, L., et al. 2018, MNRAS, 479, 2374

[99] Daniele Malesani and Niels Bohr. 2018, GCN circ. 22996

[100] De Naurois, M. 2005, in Towards a Network of Atmospheric Cherenkov Detectors VII, Palaiseau, France, 149–162

[101] De Naurois, M. 2012, Habilitation à diriger des recherches, Université Pierre et Marie Curie - Paris VI

[102] de Naurois, M. & Mazin, D. 2015, Comptes Rendus Physique, 16, 610–627

[103] de Naurois, M. & Rolland, L. 2009, Astropart. Phys., 32, 231–252

[104] Deil, C., Zanin, R., Lefaucheur, J., et al. 2017, in International Cosmic Ray Conference, Vol. 301, 35th International Cosmic Ray Conference (ICRC2017), 766

[105] DeYoung, T. & HAWC Collaboration. 2012, Nuclear Instruments and Methods in Physics Research A, 692, 72

[106] Dobie, D., Kaplan, D. L., Murphy, T., et al. 2018, ApJ, 858, L15

[107] Dobie, D., Murphy, T., Kaplan, D. L., et al. 2019, PASA, 36

[108] Domínguez, A., Primack, J. R., Rosario, D. J., et al. 2011, MNRAS, 410, 2556

[109] Ducoin, J.-G., Corre, D., Leroy, N., & Le Floch, E. 2020, MNRAS, 492, 4768

[110] Eichler, D., Livio, M., Piran, T., & Schramm, D. N. 1989, Nature, 340, 126

[111] Einstein, A. 1916, Sitzungsberichte der Königlich Preußischen Akademie der Wissenschaften, Berlin), 688

[112] Einstein, A. 1918, Sitzungsberichte der Königlich Preußischen Akademie der Wissenschaften, Berlin), 154

[113] Einstein, A. 2005, Ann. Phys. (Berl.), 14, 517

[114] Evans, P. A., Beardmore, A. P., Page, K. L., et al. 2009, MNRAS, 397, 1177

[115] Evans, P. A., Beardmore, A. P., Page, K. L., et al. 2007, A&A, 469, 379

[116] Fairhurst, S. 2009, New J. Phys., 11, 123006

[117] Falcke, H. & Rezzolla, L. 2014, A&A, 562, A137

[118] Fermi, E. 1949, Phys. Rev., 75, 1169

[119] Fermi-LAT Collaboration, Ajello, M., Atwood, W. B., Axelsson, M., et al. 2021, Nature Astronomy, 5, 385

[120] Feroci, M., Hurley, K., Duncan, R. C., & Thompson, C. 2001, ApJ, 549, 1021

[121] Finke, J. D., Razzaque, S., & Dermer, C. D. 2010, ApJ, 712, 238

[122] Finstad, D., De, S., Brown, D. A., Berger, E., & Biwer, C. M. 2018, ApJ, 860, L2

[123] Fishman, G. J., Meegan, C. A., Wilson, R. B., et al. 1994, ApJS, 92, 229

[124] Fong, W., Berger, E., Margutti, R., & Zauderer, B. A. 2015, ApJ, 815, 102

[125] Forbush, S. E. 1946, Phys. Rev., 70, 771

[126] Franceschini, A., Rodighiero, G., & Vaccari, M. 2008, A&A, 487, 837

[127] Fraschetti, F. 2018, JCAP, 2018, 054

[128] Frederiks, D., Golenetskii, S., Aptekar, R., et al. 2016, GCN circ. 19613

[129] Funk, S., Hermann, G., Hinton, J., et al. 2004, Astropart. Phys., 22, 285–296

[130] Galama, T. J., Vreeswijk, P. M., van Paradijs, J., et al. 1998, Nature, 395, 670

[131] Gehrels, N., Cannizzo, J. K., Kanner, J., et al. 2016, ApJ, 820, 136

[132] Gehrels, N., Chincarini, G., Giommi, P., et al. 2004, ApJ, 611, 1005

[133] Ghosh, S., Chatterjee, D., Kaplan, D. L., Brady, P. R., & Sistine, A. V. 2017, Publ. Astron. Soc. Pac., 129, 114503

[134] Gilmore, R. C., Somerville, R. S., Primack, J. R., & Domínguez, A. 2012, MNRAS, 422, 3189–3207

[135] Goldstein, A., Fletcher, C., Veres, P., et al. 2020, ApJ, 895, 40

[136] Golenetskii, S., Aptekar, R., Frederiks, D., et al. 2015, GCN circ. 17703

[137] Gomez, S., Hosseinzadeh, G., Cowperthwaite, P. S., et al. 2019, ApJ, 884, L55

[138] Górski, K. M., Hivon, E., Banday, A. J., et al. 2005, ApJ, 622, 759

[139] Gossan, S. E., Sutton, P., Stuver, A., et al. 2016, Phys. Rev. D, 93, 042002

[140] Graham, M. J., Ford, K. E. S., McKernan, B., et al. 2020, Phys. Rev. Lett., 124, 251102

[141] Gropp, J., Kennea, J. A., Klingler, N. J., et al. 2019, GCN circ. 23688

[142] Gruber, D., Goldstein, A., von Ahlefeld, V. W., et al. 2014, ApJS, 211, 12

[143] Hajela, A., Margutti, R., Alexander, K. D., et al. 2019, ApJ, 886, L17

[144] Hallinan, G., Corsi, A., Mooley, K. P., et al. 2017, Science, 358, 1579

[145] Hamburg, R., Veres, P., Meegan, C., et al. 2019, GCN circ. 23707

[146] Harris, C. R., Millman, K. J., van der Walt, S. J., et al. 2020, Nature, 585, 357–362

[147] Hassan, T., Hoang, J., López Moya, M., et al. 2017, in International Cosmic Ray Conference, Vol. 301, 35th International Cosmic Ray Conference (ICRC2017), 807

[148] Hauser, M., Möllenhoff, C., Pühlhofer, G., et al. 2004, Astron. Nachr., 325, 659

[149] Heintz, K. E., Prochaska, J. X., Simha, S., et al. 2020, ApJ, 903, 152

[150] Heitler, W. 1954, Quantum theory of radiation

[151] H.E.S.S. collaboration. 2017, GCN circ. 21084

[152] H.E.S.S. collaboration. 2019, GCN circ. 25237

[153] H.E.S.S. collaboration. 2019, GCN circ. 25566

[154] H.E.S.S. collaboration. 2021, in preparation

[155] H.E.S.S. collaboration. 2021, accepted by ApJ

[156] H.E.S.S. collaboration. 2021, ApJ, 919, 106

[157] H.E.S.S. Collaboration, Abdalla, H., Abramowski, A., et al. 2017, A&A, 597, A115

[158] H.E.S.S. Collaboration et al. 2021, Science, 372, 1081

[159] Hillas, A. M. 1984, ARA&A, 22, 425

[160] Hillas, A. M. 1985, in International Cosmic Ray Conference, Vol. 3, 19th International Cosmic Ray Conference (ICRC19), Volume 3, 445

[161] Hillas, A. M., Akerlof, C. W., Biller, S. D., et al. 1998, ApJ, 503, 744

[162] Hinton, J. & Ruiz-Velasco, E. 2020, J. Phys. Conf. Ser., 1468, 012096

[163] Hirata, K., Kajita, T., Koshiba, M., et al. 1987, Phys. Rev. Lett., 58, 1490

[164] Hjorth, J., Levan, A. J., Tanvir, N. R., et al. 2017, ApJL, 848, L31

[165] Hoang, J., Will, M., Inoue, S., et al. 2019, in International Cosmic Ray Conference, Vol. 36, 36th International Cosmic Ray Conference (ICRC2019), 697

[166] Hofverberg, P., Kankanyan, R., Panter, M., et al. 2013, in International Cosmic Ray Conference, Vol. 33, International Cosmic Ray Conference, 3092

[167] Hoischen, C., Balzer, A., Bissaldi, E., et al. 2017, in International Cosmic Ray Conference, Vol. 301, 35th International Cosmic Ray Conference (ICRC2017), 636

[168] Hoischen, C., Füßling, M., Ohm, S., et al. 2021, in preparation

[169] Holder, J., VERITAS Collaboration, & Lynch, R. S. 2019, in International Cosmic Ray Conference, Vol. 36, 36th International Cosmic Ray Conference (ICRC2019), 698

[170] Holler, M., de Naurois, M., Zaborov, D., Balzer, A., & Chalmé-Calvet, R. 2015, in International Cosmic Ray Conference, Vol. 34, 34th International Cosmic Ray Conference (ICRC2015), 980

[171] Hu, K., Baring, M. G., Wadiasingh, Z., & Harding, A. K. 2019, MNRAS, 486, 3327–3349

[172] Hu, Y. D., Castro-Tirado, A. J., Kumar, A., et al. 2020, arXiv e-prints, arXiv:2009.04021

[173] Hunter, J. D. 2007, Comput. Sci. Eng., 9, 90

[174] IceCube Collaboration. 2019, GCN circ. 25192

[175] Čerenkov, P. A. 1937, Phys. Rev., 52, 378

[176] Inan, U. S., Lehtinen, N. G., Moore, R. C., et al. 2007, Geophysical Research Letters, 34, L08103

[177] Insight-HXMT. 2020, SGR J1935+2154 burst list, Accessed on January 2021

[178] Ioka, K., Hotokezaka, K., & Piran, T. 2016, ApJ, 833, 110

[179] James, C. W., Prochaska, J. X., Macquart, J. P., et al. 2021, arXiv e-prints, arXiv:2101.08005

[180] Jiang, J.-C., Wang, W.-Y., Luo, R., et al. 2020, Res. Astron. Astrophys., 20, 056

[181] Johnston, S., Bailes, M., Bartel, N., et al. 2007, PASA, 24, 174

[182] Jonas, J. & MeerKAT Team. 2016, in MeerKAT Science: On the Pathway to the SKA, 1

[183] Kaneko, Y., Gogus, E., Younes, G., et al. 2014, GCN circ. 16577

[184] Kashiyama, K., Ioka, K., & Mészáros, P. 2013, ApJL, 776, L39

[185] Kasliwal, M. M., Nakar, E., Singer, L. P., et al. 2017, Science, 358, 1559

[186] Kaspi, V. M. & Beloborodov, A. 2017, ARA&A, 55, 261

[187] Kathirgamaraju, A., Barniol Duran, R., & Giannios, D. 2018, MNRAS, 473, L121

[188] Katz, J. 2018, Progress in Particle and Nuclear Physics, 103, 1–18

[189] Keane, E. F., Barr, E. D., Jameson, A., et al. 2018, MNRAS, 473, 116

[190] Keane, E. F., Johnston, S., Bhandari, S., et al. 2016, Nature, 530, 453

[191] Kilpatrick, C. D., Foley, R. J., Kasen, D., et al. 2017, Science, 358, 1583–1587

[192] Kirsten, F., Snelders, M. P., Jenkins, M., et al. 2020, Nature Astronomy

[193] Klebesadel, R. W., Strong, I. B., & Olson, R. A. 1973, ApJL, 182, L85

[194] Klein, O. & Nishina, T. 1929, Zeitschrift fur Physik, 52, 853

[195] Klimenko, S., Vedovato, G., Drago, M., et al. 2011, Phys. Rev. D, 83, 102001

[196] Klimenko, S., Vedovato, G., Drago, M., et al. 2016, Phys. Rev. D, 93, 042004

[197] Kotera, K. & Silk, J. 2016, ApJL, 823, L29

[198] Kozlova, A., Golenetskii, S., Aptekar, R., et al. 2016, GCN circ. 19438

[199] Kozlova, A. V., Israel, G. L., Svinkin, D. S., et al. 2016, MNRAS, 460, 2008–2014

[200] Krymskii, G. F. 1977, Dokl. Akad. Nauk SSSR, 234, 1306

[201] Kumar, P., Hernández, R. A., Bošnjak, Ž., & Barniol Duran, R. 2012, MNRAS, 427, L40

[202] Kumar, P. & Linder, E. V. 2019, Phys. Rev. D, 100

[203] Kumar, P., Shannon, R. M., Osłowski, S., et al. 2019, ApJL, 887, L30

[204] Kumar, P., Shannon, R. M., Osłowski, S., et al. 2019, ApJL, 887, L30

[205] Lamb, R. C., Akerlof, C. W., Biller, S., et al. 1995, in International Cosmic Ray Conference, Vol. 2, International Cosmic Ray Conference, 491

[206] Lazzati, D., López-Cámara, D., Cantiello, M., et al. 2017, ApJL, 848, L6

[207] Le Tiec, A. & Novak, J. 2017, Theory of Gravitational Waves, 1–41

[208] Levan, A. J., Cenko, S. B., Perley, D. A., & Tanvir, N. R. 2017, GCN circ. 14455

[209] Li, C. K., Lin, L., Xiong, S. L., et al. 2020, Nature Astronomy, 5, 378–384

[210] Li, T. P. & Ma, Y. Q. 1983, ApJ, 272, 317

[211] Liebling, S. L. & Palenzuela, C. 2016, Phys. Rev. D, 94, 064046

[212] Lien, A., Sakamoto, T., Barthelmy, S. D., et al. 2016, ApJ, 829, 7

[213] LIGO and Virgo Collaboration. 2020, Public Alerts User Guide

[214] LIGO Scientific Collaboration and Virgo Collaboration. 2017, GCN circ. 21513

[215] LIGO Scientific Collaboration and Virgo Collaboration. 2019, GCN circ. 24503

[216] LIGO Scientific Collaboration and Virgo Collaboration. 2019, GCN circ. 24584

[217] LIGO Scientific Collaboration and Virgo Collaboration. 2019, GCN circ. 25187

[218] LIGO Scientific Collaboration and Virgo Collaboration. 2019, GCN circ. 25208

[219] LIGO Scientific Collaboration and Virgo Collaboration. 2019, GCN circ. 25324

[220] LIGO Scientific Collaboration and Virgo Collaboration. 2019, GCN circ. 26334

[221] LIGO Scientific Collaboration and Virgo Collaboration. 2020, GCN circ. 26734

[222] LIGO Scientific Collaboration and Virgo Collaboration. 2020, GCN circ. 26759

[223] LIGO Scientific Collaboration and Virgo Collaboration. 2020, GCN circ. 26807

[224] LIGO Scientific Collaboration and Virgo Collaboration. 2020, GCN circ. 27184

[225] LIGO Scientific Collaboration and Virgo Collaboration. 2020, GCN circ. 27262

[226] LIGO Scientific Collaboration and Virgo Collaboration. 2020, LIGO/Virgo O3 Public Alerts

[227] Lin, L., Göğüş, E., Roberts, O. J., et al. 2020, ApJ, 893, 156

[228] Lin, L., Göğüş, E., Roberts, O. J., et al. 2020, ApJ, 902, L43

[229] Lin, L., Zhang, C. F., Wang, P., et al. 2020, Nature, 587, 63

[230] Linsley, J. 1985, in International Cosmic Ray Conference, Vol. 7, 19th International Cosmic Ray Conference (ICRC19), Volume 7, 163–166

[231] Liu, T., Romero, G. E., Liu, M.-L., & Li, A. 2016, ApJ, 826, 82

[232] Loeb, A. 2016, ApJ, 819, L21

[233] Longair, M. S. 2011, High Energy Astrophysics (Cambridge university press)

[234] Lorimer, D. R., Bailes, M., McLaughlin, M. A., Narkevic, D. J., & Crawford, F. 2007, Science, 318, 777

[235] LVC collaboration. 2020, GCN circ. 24621

[236] Lyman, J. D., Lamb, G. P., Levan, A. J., et al. 2018, Nature Astronomy, 2, 751

[237] Lynch, R., Vitale, S., Essick, R., Katsavounidis, E., & Robinet, F. 2017, Phys. Rev. D, 95, 104046

[238] Lyubarsky, Y. 2014, MNRAS, 442, L9

[239] Lyubarsky, Y. 2021, Universe, 7, 56

[240] Lyutikov, M. 2013, ApJ, 768, 63

[241] Macquart, J. P., Prochaska, J. X., McQuinn, M., et al. 2020, Nature, 581, 391

[242] Maggiore, M., Broeck, C. V. D., Bartolo, N., et al. 2020, JCAP, 2020, 050–050

[243] MAGIC Collaboration, Acciari, V. A., Ansoldi, S., et al. 2020, arXiv e-prints, arXiv:2012.07193

[244] MAGIC Collaboration, Acciari, V. A., Ansoldi, S., et al. 2019, Nature, 575, 459

[245] Mapelli, M., Giacobbo, N., Toffano, M., et al. 2018, MNRAS, 481, 5324–5330

[246] Marcote, B., Nimmo, K., Hessels, J. W. T., et al. 2020, Nature, 577, 190

[247] Margalit, B., Berger, E., & Metzger, B. D. 2019, ApJ, 886, 110

[248] Margutti, R., Alexander, K. D., Xie, X., et al. 2018, ApJL, 856, L18

[249] Martin, R. G., Nixon, C., Xie, F.-G., & King, A. 2018, MNRAS, 480, 4732

[250] Matar, J., Nehmé, C., & Sauvage, M. 2017, in SF2A-2017: Proceedings of the Annual meeting of the French Society of Astronomy and Astrophysics, ed. C. Reylé, P. Di Matteo, F. Herpin, E. Lagadec, A. Lançon, Z. Meliani, & F. Royer, Di

[251] Mauch, T., Cotton, W. D., Condon, J. J., et al. 2020, ApJ, 888, 61

[252] Mazin, D. 2019, in International Cosmic Ray Conference, Vol. 36, 36th International Cosmic Ray Conference (ICRC2019), 741

[253] Mazin, D., Cortina, J., & Teshima, M. 2017, in American Institute of Physics Conference Series, Vol. 1792, 6th International Symposium on High Energy Gamma-Ray Astronomy, 080001

[254] McNamara, P., Vitale, S., & and, K. D. 2008, CQG, 25, 114034

[255] Mereghetti, S., Savchenko, V., Ferrigno, C., et al. 2020, GCN circ 29381

[256] Mereghetti, S., Savchenko, V., Ferrigno, C., et al. 2020, ApJ, 898, L29

[257] Messick, C., Blackburn, K., Brady, P., et al. 2017, Phys. Rev. D, 95, 042001

[258] Meszaros, P. & Rees, M. J. 1994, MNRAS, 269, L41

[259] Metzger, B. D. & Berger, E. 2012, ApJ, 746, 48

[260] Metzger, B. D., Margalit, B., & Sironi, L. 2019, MNRAS, 485, 4091

[261] Metzger, B. D., Martínez-Pinedo, G., Darbha, S., et al. 2010, MNRAS, 406, 2650

[262] Mooley, K. P., Frail, D. A., Dobie, D., et al. 2018, ApJ, 868, L11

[263] Murase, K., Kashiyama, K., Mészáros, P., Shoemaker, I., & Senno, N. 2016, ApJL, 822, L9

[264] Murase, K., Toomey, M. W., Fang, K., et al. 2018, ApJ, 854, 60

[265] Nan, R., LI, D., JIN, C., et al. 2011, International Journal of Modern Physics D, 20, 989–1024

[266] Nava, L. 2018, International Journal of Modern Physics D, 27, 1842003

[267] Nishizawa, A., Taruya, A., Hayama, K., Kawamura, S., & Sakagami, M.-a. 2009, Phys. Rev. D, 79

[268] Nitz, A. H., Dal Canton, T., Davis, D., & Reyes, S. 2018, Phys. Rev. D, 98, 024050

[269] Nynka, M., Ruan, J. J., Haggard, D., & Evans, P. A. 2018, ApJ, 862, L19

[270] Nysewander, M., Fruchter, A. S., & Pe'er, A. 2009, ApJ, 701, 824

[271] Olausen, S. A. & Kaspi, V. M. 2014, ApJS, 212, 6

[272] Oliphant, T. E. 2006, A guide to NumPy, Vol. 1 (Trelgol Publishing USA)

[273] Page, E. S. 1954, Biometrika, 41, 100

[274] Palmer, D. 2019, GCN circ. 25552

[275] Parsons, R. D. & Hinton, J. A. 2014, Astropart. Phys., 56, 26

[276] Pasquale, M. D., Schady, P., Kuin, N. P. M., et al. 2010, ApJ, 709, L146

[277] Patek, C. & Chime/Frb Collaboration. 2019, The Astronomer's Telegram, 13013, 1

[278] Patricelli, B. et al. 2018, GW COSMoS: Gravitational Wave COmpact binary SysteM Simulations

[279] Perets, H. B., Li, Z., Lombardi, J. C., & Milcarek, S. R. 2016, ApJ, 823, 113

[280] Perley, R., Napier, P., Jackson, J., et al. 2009, Proceedings of the IEEE, 97, 1448–1462

[281] Perley, R. A., Chandler, C. J., Butler, B. J., & Wrobel, J. M. 2011, ApJ, 739, L1

[282] Perna, R., Lazzati, D., & Cantiello, M. 2018, ApJ, 859, 48

[283] Perna, R., Lazzati, D., & Farr, W. 2019, ApJ, 875, 49

[284] Perna, R., Lazzati, D., & Giacomazzo, B. 2016, ApJL, 821, L18

[285] Petroff, E., Burke-Spolaor, S., Keane, E. F., et al. 2017, MNRAS, 469, 4465

[286] Petroff, E., Hessels, J. W. T., & Lorimer, D. R. 2019, A&ARv, 27, 4

[287] Petroff, E., Houben, L., Bannister, K., et al. 2017, arXiv e-prints, arXiv:1710.08155

[288] Piran, T. 1999, Phys. Rep., 314, 575–667

[289] Piro, A. L. & Kollmeier, J. A. 2018, ApJ, 855, 103

[290] Piron, F. et al. 2019, GCN circ. 25574

[291] Platts, E., Weltman, A., Walters, A., et al. 2019, Phys. Rep., 821, 1–27

[292] Poincaré, H. 1905, Acad. Sci., 1504

[293] Poole, T. S., Breeveld, A. A., Page, M. J., et al. 2007, MNRAS, 383, 627

[294] Popov, S., Postnov, K., & Pshirkov, M. 2018, Int. J. Mod. Phys. D, 27, 1844016

[295] Popov, S. B. & Postnov, K. A. 2010, in Evolution of Cosmic Objects through their Physical Activity, ed. H. A. Harutyunian, A. M. Mickaelian, & Y. Terzian, 129–132

[296] Popov, S. B. & Postnov, K. A. 2013, arXiv e-prints, arXiv:1307.4924

[297] Popov, S. B. & Pshirkov, M. S. 2016, MNRAS, 462, L16

[298] Prahl, J. 1999, arXiv e-prints, arXive:9909399

[299] Price-Whelan, A. M., Sipőcz, B. M., Günther, H. M., et al. 2018, AJ, 156, 123

[300] Rau, A., McBreen, S., Kruehler, T., & Greiner, J. 2009, GCN circ. 9353

[301] Reichherzer, P., Schüssler, F., Lefranc, V., et al. 2021, The Astrophysical Journal Supplement Series, 256, 5

[302] Reitze, D., Adhikari, R. X., Ballmer, S., et al. 2019, in Bulletin of the American Astronomical Society, Vol. 51, 35

[303] Resmi, L., Vink, J., & Ishwara-Chandra, C. H. 2020, arXiv e-prints, arXiv:2010.14334

[304] Rhodes, B. 2011, Astrophysics Source Code Library, 12014

[305] Ricciarini, S., Yoshida, A., Sakamoto, T., et al. 2020, GCN circ. 29383

[306] Ridnaia, A., Golenetskii, S., Aptekar, R., et al. 2019, GCN circ. 26242

[307] Ridnaia, A., Golenetskii, S., Aptekar, R., et al. 2020, The Astronomer's Telegram #13688

[308] Ridnaia, A., Golenetskii, S., Aptekar, R., et al. 2020, GCN circ. 27554

[309] Ridnaia, A., Golenetskii, S., Aptekar, R., et al. 2020, GCN circ. 27631

[310] Ridnaia, A., Golenetskii, S., Aptekar, R., et al. 2020, GCN circ. 27667

[311] Ridnaia, A., Golenetskii, S., Aptekar, R., et al. 2020, GCN circ. 27715

[312] Ridnaia, A., Golenetskii, S., Aptekar, R., et al. 2020, GCN circ. 29373

[313] Ridnaia, A., Golenetskii, S., Aptekar, R., et al. 2020, GCN circ 29373

[314] Ridnaia, A., Svinkin, D., Frederiks, D., et al. 2021, Nature Astronomy, in press

[315] Roberts, O. & Meegan, C. 2018, GCN circ. 22981

[316] Roberts, O., Wood, J., von Kienlin, A., Veres, P., & Younes, G. 2020, GCN circ 29374

[317] Roberts, O., Wood, J., von Kienlin, A., Veres, P., & Younes, G. 2020, GCN circ 29388

[318] Robertson, P. 2012, arXiv e-prints, arXiv:1210.0987

[319] Rodrigues, X., Biehl, D., Boncioli, D., & Taylor, A. M. 2019, Astropart. Phys., 106, 10

[320] Rolke, W. A., López, A. M., & Conrad, J. 2005, Nuclear Instruments and Methods in Physics Research A, 551, 493

[321] Roming, P. W. A., Kennedy, T. E., Mason, K. O., et al. 2005, Space Science Reviews, 120, 95–142

[322] Salim, S., Boquien, M., & Lee, J. C. 2018, ApJ, 859, 11

[323] Salim, S., Lee, J. C., Janowiecki, S., et al. 2016, ApJS, 227, 2

[324] Salim, S., Lee, J. C., Janowiecki, S., et al. 2016, ApJS, 227, 2

[325] Sari, R. & Esin, A. A. 2001, ApJ, 548, 787

[326] Sari, R., Piran, T., & Narayan, R. 1998, ApJL, 497, L17

[327] Scargle, J. D. 1998, ApJ, 504, 405–418

[328] Schilling, R. & Geo 600 Team. 1998, in American Institute of Physics Conference Series, Vol. 456, Laser Interferometer Space Antenna, Second International LISA Symposium on the Detection and Observation of Gravitational Waves in Space, ed. W. M. Folkner, 217–221

[329] Scholz, P. 2020, The Astronomer's Telegram #13681

[330] Schüssler, F. 2019, Habilitation à diriger des recherches, Sorbonne Université

[331] Seglar-Arroyo, M. 2019, Theses, Université Paris Saclay (COmUE)

[332] Seglar-Arroyo, M., Ashkar, H., Bonnefoy, S., et al. 2019, Searches for counterparts of gravitational waves at very high energies with H.E.S.S

[333] Seglar-Arroyo, M., Bissaldi, E., Bulgarelli, A., et al. 2019, in International Cosmic Ray Conference, Vol. 36, 36th International Cosmic Ray Conference (ICRC2019), 790

[334] Shannon, R., Macquart, J.-P., Bannister, K., et al. 2018, Nature, 562

[335] Shannon, R. M., Macquart, J. P., Bannister, K. W., et al. 2018, Nature, 562, 386

[336] Siegel, M. H., Burrows, D. N., Deich, A., et al. 2018, GCN circ. 22973

[337] Singer, L. 2020, Early-Warning Alerts

[338] Singer, L. P., Chen, H.-Y., Holz, D. E., et al. 2016, ApJS, 226, 10

[339] Singer, L. P., Chen, H.-Y., Holz, D. E., et al. 2016, ApJ, 829, L15

[340] Singer, L. P. & Price, L. R. 2016, Phys. Rev. D, 93, 024013

[341] Singer, L. P., Price, L. R., Farr, B., et al. 2014, ApJ, 795, 105

[342] Spitler, L. G., Cordes, J. M., Hessels, J. W. T., et al. 2014, ApJL, 790, 101

[343] Staley, T. D. & Fender, R. 2016, arXiv e-prints, arXiv:1606.03735

[344] Swinbank, J. D., Allan, A., & Denny, R. B. 2017, VOEvent Transport Protocol Version 2.0, IVOA Recommendation 20 March 2017

[345] Takami, H., Kyutoku, K., & Ioka, K. 2014, Phys. Rev. D, 89, 063006

[346] Tam, P.-H. T. 2014, Int. J. Mod. Phys. Conf. Ser., 28, 1460174

[347] Tam, P.-H. T., Tang, Q.-W., Hou, S.-J., Liu, R.-Y., & Wang, X.-Y. 2013, ApJ, 771, L13

[348] Tavani, M., Barbiellini, G., Argan, A., et al. 2009, A&A, 502, 995–1013

[349] Tavani, M., Casentini, C., Ursi, A., et al. 2021, Nature Astronomy, 5, 401–407

[350] Tendulkar, S. P., Bassa, C. G., Cordes, J. M., et al. 2017, ApJ, 834, L7

[351] Thompson, C. & Duncan, R. C. 2001, ApJ, 561, 980–1005

[352] Tohuvavohu, A. 2020, The Astronomer's Telegram #13758

[353] Totani, T. 2013, PASJ, 65, L12

[354] Troja, E., Piro, L., van Eerten, H., et al. 2017, Nature, 551, 71–74

[355] Troja, E., van Eerten, H., Zhang, B., et al. 2020, MNRAS, 498, 5643

[356] Troja, E., van Eerten, H., Ryan, G., et al. 2019, MNRAS, 489, 1919

[357] Unnikrishnan, C. S. 2013, Int. J. Mod. Phys. D, 22, 1341010

[358] Ursi, A. et al. 2020, The Astronomer's Telegram #13682

[359] Valeev, A. F., Castro-Tirado, A. J., Hu, Y.-D., et al. 2019, GCN circ. 25565

[360] van Rossum, G. 1995, Python tutorial, Tech. Rep. CS-R9526, Centrum voor Wiskunde en Informatica (CWI), Amsterdam

[361] Veitch, J., Raymond, V., Farr, B., et al. 2015, Phys. Rev. D, 91, 042003

[362] Verbiest, J. P. W., Oslowski, S., & Burke-Spolaor, S. 2021, arXiv e-prints, arXiv:2101.10081

[363] Veres, P. & Mészáros, P. 2014, ApJ, 787, 168

[364] Vieyro, F. L., Romero, G. E., Bosch-Ramon, V., Marcote, B., & del Valle, M. V. 2017, A&A, 602, A64

[365] von Kienlin, A., Meegan, C. A., Paciesas, W. S., et al. 2014, ApJS, 211, 13

[366] von Kienlin, A., Meegan, C. A., Paciesas, W. S., et al. 2020, ApJ, 893, 46

[367] Wakely, S. P. & Horan, D. 2008, in International Cosmic Ray Conference, Vol. 3, International Cosmic Ray Conference, 1341–1344

[368] Weber, J. 1960, Phys. Rev., 117, 306

[369] Weekes, T. C., Cawley, M. F., Fegan, D. J., et al. 1989, ApJ, 342, 379

[370] Wei, J., Cordier, B., Antier, S., et al. 2016, arXiv e-prints, arXiv:1610.06892

[371] Weisberg, J. M., Taylor, J. H., & Fowler, L. A. 1981, SciAm, 245, 74

[372] Wheaton, W. A., Ulmer, M. P., Baity, W. A., et al. 1973, ApJL, 185, L57

[373] Winkler, C. 1995, Exp. Astron, 6, 71

[374] Wyatt, S. D., Tohuvavohu, A., Arcavi, I., et al. 2020, ApJ, 894, 127

[375] Xue, R. R., Tam, P. H., Wagner, S. J., et al. 2009, ApJ, 703, 60

[376] Yamasaki, S., Totani, T., & Kiuchi, K. 2018, PASJ, 70, 39

[377] Yamazaki, R., Asano, K., & Ohira, Y. 2016, Progress of Theoretical and Experimental Physics, 2016 [https://academic.oup.com/ptep/article-pdf/2016/5/051E01/9620709/ptw042.pdf], 051E01

[378] Younes, G. & Kouveliotou, C. 2016, GCN circ. 19546

[379] Younes, G., Kouveliotou, C., Hamburg, R., & Burns, E. 2016, GCN circ. 19598

[380] Younes, G. Y. 2016, GCN circ. 19437

[381] Yu, H.-F. & Veres, P. 2016, GCN circ. 19434

[382] Zhang, B. 2016, ApJL, 827, L31

[383] Zhang, B. 2018, ApJL, 854, L21

[384] Zhang, C. F., Mereghetti, S., Savchenko, V., et al. 2020, The Astronomer's Telegram #13699

[385] Zhang, R. C., Zhang, B., Li, Y., & Lorimer, D. R. 2020, MNRAS, 501, 157–167

[386] Zhang, S.-N., Li, T., Lu, F., et al. 2020, Sci.China Phys., Mech., 63, 249502

[387] Zhang, S.-N., Liu, Y., Yi, S., Dai, Z., & Huang, C. 2016, arXiv e-prints, arXiv:1604.02537

[388] Zhang, S.-N., Tuo, Y.-L., Xiong, S.-L., et al. 2020, The Astronomer's Telegram #13687

[389] Zhang S.-N., Z. B. & Lu, W.-B., o. b. o. I.-H. t. 2020, The Astronomer's Telegram #13692

[390] Zheng, Z., Ofek, E. O., Kulkarni, S. R., Neill, J. D., & Juric, M. 2014, ApJ, 797, 71

[391] Zhou, P., Zhou, X., Chen, Y., et al. 2020, ApJ, 905, 99

[392] Zonca, A., Singer, L., Lenz, D., et al. 2019, J. Open Source Softw., 4, 1298

[393] Zou, L., Zhou, Z.-M., Xie, L., et al. 2019, ApJ, 877, 153

[394] ZTF and GROWTH collaborations. 2019, GCN circ. 25199

[395] ZTF and GROWTH collaborations. 2019, GCN circ. 25207

Appendices

Appendix A

The *updated* H.E.S.S. GRB follow-up program

A.1 New considerations for GRB experts on call shifts

Due to the established link between X rays and VHE γ rays, the H.E.S.S. GRB experts on call now give more attention to the X-ray flux from GRBs in order to decide on follow-up. The X-ray flux can be estimated either by using the fluence of the burst or by using early reported X-ray measurements and using a time-decay function. If the X-ray flux, therefore the supposedly similar VHE flux, is above the H.E.S.S. threshold flux after 2 hours of observations ($\sim 10^{-11}$ erg cm^{-2} s^{-1} derived from the H.E.S.S. observation of GRB 180720B), then the VHE flux level is expected to be around the level of detectability by H.E.S.S. Several tools are provided to the experts on call in order to help them compute this flux. Due to the relation between the X-ray and the VHE flux and to the fact that VHE GRBs are detected several hours and days after the initial burst, H.E.S.S now follows all GRBs by Swit-BAT with a maximum delay of 12 hours with or without redshift information. If the redshift is identified to be less than ~ 1, the maximum allowed delay is extended to 24 hours.

My contribution to the GRB expert on call shifts: I took 6 GRB burst advocate shifts and became an expert in GRB follow-up observation scheduling. I also provided technical and science support for newly formed experts and shifters. During my GRB shifts, I found several corner cases and provided solutions for future experts on call to deal with similar cases. Moreover, I re-wrote the GRB follow-up procedure manual for GRB contact person with a set of guidelines to follow in order to assess the importance of

a GRB and help the expert on call determine if it would be worth observing a GRB or not. Finally, I developed a tool that computes the visibility of a source (like a GRB) on the sky of a given observatory with the different observation conditions during a night. An example of the output of this script is given in Fig. 1.13. This tool has been useful for the follow-up of transient events, whose localization is reported in a non-machine-readable format and can be used for any telescope. I also contributed to the tools that help estimate the X-ray flux from a GRB at a given time.

A.2 Follow-up of candidate VHE GRBs with ATCA

Another lesson learned from the H.E.S.S. detected VHE GRBs is the lack of simultaneous radio and VHE observations useful for modeling the spectrum of the source. In fact, the radio band offers the unique possibility for probing the synchrotron photon index in the un-cooled part of the emission spectrum. The optical part of the spectrum is often affected by host extinction and there is no guarantee that Swift-XRT will detect synchrotron photons below the cooling break that depends on the synchrotron energy peak E_{syn}.

For the above reasons, radio transient astronomers have teamed up with members of the HESS collaboration to perform an ATCA rapid-response triggering and monitoring program if a hint of a VHE signal is detected in the H.E.S.S. real-time analysis during a GRB follow-up. Since ATCA is located on the east side of the Australian continent, I assess the accessibility of the instrument to H.E.S.S. visible GRBs. For that I compute a plot presented in Fig. A.1 that shows the common regions in the sky ATCA and H.E.S.S. sky where a GRB could be observed simultaneously.

To provide a more quantitative assessment, I calculate the duration of overlapping time windows for random sky directions throughout one year of a joint program. I provide in Fig. A.2 an example of one night where a source would be observable simultaneously by H.E.S.S. and ATCA. The latter is able to observe at zenith angles up to 75 deg and being a radio telescope is not constrained by darkness and moonlight observation conditions.

I expand the calculation for random positions in the sky throughout a whole year. These calculations take into account the main constraints on HESS observations, which are dominated by requiring astronomical dark conditions. Fig. A.3 shows the probability density of the duration of the overlapping observation windows distribution for a source falling in the H.E.S.S. and ATCA overlapping sky. In some regions of the sky, a source could potentially be observed simultaneously by H.E.S.S. and ATCA up to 8

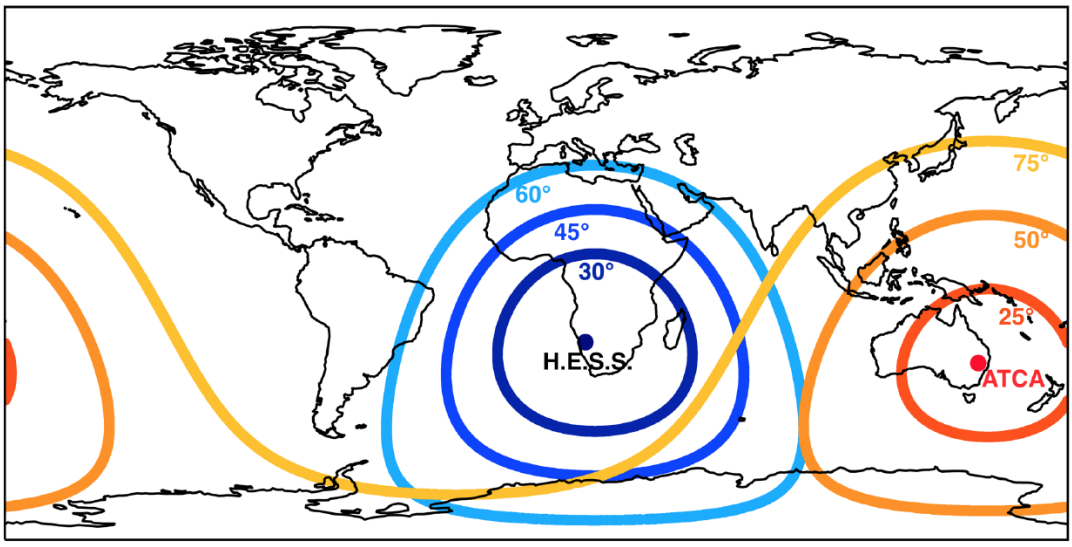

Figure A.1: Overlapping accessible fields of HESS and ATCA for typical zenith angle ranges.

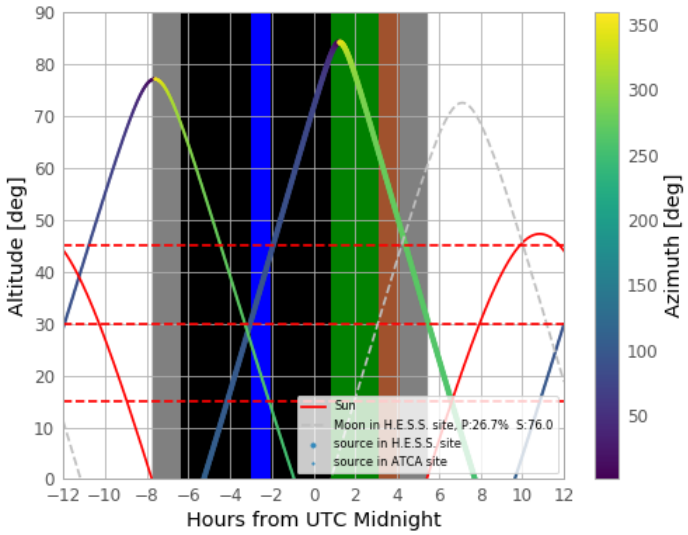

Figure A.2: Altitude of a source as seen from the H.E.S.S and ATCA site at a given time. The region shaded in black represents H.E.S.S. dark time observation conditions. The green region represent the time when H.E.S.S. can observe under moderate moonlight. The brown region represents times when H.E.S.S. can not observe due to high moon light levels. The blue region represents times where visibility conditions are suitable to observe the source simultaneously by both instruments. The label provided the moon phase and the separation from the source in the H.E.S.S. site at a given time.

hours. The proposal was accepted and since then H.E.S.S. is able to trigger prompt ATCA observations if hints of VHE detection are found in the real-time analysis. ATCA obsrvations will allow to probe the rise of the radio synchrotron emission from GRB in the *afterglow* phase. While the amount of shared sky between ATCA and HESS is limited (see Fig. A.1), and in some instances radio observations may need

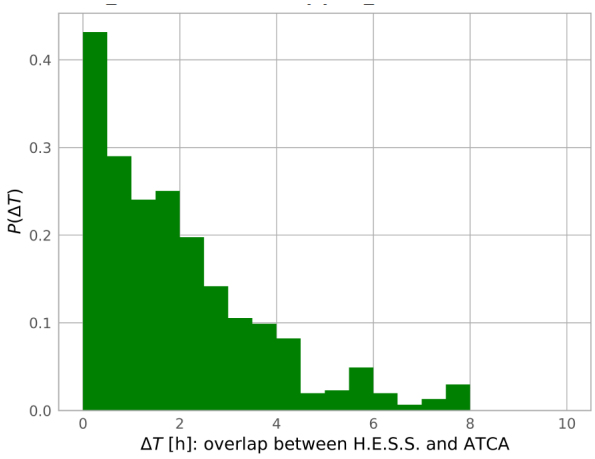

Figure A.3: Distribution of the joint observation windows between HESS and ATCA illustrating the potential for simultaneous observations.

to wait up to 16 hr before ATCA can be on-target, this delay does not impact our rapid-response science goal to track the rise of the GRB afterglow emission, which usually switches on between 4 and 16 hours post-burst [39].

A.3 Ongoing projects: Fermi-GBM tiling

We learn from GRB 190829A, in particular from the rise of the X-ray afterglow emission after the initial burst that observations of GRBs can be extended to even low luminosity bursts and that we can expand the number of total GRBs observed per year in order to explore more ”diversity” in GRB emission. Among current GRB observatories, Fermi-GBM has the highest rate of detected GRBs per year. Unlike Swift GRBs, Fermi-GBM GRBs are often poorly localised due to the different detection techniques used for both detectors (see Sec. 2.1.2). The procedure in H.E.S.S. until 2020 was to observe only GBM alerts with a final localisation uncertainty < 2 deg (corresponding roughly to the H.E.S.S. FoV radius) and $\mathrm{sig} > 10$. However, the reported uncertainty is only statistical, and the addition of a systematic uncertainty can increase the localisation uncertainty by several degrees. GBM produces maps for final ground alerts. The ground alerts have been in production since the beginning of the mission [90]. A new pipeline called RoboBA began to produce improved localization maps in HEALPix format. RoboBA has been improved over time, including an updated version running since September 2019 [135], and currently supplies the map’s image URLs over dedicated GCNs `Fermi-GBM-FINAL-POSITION` notices.

The GRB team suggested to implement a tiling strategy of these HEALPix GBM alerts maps in order to improve the coverage of GBM GRBs and increase the number of followed-up GRBs in general. A

study on all GBM alerts final localisation maps from 2008 till 2020, computed with the updated version of RoboBA (total of 2923 maps, 316 maps taken from the live stream database and 2607 retroactive maps), aims to compare the HEALPix maps versus the true localisation of the GRB. Only the GRBs that have a localisation uncertainty $<$ 1 deg or are localised by other precision instruments like BAT are taken into consideration. Moreover, all GRBs with $\mathrm{sig} < 10$ and a positional statistical uncertainty $>$2 deg have been filtered out. The true position of the GRBs (deduced from high precision instruments for example) is compared against the probability of localisation supplied by the HEALPix maps. It seems that around half of the GRBs are localised in a area smaller than 50 deg^2 around the center of the localisation hotspot corresponding to around 4 H.E.S.S. FoVs. The results are shown in Fig. A.4. This hints that a tiling strategy might be effective.

Moreover, another study on a sample of previously H.E.S.S. observed Fermi GRBs (detected by GBM + LAT) shows that the current H.E.S.S. observation strategy of GBM GRBs (pointing on the central position with a wobble offset of 0.5 deg) only finds the true position in 30% to 40% of the cases. The x-axis of Fig. A.5 shows the localisation error of Fermi-GBM GRBs reported in the GCNs. The y-axis shows the angular distance between the central position reported by the GBM GCNs (position that will be observed by H.E.S.S.) and the true position reported by LAT. Since H.E.S.S only observed GRBs with localisation errors $<$ 2 deg, we only consider those. It seems that there is only a 30% to 40% chance that the GRB falls in the H.E.S.S FoV.

In order to assess the feasibility of a tiling strategy, I simulate the H.E.S.S. response to GBM alerts. A total of 276 GBM alerts arrived in 2019. H.E.S.S. observed 3 of them (In the last 3 years, 3 to 5 GBM per year are observed by H.E.S.S.). The final localisation maps are computed by the updated version of RoboBA. These alert localisation maps and arrival times are injected in the GW testing pipeline (see Sec. 3.5). Since GRBs are detected at large distances (and galaxy catalogs are incomplete at these distances), the `PGWinFoV` algorithm is used. The total covered probability of all the maps throughout a year versus the number of potential pointings that can be taken during the entire night following the arrival of the GRB alerts are shown in Fig. A.6.

I note that among all the GBM GRBs in 2019, 52 are localised by other instruments like BAT and their true position is known. From the portion of GRBs that could be covered by H.E.S.S this number drops to 15. 8 of these localised GRBs would have been observed by H.E.S.S. with less than 8 pointings (4 hours of observations). If we plot these 8 GRB tiling results we see that the ones with $> 40\%$ H.E.S.S. coverage

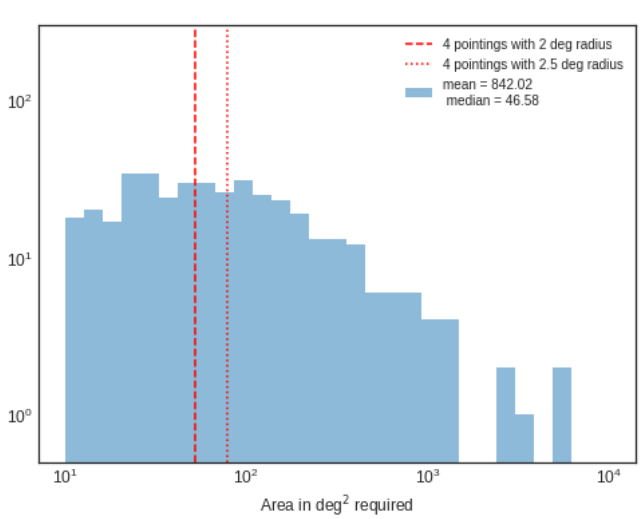

Figure A.4: The area required to be scanned before the capture of the true position of the GRB by H.E.S.S. From Private communication with Sylvia Zhu.

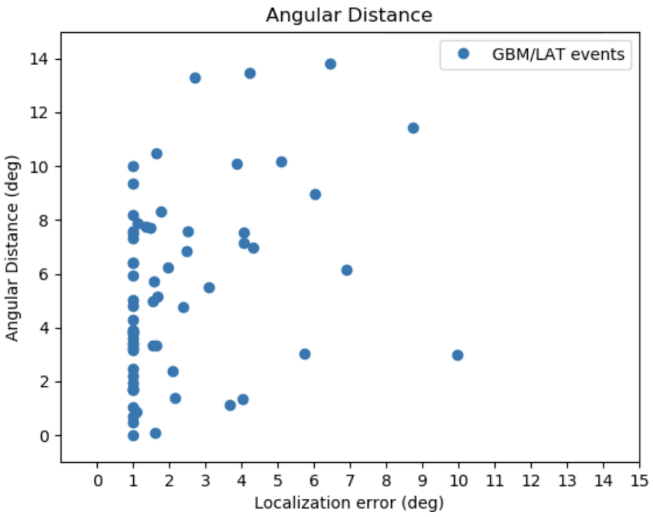

Figure A.5: Separation of the central position reported by GBM and the true position reported by LAT versus the localisation error by GBM. From Private communication with Mathieu de Bony.

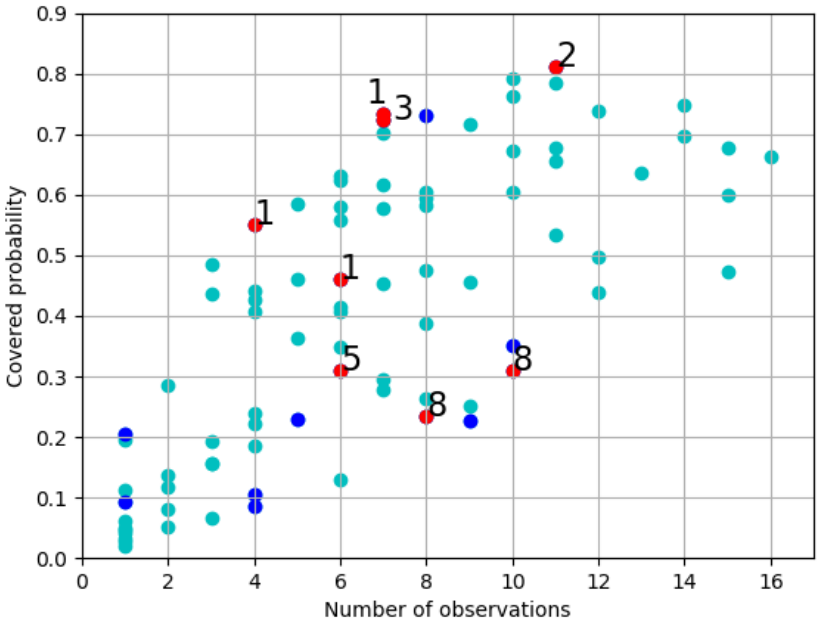

Figure A.6: Covered probability by H.E.S.S. tiling vs the number of pointings over a whole night after the trigger. The blue dots represent GRBs covered by H.E.S.S. with a known true position. The red dots represent the GRBs with a known true position that could be found by the H.E.S.S. tiling. The number next to each red dot represents the number of pointings performed in order for H.E.S.S. to find the true location of the source.

require less than 3 pointings to find the true position of the GRB and get VHE observations of the true source. However following all GBM GRBs where H.E.S.S. can cover 40% of the localisation regions (without adding a cut on the maximum allowed delay) requires a significant telescope time ($\sim$40 GBM GRBs follow-up observations), and will not be feasible for facilities like H.E.S.S. leading several astrophysical programs. On the other hand, if we choose to follow the GRBs where H.E.S.S. can cover more than 70% of the localisation region, it will give roughly 10 GBM GRB observations per year (in addition to the GRBs triggered by other instruments). From this study I estimate that H.E.S.S. will be able to cover the true position for $\sim$ 75% of the GBM tiled GRBs (3 out of 4 per year in Fig. A.6) with a knows true position. Since the number of GBM GRBs used in this study is not very large, this study should be extended to all the available data since 2008 in order to have a better estimated number. Due to the fact that we do not know the true position of all GBM GRBs used in this study, I cannot conclude on the fraction of GRBs found by H.E.S.S. from the entire GBM data set. These simulations take into consideration current H.E.S.S observation and visibility conditions; the low duty cycle of H.E.S.S. plays a major role in the inability to cover the true positions, either due to the fact that half of the GRBs are estimated to be in the northern hemisphere unreachable for H.E.S.S, or due to the fact that they arrived during the full Moon period where H.E.S.S observations are stopped for $\sim$ 2 days due to high level of moonlight.

I modify the ToO alert system to include a *test* plugin[1] that handles the tiling of GBM maps similarly to GWs and sends alerts as response to GBM alerts to the GRB team working on this implementation. Final cuts will be determined when the larger study is achieved for all GBM alerts since 2008 and the monitoring of the test module is over. For now GBM GRBs are followed only if the maximum follow-up delay does not exceed 4 hours and the observations occur during the whole night. The maximum allowed observation delay is expected to be loosened in the future when the tiling strategies are implemented. Unlike GW maps, GBM localisation maps are not instantly available on the web after an alert is received and only the image's URL is reported. The GBM plugin will search for the correct fits map to download and will check every minute for an update in case the map is not uploaded yet. On average it takes 10 to 15 minutes for GBM localisation fits files to become available. If after 20 minutes the maps is still not available, the GBM plugin will discard the alert. During this time, the H.E.S.S. ToO alert system will still be able to handle other incoming alerts in parallel.

[1] The plugins mentioned here are not scripts or modules like the ones described in Sec. 4.1, they are instead additions to the overall Too follow-up system that include modifications and updates of all the modules.

Appendix B

Results of the BBH GW follow-up with H.E.S.S. for GW170814, S190512at and S200224ca

Position	Start time (UT)	RA J2000 (deg)	DEC J2000 (deg)	Duration (min)	Zenith angle (deg)
1	2017-08-17 00:10	39.58	-48.72	28	50
2	2017-08-17 00:40	45.78	-45.59	26	49
3	2017-08-18 00:10	39.24	-51.27	28	50
4	2017-08-18 00:40	46.49	-42.76	28	48
5	2017-08-18 01:10	48.47	-39.77	28	44
6a	2017-08-18 01:40	44.85	-48.39	12	39
6b	2017-08-18 01:58	44.85	-48.39	9	36
7	2017-08-18 23:56	38.58	-46.20	28	50
6c	2017-08-19 00:26	44.85	-48.39	28	50
8	2017-08-19 00:56	49.24	-37.13	28	46
9	2017-08-19 01:26	42.29	-46.26	28	37
10	2017-08-19 01:56	-34.50	-46.26	28	34
11	2017-08-19 02:26	49.86	-42.37	28	31

Table B.1: H.E.S.S. observations of GW170814 BBH merger GW event.

Position	Start time (UT)	RA J2000 (deg)	DEC J2000 (deg)	Duration (min)	Zenith angle (deg)
1a	2019-05-13 01:14	250.31	-26.61	28	14
1b	2019-05-13 01:45	250.31	-26.61	28	21
2	2019-05-13 02:14	251.72	-27.95	22	26
3a	2019-05-13 02:38	248.91	-25.28	20	34
3b	2019-05-13 03:01	248.91	-25.28	28	39
5	2019-05-13 03:29	254.53	-27.95	28	40

Table B.2: H.E.S.S. observations of S190512at BBH merger GW event.

Position	Start time (UT)	RA J2000 (deg)	DEC J2000 (deg)	Duration (min)	Zenith angle (deg)
1	2020-02-25 01:21	174.99	-9.90	28	20
2	2020-02-25 01:52	173.58	-6.58	28	29
3	2020-02-25 02:21	176.31	-13.02	10.2	30

Table B.3: H.E.S.S. observations of S200224ca BBH merger GW event.

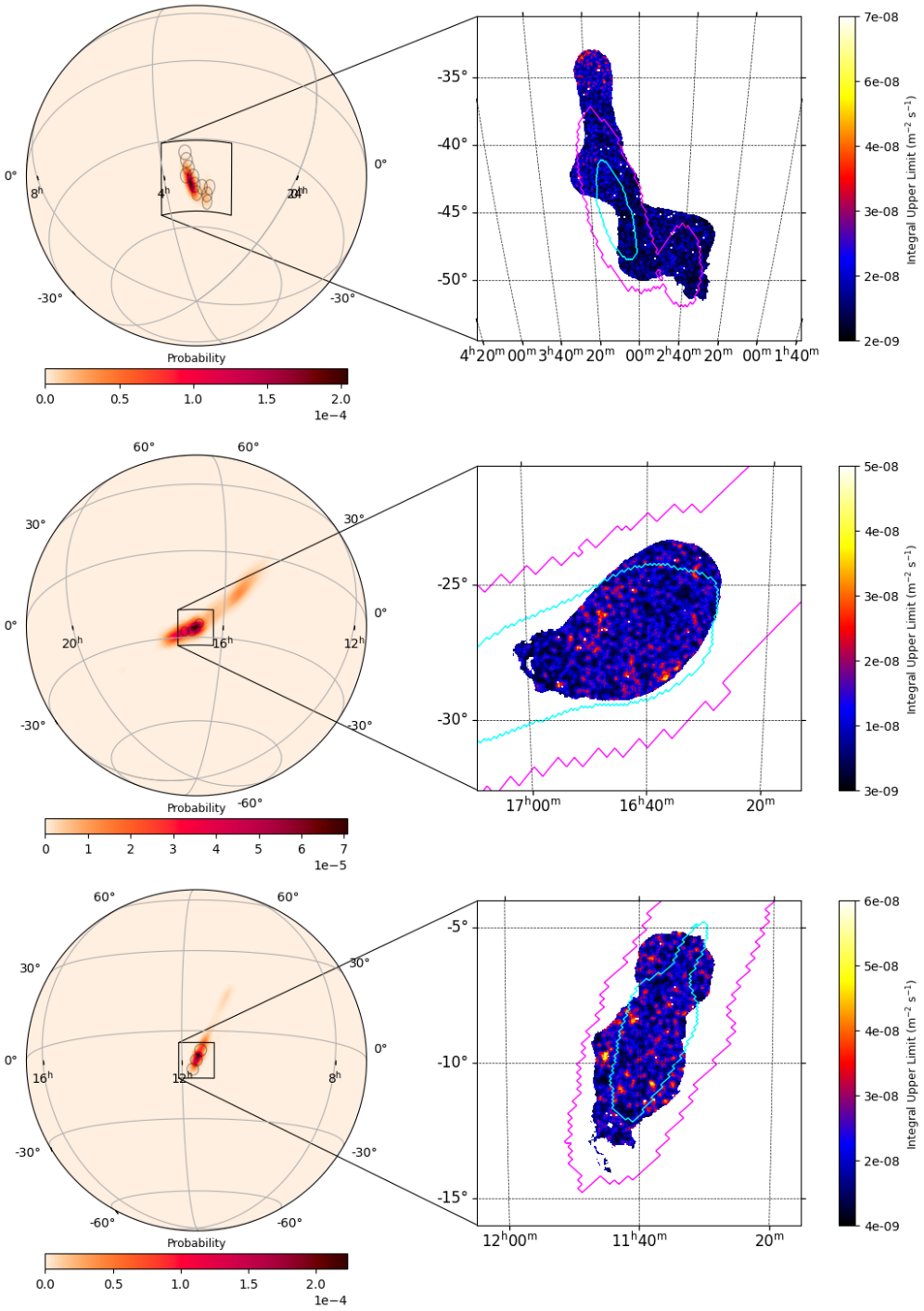

Figure B.1: Integral upper limit maps computed from the H.E.S.S. observations of GW170814 (upper), S190512at (middle) and S200224ca (lower) BBH events presented in Tab. B.1, B.2 and B.3 assuming an E^{-2} source spectrum and a 1-10 TeV energy range. The magenta and cyan lines represent respectively the 90% and 50% localisation contours of the newest published GW map in [4] for GW170814, in [13] for S190512at and in [225] for S200224ca.

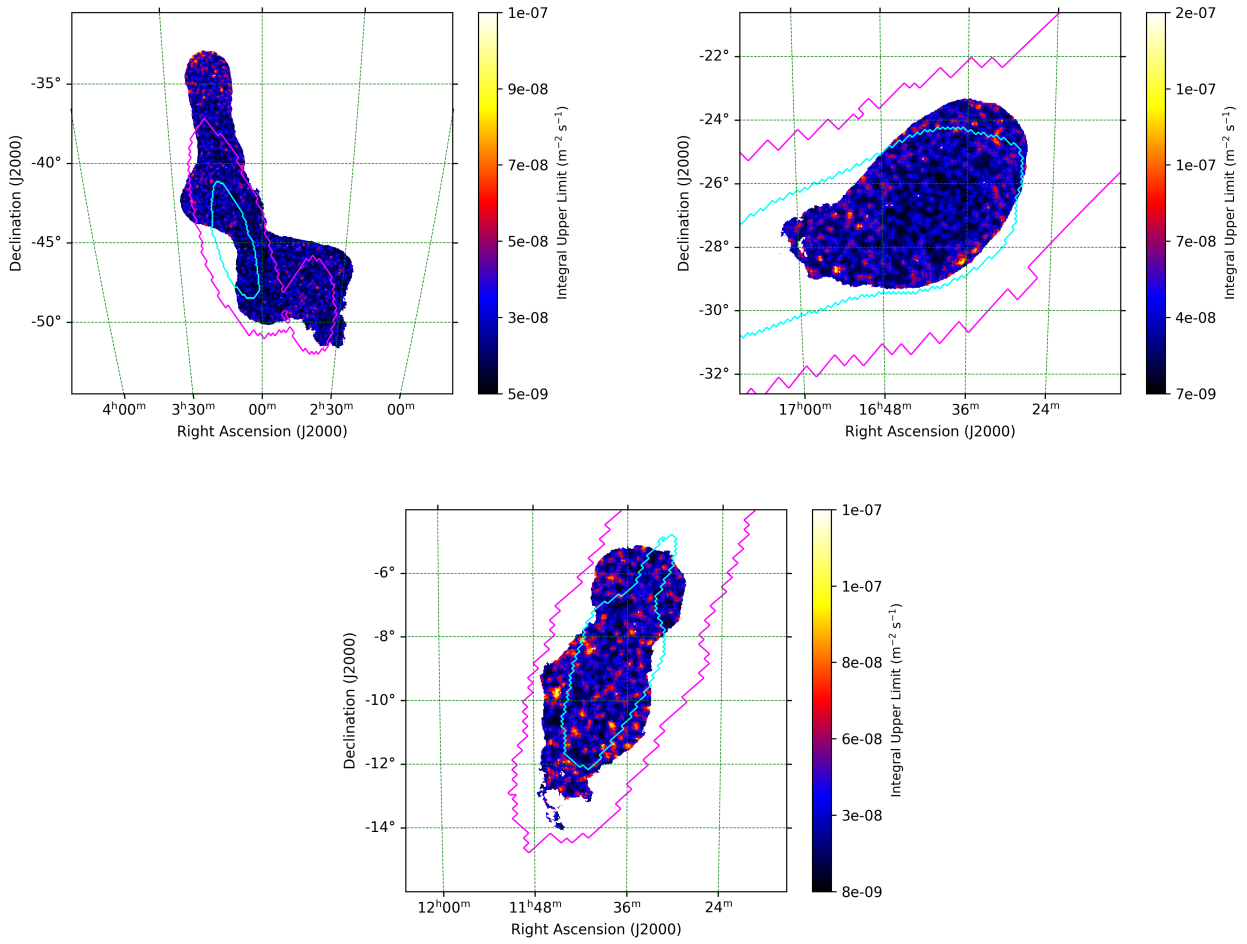

Figure B.2: Integral upper limit maps computed from the H.E.S.S. observations of GW170814 (upper left) events presented, S190512at (upper right) and S200224ca (lower) presented in Tab. B.1 B.2 and B.3. We assume an internal E^{-2} source spectrum with EBL absorption effect and a specific energy range as shown in Tab. 5.3. The magenta and cyan lines represent respectively the 90% and 50% localisation contours of the newest published GW map in [4] for GW170814, in [13] for S190512at and in [225] for S200224ca.

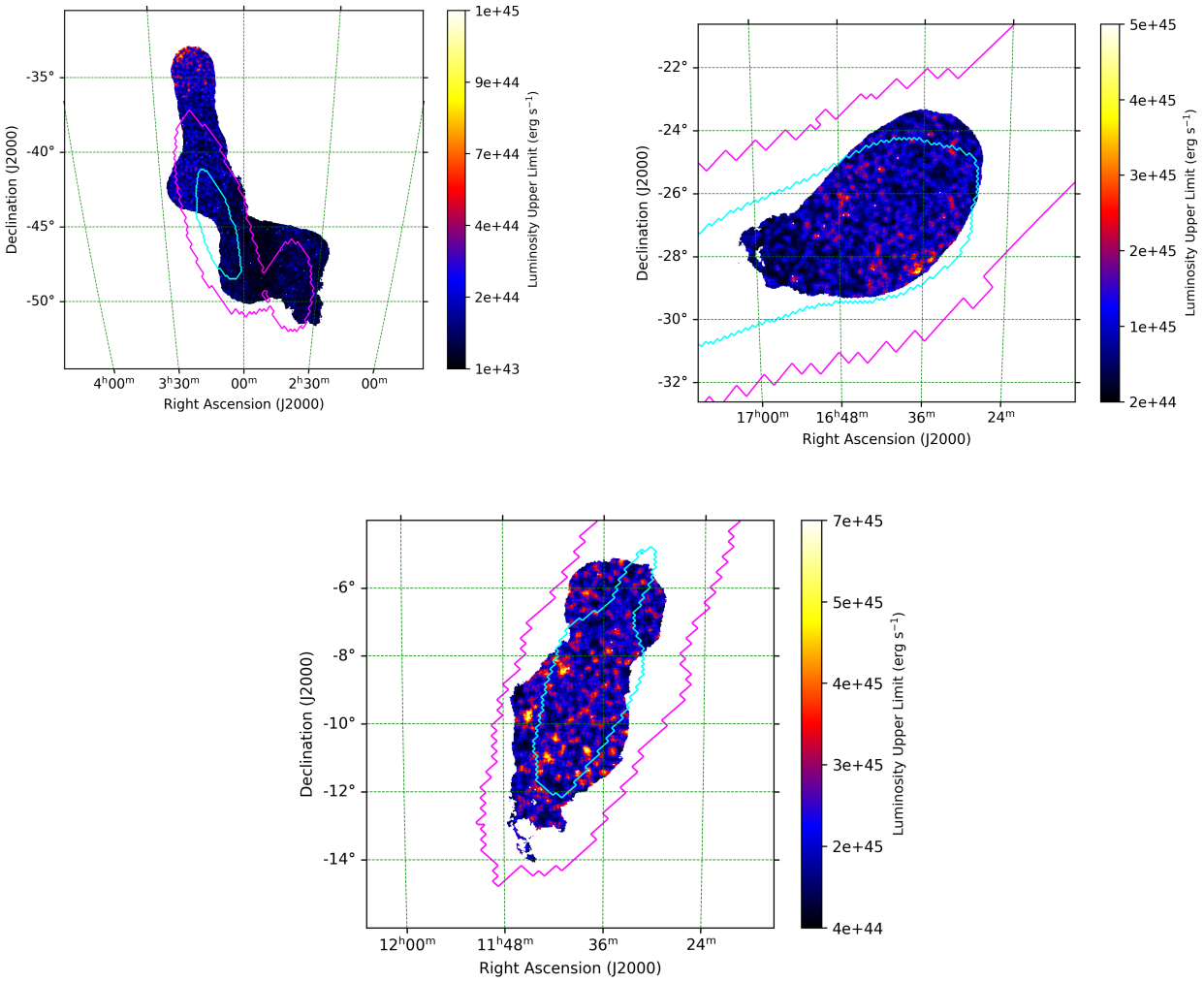

Figure B.3: Luminosity upper limit maps computed from the H.E.S.S. upper limit map for GW170814 (upper left), S190512at (upper right) and S200224ca (lower) presented in Fig. B.1 (assuming an E^{-2} source spectrum and a 1-10 TeV energy range) and taking into consideration the per-pixel variation of the mean distance and redshift in the newest GW maps. The magenta and cyan lines represent respectively the 90% and 50% localisation contours of the newest published GW map in [4] for GW170814, in [13] for S190512at and in [225] for S200224ca.

Appendix C

Comparison plots for the M++ analysis of BBH mergers

C.1 Comparison of the M++ analysis configurations

In the following the derived maps are preliminary and not used for the final publication of the results.

In Fig. C.1, I show integral upper limit maps computed for the S190512at GW event with data from all five telescopes and data from the four 12-m telescopes only. The analysis used is `M++ HESS-II Stereo Loose` and `M++ HESS-I Stereo Loose` respectively. The distribution of the entries for both maps are presented in Fig. C.2. The histograms show a similar distribution of the entries with comparable mean and median upper limit with a difference $< 8\%$. Similar results are found for all the other GW events.

In Fig. C.3 I show integral upper limit maps computed for the S190512at GW event with data from the four telescopes with *loose* and *standard* cuts. The analysis used is `M++ HESS-I Stereo Loose` and `M++ HESS-I Stereo Std` respectively. The distribution of the entries for both maps are presented in Fig. C.4. The histograms show a similar distribution of the entries with comparable mean and median upper limit with a difference $< 3\%$.

Similar results are found for all the other GW events. Therefore I conclude that the sensitivity for all three types of analysis is similar and should not play a major role in the choice of analysis.

I note that for CT1-4 and *Loose* configurations, the effective FoV is larger than for CT1-5 and *Standard* configurations, hence a larger number of entries is expected for the CT1-5 and the *Loose* analysis.

Tab. C.1 shows the difference in energy threshold for the four events analysed in this study for the M++

`HESS-I Stereo Loose` and `M++ HESS-I Stereo Std` analysis. In Tab. C.2, I show the effective coverage of the observations for each events using the maps from the *update* GCN notices distributed and not from the final published maps.

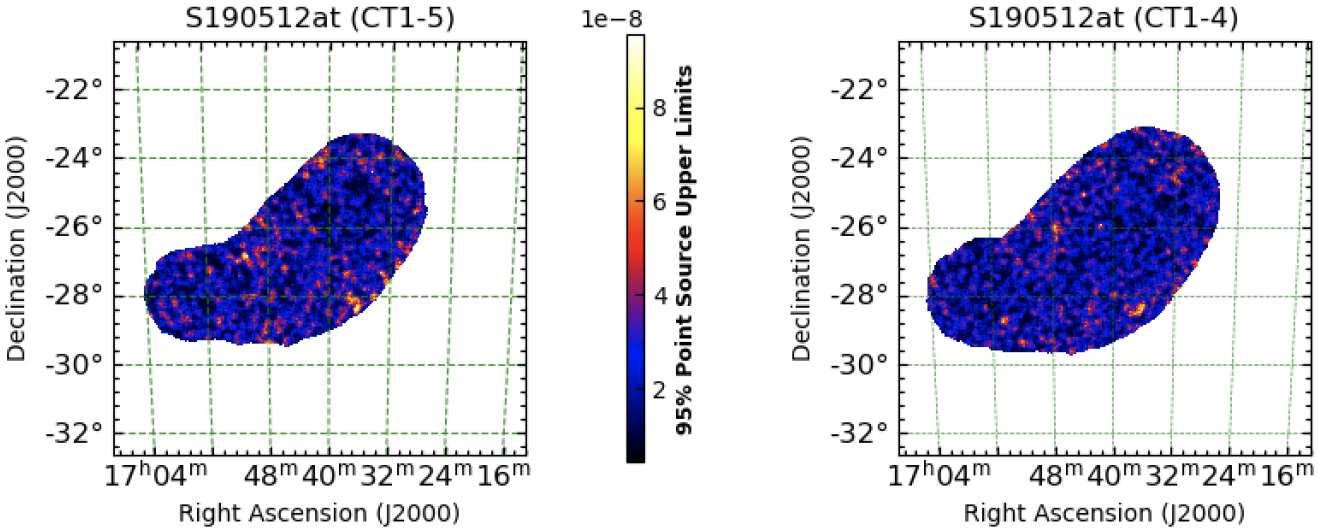

Figure C.1: UL maps determined from the S190512at follow-up with the M++ `HESS-II Stereo Loose` (left) and `M++ HESS-I Stereo Loose` (right) considering an E^{-2} spectrum for $\mathrm{E} > 0.28\,\mathrm{TeV}$ corresponding to the highest threshold from the two analysis.

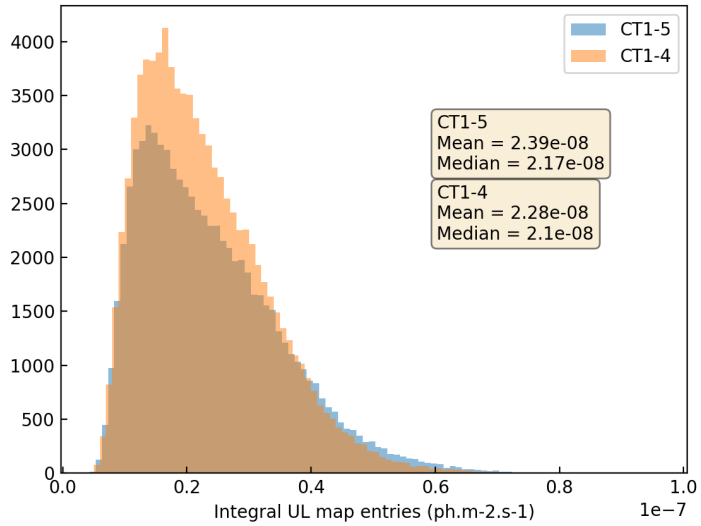

Figure C.2: Distribution of the UL maps in Fig. C.1 determined from the S190512at follow-up with the `M++ HESS-II Stereo Loose` and `M++ HESS-I Stereo Loose`.

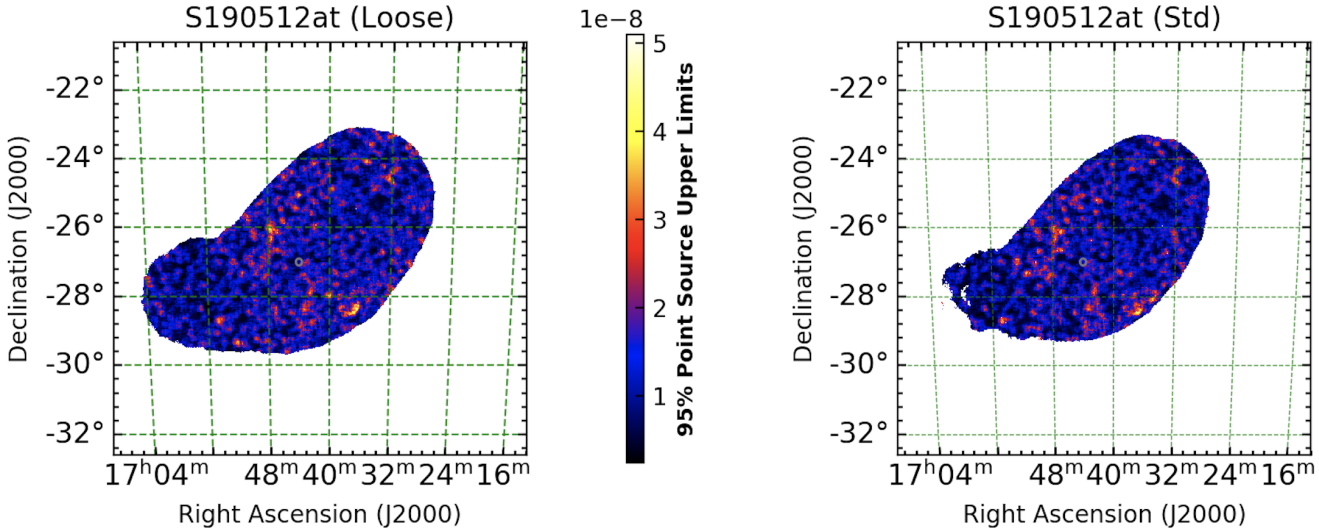

Figure C.3: UL maps determined from the S190512at follow-up with the `M++ HESS-I Stereo Loose` (left) and `M++ HESS-I Stereo Std` (right) considering an E^{-2} spectrum for $1\,\mathrm{TeV} < \mathrm{E} < 10\,\mathrm{TeV}$.

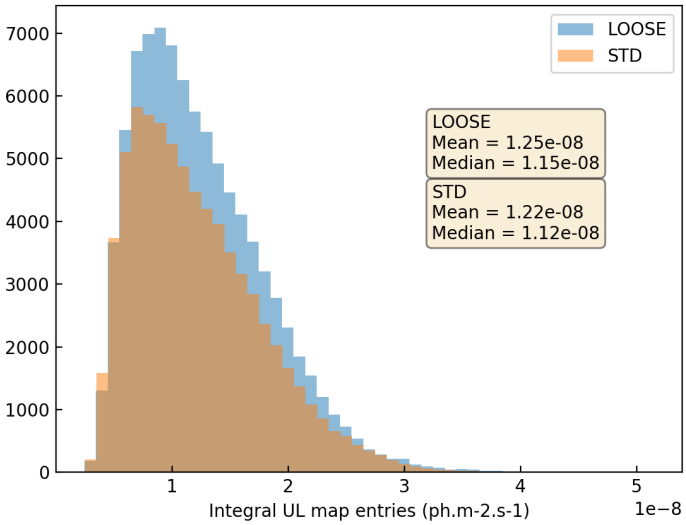

Figure C.4: Distribution of the UL maps in Fig. C.3 determined from the S190512at follow-up with the `M++ HESS-I Stereo Loose` and `M++ HESS-I Stereo Std`.

Analysis	GW170814	S190512at	S190728q	S200224ca
HESS-I Stereo Loose	0.37 TeV	0.32 TeV	0.32 TeV	0.19 TeV
HESS-I Stereo Std	0.42 TeV	0.31 TeV	0.35 TeV	0.22 TeV

Table C.1: Energy threshold determined from two types of data analysis of four GW events follow-up.

	GW170814	S190512at	S190728q	S200224ca
`HESS-I Stereo Loose`	86.6%	30.7&	82.3%	72.1%
`HESS-I Stereo Std`	75.4%	25.8%	78.2%	66.7%

Table C.2: Effective coverage determined from two types of data analysis of four GW events follow-up using maps distributed in the *update* GCN notices.

C.2 Comparison plots for E_{th}

Here I show $E_{thr,pos}$ maps for the GW170814 event using different methods. In Fig. C.5 and C.6 I compare the results for when a time weighted method following Eq. 5.5 and when a maximum threshold method following Eq. 5.4 is used. I find that both methods lead to similar values of the median E_{thr}, with a difference of $\sim$ 12%. I then show for a time weighted method the resulting $E_{thr,pos}$ maps for a $\psi_{\mathrm{cut}} = 2\,\mathrm{deg}$ and a $\psi_{\mathrm{cut}} = 2.5\,\mathrm{deg}$. The difference between the resulting median values is in the order of $\sim$6%.

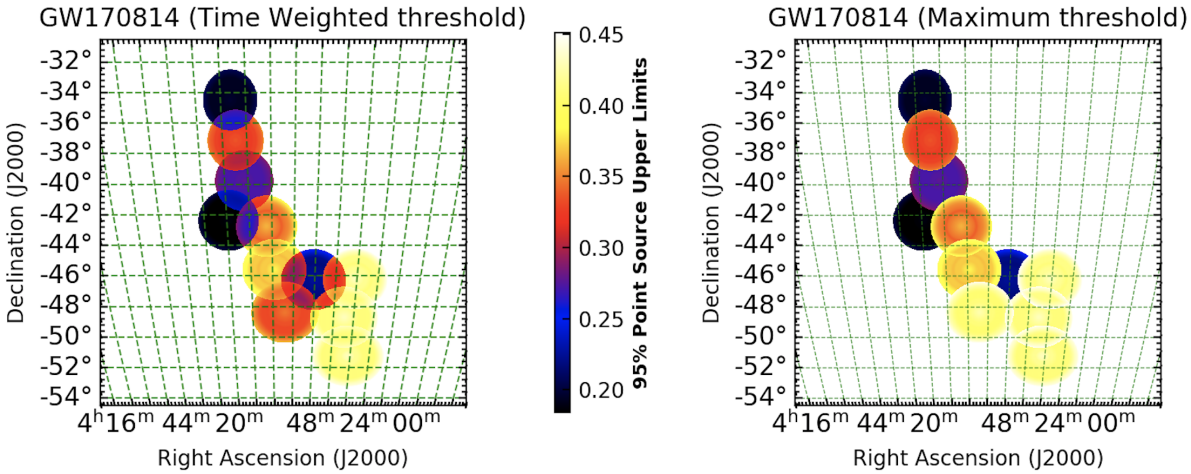

Figure C.5: Energy threshold map computed for $\psi_{\mathrm{cut}} = 2\,\mathrm{deg}$ with time weighted off-axis (left) (following Eq. 5.5) and a maximum value (right) (following Eq. 5.4) $E_{thr,pos}$.

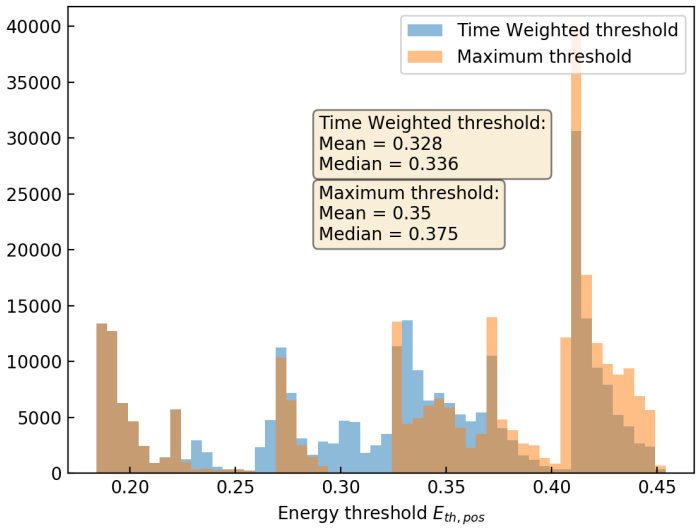

Figure C.6: Distribution of the entries in Fig. C.5.

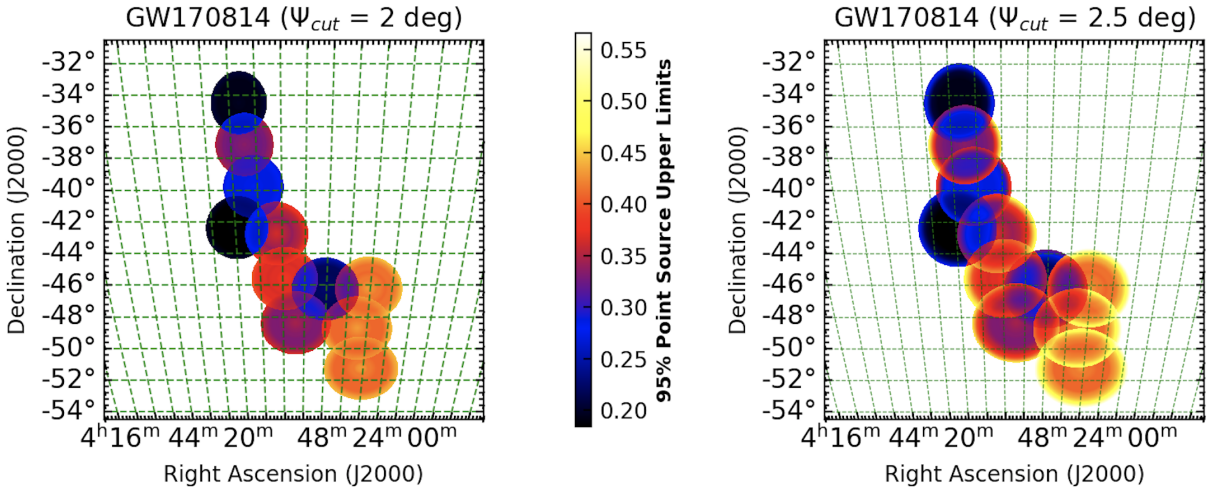

Figure C.7: Energy threshold map computed with a time weighted off-axis $E_{thr,pos}$ for a $\psi_{\rm cut} = 2\,\deg$ (left) and a $\psi_{\rm cut} = 2.5\,\deg$ (right).

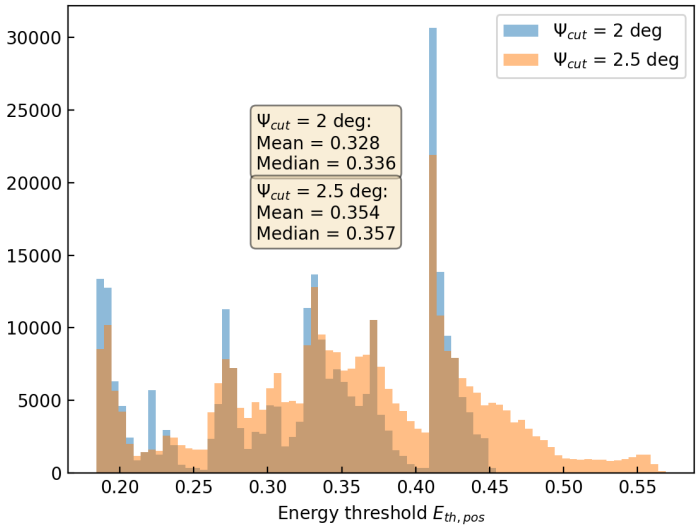

Figure C.8: Distribution of the entries in Fig. C.7.

C.3 Comparison plots for $E_{max} = 10$ and $E_{max} = 100$

In Fig.C.9 I show the UL maps an their distribution in Fig. C.10 considering $\rm E_{max} = 10\,TeV$ and $\rm E_{max} = 100\,TeV$. The difference is $\sim$ 3%

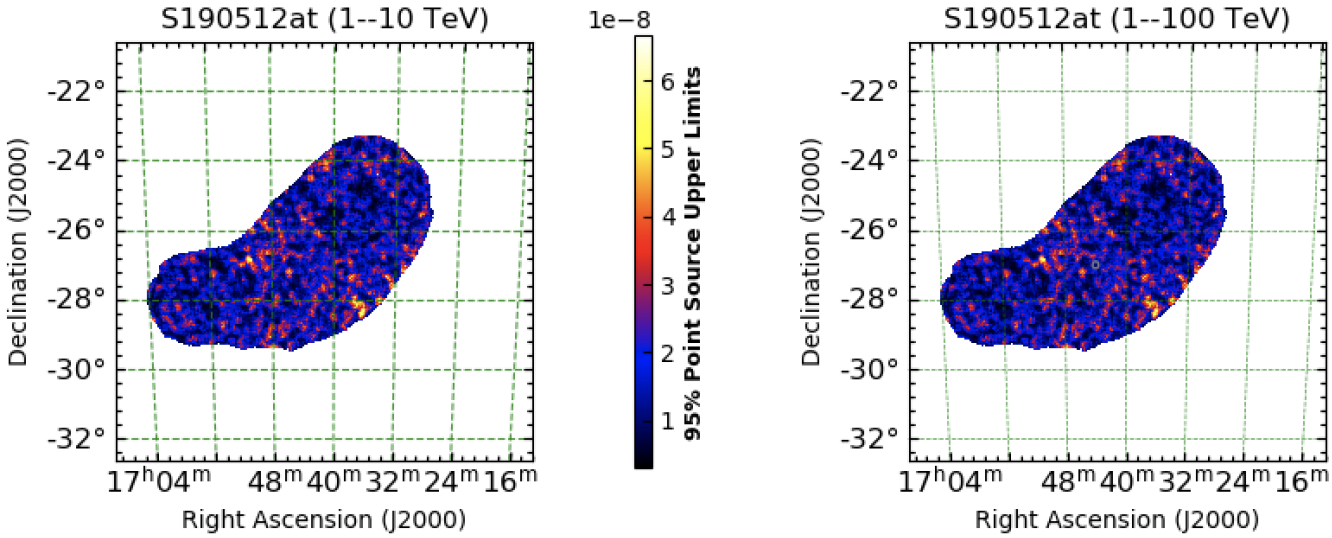

Figure C.9: Upper limit maps computed with $\mathrm{E_{max}} = 10\,\mathrm{TeV}$ (left) and $\mathrm{E_{max}} = 100\,\mathrm{TeV}$ (right) for S190512at GW event follow-up.

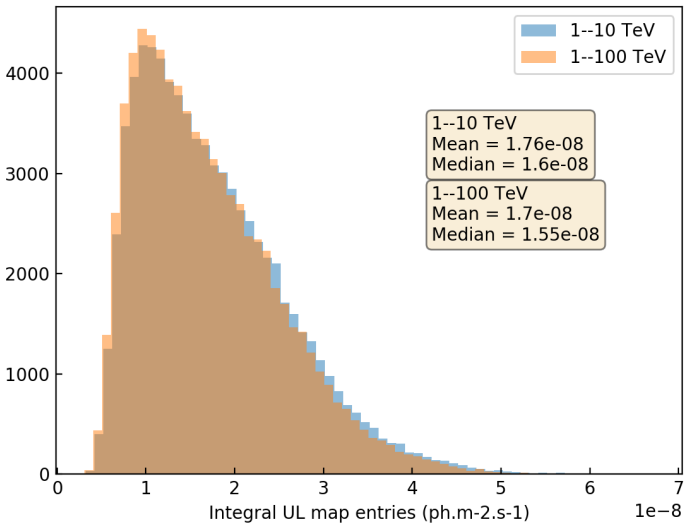

Figure C.10: Distribution of the entries in Fig. C.9.

université PARIS-SACLAY

ÉCOLE DOCTORALE
Particules, hadrons, énergie et noyau : instrumentation, imagerie, cosmos et simulation (PHENIICS)

Titre : Astrophysique transitoire et multi-messager avec les télescopes à imagerie Tcherenkov atmosphérique

Mots clés : Rayon Gamma -- Phénomène Transitoire -- Onde gravitationnelle -- Sursaut gamma - Sursaut radio rapide -- Multimessager

Résumé : Je recherche des émissions de très hautes énergies (VHE) à partir de trois types de sources transitoires : les ondes gravitationnelles, les sursauts gamma qui peuvent en émerger et les sursauts radio rapides. Pour les ondes gravitationnelles, la localisation des évènements sur plusieurs dizaines de degrés dans le ciel nécessite un traitement spécial pour le suivi. J'optimise des stratégies de suivi ondes gravitationnelles qui reposent sur la maximisation de la probabilité de détection d'émission électromagnétique homologue, soit en utilisant uniquement des cartes de localisation, soit en utilisant aussi la distribution locale des galaxies dans l'Univers. Les outils développés sont testés et évalués. À l'aide de ces outils et des compétences acquises, je développe un système de réponse automatique aux alertes ondes gravitationnelles pour les télescopes H.E.S.S. et LST et aux alertes UTMOST pour H.E.S.S. Je contribue à la mise à jour du programme de H.E.S.S. de suivi de sursaut gamma. Avec les outils mis en place, H.E.S.S a observé 6 événements ondes gravitationnelles, dont 4 fusions de trous noires. D'autres sources transitoires sont également observées par H.E.S.S., dont le sursaut gamma GRB 190829A, la fusion d'étoile à neutron GW170817 (à long terme aussi), des sursauts radio rapides et la source SGR 1935+2145. GRB 190829A est le troisième sursaut gamma détecté à très hautes énergies au sol. Les données VHE, sont analysées (ainsi que les données X et UV pour FRB 20171019A) pour les autres sources. Aucune émission significative de VHE n'a été trouvée durant les suivis des fusions de trous noirs et durant la campagne d'observation à long terme de GW170817, ainsi que pour les sursauts radio rapide et la source SGR 1935+2154. Je déduis des limites supérieures et publie ces résultats. Les limites déduites permettent de contraindre le champ magnétique dans le vestige de GW170817, de placer des limites supérieures sur l'émission VHE persistante et transitoire provenant des sursauteurs gamma mou, et d'établir des perspectives pour O4.

Title: Transient Multi-messenger Astrophysics with Imaging Atmospheric Cherenkov Telescopes

Keywords: Gamma-ray -- Transient -- GW -- GRB -- FRB -- Multi-messenger

Abstract: I hunt very-high-energy (VHE) emission from three classes of transient sources: Gravitational waves (GW), their possible gamma-ray bursts (GRB) counterparts and fast radio bursts (FRB). I tackle three types of challenges: Pre-observation, focusing on efficient scheduling, observation planning and fast telescope response; in-observation, focusing on efficient data acquisition on the transients as an expert on call; post-observation, focusing on efficient data analysis in the search for a significant signal. For the GW events, the poor localization requires a special treatment for the follow-up. I work on the optimization of GW follow-up strategies that rely on the maximization of the probability of detecting counterparts to transient GW events either by using solely GW localization maps or by correlating the local distribution of the galaxies in the Universe with GW maps. The tools are combined in a GW scheduler, tested and assessed. Using the developed tools and acquired skills, I develop automatic response schemes to GW alerts for the H.E.S.S. and LST telescopes and a response to UTMOST FRB alerts for H.E.S.S. I also contribute to the update of the GRB program in H.E.S.S. on the technical follow-up front. With the implemented tools, H.E.S.S observed 6 GW events, of which 4 BBH mergers. Other transient sources, for which I am involved in the analysis, are observed also by H.E.S.S.: GRB 190829A, GW170817 (long-term), FRB events and the soft gamma-ray repeater (SGR) SGR 1935+2145. GRB 190829A is the third GRB to be observed at VHE energies on the ground and the second one by H.E.S.S. The VHE data (in addition to the X-ray and UV data for FRB 20171019A) is analysed for the other transients. No significant VHE emission was found during the BBH merger follow-up and the GW170817 long-term follow-up observation campaigns. The same non-detection was found for the FRBs and SGR 1935+2154. For those, a search for variability on the minutes to sub-seconds scale did not lead to any significant detection either. Upper limits are derived from the observations of the transients presented above. These results are published and the upper limits permit to constrain the magnetic field in the GW170817 remnant, to constrain the persistent and transient emission from SGR bursts and to derive prospects for the fourth GW observation run, O4.

Maison du doctorat de l'Université Paris-Saclay
2ème étage aile ouest, Ecole normale supérieure Paris-Saclay
4 avenue des Sciences,
91190 Gif sur Yvette, France